ABSTRACT

Title of dissertation: A SEARCH FOR RELATIVISTIC
MAGNETIC MONOPOLES WITH THE
ICECUBE 22-STRING DETECTOR

Brian J. Christy, Doctor of Philosophy, 2011

Dissertation directed by: Professor Kara Hoffman
Department of Physics

Magnetic monopoles are particles which act as a source for divergent magnetic fields, equivalent to a proton's electric field. Beyond simply adding the final symmetry to Maxwell's equations, their existence would solve numerous outstanding problems in the particle physics community. However, no conclusive evidence for their existence has been found.

Magnetic monopoles possess many unique characteristics that allow for detection from a variety of experimental methods. One property is the large scaling of the Cherenkov radiation (~ 8300) compared to electrically charged particles. Magnetic monopoles are postulated to be extremely heavy ($\sim 10^4 - 10^{17}$ GeV). However, they would be topologically stable and accelerated via magnetic field lines throughout the universe, potentially reaching energies $\sim 10^{15}$ GeV. Therefore, searches for relativistic magnetic monopoles incident on Earth are an important piece to the overall experimental search.

The IceCube neutrino observatory, located at the South Pole, offers a novel environment to search for these particles. IceCube is a km^3 grid of light sensors

buried deep within the Antarctic Ice Shelf and represents the most colossal neutrino telescope in the world. The large instrumented volume and relatively clear glacial ice allows for a significant improvement in sensitivity to the bright tracks relativistic magnetic monopoles would exhibit.

The main background comes from large muon bundles produced in air showers generated by the highest energy cosmic rays. The depth of the detector allows for a limited rejection of these events from the Southern Hemisphere, while the Earth acts as an opaque shield to these events traveling from the Northern Hemisphere. In contrast, a large range of potential magnetic monopole masses and energies considered ($M \gtrsim 10^7 \, \mathrm{GeV}$, $E \gtrsim 10^{11} \, \mathrm{GeV}$) can travel completely through the Earth while remaining relativistic.

This dissertation details the first search performed for these relativistic magnetic monopoles with IceCube data. The data is from 2007, when IceCube operated as a partially completed detector with an instrumented volume of ~ 0.2 km^3. It considers monopoles at four discrete speeds: $\beta = 0.76, 0.8, 0.9, 0.995$, ranging from just above the Cherenkov threshold in ice to a boost factor of 10. Discrimination between a potential magnetic monopole signal and background is achieved by considering the brightness and direction of the event. After an initial search revealed deficiencies in the simulated background model, a more conservative analysis produces limits that are $\sim 10 \, \mathrm{x}$ better than previous searches. The final limits are then transformed to be a limit on an isotropic flux at the Earth's surface, due to the dependence on direction to the overall sensitivity of the analysis.

A SEARCH FOR RELATIVISTIC MAGNETIC MONOPOLES WITH THE ICECUBE 22-STRING DETECTOR

by

Brian John Christy

Dissertation submitted to the Faculty of the Graduate School of the
University of Maryland, College Park in partial fulfillment
of the requirements for the degree of
Doctor of Philosophy
2011

Advisory Committee:
Dr. Kara Hoffman, Chair/Advisor
Dr. Gregory Sullivan
Dr. Erik Blaufuss
Dr. Zackaria Chacko
Dr. Cole Miller, Dean's Representative, Dept. of Astronomy

Dedication

For Isaac Dean Christy

Your papa loves and misses you very much

Acknowledgments

There is a very long list of people to thank without whom this work would never have been done. An abbreviated attempt is presented here.

I would like to thank all those who helped me professionally through this. Kara, for agreeing to take me on as a student and introducing me to IceCube (and the South Pole). Greg, for keeping me focused on the big reasons one even cares about magnetic monopoles. Erik, for his infinite help in keeping the cluster running. Troy, Christian, and Don, for their patience in dealing with my computer skills. Above all, Alex for convincing me to study magnetic monopoles (still not sure if that deserves a thank you) and Henrike for all her help with datasets and random questions as I reached the end. Finally, I would like to thank John, Ralf, Phil, Peter, Kevin, Warren, Mike, Rob, and Josh for the endless hours of stupid questions and distractions that sharing an office provides.

I would like to thank all those who helped me personally as well. My father, who inspired me to science. My mother, who taught me to remain humble (even after I get a Ph.D.). My family and friends, who provided the best times of these last few years and helped me keep my sanity. My amazing wife Kristen, who never stopped believing in me. My son John, whose smile at the end of a long day made it all worth it.

In closing, I would like to thank God. Not in the generic sense that many often invoke, but in a very real sense in which He guided me through the most challenging times I have ever faced. His grace has been sufficient to supply all my needs.

Table of Contents

List of Tables

List of Figures

List of Abbreviations

Chapter 1

Introduction

The search for magnetic monopoles has yielded no conclusive evidence for their existence. Despite this, every time new opportunities avail themselves, the search is vigorously renewed. This drive arises from the multiple problems their existence would solve, most notably the quantization of electric charge. Magnetic monopoles find a natural home in many Grand Unified Theories (GUTs) as topological defects for certain symmetry breaking schemes. Add to this the symmetry that such a particle would add to Maxwell's Equations, and the quest for their discovery becomes quite understandable. A new regime of study that is becoming available now is that of large scale neutrino telescopes. In particular, the ability of these types of telescopes to detect Cherenkov emitting muons is ideal for a relativistic magnetic monopole since the intensity of radiation is much larger than that of a single muon. This dissertation will describe the first search using the IceCube neutrino telescope.

An original analysis was developed in a completely blind fashion, in which only a small sample of the experimental data ('burn sample') was considered while devising the final cuts. After unblinding the remaining data sample, a significant excess of real events were observed that demonstrated a lack of quality in the simulation previously un-noticed due to the low statistics in the burn sample. After determining these events were background and not a true monopole signal, a simpli-

fied analysis was developed. This analysis, though a posteriori, is still performed in a blind fashion in that the final cut optimization is found based solely on simulated data. For a discussion on the questions of bias that this process raises, see Appendix D.

The outline of this dissertation is as follows:

- Chapter 2 will provide the background to magnetic monopoles.

- Chapter 3 will give an overview of neutrino astronomy

- Chapter 4 will describe the IceCube detector.

- Chapter 5 will give an overview of the datasets employed.

- Chapter 6 will detail various methods used for the analysis.

- Chapter 7 will describe the original selection of magnetic monopoles from a background of muons and neutrinos produced by cosmic rays.

- Chapter 8 will summarize the results of the original analysis and what deficiencies were found.

- Chapter 9 will describe the motivation for changes in the new, a posteriori, analysis

- Chapter 10 will discuss the systematic uncertainties

- Chapter 11 will present the final results

- Chapter 12 will summarize the analysis and discuss future potential improvements.

Chapter 2

Magnetic Monopoles

2.1 History of Magnetism

Magnetism has a long history, likely first discovered by the Chinese before medieval times[1]. The first recorded systematic study was performed by Petrus Peregrinus de Maricourt while crusading in King Charles of Anjou's siege on the town of Lucera, Italy in 1269[2]. In letters written to a friend, he described placing a thin iron sheet upon a lump of magnetite, marking the lines in which it would orient itself. From this, the word 'pole' first entered the lexicon to describe where the lines would intersect. While truly a momentous achievement, he belies his scientific insights by also spending an entire section describing ideas for a perpetual motion machine.

The next major advance in understanding magnetism was William Gilbert's seminal work *On the Loadstone and Magnetic Bodies*[3]. He was the first to associate the Earth as a giant loadstone. This represented a tremendous step forward in unifying observations on different scales into a single scientific concept. He performed countless meticulous experiments with different loadstone shapes and used the results to refute many claims by others on its mysterious properties. A personal favorite claim: placing a loadstone under a spouse's pillow will make them awake should they be cheating.

As science moved into a quantitative age, the first direct formulas for magnetic force were derived by Coulomb[4], who used long thin magnets to demonstrate magnetic poles exhibited the same force relations of electric charges. Further work by Ampere[5] asserted that magnetism was solely a result of electric currents, representing the first step in unifying the magnetic and electric forces as well as giving an argument for the non-existence of magnetic monopoles. This idea became enshrined in standard physics with the revolutionary work of J.C. Maxwell[6], who fully unified electricity and magnetism. This can be expressed with the following formulas (with the modern notation used by Oliver Heaviside after selecting formulas from an earlier Maxwell paper[7]):

$$\nabla \cdot \vec{E} = 4\pi\rho_e$$
$$\nabla \cdot \vec{B} = 0$$
$$\nabla \times \vec{B} - \frac{1}{c}\frac{\partial \vec{E}}{\partial t} = \frac{4\pi}{c}\vec{j_e}$$
$$-\nabla \times \vec{E} - \frac{1}{c}\frac{\partial \vec{B}}{\partial t} = 0$$
(2.1)

The zero terms represent the physical absence of magnetic charge and magnetic currents, which would require a magnetic monopole. However, there is no aspect of the theory that requires these terms to be zero, and one could easily modify the formulas to be:

$$\nabla \cdot \vec{E} = 4\pi\rho_e$$
$$\nabla \cdot \vec{B} = 4\pi\rho_m$$
$$\nabla \times \vec{B} - \frac{1}{c}\frac{\partial \vec{E}}{\partial t} = \frac{4\pi}{c}\vec{j_e}$$
$$-\nabla \times \vec{E} - \frac{1}{c}\frac{\partial \vec{B}}{\partial t} = \frac{4\pi}{c}\vec{j_m}$$
(2.2)

Despite suggestions of their existence by P. Curie[8] and experimental claims

by Ehrenhaft[9], it has been generally accepted that magnetic monopoles do not exist. However, advances in the twentieth century have found new motivations for magnetic monopoles, renewing the intensity with which science has searched for them. For a more complete overview of the literature, see [10].

2.2 Charge

In 1931, Dirac demonstrated that the quantum mechanical system of an electric and magnetic monopole requires all electric and magnetic charges to be quantized via the relation $g = Ne/2\alpha$, where α is the fine structure constant $(\sim \frac{1}{137})$[11].

This represents a crucial result, as the existence of a single magnetic monopole would answer the question of charge quantization. Its value would set the value of the basic electric charge. In order for this relation to hold, any further charge that is added would be constrained to integral multiples of these two basic charges. As Dirac noted, 'it would be odd for nature not to utilize it'.

Since that time, this condition has been derived in many ways. Two methods are presented. The first is a semi-classical argument taken from Jackson's text on Electrodynamics[12]. The second is a fully quantum mechanical version by Wu and Yang[13], as summarized in J.J. Sakurai's text on quantum mechanics[14].

2.2.1 Semi-Classical Derivation

Consider a magnetic monopole situated at the origin and a proton moving at speed v in the z-direction at some impact parameter b away in the x-direction (see
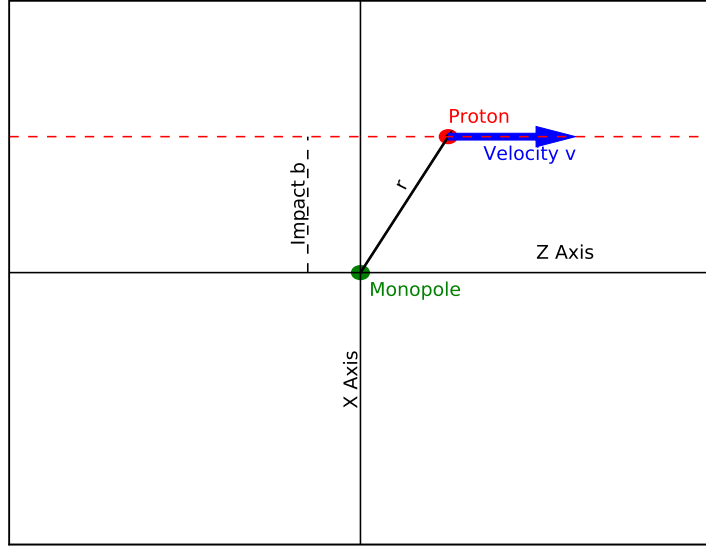
Figure 2.1: Schematic drawing of setup for semi-classical derivation of charge quantization

Figure 2.1). Let the proton cross the x axis at time $t = 0$. Analogous to the electric field produced by a point charge, the magnetic monopole will produce a magnetic field of $\vec{B} = \frac{g}{4\pi r^2}\hat{r}$ where g is the magnetic charge (in SI units, to remain consistent with Jackson). This would cause the proton to feel a resulting force of

$$F_y = ev_z B_x = \frac{egv\sin\theta}{4\pi r^2} = \frac{egvb}{4\pi(b^2 + (vt)^2)^{\frac{3}{2}}} \tag{2.3}$$

If one assumes the impact parameter b is large enough that deflections into the y direction can be ignored, then the change in momentum the proton will feel for the entire path can be written as

$$\Delta p_y = \frac{egvb}{4\pi}\int_{-\infty}^{\infty}\frac{dt}{(b^2 + (vt)^2)^{\frac{3}{2}}} = \frac{eg}{2\pi b} \tag{2.4}$$

6

The corresponding change in angular momentum in the z-direction will be

$$\Delta L_z = b \Delta p_y = \frac{eg}{2\pi} \tag{2.5}$$

Notice that the impact parameter b is completely removed, allowing for the assumption that it is large. The final step represents the 'semi-classical' approximation by stating that changes in angular momentum should be quantized in units of $\hbar$. Hence, one arrives at the final quantization condition that

$$\frac{eg}{2\pi} = \frac{Nh}{2\pi} \therefore g = \frac{Nh}{e} = \frac{NZ_0 e}{2\alpha} \tag{2.6}$$

Here, $\alpha = \frac{e^2}{4\pi\epsilon_0 \hbar c} \rightarrow \frac{e^2}{\hbar c}$ and $Z_0 = \sqrt{\frac{\mu_0}{\epsilon_0}} \rightarrow 1$ in switching to Gaussian units.

2.2.2 Quantum Mechanical Derivation

Consider again a magnetic monopole situated at the origin and magnetic field of $\vec{B} = \frac{g}{r^2}\hat{r}$, with g representing the magnetic charge (in Gaussian units). One possible magnetic potential associated with this field is $A = \frac{g(1-\cos\theta)}{r\sin\theta}\hat{\phi}$. This potential is singular for $\theta = \pi$. In fact, any potential created must be singular at some value since vector calculus still demands $\triangledown \cdot B = \triangledown \cdot (\triangledown \times A) = 0$ if A is non-singular. A possible treatment of this problem is to define a second potential with a different singularity and use both to cover the entire space. Wu and Yang choose the following:

$$A^{(\mathrm{I})} = \frac{g(1-\cos\theta)}{r\sin\theta}\hat{\phi} \quad if\theta \neq \pi$$
$$A^{(\mathrm{II})} = -\frac{g(1+\cos\theta)}{r\sin\theta}\hat{\phi} \quad if\theta \neq 0 \tag{2.7}$$

7

One common result from quantum mechanics is when two potentials describe the same space, they must be related by a gauge transformation. Here, the gauge is given by the solution of the equation $A^{(II)} = A^{(I)} + \bigtriangledown \Lambda$. This leads to a gauge of $\Lambda = -2g\phi$.

Once a potential has been defined, one may look at how different wave functions will behave within this potential. Of particular interest is that of an electron. If one constructs two electron wave-functions that correspond to the two potentials above, their wave-functions must be related by the following in the region they overlap:

$$\Psi^{(II)} = \exp\left(\tfrac{ie\Lambda}{\hbar c}\right)\Psi^{(I)}$$

One can imagine tracing a circle around the $\theta = \frac{\pi}{2}$ plane for some finite value of r. Since both wave-functions are single-valued, $\Psi^{(I)}(\theta = \frac{\pi}{2})$ must return to its original value as ϕ goes from 0 to 2π. Therefore, in order for $\Psi^{(II)}(\theta = \frac{\pi}{2})$ also to return to its original value, $\frac{2eg}{\hbar c}$ must be an integer. Letting $\alpha = \frac{e^2}{\hbar c}$, one is left with the final Dirac quantization condition:

$$\frac{2eg}{\hbar c} = N \therefore g = \frac{N\hbar c}{2e} = \frac{Ne}{2\alpha} \tag{2.8}$$

2.3   Mass

Though the basic unit of charge for the magnetic monopole can be found exactly, nothing in the derivation provides any information about its mass. Information on the mass was not available until 1974 when t'Hooft and Polyakov

independently noticed the prediction of a particle with the Dirac charge[15, 16] that arises in Grand Unified Theories (GUTs). The particle appears as a topological defect representing the twisting of the Higgs field in a process known as the Kibble mechanism[17]. It arises when symmetry breaking within the GUT results in a U(1) subgroup. An important point to this is that GUTs require magnetic monopoles. Indeed, original estimates of their number density based on causal domains led to a prediction much larger than experimental limits[19]. It was in trying to solve this problem that motivated Alan Guth to propose the inflationary theory, realizing only afterwards the remaining cosmological problems it would solve[20].

Studying the properties of these topological defects allow for estimates of the monopole mass to be $\sim \Lambda/\alpha$, where Λ is the symmetry breaking scale. Typical GUT models (e.g. SU(5)) lead to a mass of $\sim 10^{16} - 10^{17}\,\text{GeV}$[18]. These would likely be much too heavy to achieve relativistic velocities.

However, many other mass ranges have been considered as different models for GUTs arise. So-called Intermediate Mass Monopoles(IMMs) with mass $\sim 10^5 - 10^{16}\,\text{GeV}$ may arise as a secondary symmetry breaking for models in which the original unified group undergoes multiple breaks before reaching the U(1) subgroup. An example would be the SO(10) group that would first split into SU(4)xSU(2)xSU(2) before finishing with SU(3)xSU(2)xU(1). Magnetic monopoles produced in this intermediate transition would have a mass $\sim 10^{10}\,\text{GeV}$[21].

A lower mass limit for magnetic monopoles arising from symmetry breaking can be found using the electroweak unification scale of $250\,\text{GeV}$. This leads to a mass of $4 \times 10^4\,\text{GeV}$. However, it is important to remember a magnetic monopole

Table 2.1: Various acceleration mechanisms for magnetic monopoles

Accelerator	Magnetic Field $\frac{B}{\mu G}$	Coherence Length $\frac{L}{\text{Mpc}}$	Kinetic Energy $\frac{gBL}{\text{GeV}}$
Normal galaxies	3-10	10^{-2}	$(0.3 - 1) \times 10^{12}$
Starburst galaxies	10-50	10^{-3}	$(1.7 - 8) \times 10^{11}$
AGN jets	˜100	$10^{-4} - 10^{-2}$	$1.7 \times (10^{11} - 10^{13})$
Galaxy Clusters	5-30	$10^{-4} - 1$	$3 \times 10^9 - 5 \times 10^{14}$
Extragal. sheets	0.1-1.0	1-30	$1.7 \times 10^{13} - 5 \times 10^{14}$

need not be a solution to one of these symmetry breaking problems. Hence, searches in all mass ranges are still important.

Due to the wide range of predicted values, the mass of the monopole is treated as a free parameter in the context of this search.

2.4 Acceleration Mechanisms

Magnetic monopoles produced in the early universe are topologically stable. They would accelerate via magnetic field lines throughout the cosmos following the equation $E_{\text{Kinetic}} = g \int_{path} \vec{B} \cdot \vec{dl} \sim gBL$ with L representing the field's coherence length. A variety of different sources can be used to estimate what energies are achievable for a single transit. Some of these are listed in Table 2.1 (see [22] and references therein).

Monopoles will be accelerated and de-accelerated as they random-walk through

the universe. This would produce a broad distribution of energies that should be centered on the energy from Table 2.1 times the square root of the number of expected domains the monopole travels. The energy distribution should be dominated by the extra-galactic sheets. An approximation for the number of domains is calculated in [22] as follows: Monopoles reaching the earth from the early universe would travel $H_0^{-1} \sim 5000\,\mathrm{Mpc}$. Estimating the coherent field length of extra-galactic sheets to be $\sim 50\,\mathrm{Mpc}$, the number of domains is of order $n \sim \frac{H_0^{-1}}{50\,\mathrm{Mpc}} \sim 100$. This corresponds to an energy distribution centered at $\sim 10^{15}\,\mathrm{GeV}$, providing enough energy for monopoles with masses $M \lessapprox 10^{14}\,\mathrm{GeV}$ to be relativistic. However, as with the mass, the analysis treats the kinetic energy of the magnetic monopole as a free parameter, e.g. no assumption is made about its value.

2.5   Cherenkov Radiation

The strategy of this analysis is to utilize the large underground neutrino telescope IceCube to detect magnetic monopoles traveling at relativistic speeds through the South Pole ice. The motivation to consider relativistic monopoles is due to their much brighter Cherenkov emission compared to electrically charged particles.

Cherenkov emission occurs when the particle emitting light travels faster than the light itself in the medium. This is visualized in Figure 2.2 which considers a traveling wave emitter. Below the speed of waves in the medium, the waves propagate out without overlapping and the familiar Doppler effect is observed. However, whenever the particle travels above the speed of the waves, they add coherently in a

11
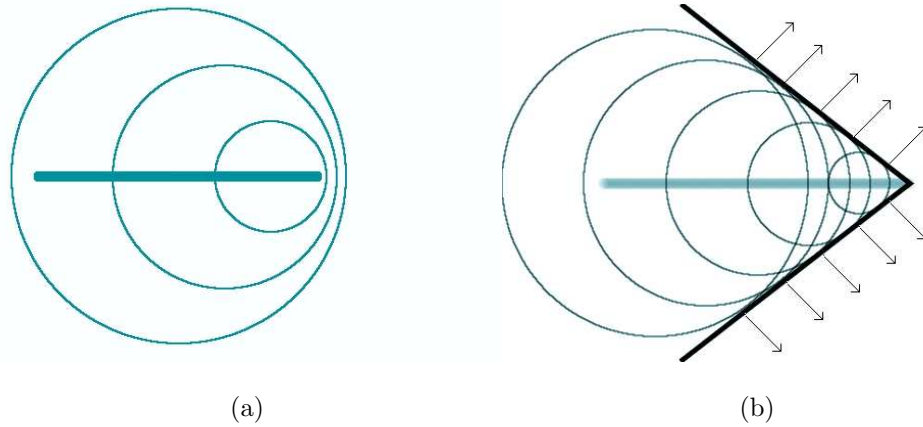
Figure 2.2: Visualization of the Cherenkov Cone. A particle that produces spherical wavefronts travels through a medium. (a) The speed of the particle is less than that of the wave. (b) The speed of the particle is greater than that of the wave.

cone shape. For light, the opening angle for the cone is equal to $\cos\theta_{\mathrm{C}} = 1/(\beta n)$ with

n representing the index of refraction. The effect was first noticed by Cherenkov in

1937[23]. For ice ($n \approx 1.33$), this corresponds to speeds greater than $\beta \approx 0.76$.

The calculation of Cherenkov emission for magnetic monopoles was first done

by Tompkins[24]. This requires two substitutions. First, the electric charge is

replaced by the magnetic one. In addition, the electric permittivity ϵ and magnetic

permeability μ must be interchanged. The result of this is to introduce a scaling

factor to the overall intensity of light emitted. The scale factor is found by comparing

the Frank-Tamm formula[25] for Cherenkov energy emission for both a muon and a

magnetic monopole, assuming $\mu = 1$ so $n = \sqrt{\epsilon}$:

$$\frac{dE}{dx}\text{ MUON} = \frac{(e)^2}{4\pi}\mu(1 - \frac{1}{(\beta n)^2})\omega d\omega$$

$$\frac{dE}{dx}\text{ MONOPOLE} = \frac{(g)^2}{4\pi}\epsilon(1 - \frac{1}{(\beta n)^2})\omega d\omega$$

$$\therefore$$

$$\frac{dE}{dx}\text{ MONOPOLE} = (\frac{gn}{e})^2\frac{dE}{dx}\text{ MUON}$$

(2.9)

Though the geometry and spectrum of the emission remain the same as an electrical charge, the interchange leads to a light output of roughly $(gn/e)^2 \sim 8300$ times larger than a bare muon traveling at the same speed. The final formula in terms of photons emitted per unit length per unit wavelength is:

$$\frac{d^2N}{dxd\lambda} = \frac{2\pi\alpha(\frac{gn}{e})^2}{(\lambda)^2}(1 - \frac{1}{(n\beta)^2})$$

(2.10)

Figure 2.3 shows the photon number yield per cm when the above formula is integrated over wavelengths between 300 and 650nm. This corresponds roughly to the thresholds of the light detectors in IceCube[26]. Thus, a relativistic magnetic monopole traveling through such a detector would appear as an incredibly bright event relative to a background of neutrino induced muons coming up through the Earth.

2.6 Energy loss in Earth

Magnetic monopoles are able to lose energy via strong, weak and electromagnetic energy loss mechanisms[22]. With the exception of the much larger coupling constant, electromagnetic losses are analogous to those of electric monopoles and are
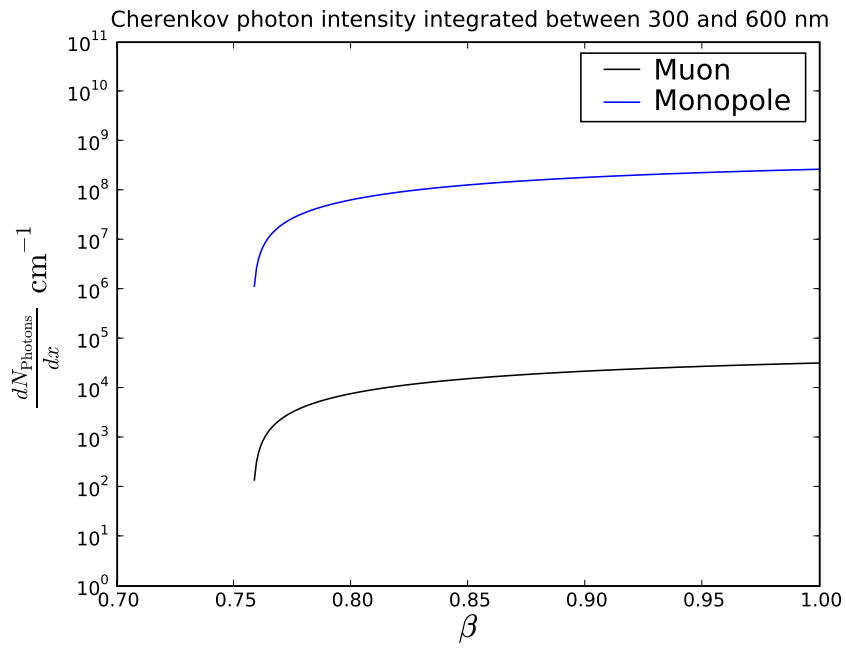
Figure 2.3: Photon intensity per cm as a function of speed for both a bare muon and a monopole. Formula is integrated over a wavelength acceptance from 300 to 650nm.

thus well understood. The strong and weak losses, however, are not well understood. Though weak losses are expected to be negligible, the strong interaction losses may be of the same order as the electromagnetic. Due to the lack of knowledge of these processes, they are generally ignored in the literature and will be for this analysis as well.

Though the brightness of monopole events would allow detection from any direction, IceCube sees a much larger background from events above the South Pole (see Section 3.4). Therefore, the analysis is most sensitive to magnetic monopoles that traverse the Earth and enter the detector from below. To determine the feasibility of such an event, the energy loss of the monopole traveling through matter must be determined. The energy loss can be divided into the collisional loss, which is roughly independent of the speed, and stochastic losses which increase with the speed.

Figure 2.4 gives the average energy loss values for both the collisional and stochastic losses of a magnetic monopole.

2.6.1 Collisional Losses

For the regime of $\beta > 0.1$ and $\gamma < 1000$, the dominant form of energy loss comes from atomic excitations and ionization of the surrounding material[27]. The amount is derived from a modified Bethe-Bloch formula:

$$\frac{dE}{dx} = (\frac{4\pi N_e (ge)^2}{m_e c^2})(log\frac{2m_e c^2 \gamma^2 \beta^2}{I_e} - \frac{1}{2} + \frac{K}{2} - \frac{\delta}{2} - B) \tag{2.11}$$
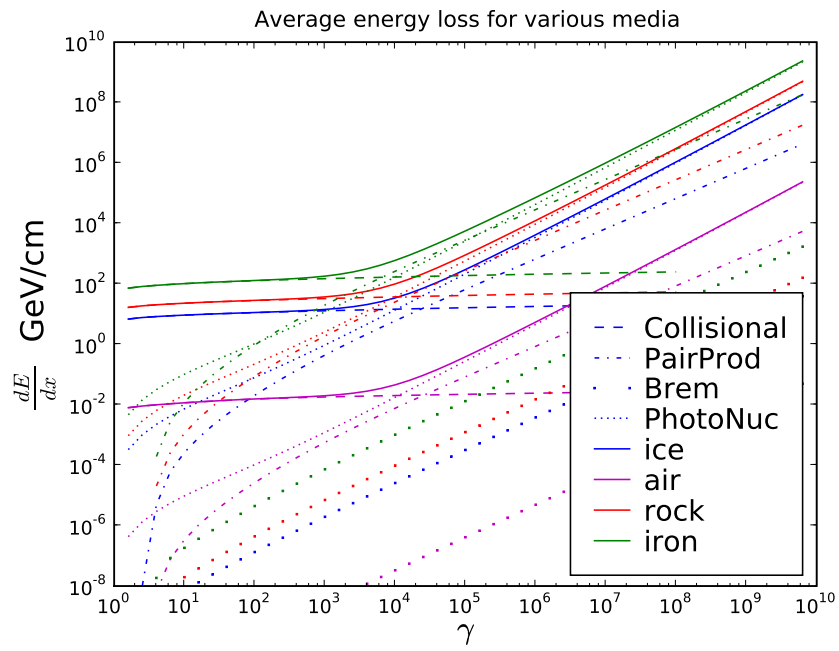
Figure 2.4: Energy loss of magnetic monopoles through matter. Color corresponds to material type, and line style corresponds to energy loss type. See text for references.

For $g = 137e/2$, the Bloch correction is $B = 0.248$ and the QED correction is $K = 0.406$. The density correction δ is found by

$$\begin{aligned}\delta_m \approx \delta_e = ln(\beta^2\gamma^2) - 2ln(\tfrac{I_e}{\hbar\omega_p}) + a(X_1 - X)^m - 1 \quad &\text{where}(X_0 < X < X_1)\\ \delta_m \approx \delta_e = ln(\beta^2\gamma^2) - 2ln(\tfrac{I_e}{\hbar\omega_p}) - 1 \qquad\qquad &\text{where}(X > X_1)\end{aligned}$$

(2.12)

Here $X = log(\beta\gamma)$ and X_0, X_1, m, and a are all fit values taken from [28].

2.6.2 Stochastic Losses

When the monopole reaches a boost value above $\gamma \approx 1000$, energy loss from stochastic mechanisms begin to become important. Pair production occurs when e^+e^- pairs are produced and subsequently annihilated. Photo-nuclear interactions arise from a virtual photon exchange between the monopole and the target nucleus. Brehmstrahlung, or braking energy, is a result of the monopole interacting with the nucleus to produce gamma rays. This term is inversely proportional to the mass of the monopole, hence it is well suppressed relative to the other two.

To model these energy losses, Monte Carlo code from the `ANITA`[29] search for ultra-relativistic magnetic monopoles is used to find average values for the stochastic energy loss as the monopole passes through the Earth. The formulas are taken from [30]. To convert from electric charges to magnetic ones, the muon mass is replaced with the monopole mass and the charge is replaced with $e/2\alpha$. The latter has the effect of increasing the number of interactions by $1/(2\alpha)^2 \approx 4700$.

2.7 Parameter Space

This search treats the mass and kinetic energy of the magnetic monopole at the Earth's surface as free parameters and the final analysis cuts include a zenith dependence. This requires the final limit calculation to consider constraints that arise on the mass and initial kinetic energy at the Earth's surface based on the energy loss the monopole experiences passing through the Earth.

To determine the angular dependence of the energy loss, simulations were run for 21 different $\cos \theta$ values ranging from -1 to 1 in increments of 0.1. For monopoles traveling below the horizon, a two-shell model of the Earth is used with an outer rock sphere of radius $R_{\text{Earth}} = 6.371 \times 10^6 \, \text{m}$ and an iron core with radius $R_{\text{Core}} = 3.486 \times 10^6 \, \text{m}$. For monopoles traveling downward, the path is assumed to be through the atmosphere and then ice, with the height of the atmosphere being $H_{\text{atmos}} = 20000 \, \text{m}$ and the depth of IceCube taken to be $D_{\text{IceCube}} = 2000 \, \text{m}$, corresponding to the middle of the detector. All properties of the different materials are taken from Table 1 in [30], with those for the density correction taken from [28].

For each angle, the path of the monopole is divided into segments where each one corresponds to the distance the monopole will travel and lose enough energy to correspond to a 0.1% change in the γ value. This ensures that the average stochastic energy losses remain accurate since they are highly dependent upon the γ value.

Figure 2.5 shows the results of these simulations for five different zenith angles. The shape of the curve can be understood as follows:

   * **The mass is large enough so the collisional loss through the Earth**

is not enough to impact its speed. The total collisional energy loss going straight through the Earth is roughly 10^{11} GeV. For masses above 10^{11} GeV, the energy loss through the Earth is not enough to slow it down to sub-relativistic speeds. Therefore, if it hits the Earth at relativistic velocities, it will remain relativistic, and the resulting acceptance is a straight line corresponding to the final speed desired. For down-going, the collisional loss is only 10^6 GeV, hence the straight line applies to lower masses. Note that if the boost factor is large enough, the energy loss will increase (from stochastic processes) and might be enough to change its speed through the Earth. Despite this, it will still remain relativistic since collisional losses dominate below $\gamma = 1000$.

* **The mass starts to fall below the necessary energy, but it still has a large enough initial kinetic energy.** The line starts to flatten out allowing only monopoles with enough initial kinetic energy to overcome collisional losses. For the up-going case, this occurs around 10^{11} GeV for masses between 10^7 GeV to 10^{11} GeV.

* **The mass is so small that stochastic losses become important.** As the mass falls so low that the initial kinetic energy leads to a large boost factor ($\sim 10^4$), the fact that energy losses increase dramatically as a function of γ reduces the ability for the monopole to make it through the Earth. Hence, the acceptance rises dramatically with initial energy.

For plots of all angles simulated, see Appendix A
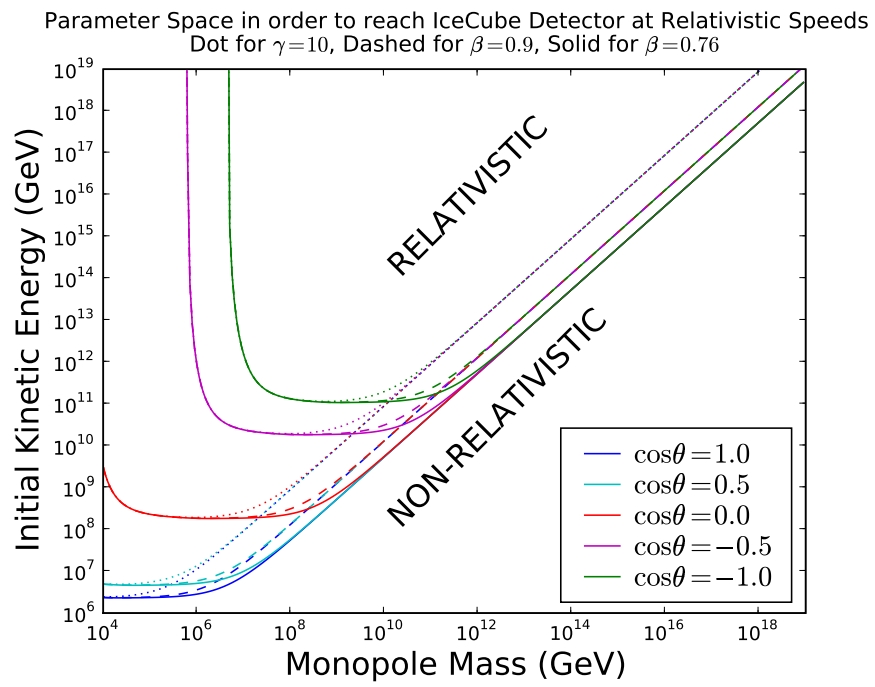
Figure 2.5: Regions in which a monopole can and cannot reach the IceCube detector traveling at relativistic speeds for all mass and initial kinetic energies at the Earth's surface

2.8 Review of Current Searches and Limits

To date, there has only been one unconfirmed detection of a possible magnetic monopole[31]. However, no event has been seen since and further experiments have led to flux limits well below what was observed.

Theoretical estimates of the number density for magnetic monopoles in the universe depend heavily upon which GUT is used and whether their creation occurs before, during, or after inflation. For this reason, experimental limits are generally given with no reference to a particular model and the result of this analysis will also be presented in a model-independent fashion.

Several strategies are employed in the search for magnetic monopoles, each with their own strengths and limitations. This section will review a sample of the most popular techniques.

2.8.1 Astrophysical Bounds

Constraints on the flux of magnetic monopoles can be inferred from astrophysical observations. Consideration of the galactic magnetic field gives rise to the Parker Limit[32]. Magnetic monopoles gain kinetic energy from the galactic magnetic field that must be replenished by the dynamo effect. If the number density is too great, this would short-circuit the field faster than its regeneration of $\approx 10^8$ years. The original limit was found to be $\Phi \leq 10^{-15} cm^{-2} sr^{-1} s^{-1}$. Further calculations taking into account the chaotic nature of the magnetic field as well as mass and velocity considerations yield limits less stringent for $\beta > 10^{-3}$[33]. Taking into

account the survival of a modeled seed field to produce the current galactic magnetic field produces much stronger limits (the so-called 'Extended Parker Bound') of $\Phi \leq \sim 10^{-16} \frac{M_{\text{MP}}}{10^{17}\,\text{GeV}} cm^{-2} sr^{-1} s^{-1}$[34].

Certain classes of GUTs predict monopoles that catalyze nucleon decay[35],[36] at relatively large cross-sections. These monopoles, upon being gravitationally captured by neutron stars, would cause the stars to heat and produce observable emissions of ultraviolet and x-ray photons. The non-observation of this effect leads to constraints on these catalyzing monopoles to $\Phi < 10^{-21} cm^{-2} sr^{-1} s^{-1}$[37],[38].

2.8.2 Induction Experiments

Induction experiments search for monopoles either by direct detection or passing materials thought to have accumulated magnetic charge (e.g. iron, magnane modules, and lunar rocks) through a super-conducting coil. Superconductors make a natural choice for magnetic monopole detectors since the magnetic flux of a Dirac monopole is $\Phi = 4\pi g = hc/e = 2\Phi_0$. Here, Φ_0 represents the flux quantum of superconductivity and the factor of 2 arises from the electric charge of Cooper pairs. The expected change in current on the super-conducting coil from the passage of a magnetic monopole would be $I(t) = \frac{\Phi_0}{L}(1 + \frac{\gamma v t}{\sqrt{(\gamma v t)^2 + b^2}})$[31] where b is the ring radius, L is the self-inductance, and t=0 corresponds to the monopole passing through the coil. This results in an overall change in current of $\Delta I = 2\Phi_0/L$ for $-\infty < t < \infty$ with a characteristic time-scale of $b/(\gamma v)$

A major source of background comes from changes in the Earth's magnetic
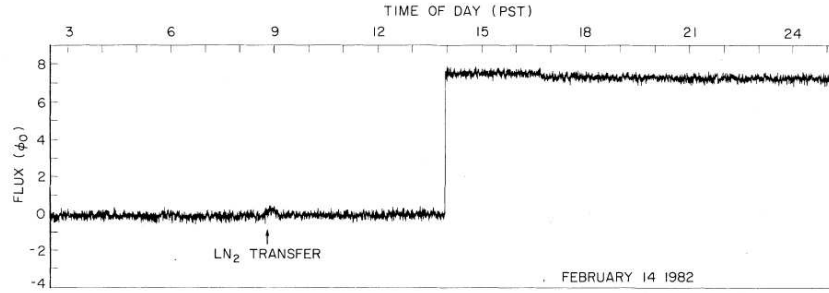
Figure 2.6: Data taken by an induction experiment on Valentine's day 1982[31]

field. A relative change as small as 10^{-11} would produce a signal similar to a monopole. Thus, great care must be taken to shield the ambient field, restricting the search to relatively small areas. This limits their power in setting limits. However, the most promising event candidate for a magnetic monopole occurred on Valentine's Day in 1982 by such an experiment. Figure 2.6 shows the current recorded. While no other explanation has been found, no confirming event has been detected either.

2.8.3 Ionization Experiments

Ionization experiments search for signatures left by magnetic monopoles colliding with nuclei as they travel some material, usually by track etching. To date, the most comprehensive search has been performed by the Monopole Astrophysics and Cosmic Ray Observatory (MACRO). It was located below the Gran Sasso mountain in central Italy and started taking data in 1989. It ran in its final configuration from early 1995 until it was shut down at the end of 2000. See [39] for a complete description of the detector.
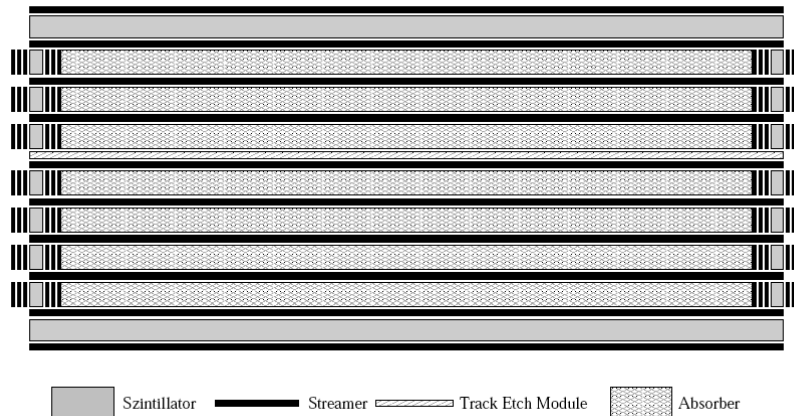
Figure 2.7: Cross-sectional view of the MACRO detector. Taken from [41]

Figure 2.7 shows a cross-sectional view of a so-called supermodule. MACRO consisted of twelve of these modules. Each one utilizes three different types of sub-detectors: Liquid scintillators, streamer chambers, and a track etch detector. The multiple detectors are designed to optimize the search for monopoles at different speeds as well as provide redundancy if an event is observed. This is especially important in the speed range of $10^{-4} < \beta < 10^{-3}$ since monopoles cannot be detected by direct ionization. Since the speed of such a monopole is comparable to that of the electrons orbiting the atom, the assumption of the Bethe-Bloch formula that the electrons are resting and free is no longer valid. The streamer chambers compensate for this by utilizing the DKPMR mechanism[42]. The chambers are composed of a mixture of He and n-Pentan. A monopole traveling through the streamer will excite the He to $20\,\mathrm{eV}$. This is then passed on through collisions to the n-Pentan. The n-Pentan ionizes and starts the streamer.
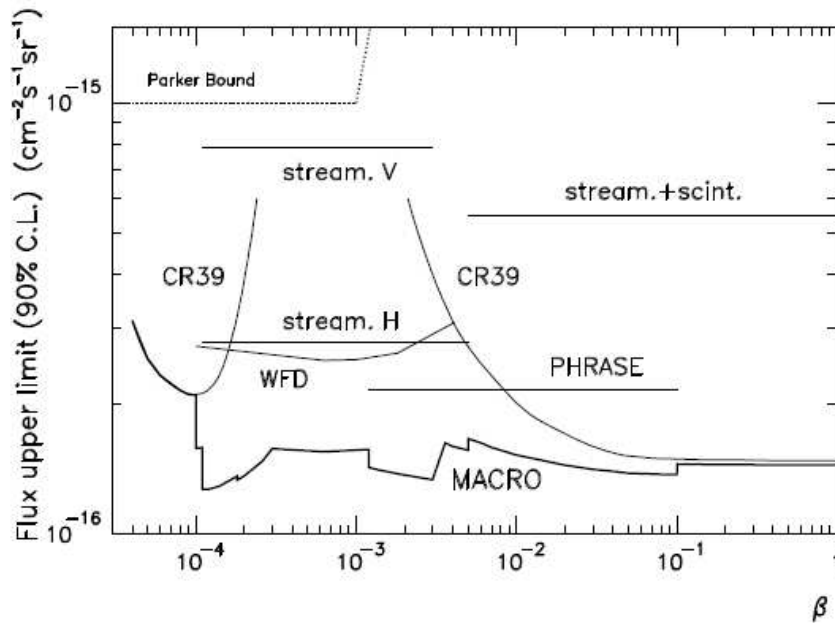
Figure 2.8: Final limits from various analyses on MACRO. Taken from [40]

Figure 2.8 shows the results of all analyses performed by the MACRO experiment and the resulting limits. The final combined limit is in general the most stringent over the full velocity range $10^{-5} < \beta < 0.8$.

One exception to the above rule is in the velocity range of $\beta \sim 10^{-3}$ where bound states of magnetic monopoles and nuclei should leave an etchable track in ancient Mica. The large exposure time ($\sim 10^9$ years) results in more stringent limits that reach $\sim 10^{-18} \, cm^{-2} sr^{-1} s^{-1}$ [43].

2.8.4 Relativistic Searches

MACRO limits are superseded in the regime of $\beta > 0.8$ by detectors utilizing the relative brightness of a magnetic monopole's Cherenkov radiation. AMANDA,

IceCube's proof-of-concept detector, provides the most stringent limits to date for speeds from $\beta = 0.8$ to $\gamma < 10^7$[44] using the same detection principle outlined herein. This represents the second result from AMANDA that was below the MACRO limit[45]. A search has also been performed by the Baikal Neutrino Telescope in Russia[46].

Other direct searches have been performed with radio Askaryan telescopes. The much larger detection areas provide more stringent limits, though the requirement of detecting the bright showers initiated by stochastic losses leads to a much higher speed threshold of $\gamma \approx 10^7$. Both RICE[47] and ANITA II[29] have performed searches with limits $\sim 10^{-19} cm^{-2} sr^{-1} s^{-1}$

Figures 2.9 and 2.10 display the current results as both a function of β and γ. An effort was made by the AMANDA analysis to unfold the result into limits at the Earth's surface as a function of monopole mass and initial kinetic energy[44]. Figure 2.11 demonstrates this result. The same procedure is done for this analysis and is described in detail in Section 11.3
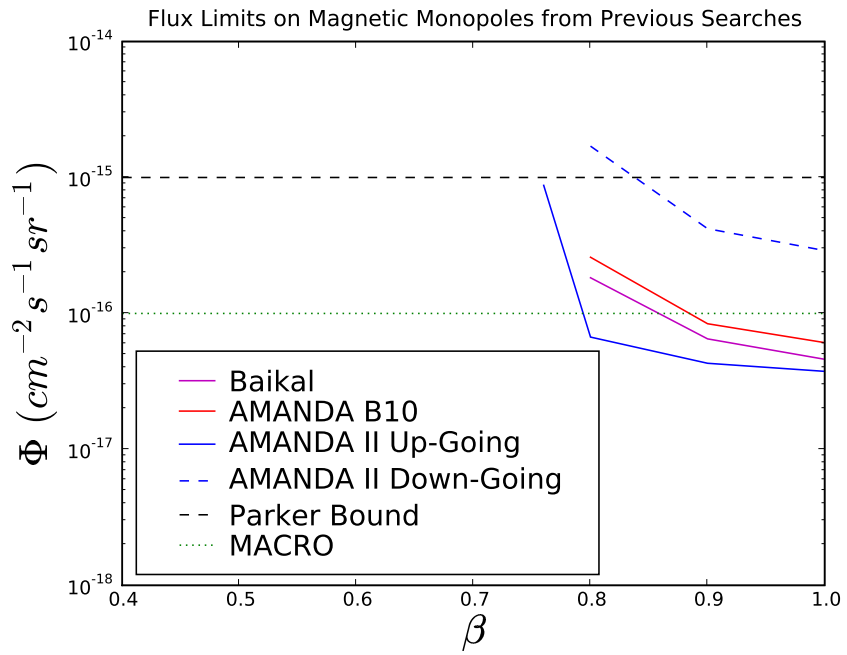
Figure 2.9: Final limits from various relativistic searches for magnetic monopoles
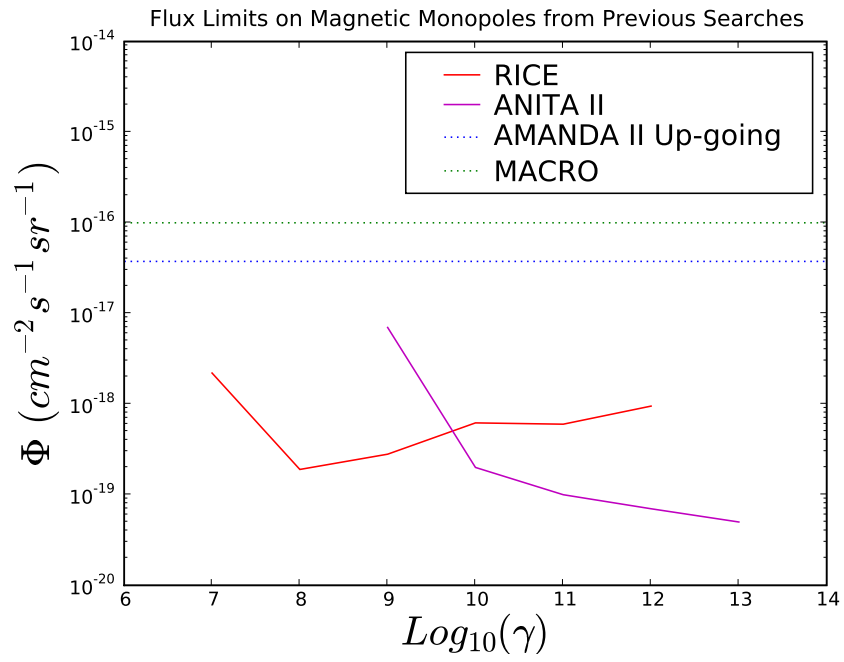
Figure 2.10: Final limits from various ultra-relativistic searches for magnetic monopoles
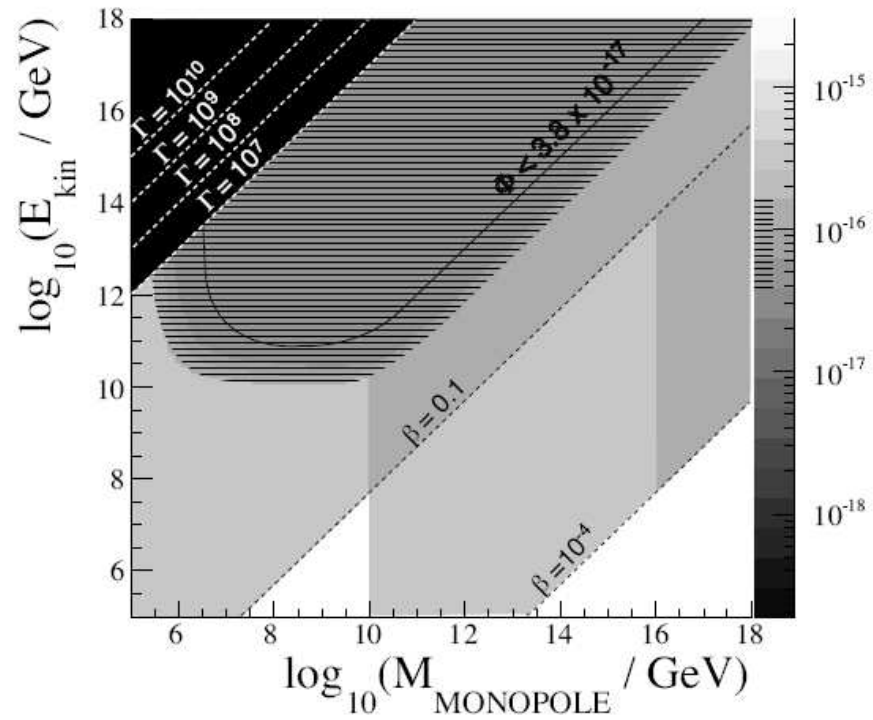
Figure 2.11: Final limits from various searches for magnetic monopoles as a function of mass and initial kinetic energy at the Earth's surface. The dark black is from radio telescopes and the light grey is from MACRO. The hatched region represents the AMANDA-II analysis. Taken from [44]

Chapter 3

Neutrino Astronomy

Neutrino astronomy represents a relatively young field but has already shown itself to be of great value. Observations of neutrinos from the sun first demonstrated the neutrino has mass[48]. Measurements of neutrinos from the supernova in 1987 allowed for a better understanding of the death of a star[49]. Both cases led to a Nobel prize and show how neutrinos, analogous to cosmic ray physics, offer great insights when considering heavenly beams.

IceCube represents a new generation of neutrino astronomy with the advent of a telescope capable of detecting neutrinos over a wide energy range from hundreds of GeV to EeV. Neutrinos represent a valuable messenger particle for astronomy since they can travel virtually unimpeded through the universe and point back to their source. This can be seen in Figure 3.1. Photons, the most traditional messenger, cannot be seen above 100 TeV since they are energetic enough to pair produce with the galactic infrared background with a mean free path much less than the galaxy. Protons and other charged particles are bent by the galactic magnetic fields and offer no directional information below energies of $\sim 10^{10}$ GeV. Neutrinos, since they are weakly interacting, do not suffer from either of these constraints and can reach the Earth at essentially all energies. The caveat, of course, is to detect them.
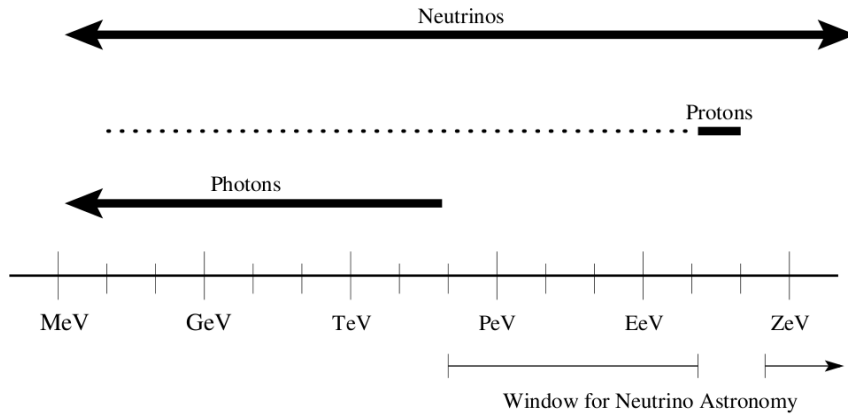
Figure 3.1: Range of energy for which three types of messenger particles are useful in astronomy. Only neutrinos cover the entire range.

The following sections will describe the motivation for building neutrino telescopes, the detection principle, the primary events that are detected, and give a summary of some recent results from IceCube.

3.1 Motivation

Measurement of the astrophysical neutrino flux and associated sources could provide valuable insight on several outstanding problems. Chief among them are the origin of the highest energy cosmic rays. Though little is understood about the processes that would produce these events, it is known that the source should have an associated flux of photons and neutrinos since the accelerated particles will

interact in the surrounding medium via

$$p + \gamma \rightarrow \Delta^+ \rightarrow \pi^+ + n$$

$$\pi^+ \rightarrow \mu^+ + \nu_\mu \rightarrow e^+ + \nu_e + \bar{\nu}_\mu + \nu_\mu$$

$$n \rightarrow e^- + p + \nu_e$$

$$or$$

$$p + \gamma \rightarrow \Delta^+ \rightarrow p + \pi^0$$

$$\pi^0 \rightarrow \gamma\gamma$$

(3.1)

The scale of IceCube is set by its main science objective in observing this astrophysical flux of neutrinos. A robust, generic upper bound was put forth by Waxman and Bahcall[50] at the level of $E_\nu^2 dN/dE_\nu \sim 10^{-8}\,\text{GeV/cm}^2/\text{sr}$. This would lead to roughly tens of events/yr/km^2. Moreover, observations of neutrinos from potential sources such as Gamma Ray Bursts, Supernova, and Active Galactic Nuclei would help answer the question of where the cosmic rays come from and allow probes deep into the underlying processes that fuel these events.

Fundamentally, though, it's curiosity and excitement about seeing what the universe has to tell. After all, whenever astronomers look through a new window, something unexpected is usually found.

3.2 Detection Principle

Neutrino telescopes operate by burying a grid of light detectors deep underground in a medium such as ice or water. The medium must be dense enough to act as a good target for the incoming neutrinos and relatively clear in order to efficiently

radiate Cherenkov light. For IceCube, this medium is the South Pole ice cap. Figure 3.2 shows how the concept works.

Neutrino telescopes are designed to detect the secondary results of charged-current interactions between neutrinos and the surrounding medium via the process $\nu_l(\bar{\nu}_l) + N \rightarrow l^+(l^-) + X$. N represents the nucleon, l the resulting lepton, and X the hadronic cascade. Ideally, they can determine the flavor, direction, and energy of the parent neutrino based on the signature left in the detector.

Muons produced by ν_μ interactions can travel on the order of kilometers in the ice, depending on energy. Since the muon travels faster than the speed of light in ice, this produces a Cherenkov cone along a track through the grid of light detectors. The hits can be used to determine the direction of the muon. For the TeV energies that IceCube is optimized for, the muon is typically within 0.25 degrees of the parent ν_μ. This makes the muon events ideal for directional information. However, since the interaction takes place outside the detector, the absolute neutrino energy cannot be determined directly. Instead, the muon energy must be inferred based on the stochastic losses observed.

Electrons produced by ν_e interactions cascade very quickly from stochastic losses on a length scale less than the sensor spacing of the detector, thus they appear as a spherical light pattern. The full containment of the light allows for a relatively good energy reconstruction but very little information can be found about direction.

Tau leptons are extremely short lived and thus decay soon after being produced. The signature in IceCube would be a 'double bang' of two cascades at both

33
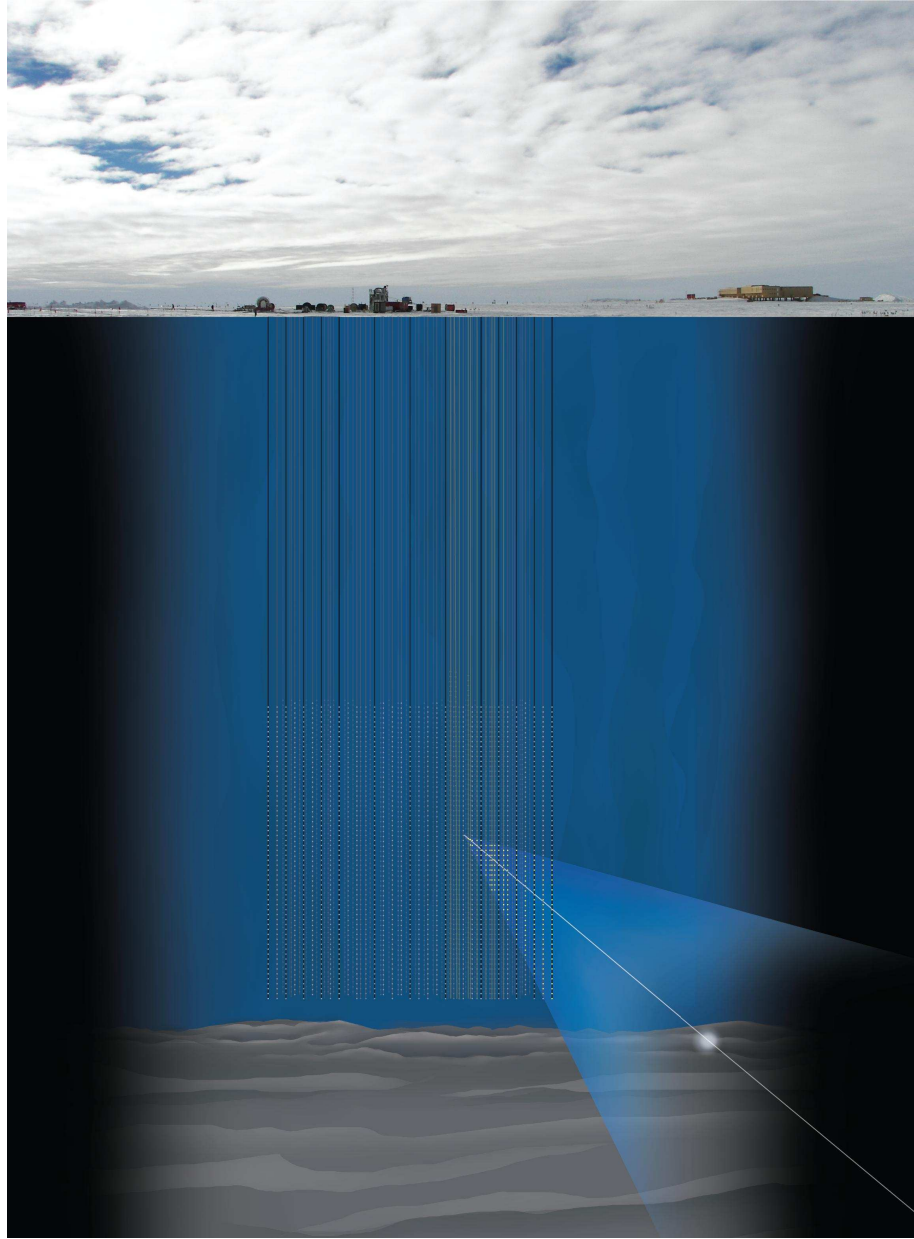
Figure 3.2: A cartoon of a muon neutrino event. The neutrino interacts in the bedrock and the resulting muon travels up through the detector producing Cherenkov light.

the production and decay vertex. This requires the two cascades to both be contained and resolvable, greatly limiting the sensitivity.

3.3 Cosmic Rays

An understanding of the cosmic ray flux is vital in extracting the science from a neutrino telescope. They present a fundamental background. On the other hand, they provide the fundamental motivation for an astrophysical neutrino flux. Hence, a thorough understanding of their properties is essential. For an in depth overview, see [51].

Cosmic ray physics has its own long and venerable history. The first revolutionary result occurred when Victor Hess went up into the atmosphere with a hot-air balloon and measured an increase in the flux of cosmic rays. For the first time, it became apparent that these charged particles are not produced by the Earth (as originally thought) but arrive from the cosmos.

Cosmic rays are composed largely of free protons, followed by helium and heavier elements. These include elements that are produced in stars (e.g. Carbon, Oxygen, Iron) and secondaries that result in interactions of the primaries in the interstellar medium (e.g. Lithium, Beryllium, and Boron). The flux at the top of the atmosphere is roughly 10000 nuclei per square meter per second. The energy dependence has been measured over a large range from hundreds of MeV to hundreds of EeV. Figures 3.3 and 3.4 show this spectrum.
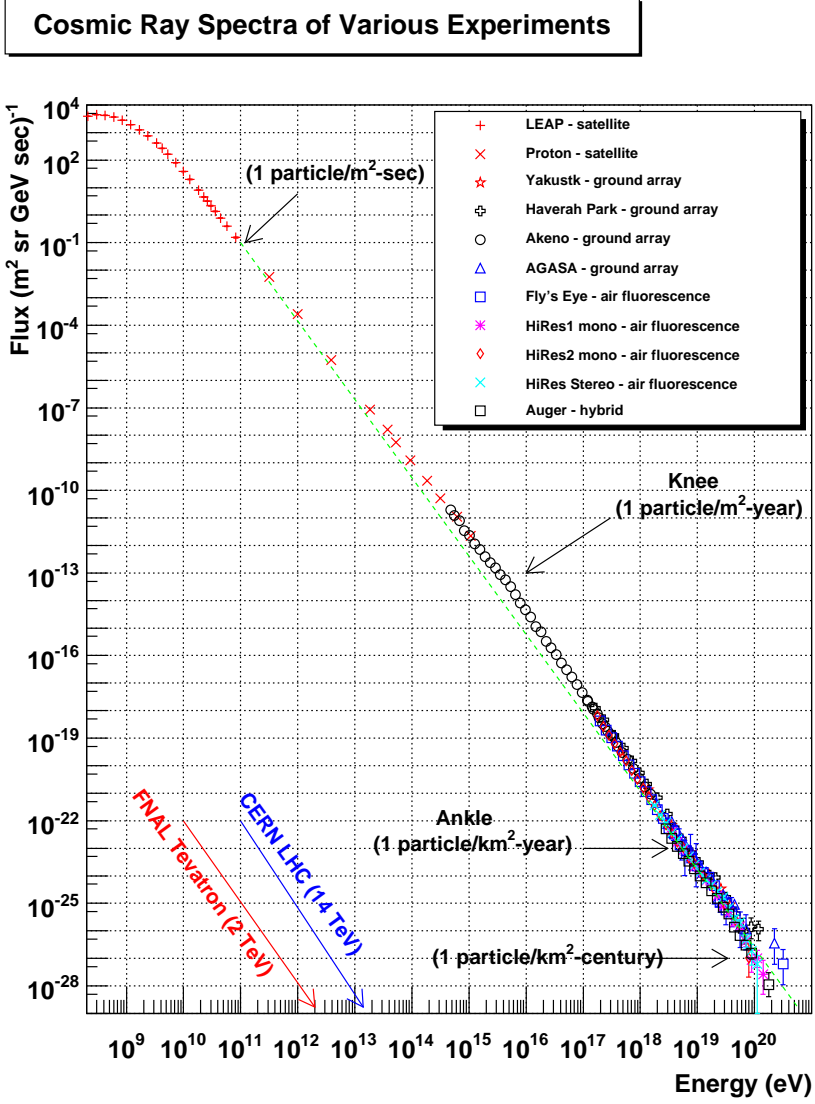
Figure 3.3: Measurements of the cosmic ray primary spectrum from several experiments. Taken from [52].
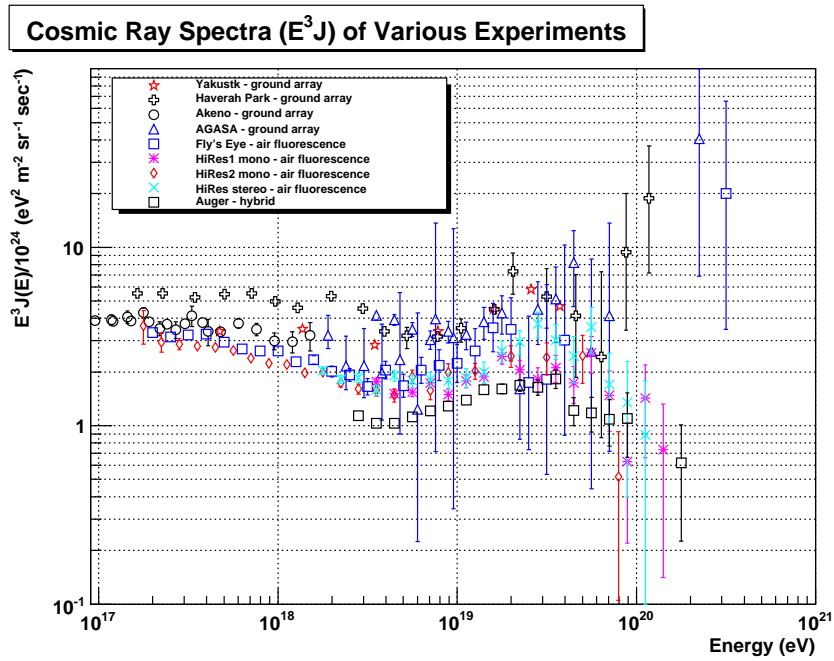
Figure 3.4: Measurements of the high energy tail in the cosmic ray primary spectrum from several experiments. Spectrum is re-weighted by E^3 to amplify features. Taken from [52].

Despite a range in flux that covers 30 orders of magnitude, the spectrum exhibits a relatively simple structure, following a power law of $dN/dE \propto E^{-\gamma}$ with three breaks. Below energies of $\sim 10^6 \, \text{GeV}$, the spectrum follows a power law with $\gamma \approx 2.7$. The spectrum steepens after this point, labeled the 'knee', to $\gamma \approx 3.1$. At $\sim 10^9 \, \text{GeV}$, the spectrum flattens again at a region labeled the 'ankle'.

The spectrum shows a sharp cutoff at $\sim 5 \times 10^{10} \, \text{GeV}$. At this point, protons will begin to interact with the 2.7 K microwave background via the same reaction from Equation 3.1, in a process known as the GZK cutoff[53]. Despite initial measurements that seemed to suggest this cutoff did not exist, it has been confirmed by high-energy cosmic ray detectors such as HiRes and Auger[54].

The reason for this shape is not completely understood and is still an active avenue of research in the community. A good overview of the current state can be found in [55]. The leading theory describes the origins as a result of Fermi acceleration[56]. This would produce an E^{-2} spectrum at the source. A steepening would occur due to interactions with inter-stellar medium which explains the observed spectrum of $E^{-2.7}$. The breaks seen in the spectrum could be caused by either a break in the source energy spectrum or a result of source location, with the latter being explained by the primary exceeding the gyro-radius of the galactic magnetic fields and leaking out of the galaxy. In both cases, the composition of the primaries will play a role, since increasing the elemental charge will both increase the energy received at the source and decrease the gyro-radius. The sharp cutoff at the knee could result from protons while the remaining spectrum below the knee and above the ankle represents cutoffs for successively heavier elements. One prominent model
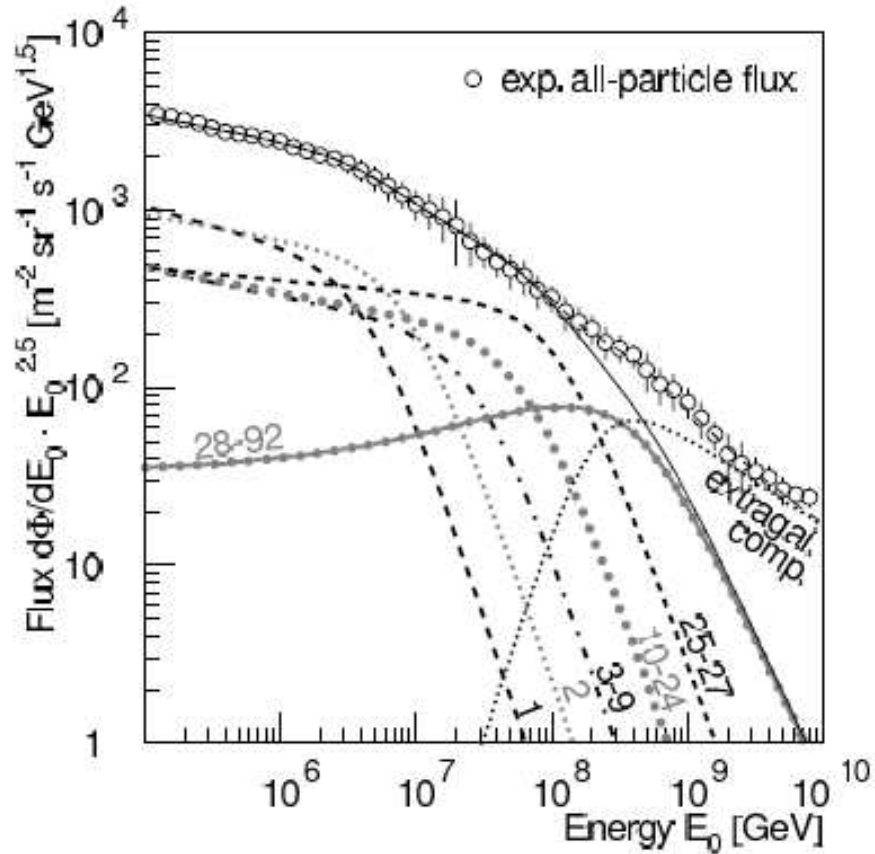
Figure 3.5: Measured flux of the cosmic ray spectrum. Each dotted line represents the atomic numbers for the different elemental fluxes used in the poly-gonato fit. Taken from [55].

suggests a flux of elements heavier than iron (the so called poly-gonato, or 'many knee' model). As described in Chapter 5, this is the standard model used by the IceCube collaboration for cosmic ray simulation. Figure 3.5 shows how this model would fit the spectrum from the knee to the ankle region.

The flattening at the ankle is believed to be a result of the extra-galactic contribution since primaries at this energy should have enough energy to escape the galaxy. Furthermore, at these energies, galactic primaries should point back to a
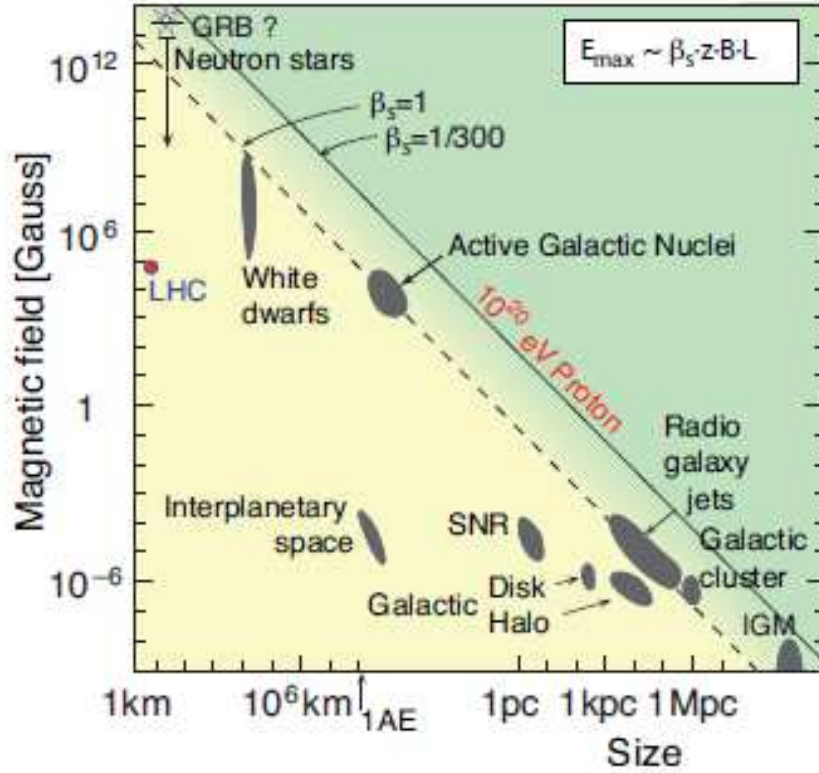
Figure 3.6: Plots of potential accelerators for the highest energy cosmic rays. The dashed line corresponds to the minimum B and L needed to accelerate protons to 10^{11} GeV assuming relativistic shock fronts, while the solid is for shock speeds of 10^6 m/s. For iron, the line would be a factor of 26 below the proton. Taken from [55].

source whereas they do not seem correlated to any known sources in the galaxy. Figure 3.6 shows a plot of energies that can be achieved by different galactic and extra-galactic sources. The maximum energy is related to the speed of the shock front that accelerates the charged particles (β_s), the magnetic field strength (B), the size of the field (L), and the charge of the particle. Remnants of supernovae are the leading candidate for cosmic rays of galactic origin but do not have enough energy to explain the extra-galactic component.

3.4   Detector Events

Fundamentally, IceCube detects light from charged particles in the hopes of observing the secondaries of neutrino interactions. The ultimate goal is the detection of neutrinos of astrophysical origin. As shown in Figure 3.7, two main types of background events are muon bundles and neutrinos, both originating from cosmic ray showers. These are produced by primaries slamming into the atmosphere and starting chain reactions that include charged mesons, which decay via reactions similar to the π^+ in Equation 3.1.

Of course, one man's background is another man's signal, and many studies have been done with these events. This includes measurements of atmospheric muon bundles to determine the anisotropy in the arrival direction of cosmic ray primaries[57] and detailed measurements of the atmospheric neutrino spectrum[58].

The dominant event type recorded by IceCube is muons resulting from cosmic ray showers above the South Pole ice cap. The motivation for building the detector deep underground is to help eliminate these events as much as possible. Despite a depth of 1.5 km below the ice surface, muons with energies of hundreds of GeV are still energetic enough to reach the detector. For the data used in this analysis, the trigger rate of the detector is $\sim 500\,\mathrm{Hz}$, while the neutrino rate is roughly six orders of magnitude less[59]. This large background is limited, however, by the fact that the muons cannot travel all the way through the Earth. By eliminating down-going events (where down is defined as towards the Earth's core), IceCube becomes most sensitive to neutrinos arriving from the northern hemisphere.
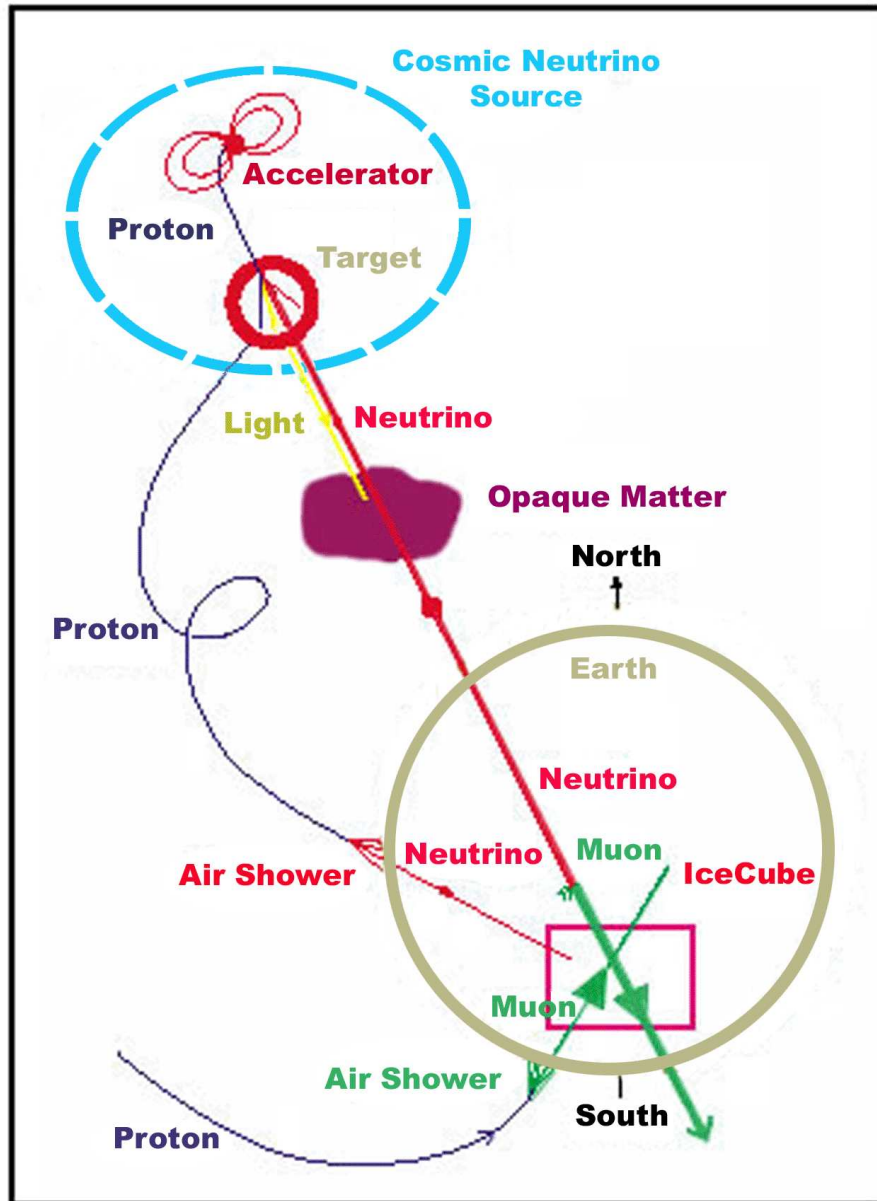
Figure 3.7: A cartoon of the different types of events that will be recorded by IceCube. Cosmic ray primaries produced in astrophysical sources interact with the Earth's atmosphere to produce air showers of neutrinos and muons. The goal is to separate these from neutrino induced muons originating from the same astrophysical sources.

Atmospheric neutrinos present a more fundamental background since they are the same event type as the astrophysical neutrinos of interest. Atmospheric ν_μ's have an energy spectrum that follows the power law $dN/dE \propto E^{-3.7}$[60], steeper than the cosmic ray primary energy spectrum by one order. This arises because the parent meson could interact in the atmosphere instead of decaying into the neutrinos.

Since the energies of interest are above 100 GeV, the muons themselves typically reach the ground before decaying, where the chance of a hadronic interaction is much larger. For this reason, the ν_e component is substantially smaller than the ν_μ and follows a steeper power law of $dN/dE \propto E^{-4.7}$. The typical ratio of the three flavors is $N_{\nu_\mu} : N_{\nu_e} : N_{\nu_\tau} = 19 : 1 : 0$[61].

A source of uncertainty in the atmospheric neutrino flux are neutrinos which result from the decay of charmed mesons. These are generally referred to as 'prompt' neutrinos to signify that the parent particles in this case decay much quicker. Since the mass of charmed mesons is much larger, they almost always decay and hence the spectrum should follow the cosmic ray primary spectrum of $E^{-2.7}$. This flatter spectrum should lead to the dominance of the prompt component for energies above $\sim 100\,\mathrm{TeV}$. However, uncertainties on charm production make the calculation of the flux highly difficult.
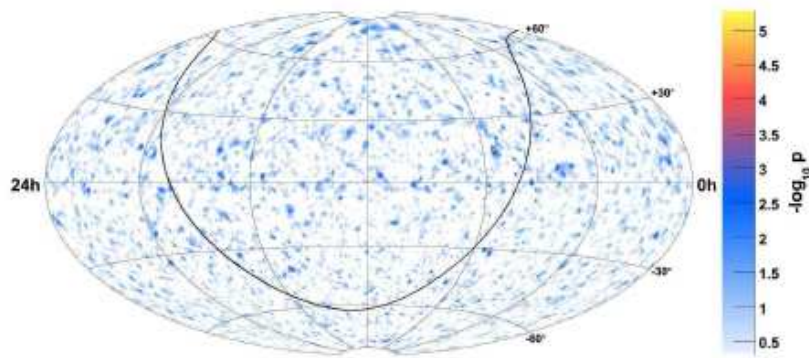
Figure 3.8: Pre-trial significance values (p-value) of the all-sky point source scan. The galactic plane is shown as the solid black curve. Taken from [62].

3.5 Selected IceCube Results

Though the full detector has just started taking data, several analyses have already been performed with the data collected each year during construction. Results from the half-completed 40 string detector, which took data from the spring of 2008 to the spring of 2009, represent the latest cycle of published results.

3.5.1 Steady State Point Source Search

One major goal of IceCube is to develop a point source sky map to detect if there are any interesting astrophysical objects producing an excess of neutrinos[62]. The search scans the northern hemisphere for an excess of neutrinos from a given direction over the background of atmospheric neutrinos. While losing sensitivity, the southern hemisphere can also be checked for higher energy events by again looking for an excess over the background rate, this time composed of atmospheric muon

bundles. In addition, several known sources can be checked using a stacking analysis to measure an excess of neutrinos. Figure 3.8 shows the all-sky map from the analysis on the 40 string detector in terms of pre-trial significances. No significant sources are observed.

3.5.2   Diffuse Neutrino Search

A second type of search looks for the diffuse flux of astrophysical neutrinos. These neutrinos should have a typical Fermi spectrum of E^{-2} since, unlike the cosmic rays, they will arrive from the source without interacting. These searches utilize the fact that this spectrum is much harder than the atmospheric one to distinguish the astrophysical neutrinos. Figure 3.9 shows the current upper limits on this flux from the 40 string IceCube detector[63] along with several theoretical fluxes(e.g. [50],[65]).

3.5.3   Gamma Ray Bursts

A third type of search for astrophysical neutrinos focuses on Gamma Ray Bursts (GRBs)[64]. The advantage here is that the GRBs occur at a specific point in space and time, and the neutrino flux should be coincident with the gamma rays observed by satellites. These results are the first to seriously probe the neutrino fluxes predicted by Waxman and Bahcall and a revised version by Guetta et al.[65]. Figure 3.10 shows the upper limit set for the 40 string detector. It should be noted that the 59 string detector result improves this by a factor of 2 and a preliminary
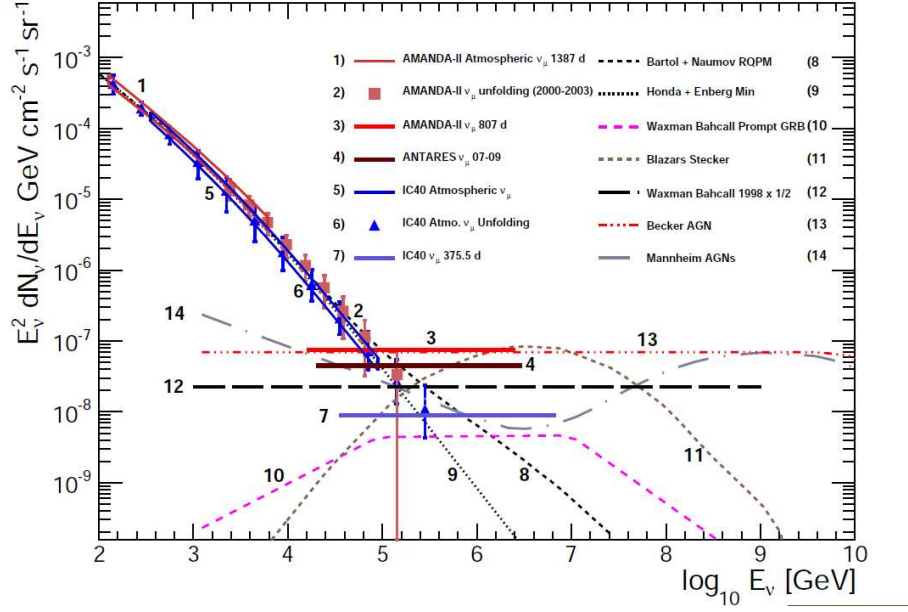
Figure 3.9: Upper limits on the diffuse flux of astrophysical neutrinos. Taken from [63].
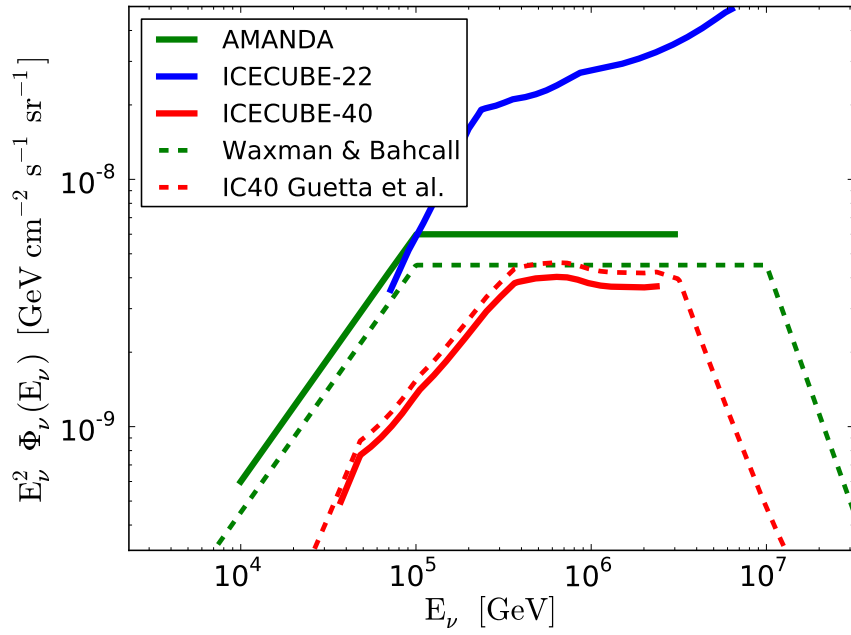
Figure 3.10: Upper limits on the flux of neutrinos from GRBs compared to theoretical models. Taken from [64].
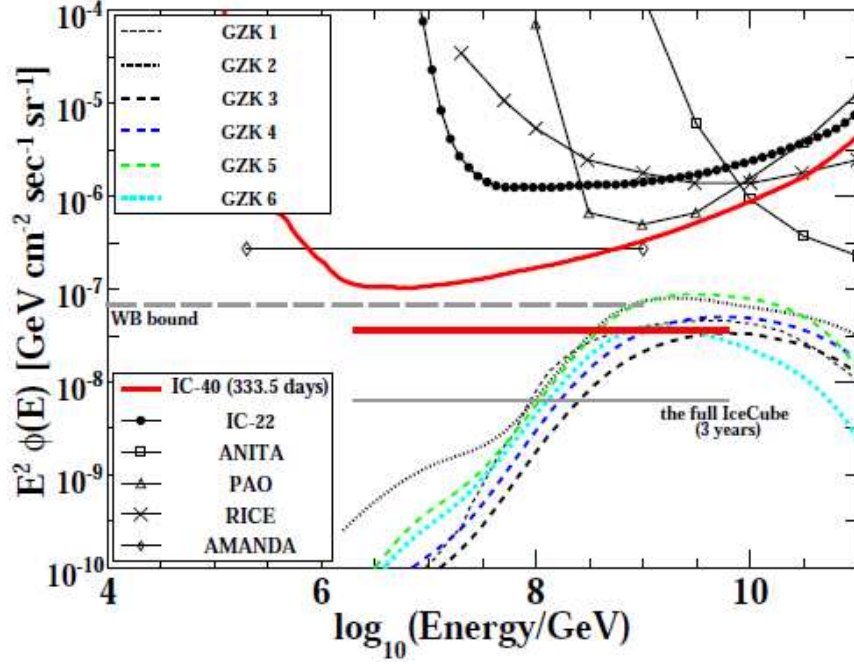
Figure 3.11: Upper limits on the flux of extremely high energy neutrinos compared to theoretical models for flux from GZK production. Taken from [67].

combined limit rules out a flux of ~ 0.22 times the Guetta et al. model[66]. An outstanding achievement, this represents the first true astrophysical result of the km^3 neutrino telescope era.

3.5.4 Extremely High Energy (EHE) Neutrinos

The cutoff in the cosmic ray primary spectrum above 10^{10} GeV should result in a flux of neutrinos produced by these primaries interacting with the ambient 2.7 K microwave background (the GZK cutoff, see Section 3.3). Figure 3.11 shows the current upper limits from IceCube, along with several models for the expected flux of GZK neutrinos.

A difficulty in this analysis is the fact that neutrino cross sections increase as a function of energy. At these extremely high energies, the Earth becomes opaque to up-going neutrinos. Thus, searches for neutrinos produced by the GZK reaction must look above the horizon and rely more on the relative brightness of the event[67]. These analyses are most similar to the searches for relativistic magnetic monopoles, since both rely on a bright signal.

Chapter 4

IceCube

IceCube is a kilometer scale neutrino telescope that is buried between 1450 and 2450 meters below the Antarctic ice surface. The strings are deployed at the South Pole and surround the decommissioned remnants of the Antarctic Muon and Neutrino Detector Array (AMANDA), which was the proof of concept experiment for IceCube. There are 86 strings of 60 light sensing Digital Optical Modules (DOMs), spaced out in a hexagonal pattern. Each string is roughly at a triangular vertex 125m away from its nearest neighbors. A schematic of the detector can be seen in Figure 4.1.

Construction on IceCube began in the austral summer of 2004-05 with a single string deployed. It has continued in each austral summer since with 8 more strings in 2005-06, 13 in 2006-07, 18 in 2007-08, 19 in 2008-09 and 20 in 2009-10. The final 7 strings were deployed during the 2010-2011 season. Each year the detector collected data using the partially completed array. Figure 4.2 shows the order in which the strings were deployed.

Data for the analysis presented was obtained in 2007, while IceCube operated with 22 strings totaling 1320 DOMs, of which 1291 were in operation. The instrumented volume was $\sim 0.2\,\mathrm{km}^3$. This can be compared to the AMANDA instrumented volume of $\sim 0.016\,\mathrm{km}^3$ and the full IceCube detector of $\sim 1\,\mathrm{km}^3$.
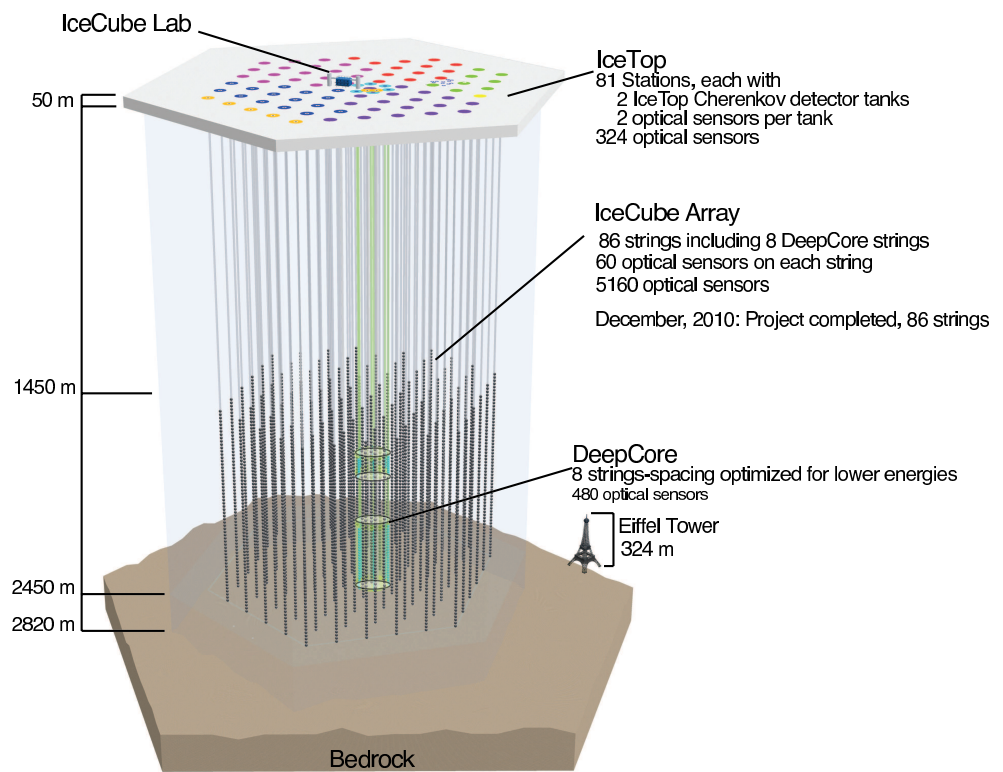
Figure 4.1: A sketch drawing of the IceCube array. Included are Deep-Core, the low energy extension to IceCube, and IceTop, the cosmic ray shower detector at the surface.
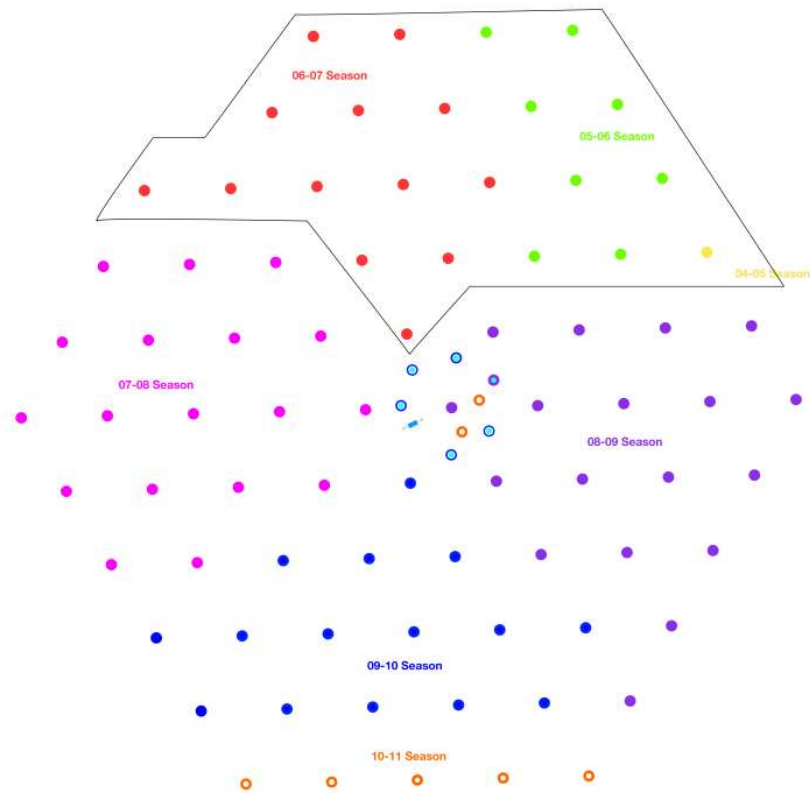
Figure 4.2: Order in which the strings were deployed in the ice, by season. This analysis considers only the strings deployed through the 2006-07 season, outlined in black.

The deployment of the strings starts with the drilling of the hole. This is done in three stages. A firn drill, which cycles hot water through a copper pipe, is used for the porous surface layer of snow. Once it reaches the solid ice, it is removed in favor of a hot-water drill. The drill employs a high pressure jet of hot water which it directs into the ice to melt a $\sim 50\,\mathrm{cm}$ diameter column down to depths of $\sim 2500\,\mathrm{m}$. Water is pumped back to the surface and reused. Once the hot-water drill has reached the final depth, it is removed and the string is lowered. The strings consist of the 60 DOMs spaced 17m apart and are strong enough to support the DOMs while the hole re-freezes. They contain a twisted wire pair that provides power and communications between the DOMs and the surface.

The detector also includes a surface array (IceTop) consisting of two tanks located above each string, each with two DOMs. IceTop can be used for the study of cosmic ray air showers and aide in both background rejection and calibration using muon bundles that pass vertically through the detector.

A third component consists of 8 strings with high quantum efficiency DOMs located in the center of the detector in the deepest part of the ice. Termed DeepCore, these densely packed strings use the surrounding array as a veto to achieve 4π sensitivity. This will allow for searches of neutrinos below the 100 GeV threshold of the standard detector and will be instrumental in many analyses including the search for dark matter.

The following sections will describe the detector operation in time order from light produced by the charge particles through data being sent via satellite to the north.

4.1 Polar Ice

Though not man-made, the largest part of the IceCube detector is the instrumented polar ice used as the Cherenkov medium for light producing particles. In order to accurately measure events within IceCube, a thorough understanding of the optical properties of the ice is needed. These properties depend on the amount of dust and bubbles that build up in layers within the ice, corresponding to geological events that occurred when the ice was formed. These layers are roughly horizontal over the range of IceCube and can be approximated by a simple depth dependence. The properties can be defined as the scattering and absorption lengths for light within the medium. Scattering results in the photon being redirected, thus affecting both the timing and original direction information, while absorption results in the photon disappearing. The ice used by IceCube is remarkably clear, and absorption lengths are $\sim$ 100 m, allowing light to be seen by many DOMs. Meanwhile, scattering lengths are $\sim$ 20 m which, combined with a DOM spacing of 17 m, means most light seen is scattered. By comparison, the first km of ice at the surface is dominated by bubbles which results in scattering lengths of $\sim$ 0.5 m[68]. Note this is another fundamental motivation for building the detector so deep. There is one especially large dust layer between 2000 m and 2100 m where scattering lengths fall to 4 m and absorption lengths fall to 30 m. Figure 4.3 shows the complete scattering and absorption lengths as a function of depth and wavelength.
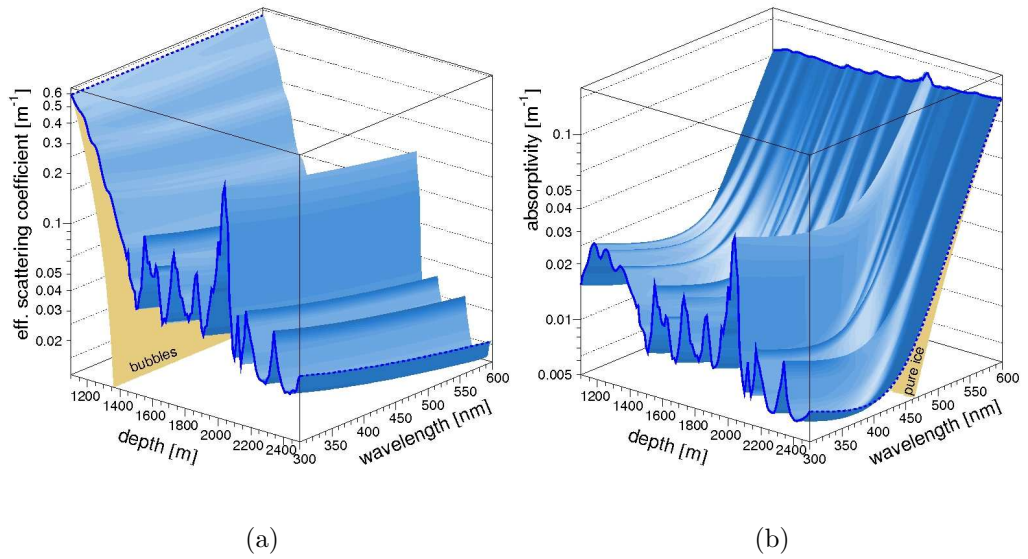
Figure 4.3: Visual representation of the (a) scattering and (b) absorption coefficients as a function of depth and wavelength. Taken from [68].

4.2 Digital Optical Module (DOM)

The DOM is the cornerstone of the detector and is responsible for signal capture, digitization, time stamping, and several calibration procedures. It consists of a Photo-multiplier tube (PMT) to detect light, on-board electronics to digitize the signal and control logic, and 12 LED's arranged in a circular pattern that can emit light for calibration studies. It is surrounded by a mu-metal shield to decrease the effect of Earth's magnetic field on the electrons within the PMT. All this is housed within a 13mm thick pressurized glass sphere capable of withstanding the pressure caused by deep deployment. This can be seen in Figure 4.4. For a more complete discussion, see [70].
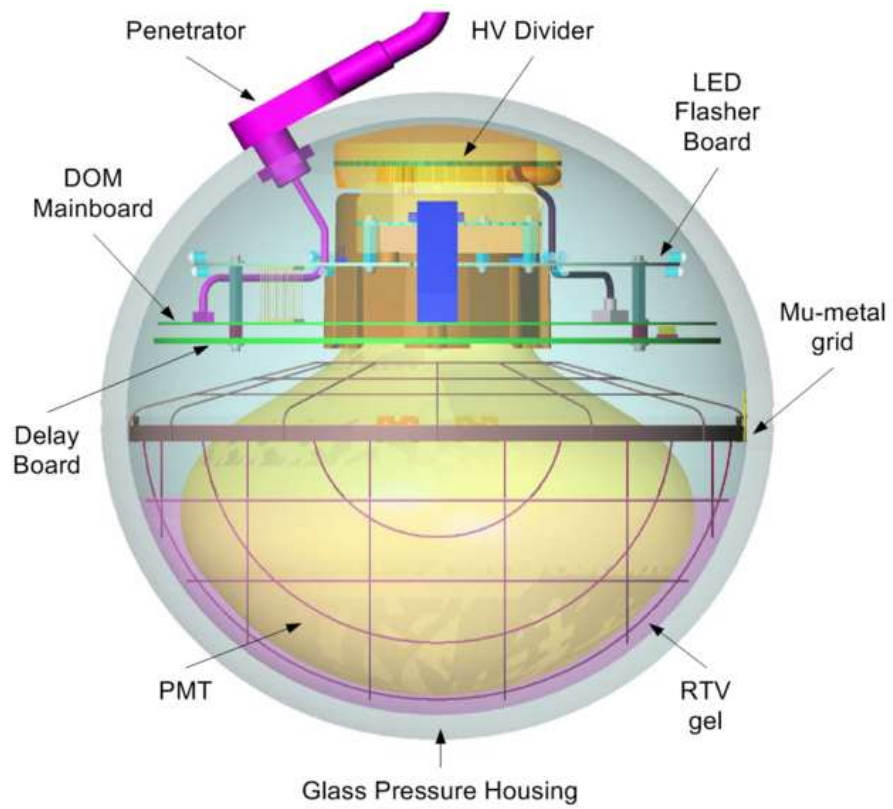
Figure 4.4: A sketch drawing of the DOM.
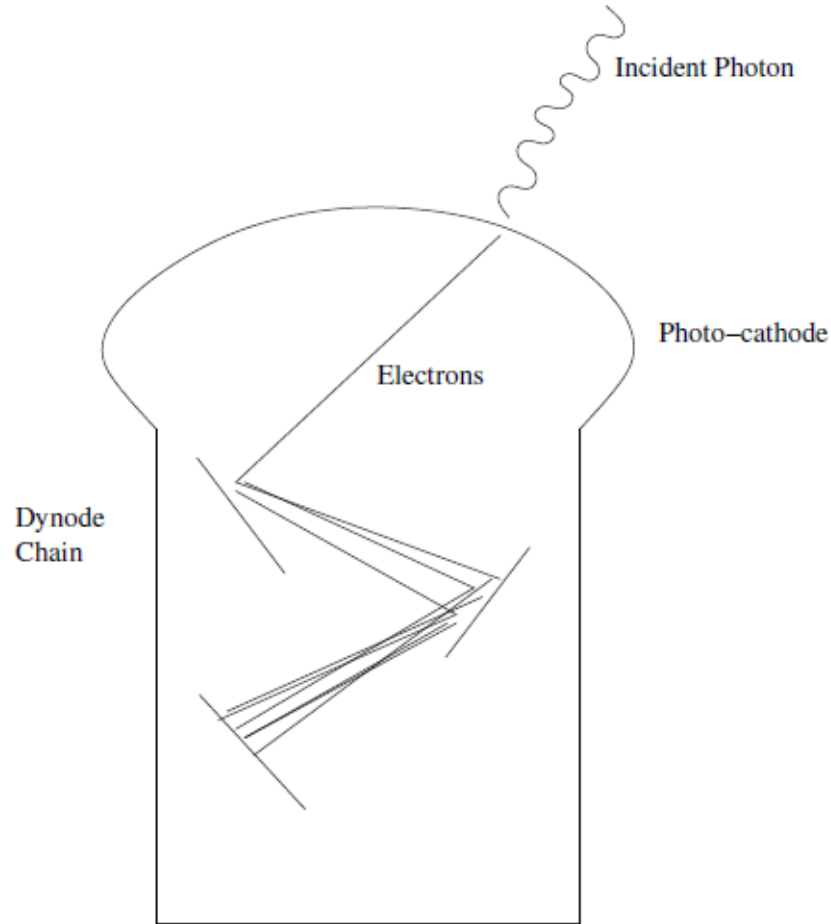
Figure 4.5: A schematic of the PMT operating principle. Courtesy of J. Pretz.

4.2.1 PhotoMultiplier Tube (PMT)

The DOM detects photon signals by a PMT. PMTs are used in a variety of physics experiments for their ability to produce easily measured signals of single photons with good timing accuracy. IceCube uses a HAMAMATSU R7081-02 commercial PMT with a 25 cm diameter. It was chosen based on its ability to meet the many design requirements, including a low dark noise rate of 500 Hz. For more information on the design and specifications, see [26].

Figure 4.5 demonstrates the underlying principle of a PMT. An incident photon will pass through the optically transparent glass shielding and strike a very thin Bi-alkali photo-cathode, which has a low work function, yielding a photo-electron (PE) $\sim 25\%$ of the time at the peak spectral response of 390nm. This electron is accelerated towards the first of a series of plates (dynodes) that operate at a high voltage relative to the photo-cathode (at ground). Upon striking the first plate, the excess energy frees several more electrons that are then accelerated to the next plate. The resulting chain reaction produces many electrons at the end of the series which form a current. The scaling of the PMT (electrons out over electrons in) is called the gain. This number allows a determination for how many single photo-electrons (SPEs) are recorded by the PMT and depends on the high voltage value. In tests, the nominal gain of 10^7 was achieved for HV values $\sim 1300\,\text{V}$ (see Section 4.6.3). When the multi-billion electron signal reaches the anode, a sharp current is produced.

4.2.2   DOM Mainboard

The output current from the PMT is passed to the DOM mainboard, which is responsible for the triggering, digitization, and time-stamping. A simplified block diagram of the mainboard can be seen in Figure 4.6. The signal is split into three paths: the on-board trigger and two waveform digitizers.

It is controlled by an on-board Altera EPXA-4 Field-Programmable Gate Array (FPGA), which handles all signal and communications processing. The FPGA
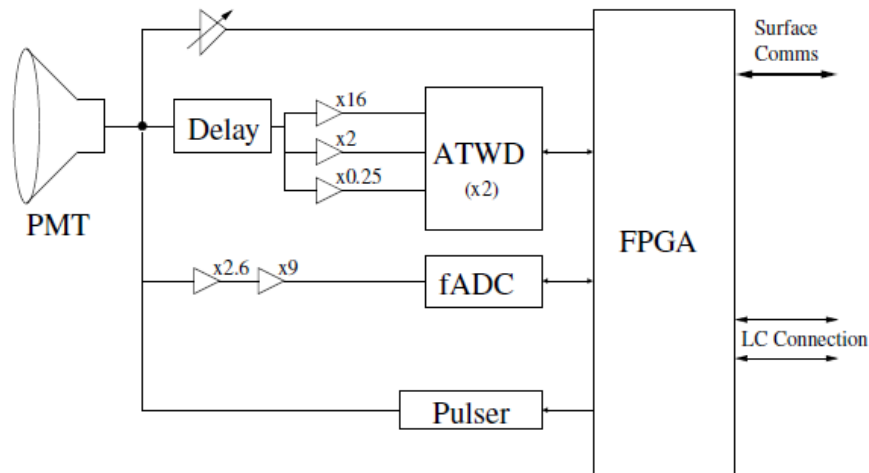
Figure 4.6: A block diagram of the DOM Mainboard electronics. For simplicity, some components have been omitted. See [70] for a complete version.

can be programmed remotely via an ARM™CPU, allowing for settings to change despite the remoteness of the DOM.

On-board Trigger The first path is to a discriminator to determine if a launch condition is met. A launch represents a PMT recording a signal large enough to exceed a pre-defined threshold. For data taken in 2007, this was nominally set to the voltage corresponding to $\sim$ 0.2 PEs. Once a crossing of the threshold has been found, the signal is re-synced to the next leading edge of the internal clock, which oscillates at 40MHz. The signal, now officially a 'hit', is then time-stamped with this leading edge value. This represents the coarse time stamp of the event. A fine time stamp can be introduced later by reconstructing the leading edge of the digitized waveform, but for this analysis the coarse time stamp is sufficient.

Once a hit has been determined, the DOM sends a signal to the two nearest DOMs above and below. The FPGA will check and see if it received a comparable signal from any of the 4 DOMs surrounding it within +/- 500 ns of its launch. Only when this local coincidence requirement is met will the FPGA send the signal up to the surface. This helps significantly reduce dark noise rates.

ATWD   The second path the signal takes is through a 75ns delay line to an Analog Transient Waveform Digitizer (ATWD). The ATWD is an Application Specific Integrated Circuit (ASIC) custom designed for IceCube. It is able to record a highly detailed snapshot of the waveform for the brief time at the beginning of the launch when most of the interesting physics occurs. The nominal sampling rate is set to 300 Mega-Samples per Second (MSPS) which corresponds to 3.3 ns/sample for the 128 bins that it can record. Another important design requirement was to ensure a large dynamic range to account for signals from 0.2 photo-electrons up to 400's PEs/15ns, at which the PMT itself saturates. This is accomplished by digitizing the waveform across 3 channels representing different gain amplification values, differing by factors of 8 (16, 2, and 0.25). Figure 4.7 shows an example of the three waveforms taken from a flasher run.

The time for the discriminator to determine if an on-board trigger has been met and time stamp the hit is typically $< 50\,\mathrm{ns}$, depending on how far after a clock cycle the on-board trigger occurred. Once done, the FPGA sends the signal to the ATWD to start recording (another $\sim 20\,\mathrm{ns}$). Thus, the $75\,\mathrm{ns}$ delay line is more than adequate to ensure the ATWD starts recording before the hit information appears.
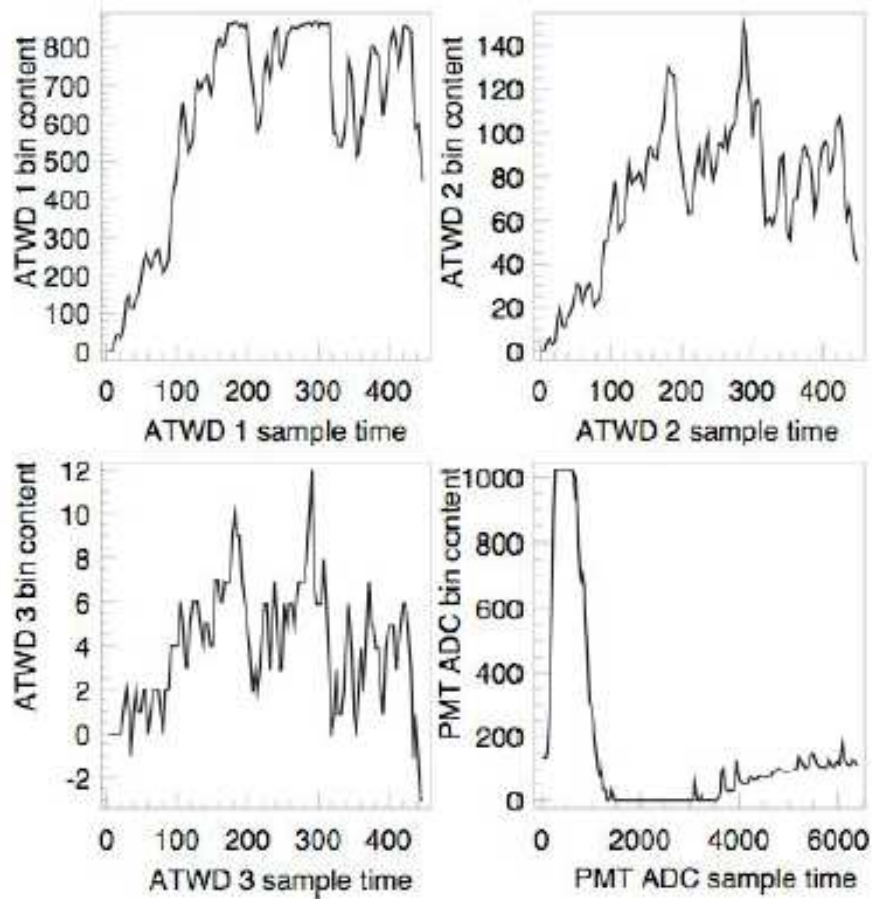
Figure 4.7: Examples of the four digitized waveforms recorded by the DOM for a flasher (bright LED) burst. Upper left is the highest amplification ATWD channel, followed by the upper right and lower left. The lower right is the long time waveform (see Section 4.2.2). Note the difference in time scales. Taken from [70].

FADC The third path is to a commercial Analog Digital Converter (FADC). [1] The FADC has a sampling speed of 40MSPS (25 ns/sample) that is synchronized with the on-board clock. With 256 samples, it can record the waveforms for up to 6.4μs. This is ideal for its purpose to provide long time information of the waveforms.

Since the sampling speed is much slower than the ATWD, the signal is first passed through a three-stage waveform shaping process. First, it is amplified by 2.6. Then, it passes through 2 identical Butterworth low-pass filters with an amplification of 3. The result is a waveform with a 180ns shaping time. The shaping is useful for this digitizer to allow for the features to be seen with the coarse 25 ns bin size. The amplifiers ensure that the digitized counts will be $\sim$ 13 counts above baseline for an SPE waveform.

The FADC is capable of continuously sampling the output signal from the PMT. When the discriminator records an on-board trigger, the bin corresponding to the time stamp as well as the three previous are included in the final, recorded waveform. The extra 75 ns at the beginning ensures the final waveform will capture the physics event.

---

[1]An unfortunate consequence of using common terminology is that after the analysis had been started, the author became aware of a controversy surrounding the naming of the FADC. It stood for either 'flash' or 'fast', though later arguments revealed both to be inaccurate. The preferred term now is PMT ADC, which is used in all publications going forward. However, for historical reasons pertaining specifically to this analysis, the original naming is retained throughout the work.

4.3   DAQ

When a hit has been recorded in the DOM and the local coincidence condition is met, the digitized waveforms are sent over the twisted wire pairs to the surface where the Data Acquisition (DAQ) system takes over. The DAQ for IceCube is responsible for building up events. It is housed in the IceCube Laboratory (ICL) that sits on the surface in the middle of the detector.

For each string, there is a dedicated DOMHub which is composed of 8 fully customizable PCI Cards known as DOM Readout (DOR) cards. They are responsible for providing power to each of the DOMs and controlling communication with them. Also within the ICL are several dedicated String Processor computers that are responsible for the time calibration of each DOM (see Section 4.6.2) and translating hits from DOM local times into a universal time (based on GPS). In the time since the data taken for this analysis, these processes have been merged into a single process, known as StringHub. The result is a stream of well ordered hits presented to the trigger.

4.4   Trigger

For each year of data, there are several trigger conditions employed to sort out when an event is interesting enough to warrant further investigation. For the year 2007, the main one was the Simple Majority Trigger (SMT 8).

The SMT 8 condition is met when there are 8 DOMs that record a hit, satisfying local coincidence, within a time window of 5 μs. The trigger window is allowed

to slide, thus the condition can be met for an arbitrarily long amount of time. Once the threshold falls below the 8 hit requirement again, the series of hits represent the trigger window. A readout window of +/- 10 μs is added to the trigger window and all hits within that window are recorded as an event.

There were other triggers in place as well, including one based on the AMANDA detector, which was still operating. Anytime there are triggered events which overlap in time, they are merged into a single event. All events in the data used passed the SMT 8 trigger, though some include much longer readout windows due to the presence of the AMANDA trigger, which had an especially long readout window of 75 ns. This increased the rate of events containing multiple physics events. The effect of this is eliminated at the analysis level with cuts that remove these coincident events (see Section 7.4).

4.5 Online Processing and Filtering

The final step in collecting data from IceCube is to pass the data over satellite to the north to be studied. However, all data recorded by the triggered events total ~ 100 Gb/day, while the satellite can send ~ 25 Gb/day. To meet this requirement, further filtering must be done in order to reduce the dataset. This is accomplished by the Processing and Filtering (PnF) system.

Figure 4.8 shows a schematic of the PnF system. Data from the DAQ is first fed through a buffer called DAQ-dispatch, which allows the systems to run independently. Once fed to the PnF, the data is sent by a server to a cluster
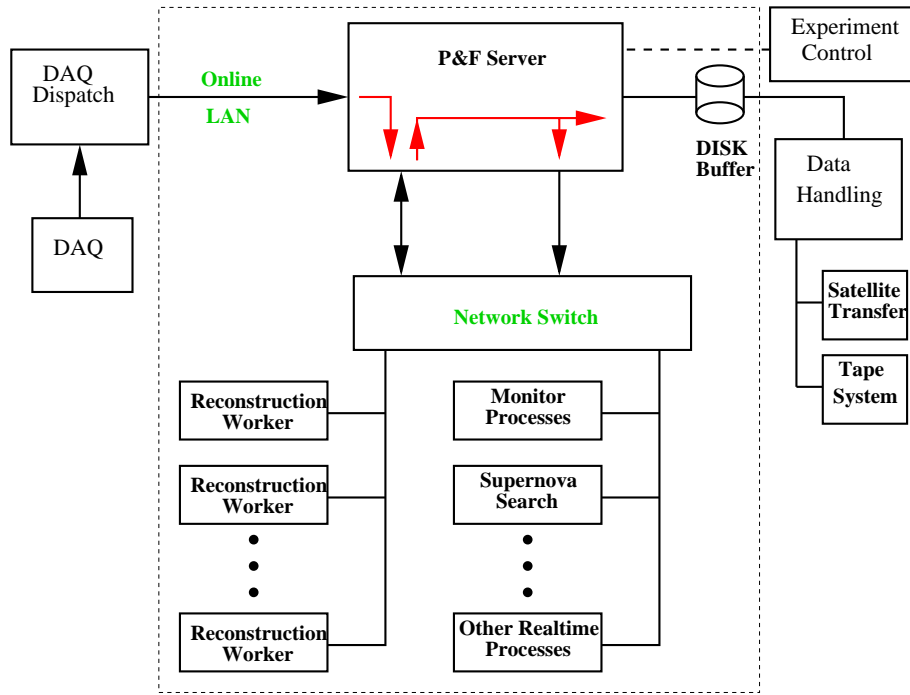
Figure 4.8: A block diagram of the PnF system.

of machines that run reconstructions and filter the data based on predetermined quality cuts.

There are several filters that the PnF uses to reduce the data. They are listed in Table 4.1. Some notable ones include: the muon filter, which is the main filter responsible for locating up-going muon tracks used in searching for muon neutrinos; the cascade filter, which is responsible for finding bright bursts of light caused by electron neutrinos, and several minimum bias filters that retain a fraction of all original data. For instance, the FilterMinBias filter keeps every 200th event that triggers the detector to allow for studies on the stability of the triggering system, at a rate of $\sim 2.75\,\mathrm{Hz}$.

Table 4.1: Physics Filter Rates During IceCube 22-string Physics Run. Prescale represents the fraction of events that are then sent north over the satellite.

Filter	Rate (Hz)	Prescale	Description
CascadeFilter	17.92	1	Electromagnetic showers
ContainedFilter	4.03	1	AMANDA/IceCube combined events passing a veto
DowngoingContainedFilter	3.09	1	Downgoing track events passing a veto
EHEFilter	1.28	1	High energy events
FilterMinBias	531.80	200	All events
IceCubeMuonFilter	19.51	1	Upgoing track events
IceTopSMT	15.39	5	All IceTop triggered events
IceTopSMT_InIceCoincidence	2.63	1	Events with IceTop and InIce activity
IceTopSMT_Large	0.93	1	Large IceTop triggered events
InIceSMT_IceTopCoincidence	13.20	5	Events with IceTop and InIce activity
JAMSMuonFilter	0.0	1	Upgoing track events in AMANDA
LowEnergyContainedFilter	4.11	1	Single string events with other cuts
MoonFilter	0.0	1	Events from moon direction (when moon is above horizon)
MuonFilter	19.51	1	Combined upgoing track events
PhysicsMinBiasTrigger	91.25	40	Events that are randomly triggered

For this analysis, the only filter used is the EHE filter. Designed to keep all very bright events regardless of direction in order to search for high energy neutrinos, it is also particularly useful for the bright nature of monopoles. The filter requirement in 2007 was for an event to record at least 80 DOM launches.

The filtered data is then written to a second buffer and awaits its chance to transmit over the South Pole Archival and Data Exchange (SPADE) system, that manages the transfer over the satellite to the north. Once it is sent north, it is stored at the computer center at the University of Wisconsin-Madison, where it is available to the entire collaboration. Though it cannot all be sent north, every triggered event is concurrently written to tapes at the South Pole in case it is ever needed in the future.

4.6   Calibration

In order to ensure the data arriving from the pole is robust, several procedures are used to calibrate the detector. This section will detail three important procedures that calibrate the position, timing, and waveform response of the DOM. All three are important inputs into the analysis reconstructions.

4.6.1   Position Calibration

The exact location of the DOMs, and hence the position of the hits to be used in reconstructions, is measured in stages. Stage one calibration is performed during the deployment of the string. The horizontal positions are measured by a

combination of hole location surveys and data taken during drilling on the drill position. The absolute vertical position is measured using highly sensitive pressure sensors located 1000 m apart along the string, combined with measurements of the water line and DOM spacing on the string. The resulting calibrations produce a position accuracy $\sim 50\,\text{cm}$ for a given DOM[69].

Stage two occurs after deployment and uses the timing information from dedicated flasher runs (i.e., the detector stops taking physics data) to measure the distances between DOMs. This typically improves the initial position by a few cm. A third stage could use timing from down-going muon information to track changes in the position over the course of physics data taking due to the ice shear. This, however, was not done for the 2007 data since the string deployment was still relatively recent.

4.6.2 Timing Calibration

All time information recorded by IceCube is set to Coordinated Universal Time (UTC). For the surface, this is set by GPS systems, but the DOMs in the ice cannot receive signals from the GPS satellites and must record times using an internal clock. The procedure for syncing this clock to the surface time is called Reciprocal Active Pulsing Calibration (RAPCal).

Calibration starts with the DOR card at the surface sending a bipolar pulse down the cable to the DOM. During transit, this waveform disperses to microsecond lengths. The DOM receives the waveform, digitizes it, and records the time

the waveform is received using the on-board oscillator (40MHz). After waiting a predefined amount of time, the DOM sends the digitized waveform, the time recorded, and a new waveform pulse identical to the one sent by the DOR card back to the surface. Upon receiving the waveform from the DOM, the DOR card digitizes it in the exact same way. The final record includes the transmit time, reception time, and digitized waveforms for both the DOM and DOR card.

To determine the offset between the DOM clock and the DOR (UTC) clock, the propagation time of the waveform must be known. With the reciprocity of the system, however, this value can be determined since the wave travels the same cable each way. Therefore, $T_{\text{prop}} = \frac{(\rho - \delta)}{2}$, where ρ is the total time from when the DOR sent the first pulse to when it received the final one, and δ is the pre-defined wait time for the DOM.

Figure 4.9 shows an example of two digitized waveforms after correcting for the transit time. Identical points, e.g. the leading edge or crossover value, are compared to determine the timing offset. The robustness of the reciprocity assumption can also be verified by comparing the rest of the waveforms to each other. In this manner, timing accuracy can be achieved to the $\sim 1 - 2\,\text{ns}$ level.

Repeating the procedure often allows for statistical errors in T_{prop} to become negligible. Furthermore, comparing the time difference between successive pulses transmitted by the DOR card to the time difference between the DOM receiving them allows for determination of the frequency ratio between the DOR clock and DOM clock.
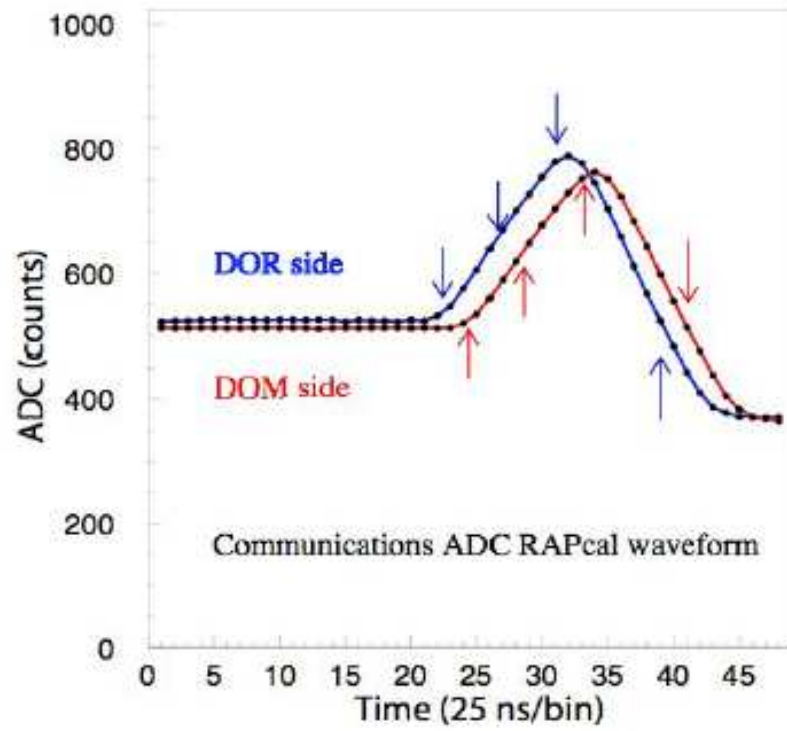
Figure 4.9: Example of two waveforms compared in the RAPCal proce-
dure. Different features of the waveforms can be compared (shown with
arrows) to determine the time offset for the DOM internal clock as well
as the robustness of the measurement itself.

During the RAPCal run, the DOM continues to capture, digitize, and buffer PMT signals. The time for the whole procedure is $\sim 1.4\,\text{ms}$ and occurs once a second, far more often than necessary for the relative stability of the DOM oscillator $(\delta f/f < 3 \times 10^{-11})$. Thus, the process is essentially invisible to data taking.

4.6.3 DOM Calibration

Once a month, a program is run on all the DOMs in the detector known as domcal. It serves two main functions:

* **Measure important values of the front-end electronics** with the goal to allow down-stream analyses to convert the raw output waveforms into physically meaningful quantities.

* **Measure the relationship between voltage and gain for each PMT** with the goal to keep the gain response of a single photo-electron to be roughly uniform over the entire detector.

Electronic Calibration   The output of the DOM is a digitized waveform in terms of a series of count values for the particular channel. In order to determine quantities such as the total charge, these values must be converted to an output voltage. The simplicity of this analysis in using only the raw FADC counts (see Section 6.1) means that knowledge of these constants to apply to the data is unnecessary. However, it is still important in order to ensure the simulation is accurately re-creating the DOM response.

On the DOM mainboard is an electronic pulser which can produce fast PMT-like pulses. The layout allows for the entire DOM readout to be driven by this pulser instead of the PMT (see Figure 4.6). To start the calibration run, this pulser is increased until it reaches a value that triggers the on-board discriminator. Once the voltage is known, the signal is sent to the waveforms to digitize. Repeating the measurement for several voltage values creates a map between the voltage and the final bin count.

PMT The next step in domcal is to measure the PMT response to a single photo-electron. The PMT high-voltage is turned on and the PMT collects data. Using the calibration values for the waveform digitizers just found, a histogram of the data in terms of charge can be calculated. An example is shown in Figure 4.10. Since anywhere along the dynode chain there is a possibility of a electron being freed to start the chain reaction, there is an exponential tail representing amplitudes lower than a single PE. This is referred to as the noise pedestal. The SPE response itself can be seen by the Gaussian curve. The position of the SPE peak can be used to calculate the gain response of the PMT. The high voltage is varied to produce a mapping to the gain. All DOMs are then set to operate with a high voltage corresponding to a gain of 10^7.
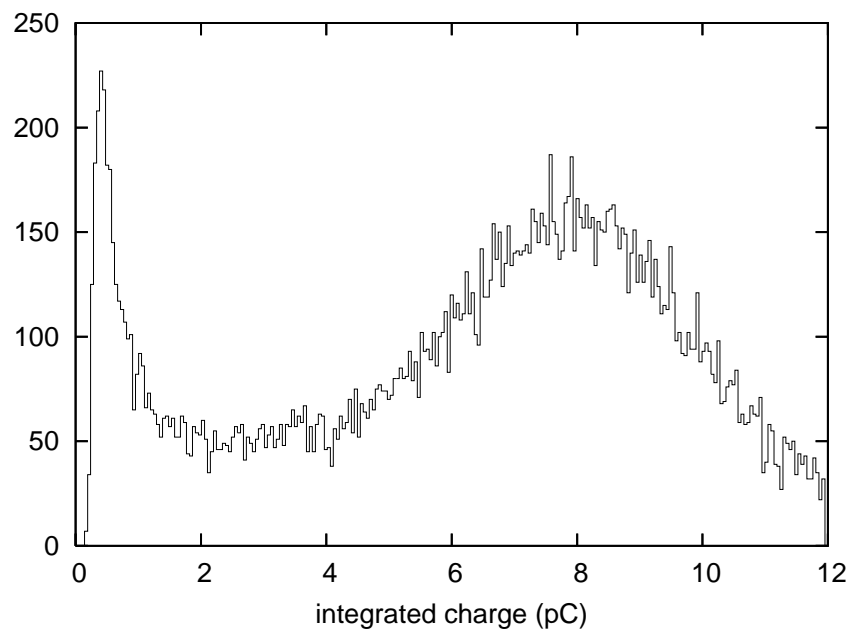
Figure 4.10: Charge histogram for a PMT voltage of 1340 V. The Gaussian peak is the SPE peak. The noise pedestal is visible as well.

Chapter 5

Datasets

This analysis utilizes a strategy of basing all cuts on simulated datasets only. Once a final optimized cut is found, it is then applied to the actual experimental data. This restricts the analyzer from allowing a bias to enter into the cut selection based on known aspects of the data.

In the ideal case, this requires a perfect ability to simulate the experimental data. Since the simulated background is not completely accurate, a ten percent 'burn sample' of the experimental data is used to verify that variables are robust.

This chapter focuses on the simulation of the datasets to be analyzed. All simulations occur within the `ICETRAY` software environment, developed specifically for the experiment. `ICETRAY` is a `C++` based analysis framework that provides classes for the various data types. It also includes a python based modular interface that allows for manipulation of the data containers.

Simulation can be broken into three main components.

* **Generators** are responsible for creating the data objects that represent the primary physics particle and its secondaries at the origin point. For monopoles and neutrinos, this is set to just outside the detector. For down-going muons from cosmic rays, this occurs in the atmosphere representing the shower that results from the primary interacting with the air.

* **Propagators** are responsible for taking the generated particle (or group of particles) and propagating them through the ice and the detector. They keep track of energy losses, secondary particles, and place resulting light sources from secondary induced cascades along the particle track when inside the detector.

* **Detector Simulation** is responsible for using the information from propagators to simulate the light traveling through the ice in the detector and the response from the DOMs. This includes the entire detector response chain up to the final trigger.

All this is done within a group of simulation projects called `ICESIM`. `ICESIM` is an extension of the `ICETRAY` framework and all the tasks above are split into separate modules to be chained together. Figure 5.1 shows what typical scripts are used to simulate the separate background and signal datasets.

5.1   Background Simulation

5.1.1   Cosmic Rays

The major background consists of muon bundles produced by a cosmic ray primary of very high energy striking the atmosphere. The independent software package `CORSIKA`[71] is responsible for modeling the resulting shower of secondary particles. There are several options for modeling the hadronic interactions of both the primary and secondaries at high energies. For this work, `SIBYLL` is used in the
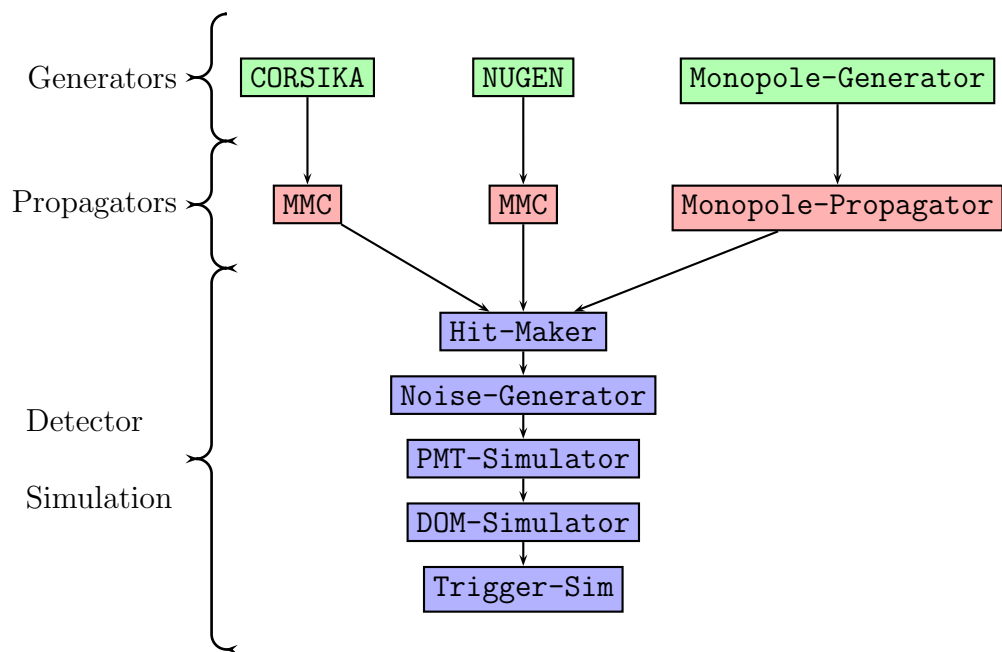
Figure 5.1: Module chain for the simulation of physics events in IceCube. Individual components explained in the text.

production.

One deficiency of CORSIKA is that it will only simulate primaries up to iron. This precludes using a poly-gonato model of the cosmic ray energy spectrum whenever the high energy tail (above $10^8\,\text{GeV}$) is important, since heavier elements up to uranium begin to add a significant contribution to the overall flux (see Figure 3.5). For most IceCube analyses, the energy range is low enough so that simulating the poly-gonato model with only the elements up to iron is sufficient. This is standard for the large scale simulation production done by the collaboration.

For this analysis, the high energy component is very important, representing the background most similar to bright monopoles. To avoid the difficulty of having no heavy elements, a two-component model of protons (for light primaries) and iron (for heavy primaries) is used based on fits to data from extensive air showers measured by KASCADE[72]. This is shown in Figure 5.2. The benefit is that the fit no longer assumes the heavy elements that CORSIKA is unable to simulate and the high energy tail is more reasonable.

Figure 5.3 illustrates the difference of the two models on the resulting energy spectrum at the online filter level. This demonstrates the lack of high energy events from poly-gonato simulation resulting from the lack of heavy elements. The difference at lower energies is due to the two-component model lacking intermediate elements. These each have slightly higher knee cut-offs and leads to an overall smoothing of the knee region. This difference is unimportant for the present analysis since the final level considers only primaries with energies above $\sim 10^9 - 10^{10}\,\text{GeV}$.

The cosmic ray primaries are generated for energies between 10^4 and $10^{11}\,\text{GeV}$

76
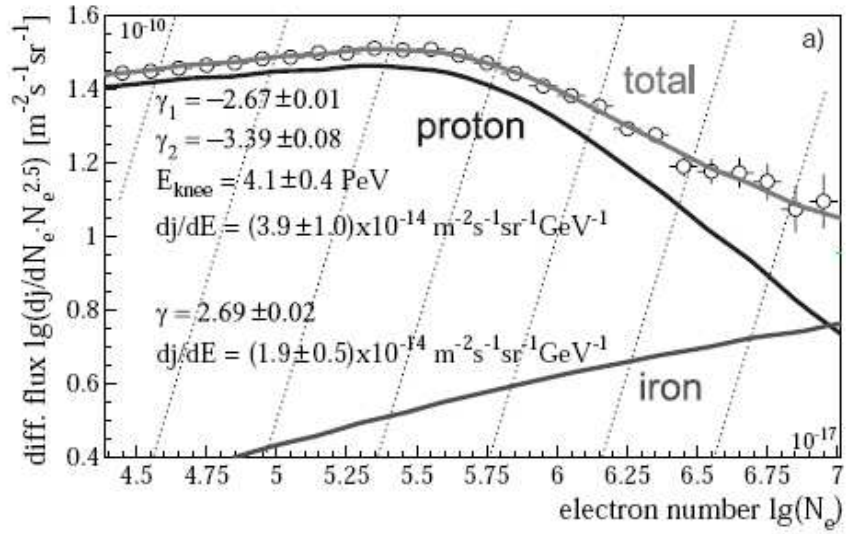
Figure 5.2: Fit of two component model to `KASCADE` data. Taken from [72]

(a)

(b)
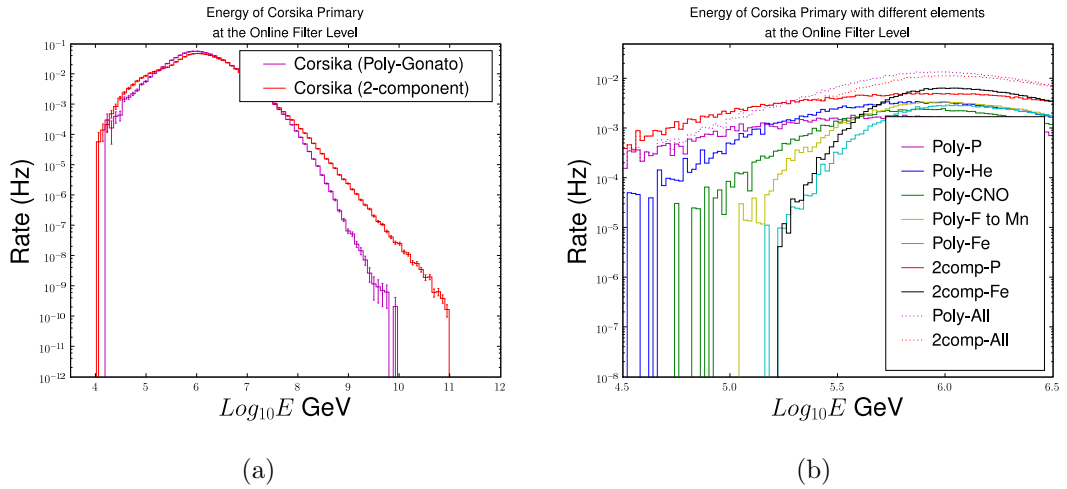
Figure 5.3: Cosmic Ray Primary Energy spectrum of the two simulated models at the online filter level. (a) Shows the overall rates and (b) shows the rates split up based on composition. The lack of high energy events for Poly-Gonato simulation results from the fact the model fits the spectrum for elements up to uranium while the simulation only produces up to iron.

Table 5.1: Values for `CORSIKA` two-component weighting functions.

Parameter	Proton	Iron
Normalization	1.98×10^4	1.07×10^4
$A_{gen}\Omega_{gen}$	1.45083×10^7	1.45083×10^7
γ_1	-2.67	-2.69
γ_2	-3.39	-3.1
E_{Knee}	$4.1 \times 10^6 \text{ GeV}$	$1.1 \times 10^8 \text{ GeV}$

with an E^{-2} weighting to allow an oversampling of the high energy events. The events were then re-weighted using the following functions:

$$
Weight(Energy) = \frac{Norm}{\Phi_{Gen}}
\begin{cases}
E^{\gamma_1 - \gamma_{gen}} & if E <= E_{\text{Knee}} \\[2ex]
\frac{E^{\gamma_2 - \gamma_{gen}}}{E_{\text{Knee}}^{\gamma_2 - \gamma_1}} & if E > E_{\text{Knee}}
\end{cases}
\tag{5.1}
$$

Here, $\Phi_{gen} = \frac{N_{gen}}{A_{gen}\Omega_{gen}T_{gen}}$ and the $E_{\text{Knee}}^{\gamma_2 - \gamma_1}$ ensures the broken power law spectrum matches at the knee value. Table 5.1 lists numerical values. The original KASCADE fit did not include values for the knee energy or γ_2 for iron, as they were outside the fit region. The iron knee value is taken as twenty-six times the proton knee following the assumption that the knee energy scales with charge. The second spectral index is taken as -3.1 to represent the general all-particle cosmic ray spectrum above the knee following the assumption that this spectrum is dominated by heavy elements.

The resulting muon bundle from the cosmic ray air shower is then passed to the Muon Monte Carlo (`MMC`) software package[73]. This is responsible for propagating the muons through the ice by tracking both the collisional and stochastic energy losses. Once inside the detector, `MMC` records individual stochastic losses to be used to determine overall light output by the muons.

One class of events that is not generated involve coincident muon bundles. This

occurs when a muon bundle triggers the detector and a second bundle in a different location and direction add hits the event before the trigger window closes. These events are especially prone to be mis-reconstructed if the second event occurs higher in the detector than the first. At the time the analysis was developed, there were no dedicated coincident muon bundle datasets available for high energy. However, quality cuts at level 3 (see Section 7.4) based on the burn sample data are designed to eliminate these events. Moreover, an estimation of the coincident rate that is relevant to the analysis shows them to be inconsequential at the final level (see Appendix B).

5.1.2 Neutrinos

A second source of background are particles produced from a charged current interaction from a neutrino. The primaries here are produced by the software package NUGEN designed specifically for IceCube. It simulates neutrinos passing through the Earth and interacting near the detector. For muon neutrinos, the resulting muon is then passed to MMC to propagate further. For electron neutrinos, the resulting electron is treated as a point-like shower since its propagation distance is small compared to the distances between DOMs.

A dataset of neutrinos can be weighted according to either an atmospheric flux or a diffuse flux (see Section 3.4). Only the atmospheric flux is studied here. For the weighting, the flux can be split into the 'conventional' and 'prompt' component. The 'conventional' flux is fairly well constrained and the particular model of Honda

et al. is used[74]. In the original analysis, the prompt model was not considered due to the uncertainty surrounding it. However, for the a posteriori analysis, the prompt model of Sarcevic et al. is taken[75].

Note that the neutrino sample is not important until the final level. At level one, which is defined as having at least two saturated hits (see Section 6.1), the atmospheric muon neutrino passing rate is roughly six orders of magnitude below the passing rate for muon bundles from cosmic rays. The reason they are included is that they can still arrive from all directions, especially in the horizontal region, which is important at the final level.

5.1.3 Detector simulation

Once a particle is simulated through the detector, the light output resulting from the combination of both the Cherenkov cone and stochastic events is propagated through the ice using `PHOTONICS`[76]. This takes into account the various ice properties from models to determine how much light reaches an individual DOM. `PHOTONICS` is a table that is generated separately, allowing quick access to photon densities and arrival times at any particular DOM as a result of a track or cascade.

In the course of this analysis, four separate ice models are used. The signal simulation uses a version of the ice model based on studies obtained from AMANDA[68], labeled `MILLENNIAL`. For the deeper ice, extrapolations were made using dust concentration data from ice cores measured at Vostok and Dome Fuji.

During the analysis, an updated version of the `MILLENNIAL` ice model was pro-
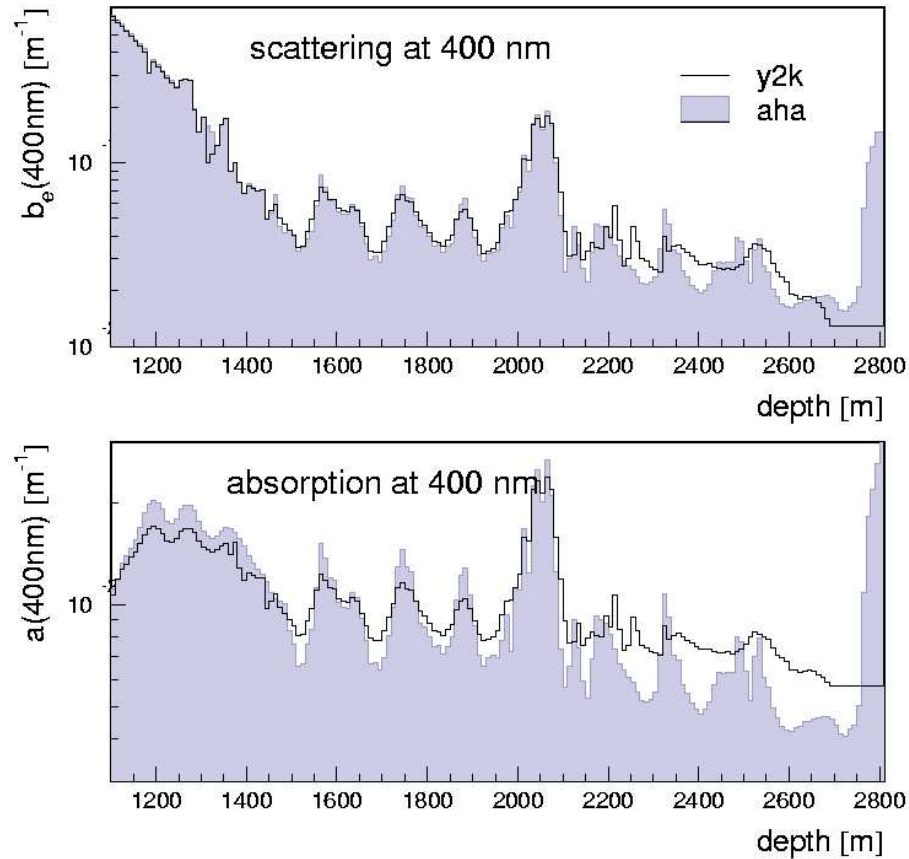
Figure 5.4: Scattering and Absorption coefficients as a function of depth for the AHA and Millennial Ice Models[77].

duced, labeled AHA. Among the various improvements were a more accurate record of the peaks and valleys associated with the scattering and absorption coefficients as well as a new extrapolation to the deep ice based on ice core data taken from East Dronning Maud Land, Antarctica. Figure 5.4 shows the scattering and absorption coefficients for the two models at the wavelength of 400nm. The background simulation was redone with this new model. Since the signal is much brighter than background and thus less sensitive to ice model variations, it was not redone.

After the original analysis was complete, a separate model was developed to

compete with `PHOTONICS` and `AHA`. Instead of creating tables to record the probabilities of a hit from a track, a new software package Photon Propagation Code (`PPC`) was developed to individually track each photon as it left the source. In addition, a new ice model based on a global fit to the flasher data labeled the South Pole ICE model (`SPICE`) was constructed[78]. While it demonstrates a better description of the dust layer structure, neither model has been adopted exclusively by the collaboration. Based on comparisons made for this particular analysis, the `SPICE` model using `PPC` is adopted for the atmospheric muon simulation in the a posteriori analysis (see Section 9.1.1). For neutrinos, an intermediate version of `SPICE`, labeled `SPICE 1`, is used. This version does not include as many updates to the scattering function and still utilizes `PHOTONICS`.

A further change to the simulation included an updated formula for the light scaling of Cherenkov emission by secondaries. The older version is based on work by C. Weibusch[79] while the latter was developed by M. Kowalski[80]. Extensive studies have yet to be done in comparing the two and in general only one version was available for a particular dataset.

Table 5.2 lists all the simulated datasets used for the analysis, including signal, and the various choices of ice models, photon propagation, and light scaling employed. Note that, for completeness, both versions of the atmospheric muon bundle simulation will be presented on plots.

Once light reaches the DOM, dedicated IceCube software modules add noise hits, simulate the PMT response, the subsequent DOM launch, and the trigger. At this point, simulated data matches the experimental data and the rest of the analysis

Table 5.2: Summary of Light Simulation Parameters of various datasets

Dataset	Ice Model	Light Propagation	Secondary Scaling Function
`CORSIKA` Original	`AHA`	`PHOTONICS`	Weibusch
`CORSIKA`	`SPICE 1`	`PHOTONICS`	Weibusch
`CORSIKA` a posteriori	`SPICE`	`PPC`	Kowalski
`NUGEN` Original	`AHA`	`PHOTONICS`	Weibusch
`NUGEN` a posteriori	`SPICE 1`	`PHOTONICS`	Weibusch
Signal	`MILLENNIAL`	`PHOTONICS`	Weibusch

proceeds the same for both.

5.2 Signal Simulation

The simulation of relativistic magnetic monopoles is a major addition to the IceCube software that was done by this work.

The generation of the magnetic monopoles is handled by a module called `Monopole-Generator`. Monopole events are generated for four different speeds: $\beta=$ 0.995, 0.9, 0.8, and 0.76. The discrete nature follows from the necessity to generate dedicated light propagation tables based on the different Cherenkov angles, and the four speeds represent what has become standard in relativistic magnetic monopole searches. 100,000 events are generated for $\beta=$ 0.995, 0.9, 0.8 while 1,000,000 events are generated for the $\beta=$ 0.76 due to low statistics in the final surviving sample.
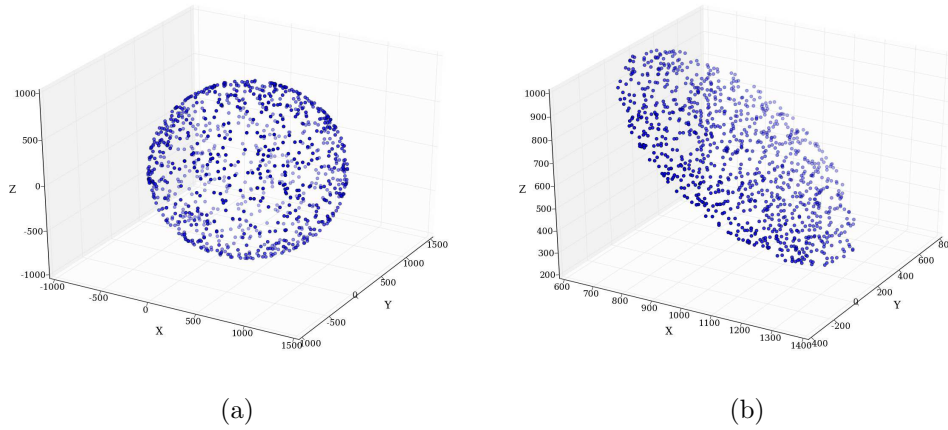
Figure 5.5: Example of how the monopoles are generated. (a) First, a position is chosen uniformly on a sphere centered at the detector. (b) Then, the monopole is generated uniformly on a disk centered at the spherical position. The coordinates represent the position of the IceCube detector, with the center being at (0,0,0). The sphere surrounds the location of the 22-string detector.

Monopole events are generated uniformly on a disk 1000m from the center of the detector. The direction is chosen randomly to produce an isotropic flux. This can be visualized in Figure 5.5. The size of the disk is 650m. The choice of disk radius is based on ensuring that it is large enough to produce the entire accepted signal while not too large in order to save on computing resources. Figure 5.6 shows that, though the disk radius is too small for the online filter (Level 0), by the first level of the analysis it is sufficient.

The propagation of magnetic monopoles is handled by a separate module called `Monopole-Propagator`. The module segments the monopole track based on how long it takes for the monopole to lose enough energy to change its kinetic energy by 0.1%, with a setting to allow for a maximum and minimum step size. For
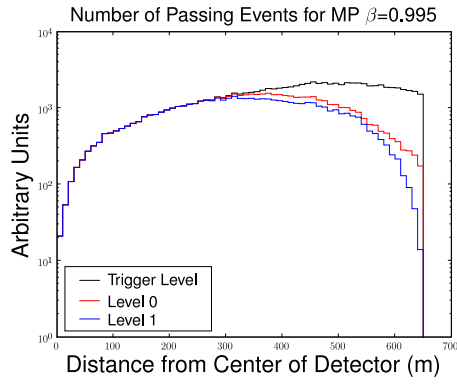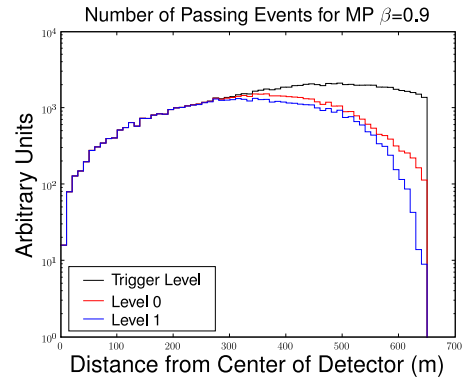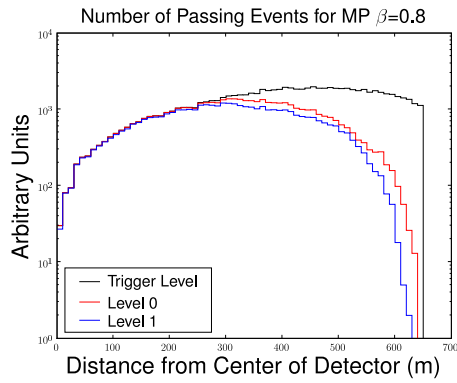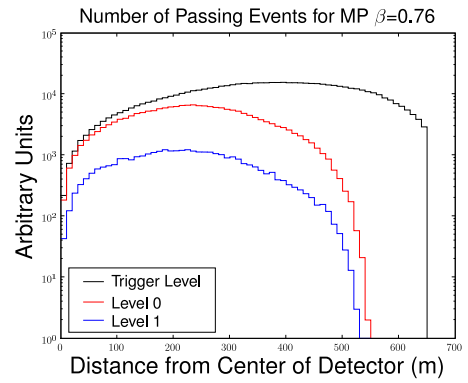
Figure 5.6: Distance from center of generated disk for signal monopoles passing various cut levels for (a) $\gamma = 10$, (b) $\beta = 0.9$, (c) $\beta = 0.8$, and (d) $\beta = 0.76$.

this analysis, the maximum step size was 10m and the minimum was 0.1cm. The purpose of segmenting the monopole track is to monitor the speed variation as it travels through the detector.

Currently, energy loss is modeled as collisional loss alone. Future plans are to extend the energy loss to include both stochastic effects and delta electrons. Delta electrons are those that the monopole 'knocks off' the ice atoms and can be given relativistic speeds even without a relativistic monopole due to the large mass difference. The resulting light would allow for possible detection down to speeds of $\beta \sim 0.52$.

The light output and propagation is modeled by a version of `PHOTONICS` specifically generated to work with cone angles associated with the different speeds simulated. The light amplitude is scaled up using the formula of Tompkins[24](see Section 2.5). Once the light is propagated to the DOM, the simulated detector response is the same as the background simulations.

All the events were generated with a mass of $10^{11}\,$GeV. The importance of mass is minimal because the light output is essentially mass-independent when only considering the Cherenkov light from collisional loss. Any mass chosen in which the speed of the monopole will remain roughly constant throughout the $\sim 1.2\,$km path through the detector will produce the same output. Appendix A details what effect this extra constraint has on the parameter space.

A sample of a simulated monopole event is shown in Figure 5.7.
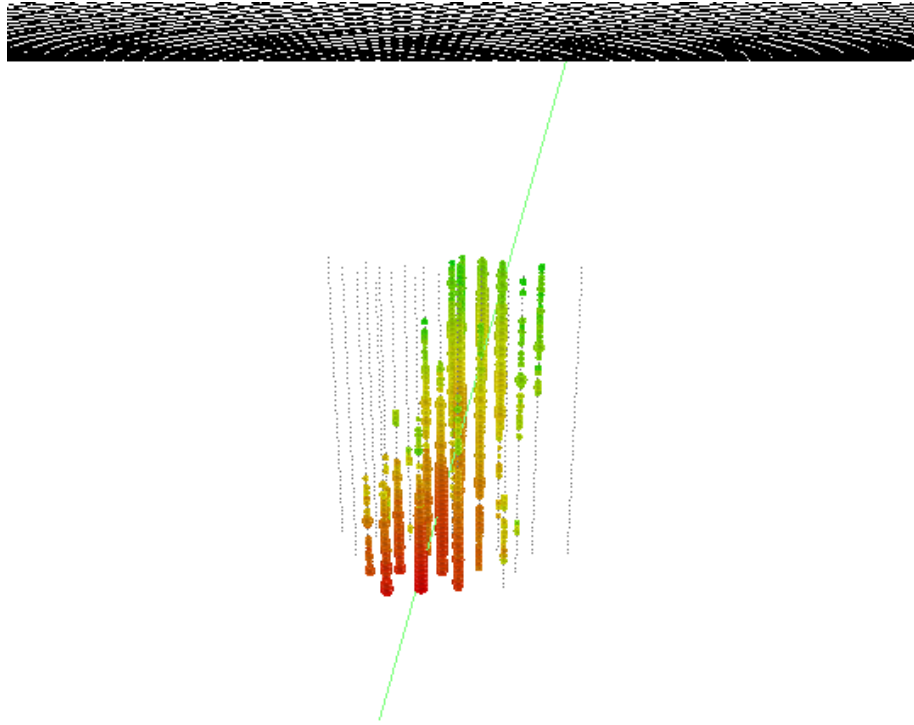
Figure 5.7: Example of a simulated magnetic monopole. The color of the hits correspond to the launch time and the size corresponds to the amount of light deposited.

5.3 Burn Sample

A ten percent sample of experimental data is 'burned' in order to ensure the background simulation is reasonably accurate. It is not used in the final analysis.

The method of data selection was to start with every run that ended in 0, allowing for the full variation of the year to be represented. The only runs considered were those that met standard criteria for a good run list as developed by the collaboration. Among the data removed included test runs, LED flasher runs, runs with little or no data, or runs with DAQ problems. This represents about 4% of the total sample. In addition, runs taken between June 16th, 2007 and July 3rd, 2007 were observed by the EHE group to have unusually high trigger rates and were also removed. This represents about 5% of the total sample.

Figure 5.8 shows the passing rates at the EHE online filter level for all data runs ending in 0. The seasonal variation is due to changes in the atmospheric pressure. When the atmosphere is warmer, it expands and increases the probability that a pion will decay before interacting. This produces more muons and increases the trigger rate. The total livetime of the final burn sample used is $\sim 2.2 \times 10^6$ s
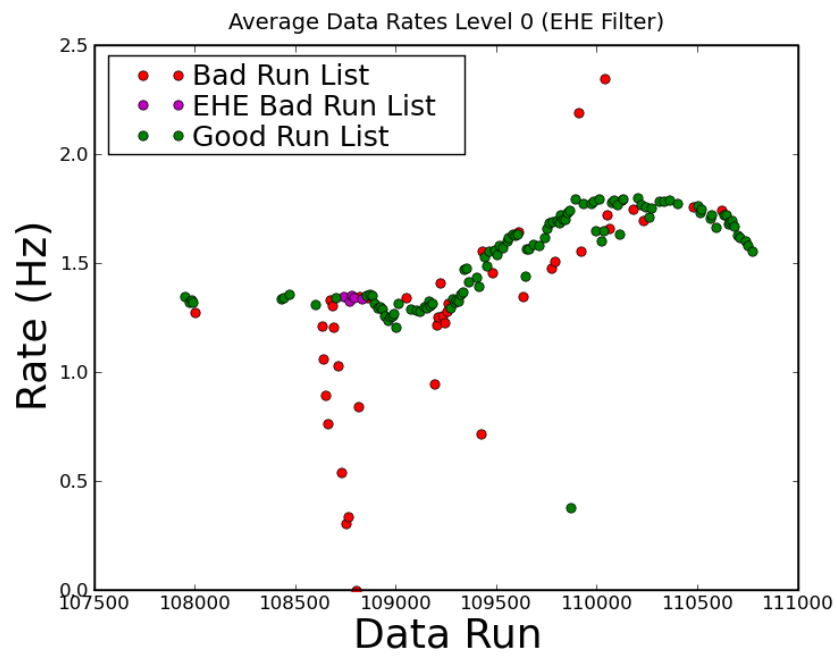
Figure 5.8: Individual run rates at the online filter level for the burn sample.

Chapter 6

Analysis Techniques

The overall goal of the analysis is to develop a set of variables which distinguish the signal (magnetic monopoles) from background (muon bundles and neutrino-induced leptons). This is accomplished by utilizing three factors of monopoles that are unique: (1) they are bright, (2) they can arrive from all directions, and (3) they can still travel long distances at speeds less than the speed of light.

Once a good distinction between the two sets can be found, an optimization is performed to find the best possible cut to use in order to maximize the sensitivity of the experiment.

The following sections will describe the methods of selecting bright events, how the speed and direction are reconstructed, and the procedure used for optimization.

6.1   Hit Definition

The fundamental piece of datum to be used by reconstructions is a hit. A hit is defined when a DOM reaches a certain threshold and the position and time are recorded. For the DOM to record a launch at all, this threshold is set to a predefined value of $\sim 0.2\,\mathrm{PEs}$. However, in this analysis, the brightness of the signal allows for a much higher threshold. This represents a novel approach compared to previous analyses.
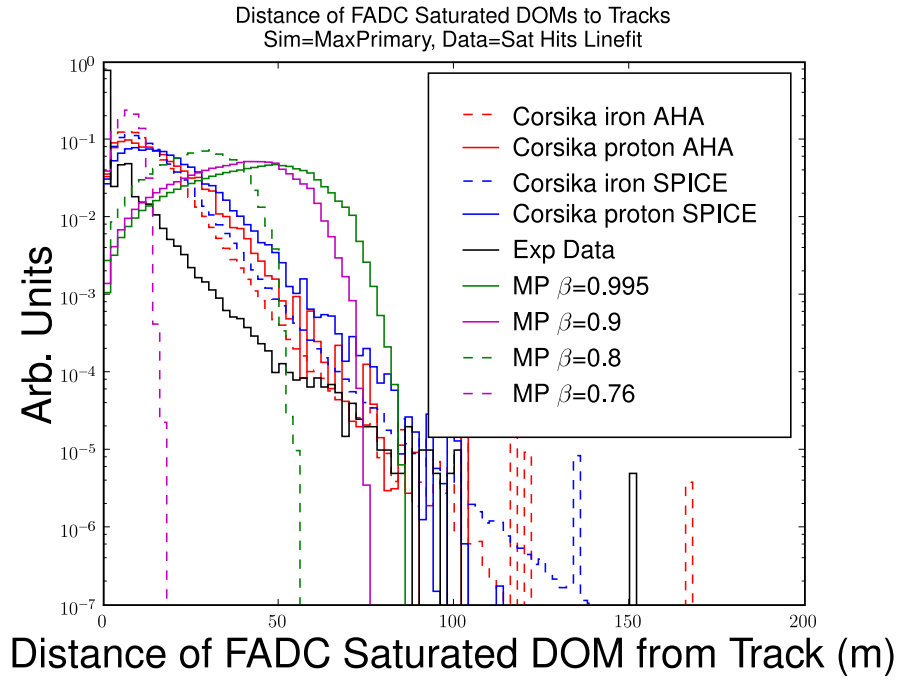
Figure 6.1: Distance from particle track to Saturated DOM. For CORSIKA, a track is defined by the primary cosmic ray. For data, it is defined by the reconstructed track.

Aside from rejecting lower energy events, the advantage of using the higher threshold means that hits will, in general, be much closer to the particles. This in turn reduces the effect of absorption and scattering. Figure 6.1 shows the distance from the hits used to the tracks for all the datasets. As can be seen, the peak is well within the 100m absorption lengths of the ice and, except for signal, the 20m scattering lengths. This results in cleaner reconstructions.

In order to define the hit, studies were done to determine both the definition of the threshold and the definition of the time.

91
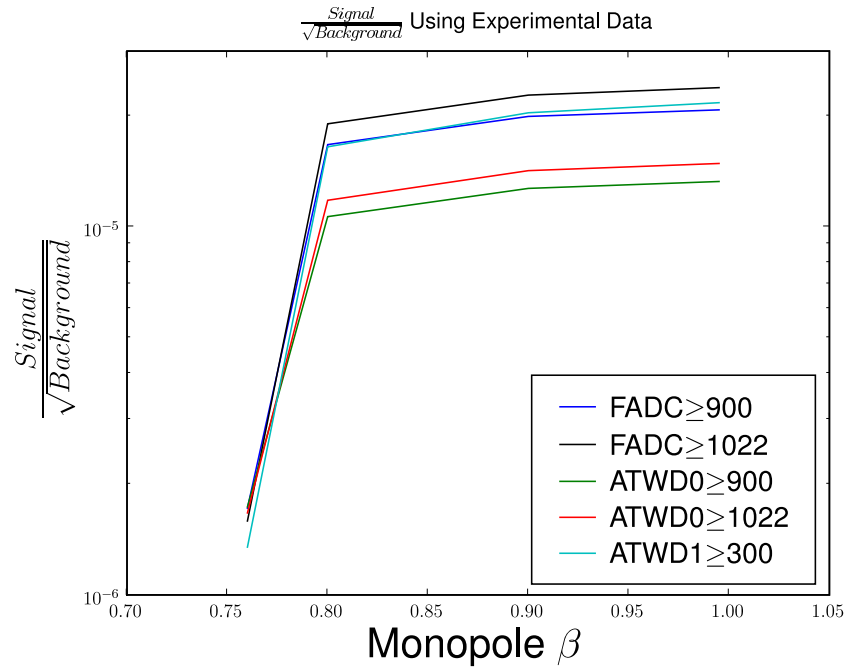
Figure 6.2: Signal over square-root background for various threshold values considered.

6.1.1 Threshold

Each waveform digitizer outputs the signal in terms of counts/bin values that directly map to the voltage recorded (see Section 4.6.3). In all cases, the count values have a maximum at 1022, corresponding to where the waveform digitizer saturates. Several thresholds for the highest count value in the waveform were studied for each of the four waveform digitizers. Figure 6.2 shows the final signal to root background that results in each threshold for the four monopole speeds assuming a cut of at least two hits. The background here is the burn sample. Of the count values considered, the best was the FADC to reach 1022 (saturation).

The FADC likely performs better due to the low-pass filter that is applied
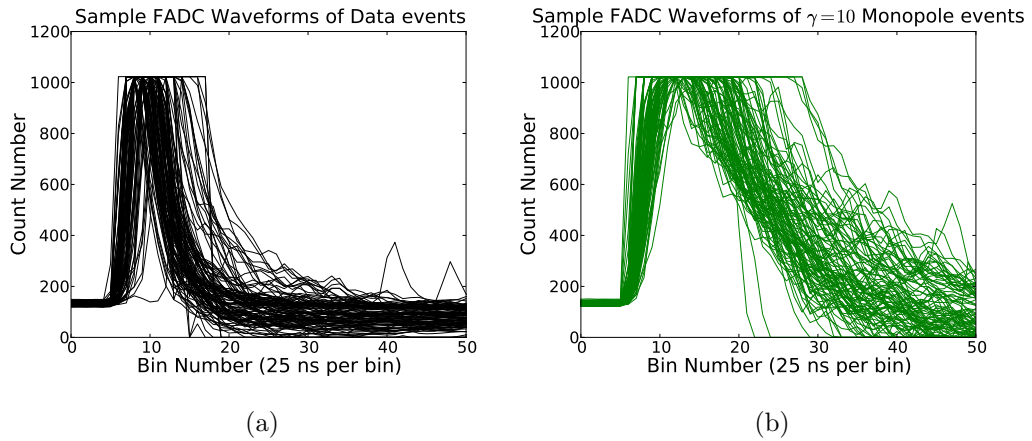
Figure 6.3: Several FADC waveforms for (a) burn sample data and (b) $\gamma = 10$ monopoles

to the waveform. Figure 6.3 shows several FADC waveforms for both the $\gamma = 10$ monopole signal and background data. The monopole light output is generated by the Cherenkov cone alone, whereas for background the stochastic secondary cascades are the dominant cause of the light being bright enough to saturate the waveform. The low-pass filter in the FADC channel focuses on selecting the longer time scale structure of the light. This process favors the smooth light output from monopoles, hence it provides a better rejection of background to signal.

6.1.2 Timing

Three definitions of the time of the hit were considered. The first choice was to take the time of the first launch of the DOM whenever a saturation occurred. This proved problematic since a single event might have multiple DOM launches. This resulted in hits where the first launch is caused by a noise and then, sometime
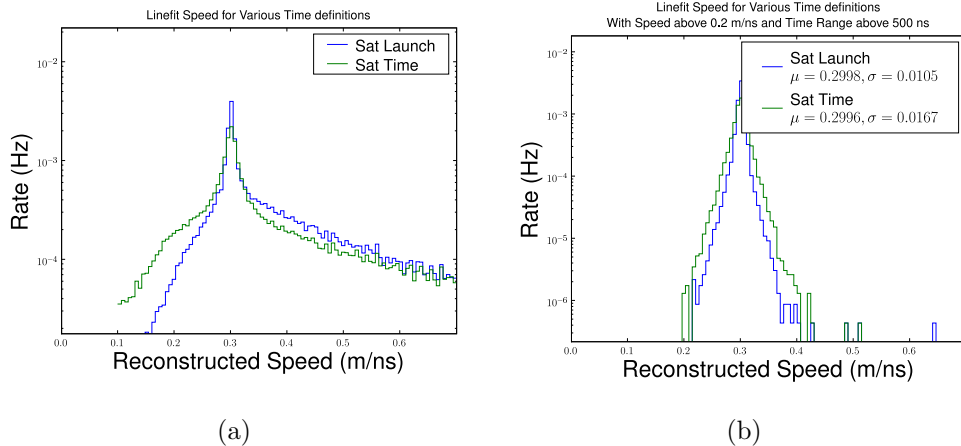
Figure 6.4: Reconstructed speed on experimental data for the two definitions of time considered. The blue represents when the time for the hits is taken as the start time of the launch, while green is when the time for the hits is when the waveform saturates. (a) The result after a cut on two hits and (b) after additional quality cuts on the event requiring it to be at least 500 ns long and have a speed above 0.2 m/ns. Also included in (b) are the mean and standard deviation of the histogrammed data.

later, the saturation happened in a second launch, resulting in a time that was much too early.

The two remaining definitions were the start time of the launch that recorded the saturation and the actual time in which the saturation happened. The latter represents the former plus 25 ns times the bin number that records the saturation. The speed reconstruction (Section 6.2) was performed for each one and in all datasets, the launch time proved more accurate. Figure 6.4 shows this result for the experimental data. The long tails are a result of poor quality events that are removed at higher levels of the analysis. For comparison, the figure also includes the same plot after two of these quality cuts have been applied (see Section 7.4). Thus, the start time of the launch recording the saturation is used.

The ultimate cause of why the launch time is better involves many factors. The dominant one is likely the fact that, especially for hits further from the track, the point at which the saturation occurs will depend increasingly on light that is scattered in the ice. Conversely, for any bright hit, the first few photons that arrive and trigger the launch will be un-scattered.

6.2 Reconstruction

A simple, analytic reconstruction is performed termed 'linefit'. The reconstruction assumes the particle passes through the detector as a plane of light and finds the least-squares solution to fitting the hits in each of the three directions. The slope values represent the reconstructed velocities in each direction, while the relative values are used to determine the direction of the particle. The solution contains the average position and time as a reference point for the particle to pass through.

Starting with the assumption of a plane wave of light, the solution can be written in the form:

$$\vec{X} = \vec{X_0} + \vec{V} \times (t - t_0) \tag{6.1}$$

where $(\vec{X_0}, t_0)$ is taken to be the average position and time of the hits.

The problem is then to find the least squares solution to the set of actual data hits (in terms of position and time) for this equation. This is found by considering the χ^2, defined as:

$$\chi^2 = \sum_{i=0}^{\text{NHits}} \frac{(\vec{X_i} - \vec{X_0} - \vec{V} \times (t_i - t_0))^2}{\sigma_i^2} \tag{6.2}$$
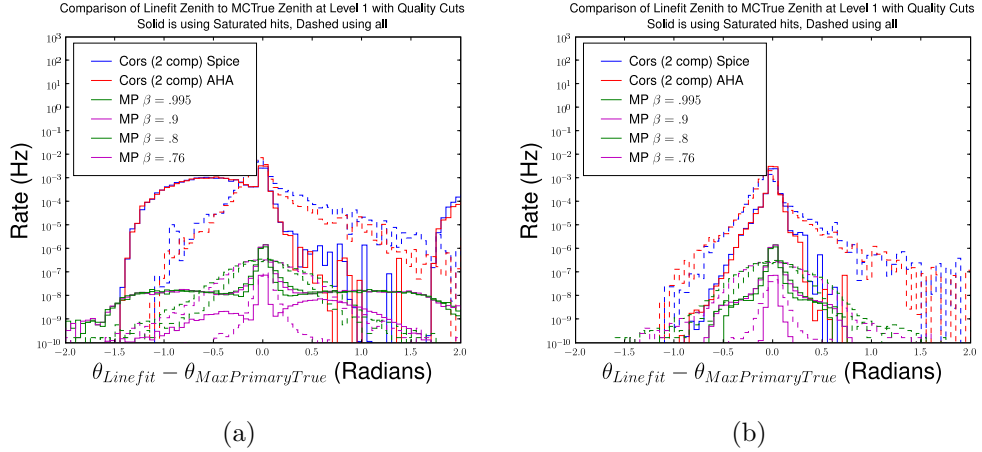
Figure 6.5: Difference of reconstructed zenith to true zenith for all simulated datasets. (a) The result after a cut on two hits and (b) after additional quality cuts on the event requiring it to be at least 500 ns long and have a speed above 0.2 m/ns

An analytic solution can be found under the assumption that all σ_i are equal. Minimizing χ^2 in each dimension and solving produces the following solution for the velocity[81]:

$$\vec{V} = \frac{\sum (\vec{X_i} - \vec{X_0})(t_i - t_0)}{\sum (t_i - t_0)^2} \tag{6.3}$$

While the assumption of a plane wave underlying the reconstruction is not physically valid, the restriction of hits to those that are very near the track improves the angular resolution from $\sim 5-10°$ down to $\sim 2°$. This is demonstrated in Figure 6.5.

The effect is also seen on the accuracy of the speed reconstruction. Figure 6.6 visualizes this. The plot is generated by taking a simulated iron event and finding the distance along the particle track that each hit represents. For example, if the track were straight down-going, the distance would be the z position of the hits.

96
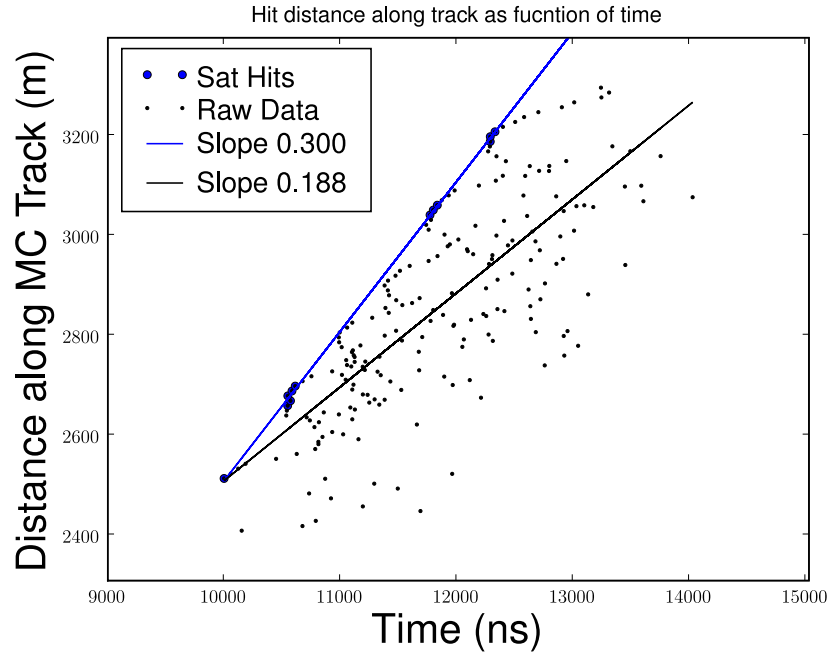
Figure 6.6: Scatter-plot of hits in time and parallel position along a track for an iron event. Blue represents hits that saturate. The lines represent the reconstructed particle, with the slope corresponding to the speed.

These positions are then plotted with the time of each hit. If the hits followed the plane-wave assumption of linefit, this would form a perfect line with slope of 0.3 m/ns. Each dot represents the actual hits, with blue representing those that saturate the DOM. The cone-like distribution is indicative of the Cherenkov nature of the actual light output. However, by fitting only the blue dots, the actual speed (slope) of the particle is much more accurate.

Other analyses use the linefit reconstruction as a first guess for likelihood based reconstructions. These reconstructions incorporate the true expectation of Cherenkov light and the ice properties involved. However, the minimal resources needed by using the analytic solution coupled with the fact that magnetic monopoles

are bright enough to generate many hits that saturate the FADC to produce more accurate reconstructions motivate using linefit alone.

6.3   Model Rejection Factor

To calculate the final limit (in the absence of discovery) on the flux of magnetic monopoles, the ratio of the Feldman-Cousins[82] upper limit to the number of expected signal events is used to scale a generic flux:

$$\Phi_{100(1-\alpha)\%} = \frac{\mu_{100(1-\alpha)\%}(n_{obs},n_b)}{N_s}\Phi$$

$$N_s = \epsilon N_{gen} = \epsilon \Phi A_{gen}\Omega_{gen}T_{live}$$

$$\therefore$$

$$\Phi_{100(1-\alpha)\%} = \frac{\mu_{100(1-\alpha)\%}(n_{obs},n_b)}{\epsilon A_{gen}\Omega_{gen}T_{live}}$$

(6.4)

Here, $\Phi_{100(1-\alpha)\%}$ represents the upper bound on the flux at the $100(1-\alpha)\%$ confidence level. This analysis uses the 90% confidence level. N_s represents the final number of expected signal events, ϵ is the efficiency of the cuts, and N_{gen} is the number of signal events generated by the Monte Carlo that would be expected given Φ and a livetime of T_{live}. Since this number is weighted based on the assumed flux, this term cancels out and the final result is independent of whichever flux one chooses. For example, if the flux is scaled up by a factor of 10, the expected signal event rate in the final cut sample would also scale by a factor of 10, and the flux limit would remain unchanged. For the rest of this dissertation, a constant signal flux of $5 \times 10^{-17} cm^{-2}sr^{-1}s^{-1}$ is assumed, roughly corresponding to the limit obtained by AMANDA[44], in order to have an idea of what the highest expected event rate

might be.

The key to the equation is $\mu_{100(1-\alpha)\%}$, which is a function of the expected number of background events and the total number of events seen in the experiment. Following the Feldman-Cousins 'Unified' approach, this produces a confidence interval that smoothly transitions from cases where the lower limit is non-zero to cases where it is zero, the latter applying to null results. The high value, or upper limit, can be used to constrain predictions of signal events.

The basic idea of constructing the confidence interval is shown in Figure 6.7. Start by assuming a particular value of the true signal, μ. Given the expected background n_b, the outcome of particular experiments is calculated based on a Poisson process. A horizontal band is formed across possible experimental outcomes (X) that cover $100(1 - \alpha)\%$ of the cases, i.e.

$$P(X \in [n_1, n_2]|\mu, n_b) = \sum_{n=n_1}^{n_2} \frac{(\mu+n_b)^n e^{-(\mu+n_b)}}{n!}$$
$$\geq 1 - \alpha$$

(6.5)

Here, the $\geq$ is a result of the discrete nature of the Poisson process, meaning an exact equality is generally not possible. These bands are then constructed for all possible true signal values. To find the confidence interval $[\mu_{lower}, \mu_{upper}]$, one draws a vertical line along the actual experimental result (X, or n_{obs}) and determines were this line intersects the bands.

One ambiguity of this method is defining the horizontal bands, since different ranges of outcomes could still cover $100(1 - \alpha)\%$. Neyman[83] originally suggested choosing the intervals such that the probability above and below the band both equal $(\alpha)/2$ for central confidence intervals while the total probability below the
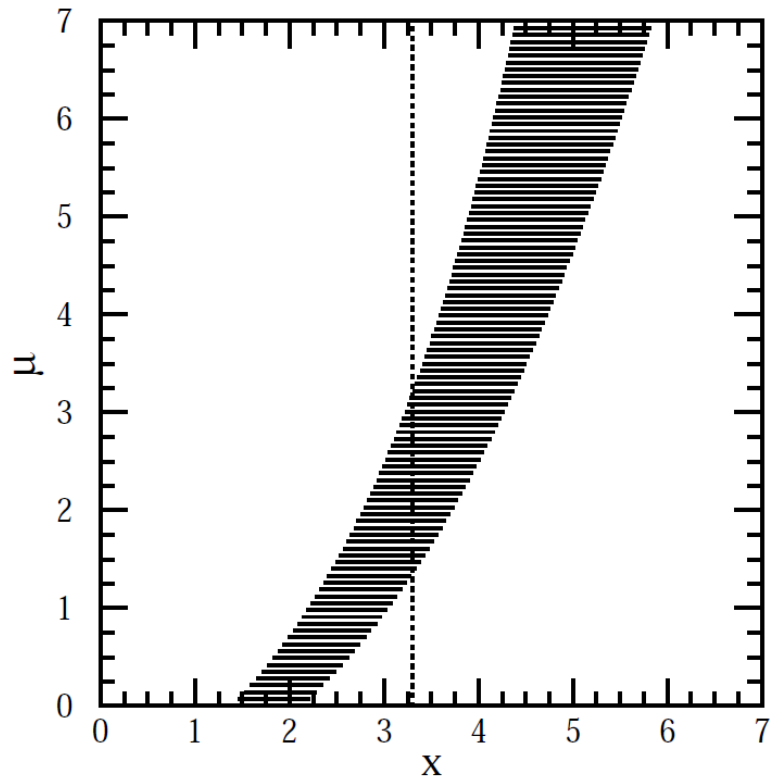
Figure 6.7: Demonstration of Confidence Belt Construction. X is the outcome of a particular experiment (signal+background) and μ is the signal. Horizontal bands cover $100(1-\alpha)\%$ of possible experimental outcomes for a given signal strength. Taken from [82]

band is α for upper confidence intervals. This presents a problem especially in cases where it is not clear before the experiment which value should be used.

Feldman and Cousins solve the problem by introducing an ordering scheme based on the log-likelihood ratio. For each experimental outcome X, the signal value μ which maximizes the likelihood is found. For the Poisson distribution with background n_b, this becomes $\mu_{best} = max(0, X - n_b)$. Then, for each μ, a scan across the possible values of X is performed calculating the ratio $R(\mu, X) = \frac{L_{\mu+n_b}(X)}{L_{\mu_{best}+n_b}(X)}$. The values of X are added to the horizontal band starting with the largest value of R and then decreasing until $100(1-\alpha)\%$ of the possible outcomes are covered. This method will produce upper limits when necessary and central limits when ideal, thus the term 'Unified' approach.

By itself, this method to calculate limits is not useful in determining the optimal cut since the final outcome of the experiment is required. Choosing a cut based on the full data sample can result in experimenter bias (see Appendix D). A way around this difficulty is to use the concept of the Model Rejection Factor(MRF)[84], defined as $\mu_{\text{Avg}100(1-\alpha)\%}/N_s$. This average upper limit is found by calculating upper limits on all possible experimental outcomes and weighting them according to the assumption that only background events are expected which have a Poisson distribution and average n_b:

$$\mu_{\text{Avg}100(1-\alpha)\%}(n_b) = \sum_{n_{obs}=0}^{\infty} \mu_{100(1-\alpha)\%}(n_{obs}, n_b) \frac{n_b^{n_{obs}}}{n_{obs}!} \exp(-n_b) \qquad (6.6)$$

By averaging over all possible values for the number of observed events, the average upper limit becomes a function of expected background alone and thus can be found

before the experiment is performed. It represents an expected value of the upper limit were the experiment to be performed many times with no existing signal. This allows optimization on the cuts in order to find the set that will, on average, produce the smallest upper limit.

Chapter 7

Original Monopole Selection

The following chapter summarizes the original cut selection. The analysis was performed in a completely blinded fashion, with cuts based on simulation and the 10% burn sample alone. Then, in the process of 'unblinding', the cuts were applied to the remaining 90% sample. Unfortunately, deficiencies in both the analysis design and background simulation led to a significant observation of 12 events compared to an expectation of ~ 0.6 events. Chapter 8 will describe the deficiencies that led to this disagreement and Chapter 9 the new, a posteriori analysis that was performed. For a discussion on the question of blindness as it applies to this analysis, see Appendix D.

Figure 7.1 shows a flowchart of the analysis. The input datasets represent simulated signal and background, as well as the 10% burn sample. For completeness, Table 7.1 contains all the passing rate information of each cut through the penultimate level. As a reminder, the background simulation uses the `AHA` ice model and the neutrino simulation only includes the conventional atmospheric flux, neglecting the prompt component.
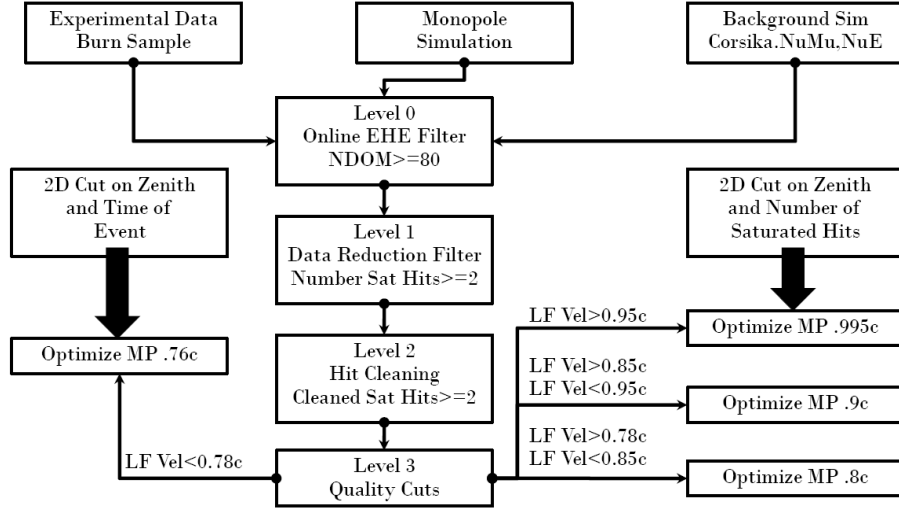
Figure 7.1: Design of the original monopole selection.

Table 7.1: Rates of background and signal datasets (events/year) for each cut level

Dataset	Level 0	Level 1	Level 2	Level 3
Burn Sample	3.25×10^7	6.78×10^5	6.78×10^5	1.61×10^5
Cors Proton	8.54×10^6	2.30×10^5	2.30×10^5	4.17×10^4
Cors Iron	6.37×10^6	2.83×10^5	2.83×10^5	1.03×10^5
Atm Conv ν_μ	$-$	18.8	18.8	0.815
Atm Conv ν_e	$-$	0.502	0.502	8.25×10^{-5}
Bkgrd Total	1.49×10^7	5.12×10^5	5.12×10^5	1.45×10^5
$\gamma = 10$	104	92.3	92.3	72.5
$\beta = 0.9$	98.6	87.5	87.5	69.6
$\beta = 0.8$	83.8	72.6	72.6	56.0
$\beta = 0.76$	33.5	6.01	6.00	3.28
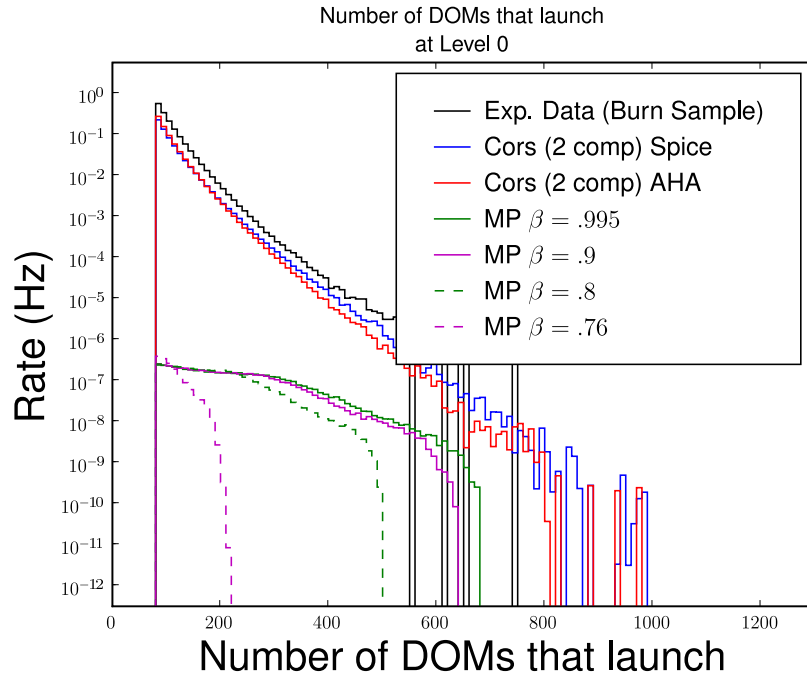
Figure 7.2: Number of DOM Launches recorded per event at the online filter level.

7.1 Level 0

The first stage of event selection begins with the online filter as described in Section 4.5. This filter keeps all events with the number of DOM launches (NDOM) greater than or equal to 80 and is designed to retain bright events that might include muon secondaries from extremely high energy neutrinos. Figure 7.2 shows the distribution of NDOM at this level.

7.2 Level 1

Once the data has been sent north from the pole, the next stage of event selection involves reducing this to a manageable size while still retaining a large
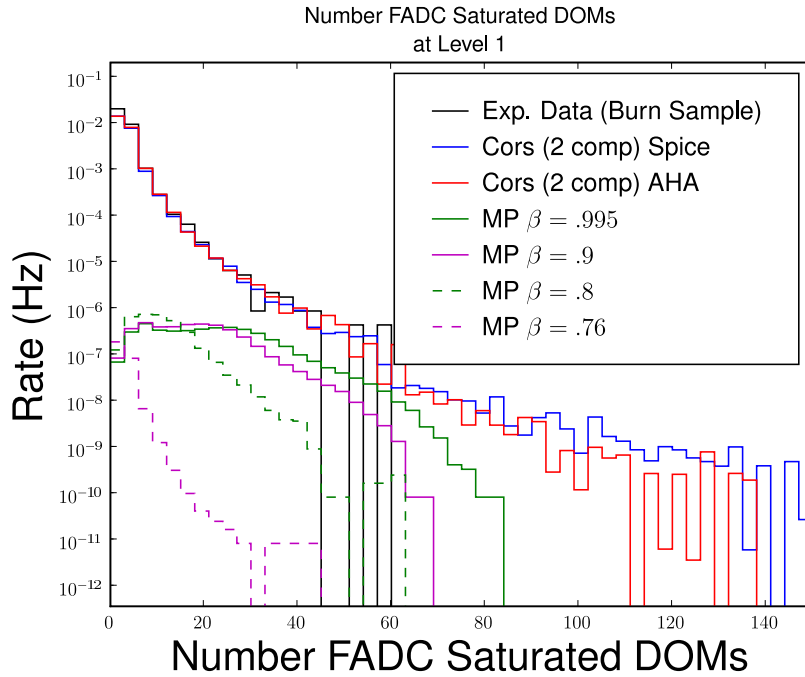
Figure 7.3: Number of DOM Launches with a saturated FADC channel recorded per event at Level 1.

fraction of the signal. This goal is met by requiring all events to have at least 2 hits that were saturated in the FADC channel (NSAT). This selection has the added function of ensuring the linefit reconstruction will be valid, since at least 2 hits are required. This eliminates $\sim 98\%$ of the background while keeping $\sim 20\%$ of the $\beta = 0.76$ signal and $\sim 80\%$ of the faster monopoles.

Figure 7.3 shows the distribution of NSAT at this level

7.3 Level 2

The goal of this level is to remove problematic hits within an event. After initially reconstructing the events, it was discovered that for some, the hit time

definition led to very erroneous results. Two examples are (1) a DOM records a noise hit and then sometime later the actual saturation event passes or (2) a coincident muon launches a DOM well before the other muon arrives to saturate it. This is analogous to the case discussed in Section 6.1.2 except here, the secondary event happens within the launch time window of $6.4\,\mu$s. The use of the launch start time for the time definition in these cases leads to large errors in the reconstruction since the time is so much earlier than it should be.

This is taken care of by scanning the data and removing all saturated hits in which the saturation occurred after the 20th bin of the FADC readout (~ 500 ns after launch). Figure 7.4 shows the distribution of time when the FADC waveform reaches a count of 1022 for all hits. The red line represents the cut applied. All hits beyond this line were removed from the event and the reconstruction was redone with the remaining hits. This represents a very loose cut in which $\sim 0.04\%$ to $\sim 0.07\%$ of hits were removed. Once removed, the level 1 cut of at least 2 saturated hits is reapplied. This results in less than $\sim 0.001\%$ of events being filtered.

7.4 Level 3

The motivation at this level is to remove all events which are poorly reconstructed. These events fall generally into one of two classes: (1) Events in which there is a bright cascade along the track that saturates a few DOMs all within the same vicinity and (2) Events which are coincident where each one saturates a DOM. The first class is problematic because the linefit reconstruction has a very short lever
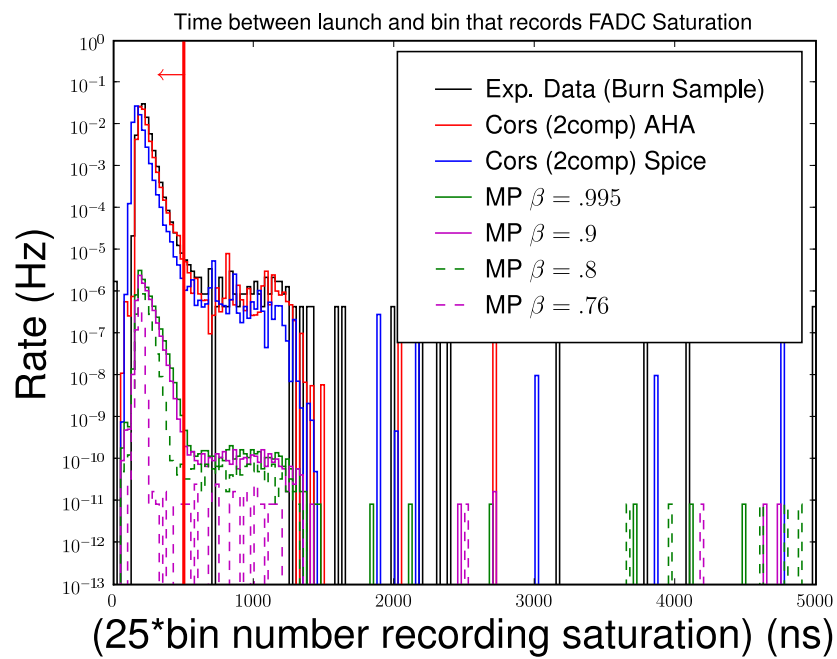
Figure 7.4: Time in which the FADC waveform saturation occurs for each hit. Above the red line are hits that are removed at Level 2.
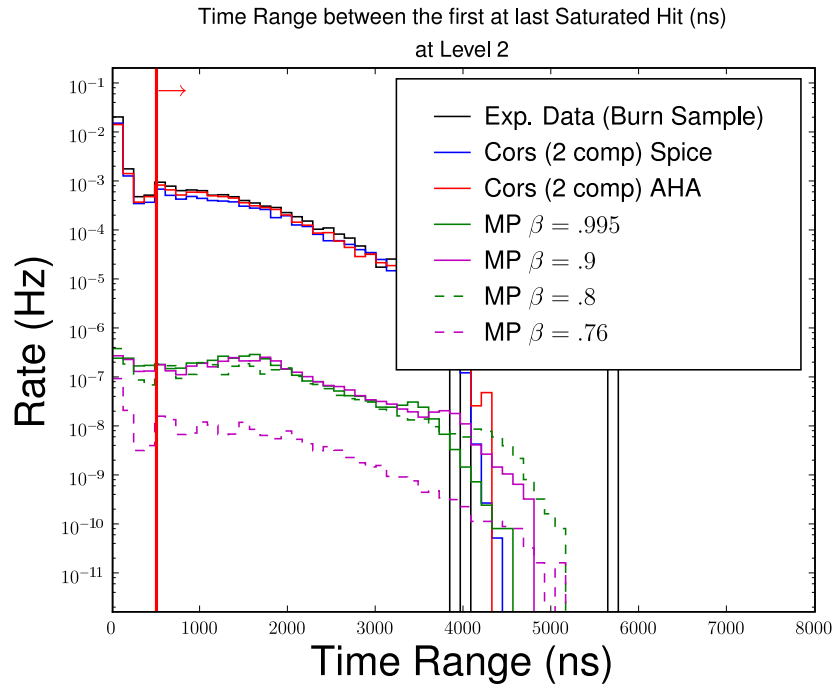
Figure 7.5: Distribution of total event time among saturated hits.

arm to work with. The second causes issues especially if the first muon to saturate a DOM passes through the lower part of the detector. In this case, the reconstruction will tend to produce an upward direction.

7.4.1 Bright Cascades

A common characteristic of events with a short lever arm caused by bright secondary cascades is that the hits occur over a relatively short amount of time. The total time of the event from the first to last saturated hit is used to distinguish them. Figure 7.5 shows the distribution of this time range (TRANGE).

The structure at the low end of the distribution can be understood on the basis of geometry. Figure 7.6 shows the a two-dimensional histogram for the burn
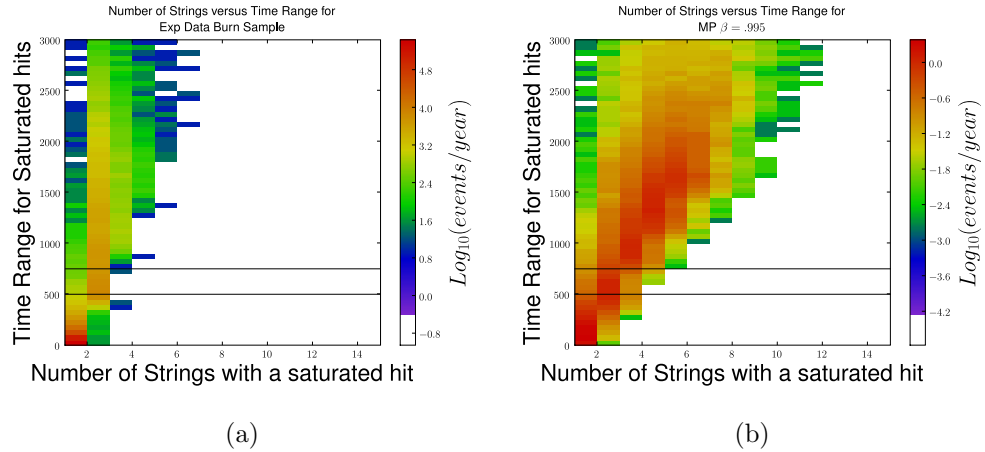
Figure 7.6: TRANGE of the saturated hits per event versus the number of strings with a saturated hit for (a) Burn sample data and (b) $\gamma = 10$ monopoles. The solid black lines correspond to TRANGE of 500 and 750 ns.

sample data and $\gamma = 10$ signal as a function of TRANGE and the number of strings that record a saturated hit (NSTRING). There is a clear correlation between the first peak, up to ~ 400 ns, and single string events. After ~ 500 ns, contributions from two string events begin to push the rate back up. Three string events begin to become important after ~ 750 ns. The number of strings themselves are not considered as a cut since, especially with $\beta = 0.76$ monopoles, some of the best quality signal events are those that are straight up going and light up a single string.

Figure 7.7 shows the passing rates of both signal and mis-reconstructed background as a function of a cut on TRANGE. Mis-reconstructed is defined as $\cos \theta < 1.5$. The burn sample data levels off due to coincident muon bundles that are not simulated. These events are considered in the next section. Therefore, the decision

110
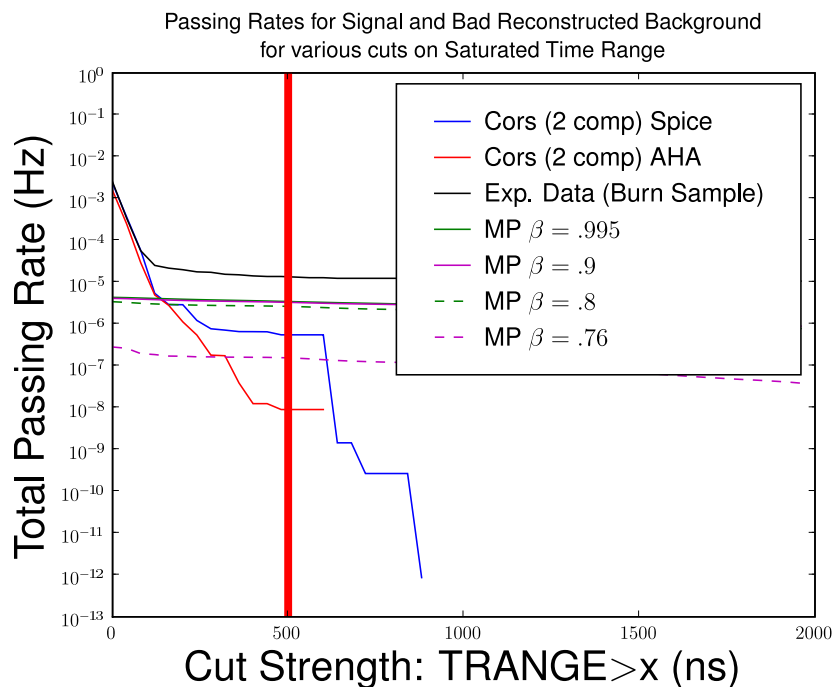
Figure 7.7: Passing Rates of an increasingly strong cut on TRANGE. For background sources, only events with the reconstructed $\cos\theta < 1.5$ are included to represent mis-reconstructed events.

of where to place the cut is motivated by the `AHA` simulated background only. See Section 9.1.3 for how this cut is changed based on the `SPICE` model.

The cut is placed at 500 ns. This results in reducing background by $\sim 75\%$ while preserving $\sim 55\%$ of the $\beta = 0.76$ signal dataset and $\sim 80\%$ of the other signal datasets. The eliminated signal events are largely events that saturate a single string in a short time frame. Unlike the ideal $\beta = 0.76$ signal events that spend a long time in the detector, these events typically pass outside the detector and are an acceptable loss since they would be hard to classify regardless.
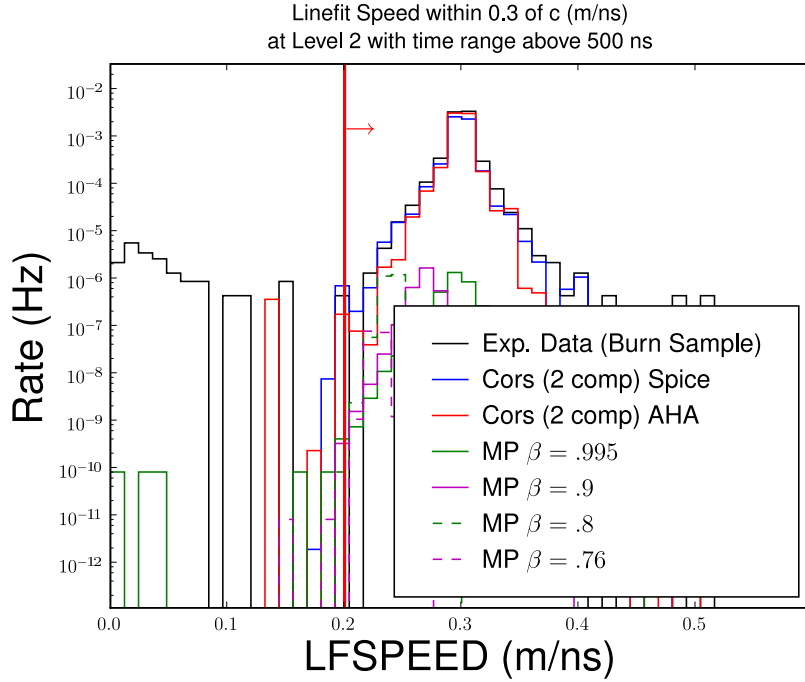
Figure 7.8: Distribution of the reconstructed linefit speed on events passing the TRANGE>500 ns cut. The red line corresponds to LFSPEED cut of 0.2 m/ns.

7.4.2 Coincident Events

As mentioned in Section 5.1.1, no simulated datasets of coincident events are used in the analysis. In order to decide on quality cuts, the burn sample is used as a guide. The first cut considered is one on the linefit speed (LFSPEED). A consequence of having two muons produce hits is that the hits will be much further apart in time for the given distance, i.e. they will not match the expectation of a single track traveling at the speed of light. Thus the speed is reconstructed to be much slower.

Figure 7.8 shows the LFSPEED distribution after the 500ns cut described above has been applied. The red line at 0.2 m/ns represents the chosen cut.
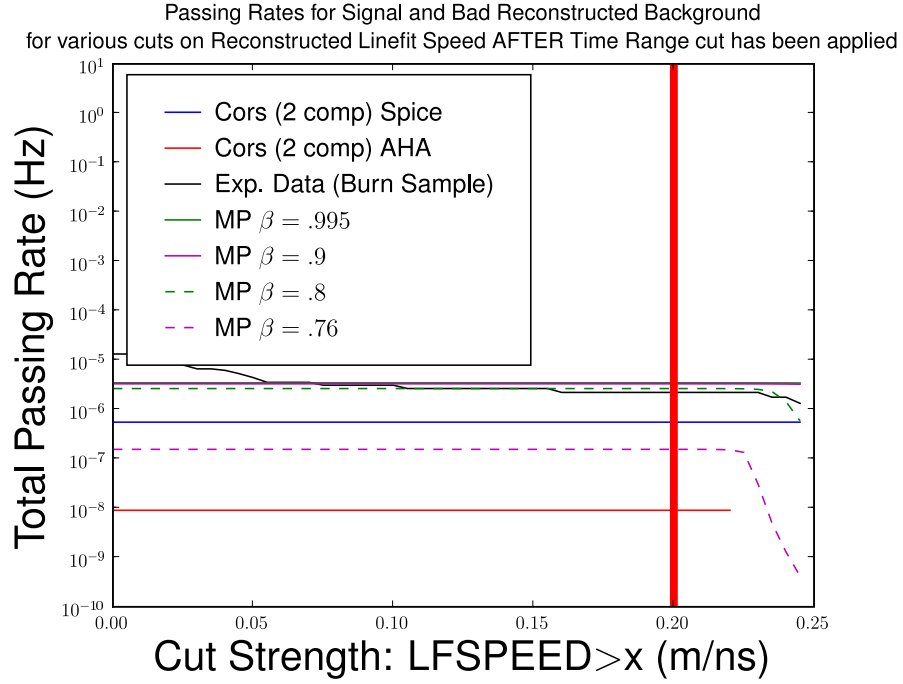
Figure 7.9: Passing Rates of an increasingly strong cut on LFSPEED. For background sources, only events with the reconstructed $\cos\theta < 1.5$ are included to represent mis-reconstructed events. The rates already reflect the TRANGE> 500 ns cut from the previous section.

This is motivated by Figure 7.9, where again the passing rates for signal and mis-reconstructed background are considered as a function of cut.

This cut is very loose, removing $< 0.2\%$ of experimental data and $< 0.02\%$ of the signal.

Once considering only events in which the reconstructed speed is above 0.2 m/ns, the 10% burn sample data had three up-going events left, as shown in Figure 7.10. One common factor of all three is that they occurred close enough in time that the linefit reconstruction using all DOM launches tended to follow the downward path of each muon while the linefit reconstruction using only saturated hits simply connected the few saturated hits and was up-going. Utilizing this difference, the final
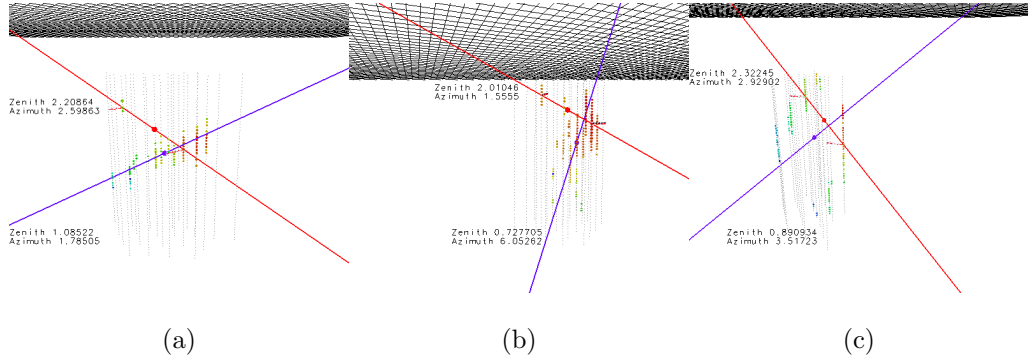
Figure 7.10: Coincident events that survive both the TRANGE and LFSPEED cuts. The red track represents the linefit reconstruction using just the saturated hits, the blue track using all the hits. In all cases, the red is up-going and the blue is down-going.

cut at this level eliminates events with a large difference in the zenith reconstruction from linefit using all DOM launches versus saturated hits. Figure 7.11 shows this distribution. The final cut chosen is to require the cosine difference to be within 0.6 of 0, based on Figure 7.12. This easily removes the three coincident events shown in 7.10. Note that the remaining two data events that are classified as misreconstructed in 7.12 are horizontal bundles, not coincident events.

As the figures show, this easily eliminates the remaining three up-going coincident events from the data.

Similar to the LFSPEED cut, this is very loose and removes $< 0.2\%$ of the background and $\sim 1\%$ of signal.
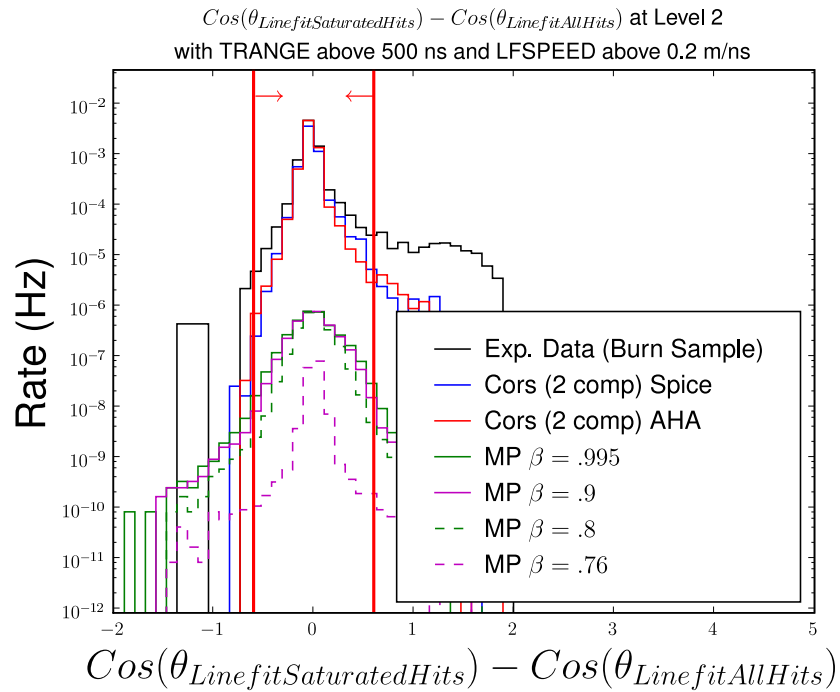
Figure 7.11: Distribution of $\cos\theta_{\text{SatHits}} - \cos\theta_{\text{AllHits}}$ on events passing the TRANGE>500 ns and LFSPEED> 0.2 m/ns cuts.

Passing Rates for Signal and Bad Reconstructed Background
for various cuts on Reconstructed Zenith Differences AFTER time range and speed cuts
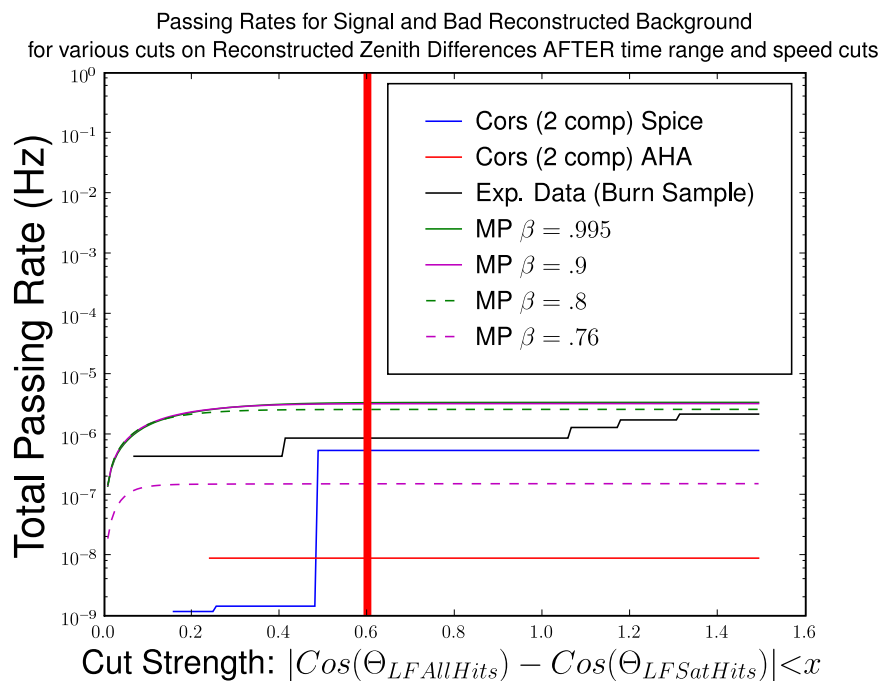
Figure 7.12: Passing Rates of an increasingly strong cut on the difference in $\cos\theta$ for the two reconstructions. For background sources, only events with the reconstructed $\cos\theta < 1.5$ are included to represent misreconstructed events. The rates already reflect the TRANGE>500 ns and speed above 0.2 m/ns cuts from the previous section.
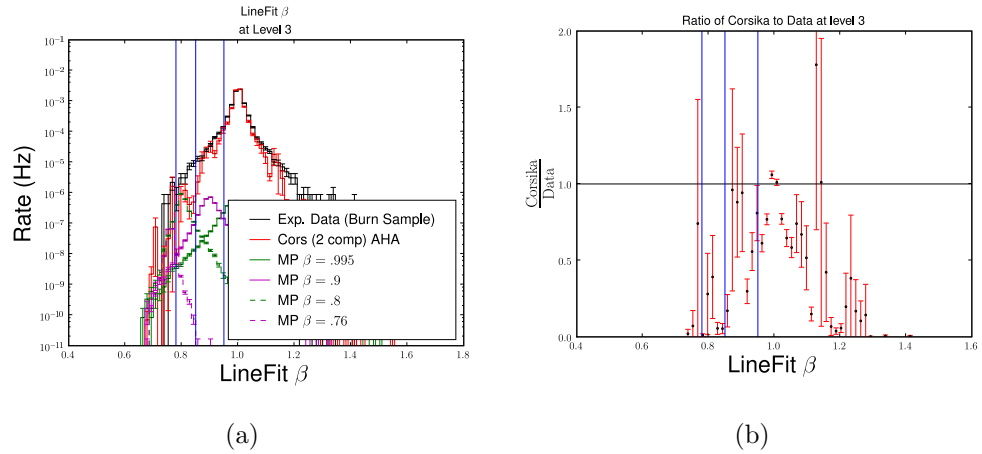
Figure 7.13: (a) Distribution of linefit speed at level 3 with vertical lines indicating where the speed bins occur. (b) The ratio of CORSIKA to Burn Sample data

7.5   Level 3 Disagreement

The strategy for the final level of the analysis is to divide the datasets into four speed bins around the four speeds of monopoles that were simulated. The goal is to utilize the fact that all background is traveling at the speed of light, so searches for the slower monopoles will benefit by focusing on events with a slower reconstructed speed. The four speed bins are: $\beta \leq 0.78$, $0.78 < \beta \leq 0.85$, $0.85 < \beta \leq 0.95$, and $\beta > 0.95$.

Figure 7.13 shows the speed distribution with vertical lines representing the bins. There is a rather strong disagreement between the burn sample data and the simulated background in the lower speed bins, especially for $0.78 < \beta \leq 0.85$. Table 7.2 lists the rates for all datasets after this speed split is performed.

When first considered, several potential issues were investigated, including the

117

Table 7.2: Background Passing Rates (in Hz) for Level 3 in each speed bin.

Dataset	$\beta > 0.95$	$0.85 < \beta \leq 0.95$	$0.78 < \beta \leq 0.85$	$\beta \leq 0.78$
Burn Sample	7.17×10^{-3}	3.40×10^{-4}	2.33×10^{-5}	3.52×10^{-6}
CORSIKA	6.80×10^{-3}	1.95×10^{-4}	2.99×10^{-6}	1.75×10^{-6}
Atm Conv ν_μ	3.26×10^{-8}	4.89×10^{-9}	2.97×10^{-10}	3.63×10^{-10}
Atm Conv ν_e	7.26×10^{-13}	5.99×10^{-13}	1.58×10^{-12}	9.56×10^{-13}
$\frac{\text{ExpData}}{\text{TotBkgrdSim}}$	1.09	1.74	7.79	2.01

ice model, the weighting of the two-component model, and the prompt atmospheric neutrino flux. However, the one that appeared to be most promising was the time resolution of the hits.

Studying the time resolution is motivated by the fact the overall rate agrees within 11%. The difference is largely in the shape of the speed distribution. This suggests that the timing might be different as opposed to overall number of hits. Datasets were generated with the hit time smeared by a Gaussian random number with σ between 5 and 25 ns. Figure 7.14 shows the linefit speed distribution of the various datasets.

To measure how well the smeared distributions match the data in shape, the histograms are normalized and the total sum of the square difference of each bin is found. The smallest value occurred for the 10 ns distribution. In a second test, several fit functions were applied to the data and CORSIKA, with the best being an absolute exponential function centered at the mean. The spread of the data fit was between that of the 10 and 15 ns datasets. The inclusion of a time smear improved the $0.78 < \beta \leq 0.85$ disagreement. Table 7.3 lists the values.

The affect of time smearing on the background event rate at the final level
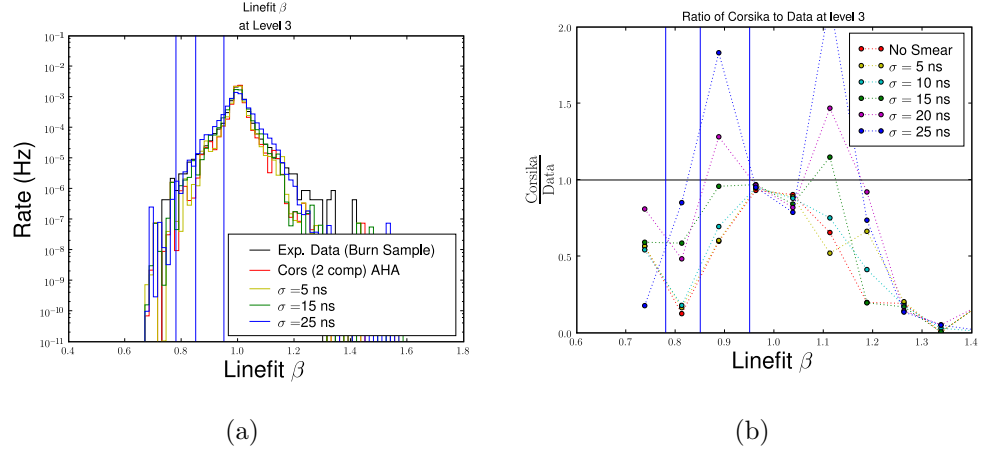
Figure 7.14: (a) Distribution of linefit speed at level 3 with time smeared datasets. (b) The ratio of the time smeared datasets to Burn Sample data

Table 7.3: Ratio of Data/MC for various smearing values generated

Time Smearing	Data/CORSIKA
5 ns	5.95
10 ns	5.56
15 ns	1.67
20 ns	2.03
25 ns	1.25

was checked for the 10, 15 and 25 ns datasets. All produced a slight decrease in the overall rate. The conclusion was that the difference was largely at a level that is removed by the final cut. Combined with the fact that only 53 burn sample and 67 `CORSIKA` events were in this bin, the decision was made to continue with the analysis and study these deviations as part of the systematic uncertainty estimate when the full data sample statistics were available. As a final precaution, more conservative choices were made for the final cut applied to slower speeds than suggested by the optimization.

In a very unlucky twist of fate, the 20 ns dataset was not checked at the final level, as it predicts almost 8 events in the full year sample. See Section 8.2 for more details.

7.6   Level 4

This level represents the final cut. The cuts developed are all based on a two dimensional cut in the $\cos\theta$ versus either NSAT($\beta = 0.995, 0.9, 0.8$) or TRANGE ($\beta = 0.76$) plane. Figure 7.15 shows the NSAT and $\cos\theta$ distributions at level 3. The up-going case is essentially background free, so a cut on either TRANGE or NSAT is chosen with no zenith dependence. For the down-going cases, a zenith dependence on the background arises where the more vertical the event, the larger NSAT and TRANGE become since it spends more time and deposits more light into the detector. Thus, a linear cut that increases with $\cos\theta$ is considered. The two pieces are joined at $\cos\theta = 0$. This type of cut can be defined by two numbers, a

120
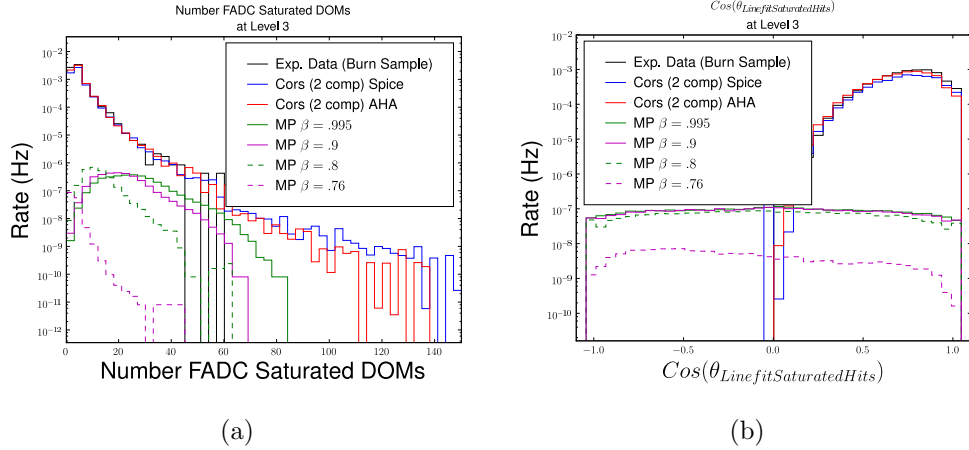
Figure 7.15: Distribution of (a) NSAT and (b) $\cos\theta$ at level 3. These variables are used for the final cuts for all but the slowest monopole.

'baseline' that represents the NSAT or TRANGE value for the up-going region, and a 'slope' that represents how steeply the line increases in the down-going region. The final cut will then be:

$$NSAT(TRANGE) > \begin{cases} Baseline & if \cos(\theta) <= 0 \\ Baseline + Slope * \cos(\theta) & if \cos(\theta) > 0 \end{cases} \qquad (7.1)$$

To determine the values of the 'slope' and 'baseline' to use in each speed bin, a search is performed scanning the two-dimensional space and choosing those which minimize the MRF (see Section 6.3). A livetime of 2.134074125×10^7 s, representing the full year's worth of data, is used in calculating the total number of expected background and signal events. Table 7.4 displays the final passing rates for each speed bin.

121

Table 7.4: Rates of background and signal datasets (events/year) for each speed bin of the final cut.

Dataset	$\beta > 0.95$	$0.85 < \beta \leq 0.95$	$0.78 < \beta \leq 0.85$	$\beta \leq 0.78$
Burn Sample	0.0	0.0	0.0	0.0
Cors Proton	6.95×10^{-4}	1.09×10^{-3}	7.26×10^{-3}	0.0
Cors Iron	6.64×10^{-2}	0.155	0.314	0.0
NuMu Conv.	1.64×10^{-2}	3.51×10^{-2}	3.03×10^{-3}	4.46×10^{-3}
NuE Conv.	9.25×10^{-6}	1.18×10^{-5}	3.37×10^{-5}	1.22×10^{-7}
Bkgrd Total	8.35×10^{-2}	0.191	0.324	4.46×10^{-3}
$\gamma = 10$	34.6	6.57	0.562	1.96×10^{-2}
$\beta = 0.9$	3.03	36.4	3.28	4.27×10^{-2}
$\beta = 0.8$	0.0	1.54	35.5	3.12
$\beta = 0.76$	0.0	0.0	1.78×10^{-3}	2.36

7.6.1 $\beta > 0.95$

This represents the tightest cut of the four speeds since this speed bin includes the speed of light and hence has much more background. Figure 7.16 shows the calculated MRF value for various baseline and slope pairs examined. The red indicates values with a high background and hence calculating the MRF became resource intensive. The minimum occurs at a baseline of 8 and slope of 115, highlighted by the white circle.

Figure 7.17 shows the two dimensional distribution of the background datasets, experimental data, and the $\beta = 0.995$ monopoles in the NSAT versus $\cos \theta$ plane. The black line represents the final cut chosen.

7.6.2 $0.85 < \beta \leq 0.95$

Figure 7.18 shows the calculated MRF values for this speed bin. The optimized baseline was found to be at 2 with a slope of 75. However, this was performed on
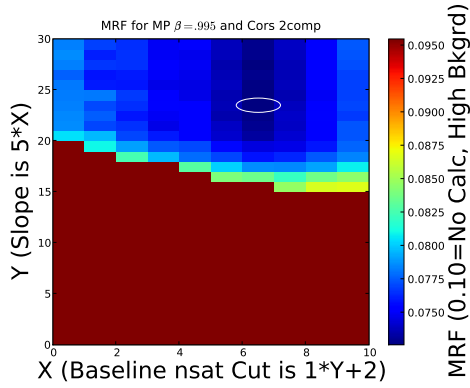
Figure 7.16: Values of the MRF for various choices of baseline and slope cuts in the $\beta > 0.95$ speed bin.

background simulation without coincident events. Since raising the baseline will dramatically reduce the chance of seeing a coincident event (see Appendix B), a conservative choice to increase this baseline to 4 was made. This had the effect of changing the MRF from 0.07022 to 0.0718, or a $\sim 2.5\%$ increase.

Figures 7.19 show the two dimensional distribution of the background datasets, experimental data, and the $\beta = 0.9$ monopoles in the NSAT versus $\cos\theta$ plane. The solid black line represents the optimized cut while the dashed line is the more conservative cut chosen.

7.6.3 $0.78 < \beta \leq 0.85$

Figure 7.20 shows the calculated MRF values for this speed bin. The optimized cut had a baseline of 4 and a slope of 10. However, as Section 7.5 demonstrates, this region has the largest disagreement between data and Monte Carlo. This motivates using a more conservative final cut. The value of the cut is chosen by considering
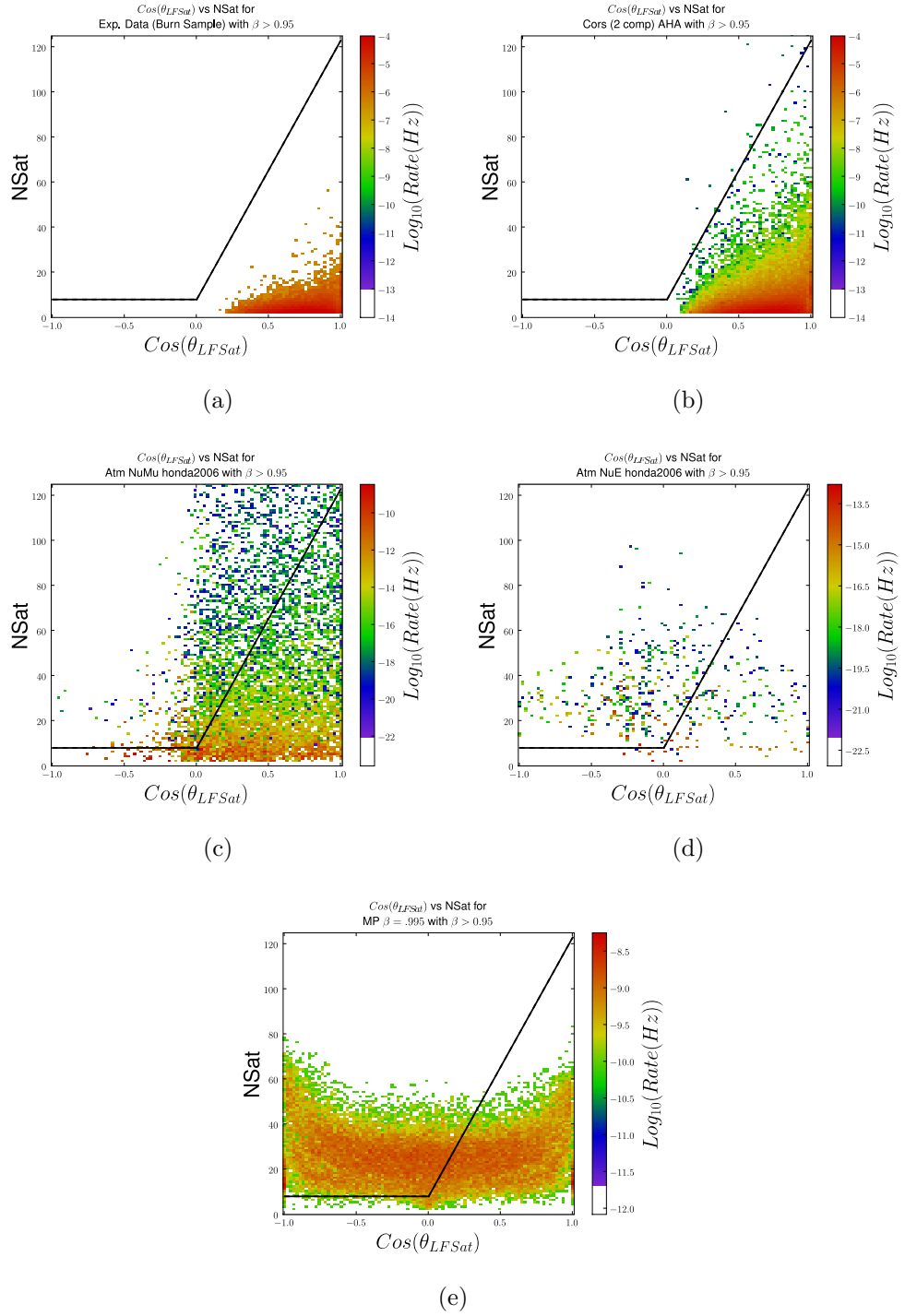
Figure 7.17: NSAT vs $\cos\theta$ in the $\beta > 0.95$ speed bin for (a) Burn Sample, (b) `CORSIKA AHA`, (c) Atmospheric Muon Neutrinos, (d) Atmospheric Electron Neutrinos, and (e) $\gamma = 10$ Monopoles. The solid line represents the cut. For `CORSIKA` and Data, the scale is the same, while for neutrinos it is five to ten orders of magnitude less.
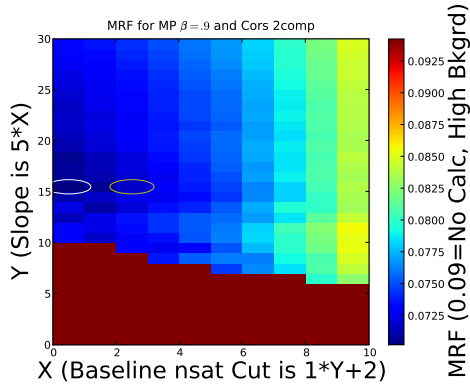
Figure 7.18: Values of the MRF for various choices of baseline and slope cuts in the $0.85 < \beta \leq 0.95$ speed bin. White represents the minimized value, yellow for the cut finally chosen.

the agreement as a function of an NSAT cut alone, i.e., simply raising the baseline. Figure 7.21 motivates the choice of raising the baseline to 6. Already the effect of running out of statistics is evident, and also precludes attempting a similar procedure with increasing the slope cut. As stated before, while the disagreement is still there, it was believed that the effect at the final level would be minimal based on the time smearing studies and since the background expectation is so low on an absolute scale. Further studies were planned after unblinding when more statistics became available.

Figures 7.22 show the two dimensional distribution of the background datasets, experimental data, and the $\beta = 0.8$ monopoles in the NSAT versus $\cos \theta$ plane. The black solid line is the optimized cut while the dashed line is the more conservative cut chosen.
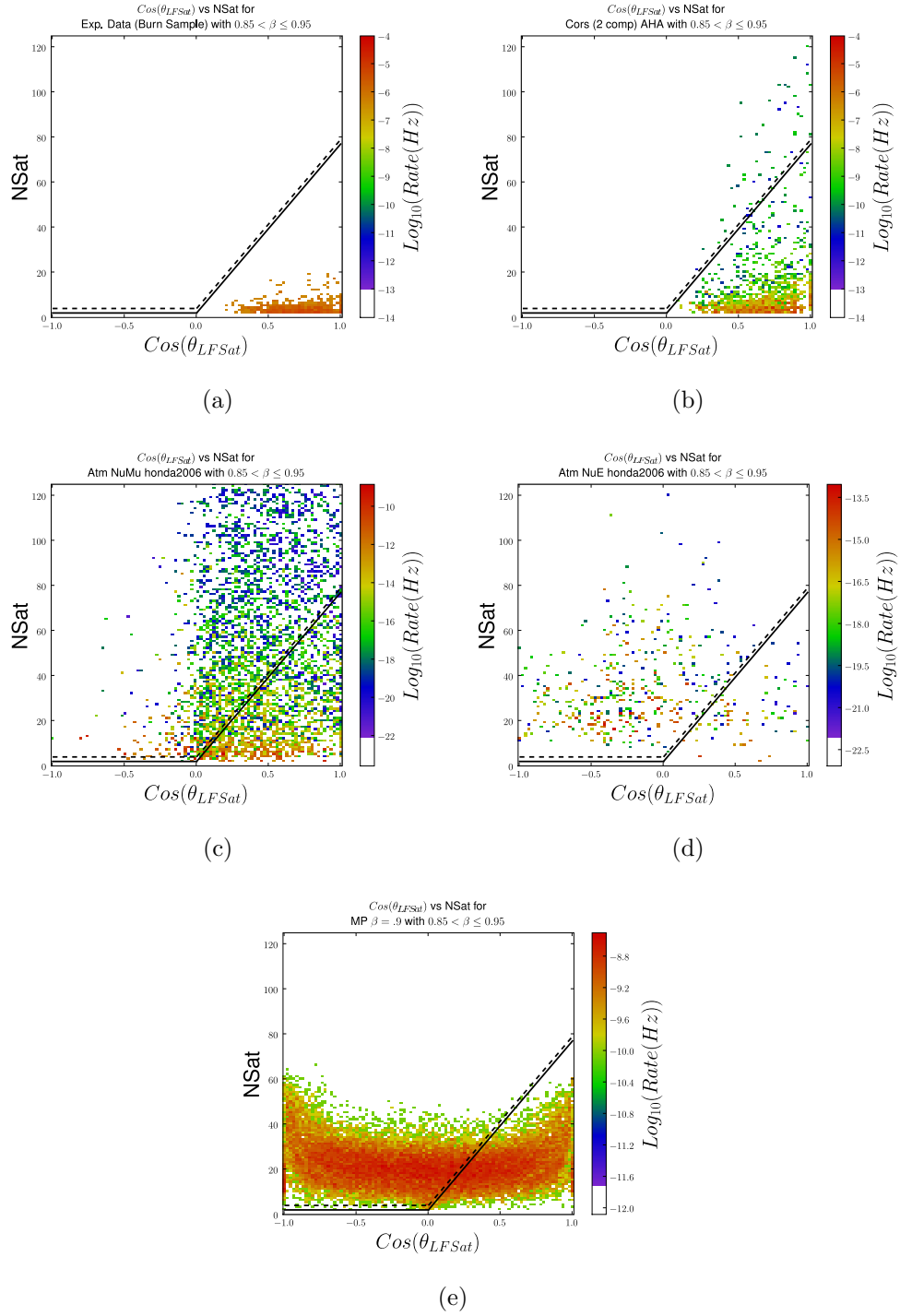
Figure 7.19: NSAT vs $\cos\theta$ in the $0.85 < \beta \leq 0.95$ speed bin for (a) Burn Sample, (b) `CORSIKA AHA`, (c) Atmospheric Muon Neutrinos, (d) Atmospheric Electron Neutrinos, and (e) $\beta = 0.9$ Monopoles. The solid line represents the optimized cut and the dashed the final cut. For `CORSIKA` and Data, the scale is the same, while for neutrinos it is five to ten orders of magnitude less.
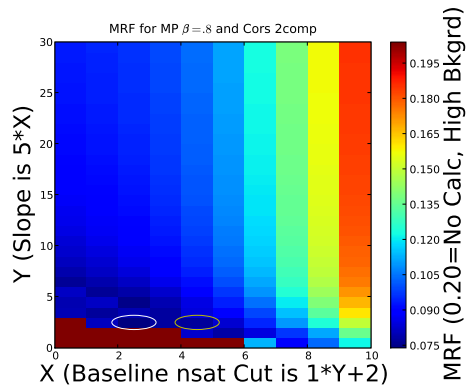
Figure 7.20: Values of the MRF for various choices of baseline and slope cuts in the $0.78 < \beta \leq 0.85$ speed bin. White represents the minimized value, yellow for the cut finally chosen.
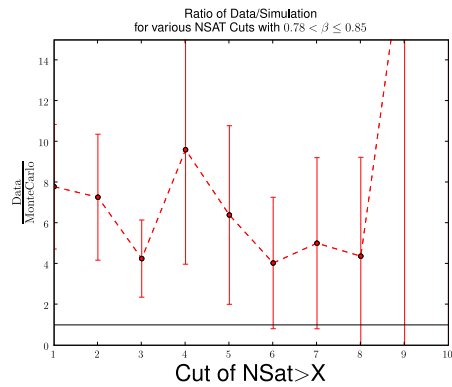
Figure 7.21: Ratio of Data/MC for $0.78 < \beta \leq 0.85$ as a function of increasing cut strength on NSAT.
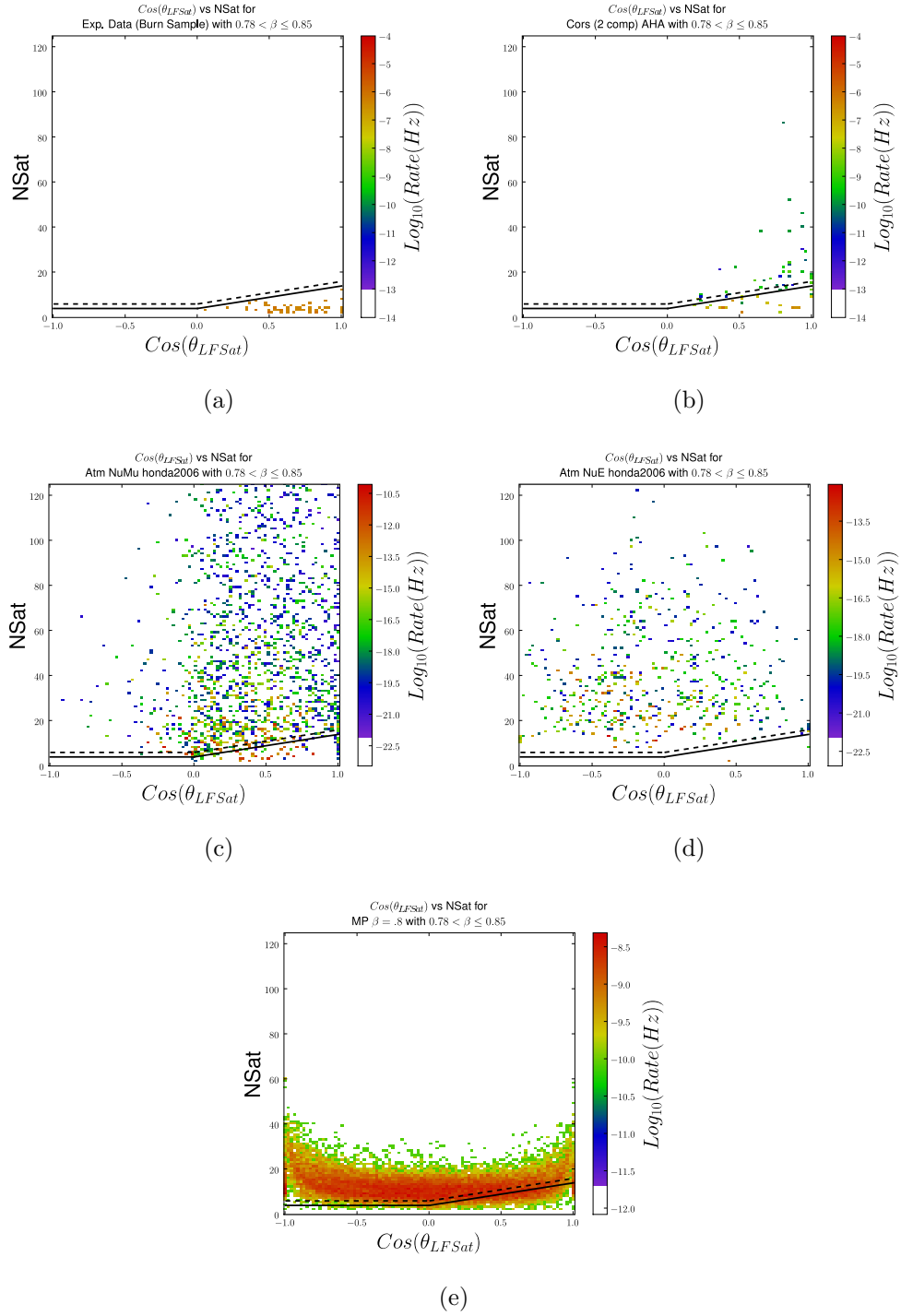
Figure 7.22: NSAT vs $\cos\theta$ in the $0.78 < \beta \leq 0.85$ speed bin for (a) Burn Sample, (b) `CORSIKA AHA`, (c) Atmospheric Muon Neutrinos, (d) Atmospheric Electron Neutrinos, and (e) $\beta = 0.8$ Monopoles. The solid line represents the optimized cut and the dashed the final cut. For `CORSIKA` and Data, the scale is the same, while for neutrinos it is five to ten orders of magnitude less.
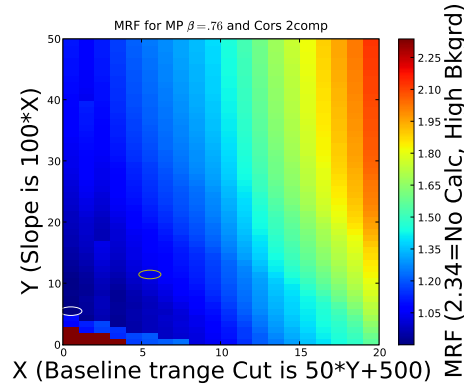
Figure 7.23: Values of the MRF for various choices of baseline and slope cuts in the $\beta \leq 0.78$ speed bin. White represents the minimized value, yellow for the cut finally chosen.

7.6.4 $\beta \leq 0.78$

For the $\beta = 0.76$ monopoles, increasing the baseline NSAT cut from the original level 1 NSAT$\geq$1 to NSAT$\geq$2 would reduce the signal by almost 60%. However, these monopoles also represent the slowest moving signal and so TRANGE was taken as the second cut parameter in addition to $\cos\theta$.

Figure 7.23 shows the calculated MRF values. The minimized value was for a baseline of 500 and a slope of 500. This optimized cut does not eliminate experimental data well. Figure 7.24 shows the final distributions together with the cut. The issue here is largely statistical. There are only 8 data and 17 `CORSIKA` events in the entire bin. However, two of the data events are very far into the region that would be kept for the minimized cut.

Constructing a more conservative cut started by raising the baseline up to 750ns following the band-like structure of the signal events. These bands are based on the distance between the hits that saturate a DOM. Since velocity is fixed at
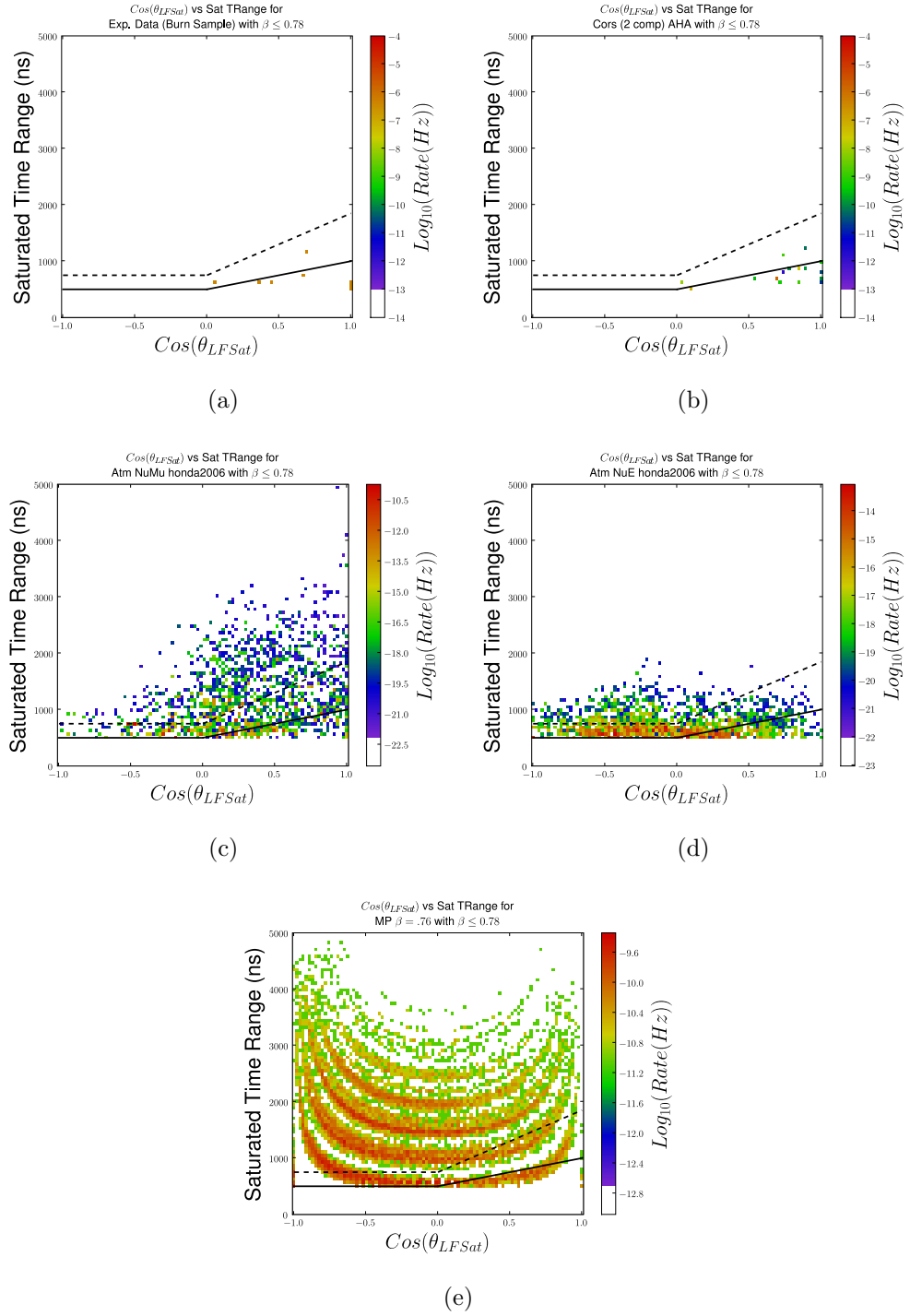
Figure 7.24: TRANGE vs $\cos\theta$ in the $\beta \leq 0.78$ speed bin for (a) Burn Sample, (b) CORSIKA AHA, (c) Atmospheric Muon Neutrinos, (d) Atmospheric Electron Neutrinos, and (e) $\beta = 0.78$ Monopoles. The solid line represents the optimized cut and the dashed the final cut. For CORSIKA and Data, the scale is the same, while for neutrinos it is five to ten orders of magnitude less.

0.76c, times of ~ 550ns represent distances of ~ 125m, which is the string spacing of the detector. This allows raising the baseline without significantly removing signal events that are much more likely to be well reconstructed. Note that the best signal events that saturate only one string are still kept, since they are at the vertical edges of the $\cos \theta$ distribution.

For the slope, given this baseline the most conservative cut within 15% of the optimal was chosen. Note that even increasing the optimized cut by 15% still leaves the final sensitivity more than a factor of 10 below existing limits. While changing the cut leads to a large change in the overall MRF, the result is interesting despite the lack of statistics.

7.6.5   Sensitivity

A measure of the effectiveness of the analysis is found by calculating the sensitivity, defined as $\Phi_{90\%} = \frac{\mu_{\text{Avg90}}(n_b)}{N_{\text{sig}}}\Phi$. This is equivalent to the final flux limit with the upper limit replaced by the average upper limit (see Section 6.3).

Since the analysis involves four signals and four cuts, the decision was made treat each experiment separately as looking for a single signal. Hence, for the $\gamma = 10$ signal, n_b and N_{sig} are found only considering those with $\beta_{\text{Reco}} > 0.95$. Table 7.5 lists the expected background, average upper limit, and sensitivity for each speed bin as a result of the final cut. Figure 7.25 displays this result relative to other experimental and theoretical limits (see Section 2.8.4).

Table 7.5: Background Rate, Average upper limit and sensitivity (in $cm^{-2}sr^{-1}s^{-1}$) for each of the four signals.

	$\gamma = 10$	$\beta = 0.9$	$\beta = 0.8$	$\beta = 0.76$
Bkgrd (events/year)	0.084	0.191	0.324	4.5×10^{-3}
μ_{Avg}	2.51	2.62	2.74	2.44
$\Phi_{\text{Sensitivity}}$	3.63×10^{-18}	3.59×10^{-18}	3.86×10^{-18}	5.18×10^{-17}
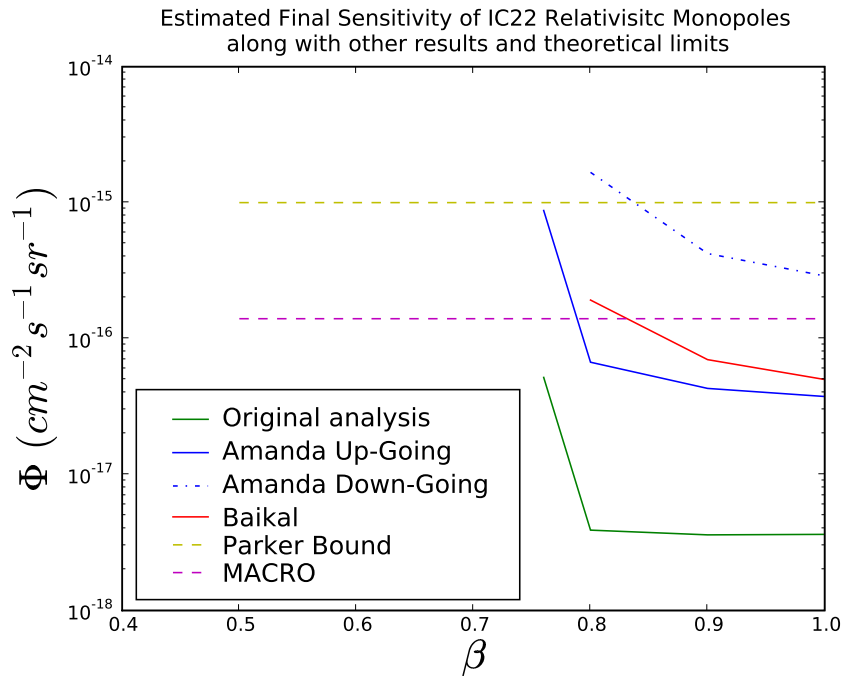
Figure 7.25: Original Sensitivities as a function of β.

Chapter 8

Original Results

After unblinding the data, there were 12 events found in the full year sample.

Three occurred in the slowest speed bin and upon visual inspection were all obvious

coincident events, a background that was not simulated in the final cut optimization.

Of the remaining nine, all were down-going and eight were in the $0.78 < \beta \leq$

0.85 speed region that represented the worst data/Monte-Carlo disagreement prior

to unblinding. It is not believed that any of the events are magnetic monopoles.

Appendix C contains the images of all 12 events and Figure 8.1 shows the two

dimensional cut plane for the final data. This section will describe the motivation

for ruling out the magnetic monopole hypothesis and what the deficiencies were in

the original analysis.

8.1   Monopole rejection

A diligent effort ensued in order to test if these events are truly magnetic

monopoles. Additional parameters were studied that allow for further distinction

between monopoles and bright muon bundles.

One promising parameter measures the average distance from the track recon-

struction to the saturated hits. Figure 8.2 shows a plot of this parameter with the

reconstructed direction for events at Level 3. The 12 surviving data events are in
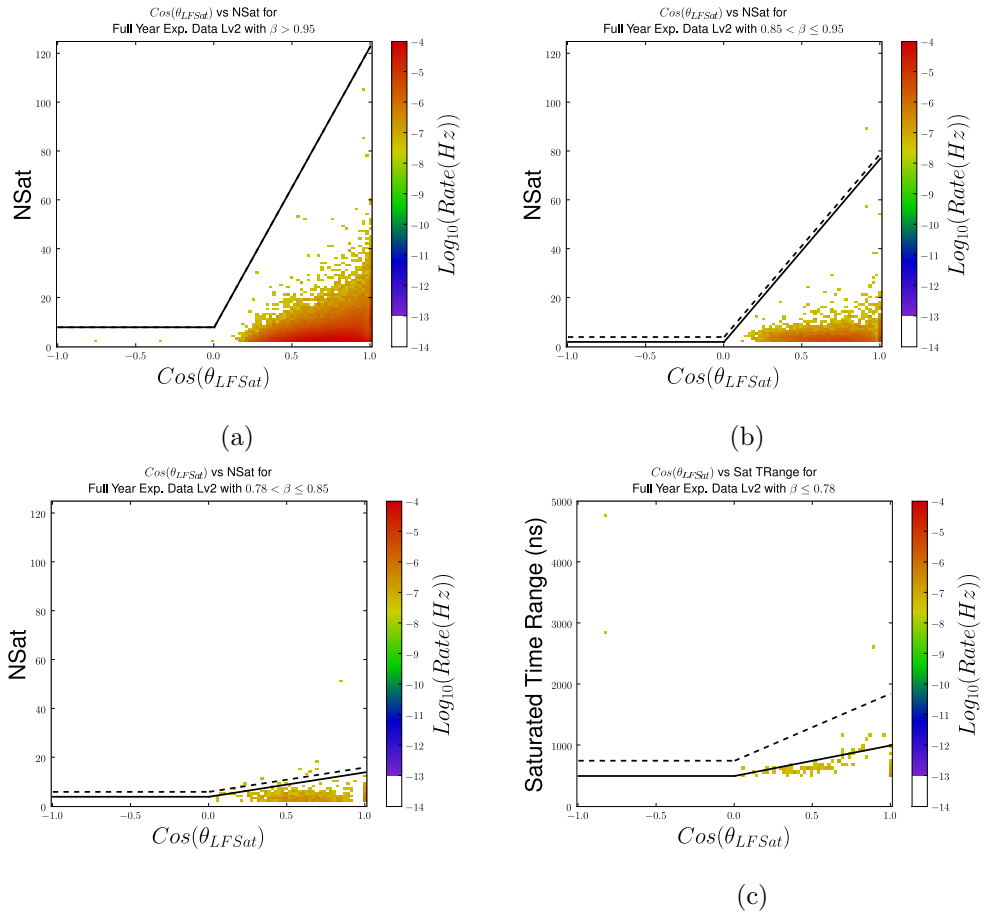
Figure 8.1: Distribution of all the data events in appropriate two-dimensional plane for each speed bin.

134
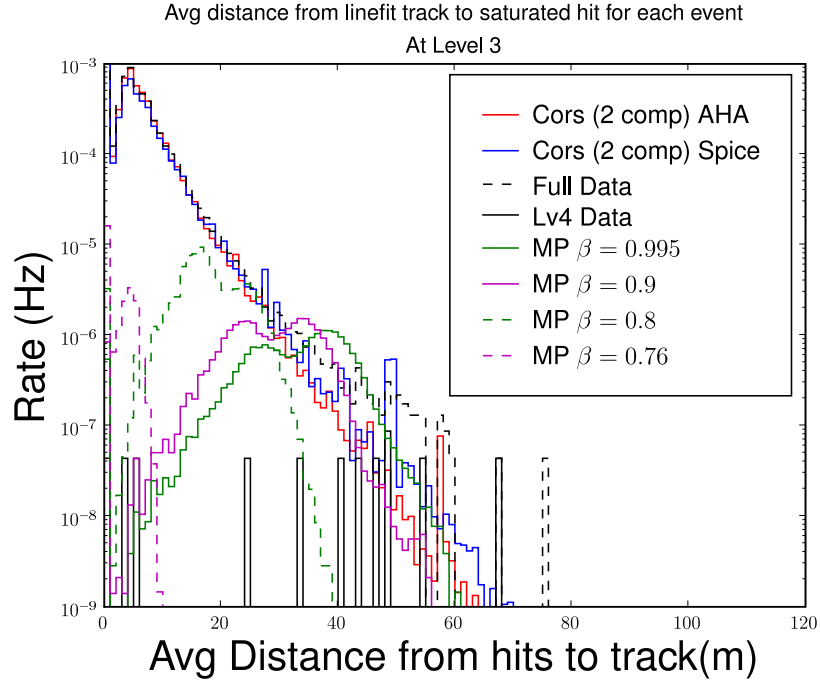
Figure 8.2: Distribution of the average distance from reconstructed track to saturated DOMs for each event. Monopoles are weighted to the down-going flux limit derived by AMANDA[44].

solid black. Note that in order to truly see if these events might be monopoles, all monopole event rates in this section are scaled assuming the much more conservative AMANDA down-going flux limit[44].

While the majority of the background muon bundles have a much lower value than signal, the very brightest (i.e., those passing the final cuts) demonstrate a larger spread than the slower monopole signal events. This is likely due to the horizontal spread in the muon bundle.

A second parameter is obtained by counting the number of bins in each FADC waveform above a certain threshold, then taking the average of this set for each event. As discussed in Section 6.1, the monopole signal is dominated by Cherenkov
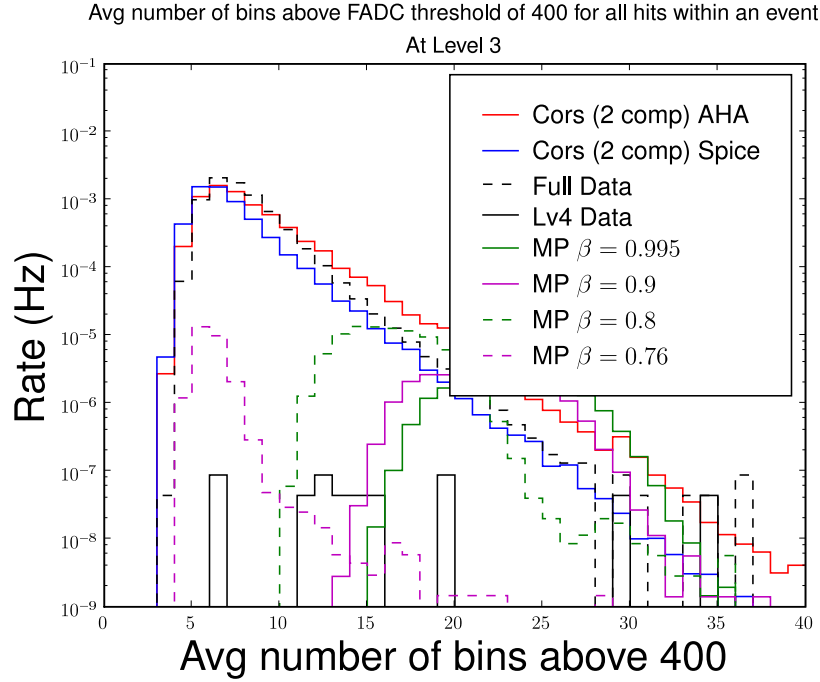
Figure 8.3: Distribution of the average number of bins of the FADC waveform above 400 counts for each event. Monopoles are weighted to the down-going flux limit derived by AMANDA[44].

light, leading to longer FADC waveforms and thus a higher value for the number of bins above a threshold (see Figure 6.3). Figure 8.3 shows the distribution for a threshold of 400 at Level 3.

Taken by themselves, each parameter suggests the data is not either slow monopoles (average saturated distance) or fast monopoles (average number of bins above 400). A first guess attempt at utilizing both pieces of information involves taking the ratio of the average distance to average number of bins. Since the average distance has better overall separating power, its importance is increased by raising it to a power, chosen by eye to be nine. This distribution is shown in Figure 8.4 both at level 3, where the final events could be either fast monopoles or background, and
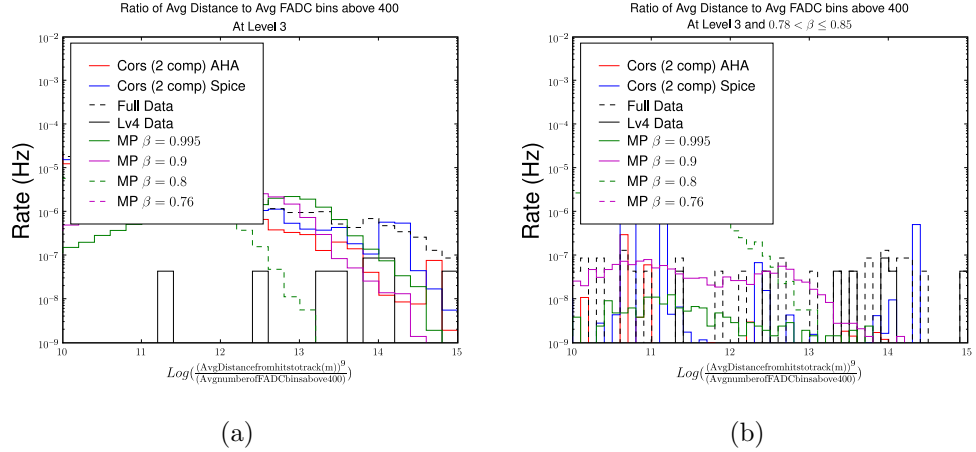
Figure 8.4: Distribution of $Log_{10}(\frac{(AverageDistancetoSaturatedHit)^9}{AverageNumberofbinsabove400})$. Monopoles are weighted to the down-going flux limit derived by AMANDA[44].

only considering $0.78 < \beta \leq 0.85$, where the difference between monopole signal and the final events is most evident.

Though not an exhaustive search, this simple ratio parameter allows for a fairly good separation of the surviving events from signal. Table 8.1 lists the values for each of the 12 surviving data events. Included are the estimated energies of the cosmic ray primary based on the total amount of light deposited in the detector, taken from the EHE working group[85].

This ratio would not be useful to eliminate the three coincident events, but they are obviously background regardless. Of the remaining nine, five have a value above 13.9 and two more are above 13.3. If the monopole signal is weighted according to the down-going flux from AMANDA, there would be less than 0.05 events per year above 13.85 within the $0.78 < \beta \leq 0.85$ speed bin. Moreover, there would be less than 0.1 events per year above 13.3 if an additional down-going constraint is

imposed. The two events that have values below 13.3 both appear to be caused by

a large cascade that produced a poor reconstruction, as distinguished by the fact

only two strings were saturated.

Table 8.1: Parameters for the 12 Data events that passed the Original Analysis Final Cut. Note that the Primary Energy is estimated by the EHE group and is only done for events with large enough light in the detector.

RunID	EventID	Speed Bin	$Log_{10}(E_{\mathrm{Prim}})$ Estimate	Average Sat Distance	Average Bins above 400	$Log_{10}(\frac{(\mathrm{AverageDistancetoSaturatedHit})^9}{\mathrm{AverageNumberofbinsabove400}})$
108869	2560659	$0.85 < \beta \leq 0.95$	9.29 ± 0.43	54.04	29.08	14.13
109908	9578727	$0.78 < \beta \leq 0.85$	8.84 ± 0.46	67.50	34.71	14.92
109498	13717945	$0.78 < \beta \leq 0.85$	-	43.53	15.93	13.54
109858	3273025	$0.78 < \beta \leq 0.85$	7.31 ± 0.53	33.52	19.4	12.44
109504	6223806	$0.78 < \beta \leq 0.85$	-	48.87	19.72	13.91
109507	3130762	$0.78 < \beta \leq 0.85$	-	48.94	12.91	14.10
109748	7628410	$0.78 < \beta \leq 0.85$	7.13 ± 0.54	46.58	12.23	13.92
109755	988134	$0.78 < \beta \leq 0.85$	7.69 ± 0.56	40.58	12.23	13.92
109987	8702286	$0.78 < \beta \leq 0.85$	7.21 ± 0.52	24.29	13.56	11.34
109325	12796685	$\beta \leq 0.78$	-	3.215	6.67	3.74
109456	3837803	$\beta \leq 0.78$	-	0	6.0	-
110522	5328671	$\beta \leq 0.78$	-	5.922	11.0	5.91

8.2 Analysis Deficiencies

While suggestive, the above studies do not conclusively rule out the monopole hypothesis since the original analysis parameters, especially LFSPEED, demonstrate the opposite, i.e. the data events that pass are more signal like than background. A complete description of the discrepancy requires discovering what the deficiencies were in the original analysis.

The answer came from systematic studies performed after the unblinding. Several variations on the CORSIKA datasets were generated to compare how the final result changes. Table 8.2 lists the passing rates at Level 3 and 4 for some of these datasets. It was noticed that the final Level 4 rate would largely be well below an event per year, but could jump wildly, for example to 8 events per year for the 20 ns time smearing dataset (see Section 7.5). This occurs when an event with a relatively low energy ($\sim 10^7$ GeV) ends up in the $0.78 < \beta \leq 0.85$ speed bin, which has the loosest cut.

For the time smearing, the event happens to be right on the edge of the $\beta = 0.85$ boundary. When the right smearing occurs, it is enough to push it into the $0.78 < \beta \leq 0.85$ region. For the SPICE, the higher statistics simply produced a low energy event that had the right characteristics.

A secondary factor involves the ice model. The SPICE model uses much cleaner values for deep ice properties than AHA. This causes the muon bundles to produce more hits that are spread out at the bottom of the detector, which in general slightly lowers the speed while increasing NSAT. This is especially true of the large muon

140

Table 8.2: Passing Rates for Background Datasets at Level 3 and 4. Shown are the overall rates and those of the $0.78 < \beta \leq 0.85$ speed bin. The time smeared datasets are defined in Section 7.5. Rates are given as events per blinded livetime (90% of full year).

	Level 3 Rate		Level 4 Rate	
Dataset	Total	$0.78 < \beta \leq 0.85$	Total	$0.78 < \beta \leq 0.85$
Data (Burn Sample)	1.55×10^5	481	0	0
All Data	1.56×10^5	532	10.81	7.21
Cors AHA	1.40×10^5	61.7	0.526	0.310
Cors Spice	1.16×10^5	466	22.9	12.1
Cors AHA 15 ns smear	1.40×10^5	288	0.511	0.285
Cors AHA 20 ns smear	1.40×10^5	237	8.20	7.98
Cors AHA 25 ns smear	1.40×10^5	384	0.501	0.271

bundles produced by high energy iron primaries, where the final expected rate goes from $\sim$ 0.3 to $\sim$ 0.5 events per year. These events occupy the energy region $> 10^{10}$ GeV, hence these rates are also uncertain. Taking the extreme case of no iron knee with the SPICE dataset (see Section 10.1), this rate quadruples to $\sim$ 2.

The final sample has one event that seems to match this energy range, while the others are all in the $10^7 - 10^8$ GeV range. This suggests that the dominant cause of the disagreement is the lack of good statistics in the lower energy regime.

To summarize, the analysis attempted a novel approach to using speed reconstruction in an effort to increase sensitivity for the slower signal. The decision to base each final cut on the optimized MRF of a given speed bin led to a situation where the cuts for each one varied rather dramatically. This is especially true when comparing the cuts between the $0.78 < \beta \leq 0.85$ bin and those for the $0.85 < \beta \leq 0.95$ bin. While the baselines were similar (6 vs. 4), the $0.85 < \beta \leq 0.95$ bin had a much steeper slope (10 vs 75). This represents a huge difference. For

example, were the $0.85 < \beta \le 0.95$ cuts applied to the $0.78 < \beta \le 0.85$ region, none of the eight events would have passed. In the end, the attempt at developing the analysis based on the low statistics, poorly understood tail of the LFSPEED distribution was simply too aggressive.

Chapter 9

A Posteriori Analysis

The main issue with the original analysis is the uncertainty and lack of statistics in the tail of the LFSPEED distribution. With this lesson learned, a new analysis is performed in which the speed binning step is removed and the cut is determined by optimizing only on the fast monopole signal. This has three consequences:

* **Slow Monopole Sensitivity becomes worse.** Without the speed bins, the final cut on the slower signal must inevitably be much tighter.

* **Fast Monopole Sensitivity improves.** One consequence of the speed binning was to lose some of the fast signal that fell into other speed bins. Thus, by removing this condition, the amount of signal for the $\beta = 0.9$ and $\gamma = 10$ monopoles increase, reducing the limit. This is actually quite desirable, as the parameter space considerations from Section 2.7 demonstrate the limits for fast monopoles cover much more of the interesting region.

* **The analysis becomes more robust relative to statistical fluctuations.** The final cut will now be optimized based on the full level 3 sample of background and signal. This represents a dramatic increase in the overall statistics of background compared to the slow speed bin optimizations done before.

In addition, the newer ice model simulations are used as the background estimate. This change motivated a slight change to the Level 3 cut selection as well.
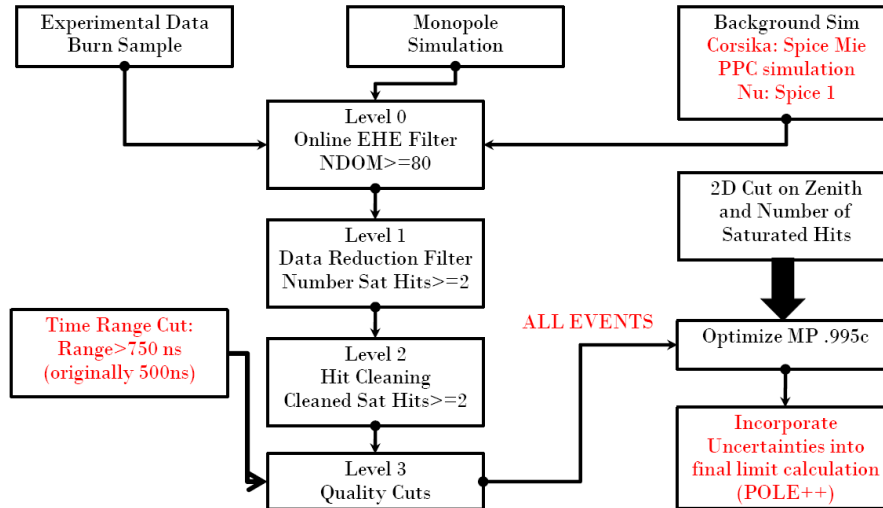
Figure 9.1: Design of the a posteriori monopole selection.

However, the cuts through Level 2 remain the exact same. Figure 9.1 shows the updated flowchart of the analysis. Changes are in red. The following sections detail the changes and final optimization of this new, a posteriori, analysis.

9.1 Changes to Analysis

9.1.1 CORSIKA

As first discussed in Section 5.1.3, the original analysis uses the `AHA` ice model for background simulation. After unblinding, a competing model was developed labeled `SPICE`. Three `CORSIKA` datasets utilizing the two-component model were available: (1) The `AHA` used in the original analysis, (2) `SPICE 1` which represents an early release of the new ice model, and (3) the `SPICE` ice model. As a reminder, Table 5.2 lists other various differences of the datasets.

Table 9.1: Comparison of three `CORSIKA` Ice models to data.

Dataset	Level 1 Rate(Hz)	MC/Data	Base=4, Slope=15 Rate(Hz)	MC/Data
Burn Sample	3.18×10^{-2}	-	7.04×10^{-5}	-
AHA	2.40×10^{-2}	0.755	6.71×10^{-5}	0.952
SPICE 1	2.62×10^{-2}	0.823	6.52×10^{-5}	0.926
SPICE	2.35×10^{-2}	0.740	7.03×10^{-5}	0.998

The decision of which dataset to use in the new analysis is made based on comparisons of fundamental observables. The first is the DOM Occupancy, which bins the hits based on DOM number. This gives a representation of how the models recreate hits as a function of depth. Figure 9.2 shows the normalized DOM Occupancy for the three datasets compared to experimental data. It is clear that while `SPICE 1` is a significant improvement over `AHA`, `SPICE` does best, especially in the deep ice. In addition, the un-normalized ratio of `CORSIKA` to Data is shown to illustrate how the actual rates compare in addition to shape.

Another fundamental observable is the launch time of the hit. Figure 9.3 shows the normalized distribution of hit times relative to the first hit in the event for all hits and saturated ones. No significant difference is seen between the three models.

The overall rates of the three models are summarized in Table 9.1. While the shape of the `SPICE` dataset matches data much better in the DOM Occupancy plots, the overall rate is much lower than the other two, especially at the lower levels. As the cut strength increases, this disagreement becomes smaller. This is especially evident by considering the ratio of `CORSIKA` to data in the two dimensional space of the final cut. This is illustrated in Figure 9.4. The major deficit in the `SPICE`

145
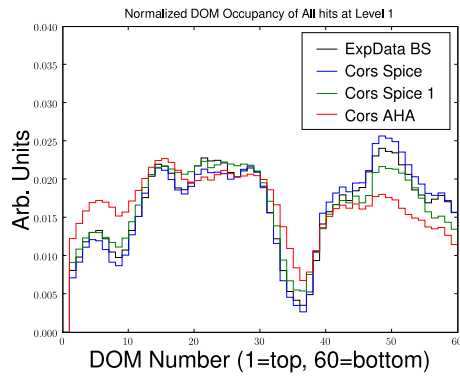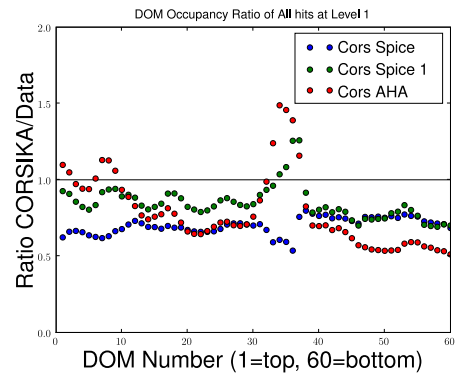
(a)   (b)
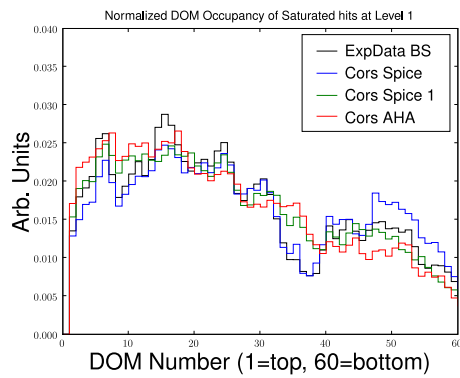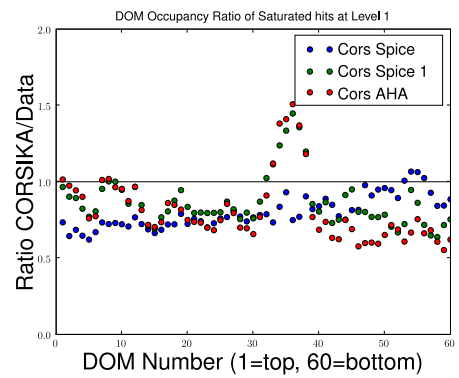
(c)   (d)

Figure 9.2: Normalized DOM Occupancy and the Un-Normalized ratio to data for various `CORSIKA` simulations considered at Level 1. Shown are the distributions for all DOM launches (a,b) and saturated hits only (c,d)
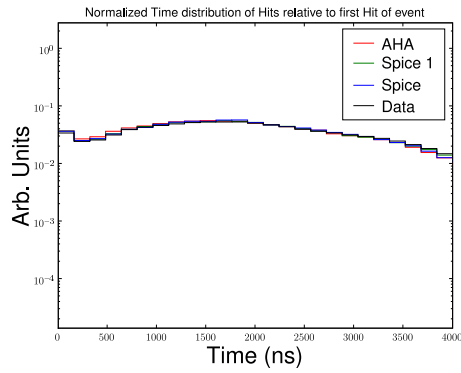
(a)
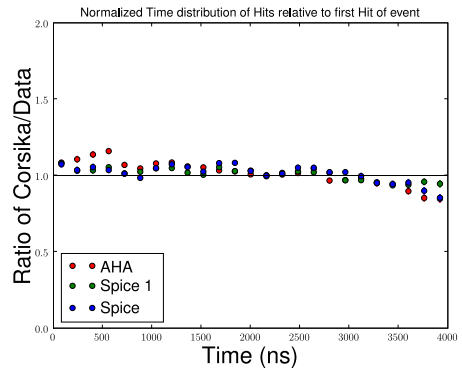
(b)
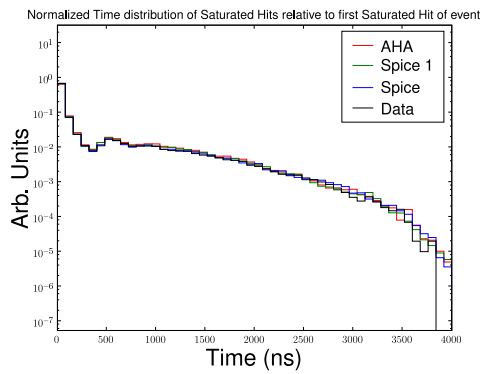
(c)
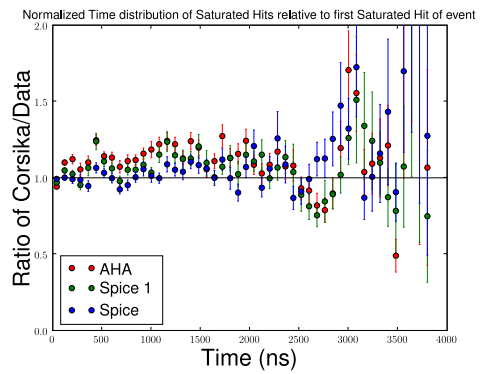
(d)

Figure 9.3: Launch Times relative to First Launch of event at Level 1. Shown are the distributions for all DOM launches (a,b) and saturated hits only (c,d)
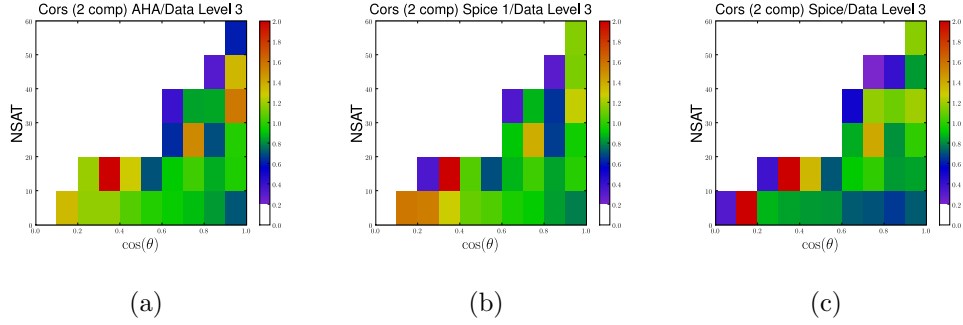
Figure 9.4: Ratio of `CORSIKA` to Data for various Ice Models. (a) `AHA`, (b) `SPICE 1`, and (c) `SPICE`

model comes from events with a low NSAT and fairly vertical $\cos\theta$. This is precisely the space that is first eliminated in the final cut. To illustrate this, Table 9.1 also includes the rates for a loose version of the final cut, with a baseline of 4 and slope of 15.

It is unclear the direct cause of the disagreement. The DOM Occupancy plots show that `SPICE 1` and `AHA` have more hits in the top of the detector and the ice layer than `SPICE`. These events are largely low energy bundles. This excess is shown in Figure 9.5. However, `SPICE` has more hits in the deep detector. The much better description of the deep ice, which plays the largest role for high energy bundles, is most important for this analysis.

The size of this disagreement is contained within the normalization uncertainty for the two-component model. Moreover, a dataset generated with the DOM efficiency scaled up by 11% improves the ratio at Level 1 to 0.947. Neither of these variations produce a dramatic effect at the final level and are both part of the systematic uncertainties discussed in the next chapter. Checks on the robustness of
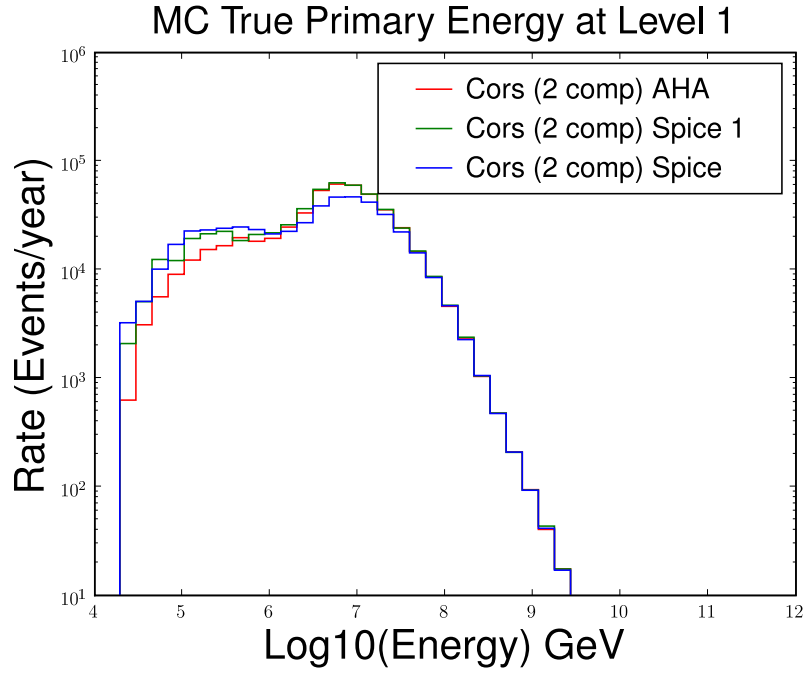
Figure 9.5: Distribution of the True Energy for the three `CORSIKA` Ice Models at
Level 1

the final analysis demonstrate the effect of changing the simulation is <1% on the

final sensitivity (see Appendix E).

Unfortunately, no high energy dataset was simulated for `SPICE` with `PHOTONICS`

or the original Weibusch function, so it is unclear whether the these changes are due

to the improved ice model or photon propagation/light scaling. However, studies of

other variables suggest it is the ice model[86].

Since the `SPICE` dataset does the best at matching the shape of the data for

the important low level variables and the overall rate normalization improves at

higher cut levels, it is used as the new background simulation.

9.1.2 Neutrinos

For neutrinos, the only two options available with significant (E^{-1}) statistics were `AHA` and `SPICE 1`. `SPICE 1` is chosen since this did better for atmospheric muons.

A second change is to include the prompt flux (see Section 5.1.2) based on the recommendation of collaborators[87]. The Sarcevic model is used[75].

The effect of each change is shown in Figure 9.6 at Level 1. The addition of the prompt is especially dramatic. However, these events are still four to five orders of magnitude below the `CORSIKA` rate as seen in Table 9.2. This does play a role at the final level, where the prompt muon component represents about a third of the final background estimate, the same as the conventional ν_μ's and muon bundles from iron primaries.

9.1.3 Quality Cuts

In the `SPICE` dataset, there is one proton event with $E = 10^{6.76}$ GeV, a time range of ~ 600 ns, a reconstructed direction just below the horizon, NSAT=8, and an expected event rate of ~ 11.3 events for the full year. This led the optimization to consistently land just beyond a cut that removes this event. The effect of this one event can be seen in Figure 7.7. To avoid this, the time range cut is tightened to 750 ns, corresponding roughly to eliminating events that only saturate two strings (see Section 7.4.1).

This tightening of the TRANGE cut increases the background rejection from
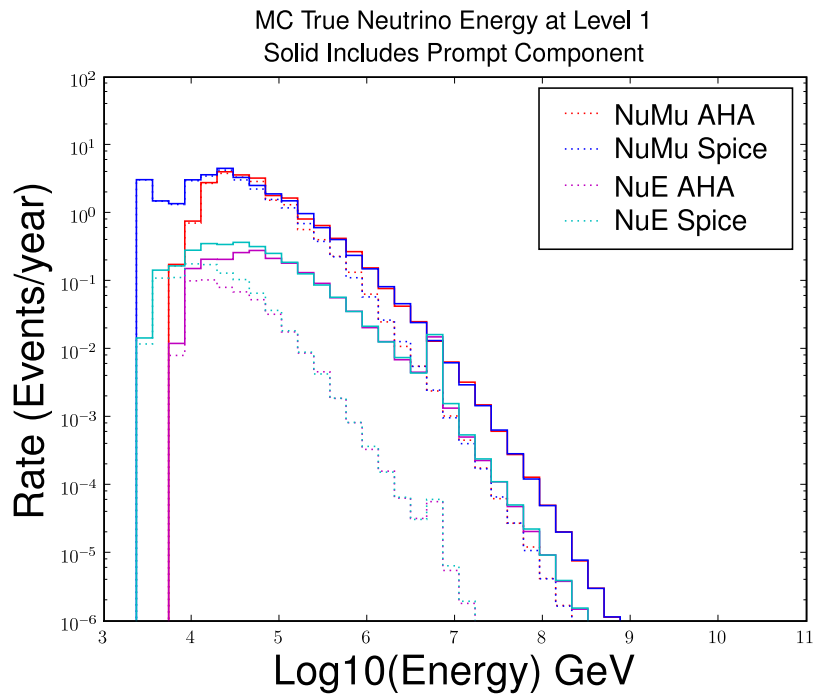
Figure 9.6: Distribution of the True Energy for the Electron and Muon Neutrino datasets. Shown are the `AHA` and `SPICE 1` ice models. The dashed lines present the conventional atmospheric flux and the solid lines show the effect of adding the prompt component.

$\sim 75\%$ to $\sim 80\%$, with the largest impact on electron neutrinos ($> 99\%$), demonstrating the effectiveness on cascades. The signal is reduced by $\sim 30\%$ as opposed to $\sim 20\%$ before, but these are largely events that pass outside the detector and only saturate one or two strings.

9.2   Optimization

The optimization is done in the same way as Section 7.6, with a piece-wise, linear cut on NSAT and $\cos(\theta)$. The signal expectation for the $\gamma = 10$ monopoles is used. A full year livetime of 2.061879425×10^7 s is used. The $\sim 3\%$ decrease is from discovering a small number of files which were listed on the good run list but not in the data warehouse. The baseline was allowed to range from 0 up to 25 in increments of 1 and the slope from 0 to 250 in increments of 5. Figure 9.7 shows the resulting model rejection factor. The final cut is a baseline of 7 and slope of 150. Figures 9.8 and 9.9 show the two-dimensional distributions of background and signal with the final cut.

Table 9.2 shows the passing rates (in events/year) for various backgrounds and signal at all levels of the analysis. As before, a flux of $5 \times 10^{-17} cm^{-2} sr^{-1} s^{-1}$ is assumed, roughly corresponding to the limits set by AMANDA.

9.3   Sensitivity

The average upper limit associated with the background expectation of 0.124 events is 2.54 events. Table 9.3 lists the final sensitivity for each of the four monopole
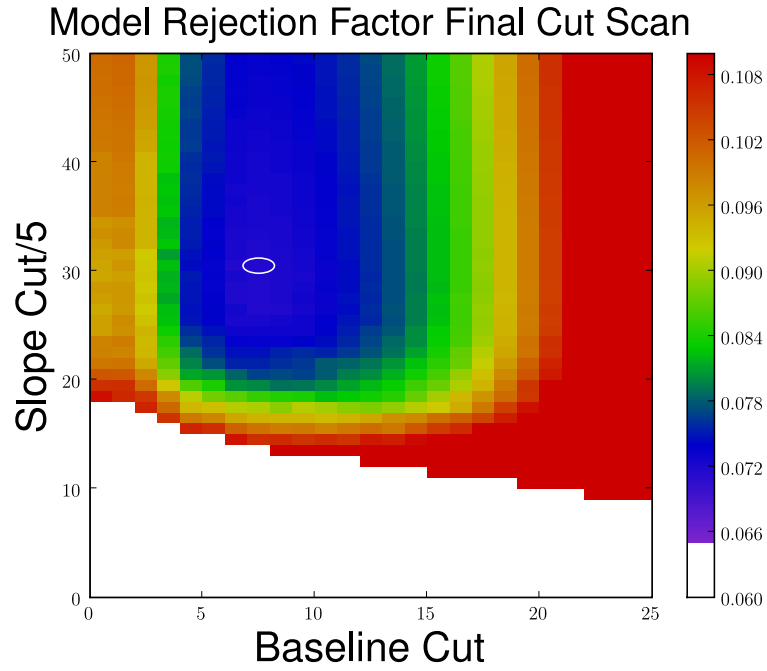
Figure 9.7: Model rejection factor with $\gamma = 10$ signal for various baseline and slope cuts

Table 9.2: Rates of background and signal datasets (events/year) for each cut level

Dataset	Level 0	Level 1	Level 2	Level 3	Final
Burn Sample	3.14×10^7	6.55×10^5	6.55×10^5	1.19×10^5	0
Cors Proton	7.35×10^6	2.66×10^5	2.65×10^5	2.93×10^4	3.61×10^{-4}
Cors Iron	5.14×10^6	2.20×10^5	2.20×10^5	6.19×10^4	4.70×10^{-2}
Atm Conv ν_μ	–	26.4	26.4	13.6	3.45×10^{-2}
Atm Prompt ν_μ	–	2.83	2.83	0.334	4.12×10^{-2}
Atm Conv ν_e	–	0.967	0.967	8.08×10^{-6}	5.52×10^{-6}
Atm Prompt ν_e	–	1.86	1.86	1.43×10^{-3}	7.39×10^{-4}
Bkgrd Total	1.25×10^7	4.85×10^5	4.85×10^5	9.12×10^4	0.124
$\gamma = 10$	100	89.2	89.2	63.4	35.6
$\beta = 0.9$	95.3	84.5	84.5	60.8	33.4
$\beta = 0.8$	81.0	70.1	70.1	46.5	22.1
$\beta = 0.76$	32.3	5.80	5.80	2.55	3.85×10^{-2}
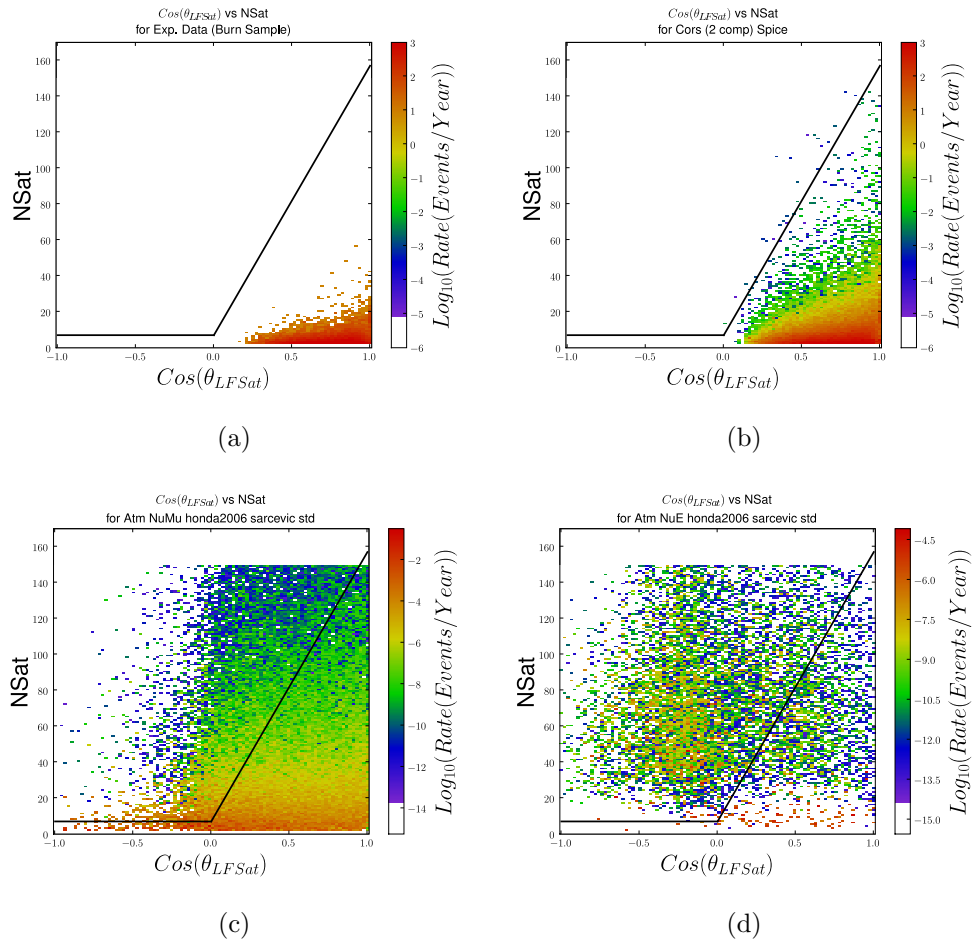
Figure 9.8: NSAT vs $\cos\theta$ for (a) Burn Sample, (b) `CORSIKA SPICE`, (c) Atmospheric Muon Neutrinos, and (d) Atmospheric Electron Neutrinos. The solid line represents the optimized cut. For `CORSIKA` and Data, the scale is the same, while for neutrinos it is five to ten orders of magnitude less.
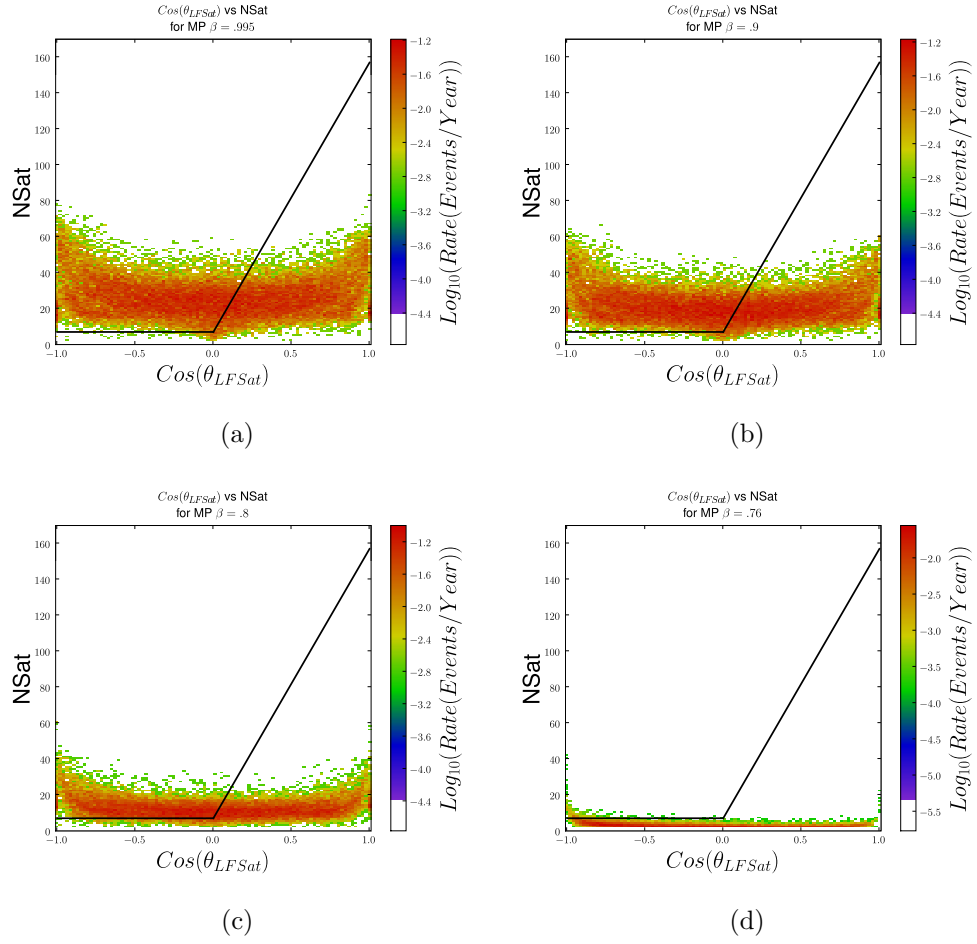
Figure 9.9: NSAT vs $\cos\theta$ for (a) $\gamma = 10$, (b) $\beta = 0.9$, (c) $\beta = 0.8$, and (d) $\beta = 0.76$ monopoles. The solid line represents the optimized cut.

Table 9.3: Sensitivity (in $cm^{-2}sr^{-1}s^{-1}$) for each of the four signals compared to final limit from AMANDA.

	$\gamma = 10$	$\beta = 0.9$	$\beta = 0.8$	$\beta = 0.76$
AMANDA Down-going	2.9×10^{-16}	4.2×10^{-16}	1.7×10^{-15}	
AMANDA Up-going	3.75×10^{-17}	4.3×10^{-17}	6.7×10^{-17}	8.75×10^{-16}
This Analysis	3.6×10^{-18}	3.8×10^{-18}	5.8×10^{-18}	3.3×10^{-15}

speed signals, compared to the flux limits from AMANDA. Comparing to Table 7.5 shows the improvement for fast monopoles while leading to a worse result for the slow ones. This is especially true of the $\beta = 0.76$ signal, where the sensitivity is no longer competitive to existing limits. Note that these results do not take uncertainties into account. See Chapter 11 for the final value.

9.4 ReUnblinding

After choosing the optimized cut based on simulation and receiving approval from the rest of the collaboration, the cut was applied to the full data sample. No events passed the final cut level. Figure 9.10 shows the resulting distribution in the final cut plane.
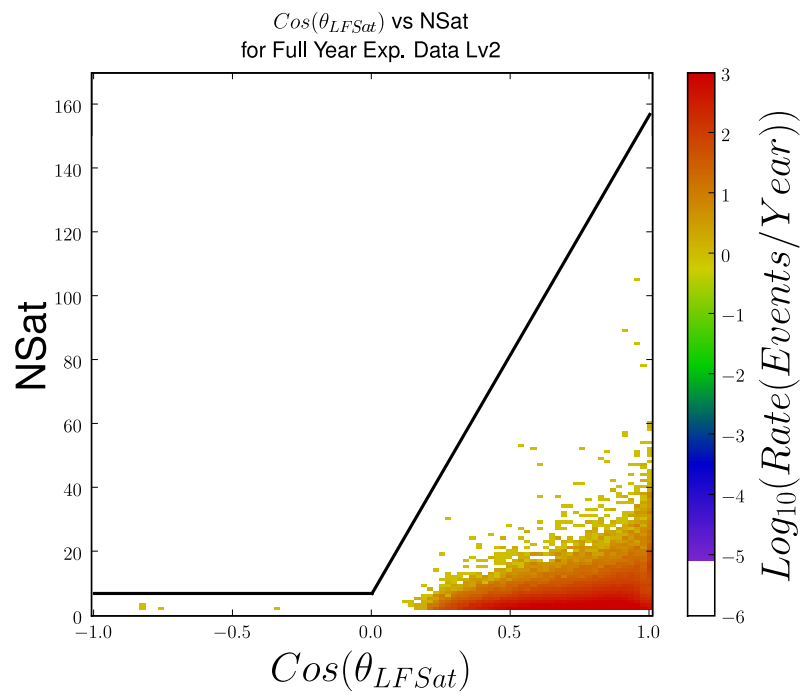
Figure 9.10: NSAT vs $\cos\theta$ for the full data sample. The solid line represents the optimized cut.

Chapter 10

Uncertainties

Uncertainties can be broadly divided into three categories: (1) theoretical uncertainties in the models used in simulation; (2) uncertainties in the detector response; and (3) statistical uncertainties. Uncertainties are studied using both Monte Carlo based estimates and numbers taken from papers and other analyses.

For Monte Carlo estimates, the uncertainty is measured by comparing the result of a varied dataset to one in which all other parameters are the same; e.g. for neutrino DOM efficiency, the varied dataset uses `AHA` so it is compared to an `AHA` dataset with no variation on DOM efficiency. A consequence of using Monte Carlo is that finite numbers introduce an additional statistical uncertainty on the estimate. For those with the largest statistical uncertainties, the estimate is taken from a looser cut as noted. For cases where Monte Carlo studies produce assymmetric results, the largest is taken as the symmetric Gaussian and then combined in quadrature for the total.

Tables 10.1 and 10.2 show the final absolute values used for all uncertainties for background and relative uncertainties for signal.

Table 10.1: Absolute Uncertainties for Background in $\frac{\text{Events}}{\text{Year}}$

Uncertainty	CORSIKA	NuMu	NuE	Total
Normalization	$\pm 1.2 \times 10^{-2}$	$\pm 8.6 \times 10^{-3}$	$\pm 1.4 \times 10^{-6}$	$\pm 1.5 \times 10^{-2}$
Spectrum	$+4.7 \times 10^{-1}$ -0.4×10^{-1}	$+1.3 \times 10^{-2}$ -1.7×10^{-2}	$+2.4 \times 10^{-4}$ -2.9×10^{-4}	$\pm 4.7 \times 10^{-1}$
MMC σ	$+4.8 \times 10^{-3}$ -1.4×10^{-3}	$+7.7 \times 10^{-3}$ -2.1×10^{-3}	-	$\pm 9.1 \times 10^{-3}$
$\nu\sigma$	-	$\pm 4.8 \times 10^{-3}$	$\pm 4.8 \times 10^{-5}$	$\pm 4.8 \times 10^{-3}$
DOM Efficiency	$+1.7 \times 10^{-2}$ -1.3×10^{-2}	$+1.5 \times 10^{-2}$ -2.9×10^{-2}	$+1.5 \times 10^{-4}$ -2.8×10^{-4}	$\pm 3.1 \times 10^{-2}$
Light	$\pm 3.7 \times 10^{-2}$	$\pm 3.1 \times 10^{-2}$	$\pm 5.4 \times 10^{-4}$	$\pm 4.9 \times 10^{-2}$
Statistical	$\pm 1.0 \times 10^{-2}$	$\pm 1.0 \times 10^{-2}$	$\pm 1.4 \times 10^{-4}$	$\pm 1.5 \times 10^{-2}$
TOTAL				$\mathbf{\pm 4.7 \times 10^{-1}}$

Table 10.2: Relative Uncertainties for Signal

Uncertainty	$\gamma = 10$	$\beta = 0.9$	$\beta = 0.8$	$\beta = 0.76$
DOM Efficiency	$+\mathbf{1.4}\%$ -1.2%	$+\mathbf{4.8}\%$ -2.9%	$+\mathbf{3.9}\%$ -5.8%	$+38\%$ $-\mathbf{42}\%$
Light(Ice Model)	0.2%	4.2%	7.1%	4.8%
Statistical	0.7%	0.7%	0.9%	6.7%
Total	1.7%	6.5%	9.2%	43%

Table 10.3: Variation of spectral parameters for CORSIKA

Parameter	Fit Value	Low (steep)	High (flat)
γ_{1P}	-2.67	-2.68	-2.66
γ_{2P}	-3.39	-3.47	-3.31
E_{kneeP} (GeV)	4.1×10^6	3.7×10^6	4.5×10^6
γ_{1Fe}	-2.69	-2.71	-2.67
γ_{2Fe}	-3.1	-3.5	-2.7
E_{kneeFe} (GeV)	1.1×10^8	9.8×10^7	1.2×10^8

10.1 Theoretical Uncertainties

10.1.1 CORSIKA

The major uncertainty with the cosmic ray simulation comes from the weighting functions used for the two-component model. In the KASCADE paper[72], each parameter is given with a one sigma uncertainty on the fit. For the overall normalization, the error of $\sim 26\%$ is taken from the paper's uncertainty for the differential flux value at the knee energy. For the uncertainty on the spectral model parameters, the CORSIKA dataset is re-weighted using the values for each spectral index and knee that give the steepest and flattest spectrum possible. These are given in Table 10.3. For the un-fit parameters of iron, the knee is varied with the same relative uncertainty as the proton knee, while γ_{2Fe} is allowed to go from -2.7, corresponding to roughly no break, to -3.5 to keep the deviation symmetric. Since the normalization is a separate uncertainty, these re-weighted datasets are all normalized to the same level 0 rate value and their differences at the final cut are studied.

This uncertainty represents the dominant factor of the total uncertainty. The final CORSIKA rates are virtually all iron and in the energy range from 10^{10} GeV to

160

the cutoff at 10^{11} GeV. The true value is likely smaller since the assumption of no iron knee is unphysical. Despite this, the actual variation of 0.47 events in the entire year is small and given the lack of a good understanding for cosmic rays in the 10 EeV region, the conservative estimate is appropriate.

A second uncertainty studied is from the cross sections as implemented in `MMC`. Two datasets were produced in which all muon cross sections for stochastic energy losses were simultaneously varied by $\pm 3\%$. These datasets were simulated with `AHA` ice model and use the updated light scaling function by Kowalski. They are compared to a dataset with the same parameters. Unfortunately, both datasets represent relatively low statistics (10% of events compared to the baseline background dataset) and the uncertainty estimate at the final cut level had a 95% statistical uncertainty. Therefore, the systematic uncertainty is re-evaluated with a looser cut of just the baseline $NSAT > 7$ while ignoring the slope cut. This reduced the statistical uncertainty to $\sim 7\%$.

10.1.2   Neutrinos

Each neutrino dataset is comprised of both a conventional and prompt atmospheric flux.

For the conventional component, the uncertainty on the normalization is taken as 25% from the Honda paper. The uncertainty on the shape of the energy spectrum is estimated by comparisons to the Bartol flux[88].

For the prompt component, the energy flux uncertainty is estimated by consid-

ering the minimum and maximum of the Sarcevic model as implemented in NEUTRINO
FLUX.

An estimate on the uncertainty of neutrino cross sections is taken from the 22
string diffuse analysis and set to 6.4%[89].

For muon neutrinos, an uncertainty from the MMC cross sections is taken from
the CORSIKA study.

10.2   Detector Uncertainties

10.2.1   Light Properties

The main uncertainty in how the light moves through the detector comes
from the limited understanding of the scattering and absorption coefficients for the
ice (i.e., the ice model). In addition, changes in the simulation to both how light
is propagated and the updated light scaling function for secondary cascades are
considered.

For CORSIKA, three datasets are available (see Chapter 5). The uncertainty is
defined based on whichever variation is larger between SPICE 1 and AHA compared
to the base of SPICE. For the final cut, this corresponded to the variation from AHA.

In addition to the ice model, this study incorporates the uncertainty in light
propagation (PHOTONICS versus PPC) as well as the effect of updating the light scaling
function.

For neutrinos, only SPICE 1 and AHA datasets were available, and the variation
between these two is used for the ice model uncertainty. To be as complete as pos-

sible, an additional uncertainty for the light scaling function is taken from `CORSIKA` datasets that were produced with both functions. The uncertainty is measured from the looser cut of $NSAT > 7$ with no slope cut (the same as the `MMC` cross sections) since the $\cos(\theta)$ distribution for neutrinos is much flatter than `CORSIKA` and thus affected differently by the slope cut.

For signal, there were no `SPICE` or `AHA PHOTONICS` tables available for the slower speeds. Hence, datasets were produced with both `MILLENNIUM` and `SPICE 1` at all four speeds with the Cherenkov angle corresponding to $\beta = 1$. This allowed a comparison of the effect of the ice model for all speeds though it assumes the effect of changing the angle is completely independent. However, separate datasets which keep the ice model constant but change the Cherenkov angle suggest the effect of the angle itself is $< 1\%$ for all but the $\beta = 0.76$ signal monopole.

Since the only light produced is from Cherenkov emission, no uncertainty in the cascade light scaling function is included. The small relative uncertainty is a consequence of monopoles being much brighter and hence more likely to produce enough un-scattered photons to launch the DOM.

10.2.2 DOM Efficiency

For `CORSIKA SPICE`, the nominal setting is for an efficiency of 0.9. Two datasets were produced with efficiency of 1.0 and 0.8, or $\pm$ 11% For neutrinos, a $\pm$ 10% sample of muon neutrinos is studied and taken to be the same for electrons. For signal, a $\pm$ 10% efficiency sample was generated locally.

10.3 Statistical

Since the background and signal rates are taken from Monte Carlo estimates, the final rate will have a statistical uncertainty corresponding to the Pythagorean sum of the weights for the surviving events.

Chapter 11

Final Results

The final limit can be found by using the result of no candidate events to calculate the upper limit. For a 90% confidence level, this is 2.31. Thus, the result would be the same as Table 9.3 with all values lowered by 9%. However, this result makes two assumptions. First, that there are no uncertainties. Second, that the detector sees an isotropic flux of signal at one of the four speeds simulated.

This chapter describes how these two assumptions are removed and presents the final limit.

11.1   Incorporating Uncertainties

Uncertainties are integrated into the final answer by using the `POLE++` program[90]. `POLE++` calculates a new confidence belt that takes uncertainties into account by treating them in a semi-Bayesean manner. The Bayesean part comes from constructing a prior PDF for the shape of the signal and background uncertainties and integrating over the true value. Once done, the final confidence belt is calculated using the frequentist method of Feldman and Cousins[82].

The general form of incorporating the uncertainties can be described as:

$$P(X|\mu + b) \rightarrow \int \int P(X|\mu + b)P(\mu|\mu')P(b|b')db'd\mu' \qquad (11.1)$$

where X is the observed number of events, μ and b are the expected signal and background rates, and μ' and b' represent the 'true' values of the signal and background rates which are unknown due to the uncertainties in the analysis. The probability functions for the expected values given a true value represent the prior PDF.

For example, suppose the signal is known but the background has an expectation b and Gaussian uncertainty of σ. The final probability function for the total number of events would be:

$$P(X|\mu + b) = \frac{1}{\sqrt{2\pi}\sigma} \int_0^\infty P(X|\mu + b') \times e^{\frac{-(b-b')^2}{2\sigma^2}} db' \qquad (11.2)$$

For this analysis, the signal uncertainties are treated as a Gaussian PDF. The background uncertainties, dominated by the uncertainty in the cosmic ray spectrum, are treated as a log-normal PDF to reflect the fact that a change in the spectral index results in an exponential change in the event rate.

Once a new event probability is calculated, it is used to construct the horizontal bands that determine the possible experimental outcomes covering 90% of the cases (see Equation 6.5). The confidence interval is then constructed in the same manner as described in Section 6.3.

Table 11.1 shows the resulting average and final upper limits for each of the four speeds. In general, the behavior is intuitive: increasing the uncertainty increases the upper limit. The one exception is the $\beta = 0.9$ case, which has a slightly lower $\mu_{90\%}$ than the $\gamma = 10$ case. This behavior is due to the definition of the best signal hypothesis, used in the denominator of the log-likelihood ratio ordering, as first

166

Table 11.1: Average and Final Upper Limits. Also shown is the case of no uncertainties, in which the upper limits are the same for all signals

	$\beta = 0.76$	$\beta = 0.8$	$\beta = 0.9$	$\gamma = 10$	No Uncertainty
Uncertainty	43%	9.2%	6.5%	1.7%	0.0
$\mu_{90\%\mathrm{Avg}}$	3.316	2.692	2.639	2.654	2.540
$\mu_{90\%}$	2.979	2.455	2.405	2.408	2.305

Table 11.2: Final Sensitivities and Limits at Detector in $cm^{-2}sr^{-1}s^{-1}$

	$\beta = 0.76$	$\beta = 0.8$	$\beta = 0.9$	$\gamma = 10$
Sensitivity	4.31×10^{-15}	6.10×10^{-18}	3.94×10^{-18}	3.73×10^{-18}
Final Limit	3.87×10^{-15}	5.57×10^{-18}	3.60×10^{-18}	3.38×10^{-18}

noticed by Hill[91]. Increasing the signal uncertainties can lead to a decrease in this value, which in turn can shift the peak ratio to higher values of X. The result of shifting horizontal bands to the right can mean for a given observation, the point where it intersects the bands vertically becomes lower. A different ordering scheme was proposed by Hill but is not shown here.[1] While not corrected, the effect is minimal.

Table 11.2 gives the final result on the limit of magnetic monopoles for each of the four speeds at the detector. Figure 11.1 shows the result together with previous experiments.

11.2 Effective Area

A common method of describing the effect of cuts on a signal is to give the effective area, which can be defined as the area expected for cuts that have an

---

[1]This scheme had been implemented into `POLE++`, but resulted in memory leaks. This is likely due to a compiler version conflict. The small effect led to the decision not to pursue this further.
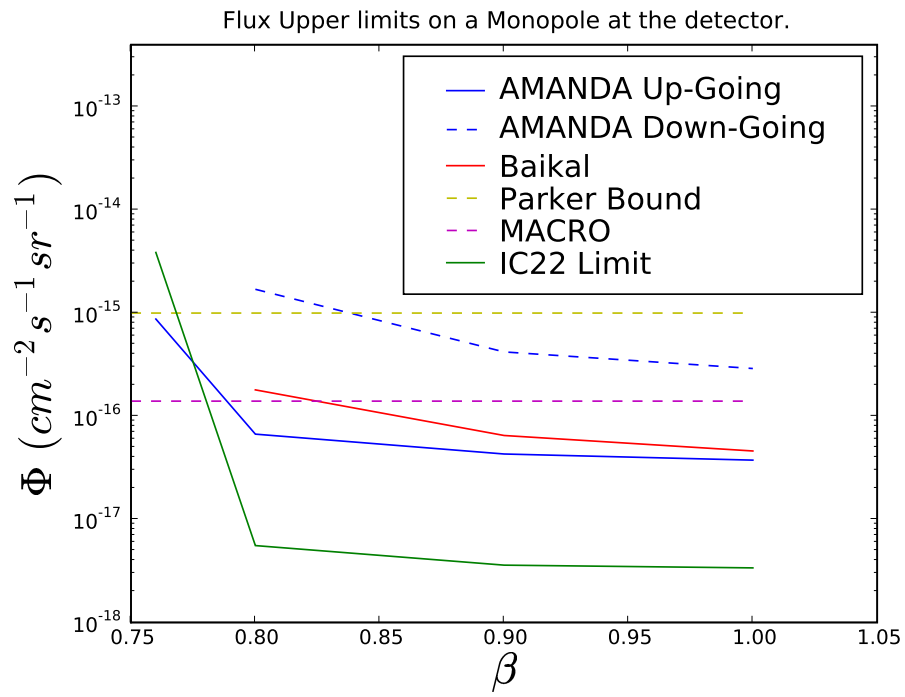
Figure 11.1: Final limits on Flux, together with other experiments.

efficiency of 100%. For the four given signal speeds, this can be written as:

$$A_{eff}^{\gamma}(\cos\theta) = \frac{N_{detected}^{\gamma}(\cos\theta)}{N_{gen}^{\gamma}(\cos\theta)} A_{gen}^{\gamma}(\cos\theta) \qquad (11.3)$$

Matching the angular bins introduced in Section 2.7, the effective area is calculated for 0.1 bins in $\cos\theta$. For each bin, $N_{detected}^{\gamma}$ is the total number of events that survive the final cut. $N_{gen}^{\gamma}(\cos\theta) = N_{gen}^{\gamma}/20$ and $A_{gen}^{\gamma}(\cos\theta) = 1.33\,\text{km}^2$, representing the fact that signal is simulated isotropically. Figure 11.2 displays the result. For numerical values, see Appendix F. Note that the acceptance is relatively uniform for the up-going region. Then, it falls dramatically, reaching zero for $\cos\theta > 0.2$. This is indicative of the two-dimensional behavior of the final cut.

11.3   Generalized Flux Limit

As mentioned in Section 2.7, the mass and initial kinetic energy are treated as free parameters in this search. The final flux limit is calculated for different values of these two parameters. This section will consider two cases. First, an isotropic flux at the detector for a monopole signal of mass M and kinetic energy $T_d = M*(\gamma_d-1)$. Second, an isotropic flux at the surface of the Earth for a monopole of mass M and kinetic energy $T_{surf} = M*(\gamma_{surf}-1)$. In each case, the flux limit from this analysis is calculated for pairs of (T,M) ranging from 10^4 to $10^{18}\,\text{GeV}$.

The final limit is found using the method described in Section 6.3. However, it is necessary to consider a more general expression for the expected number of signal events, N_s. Assuming the flux ($\Phi^{\gamma,M}$) being tested is time-independent, the
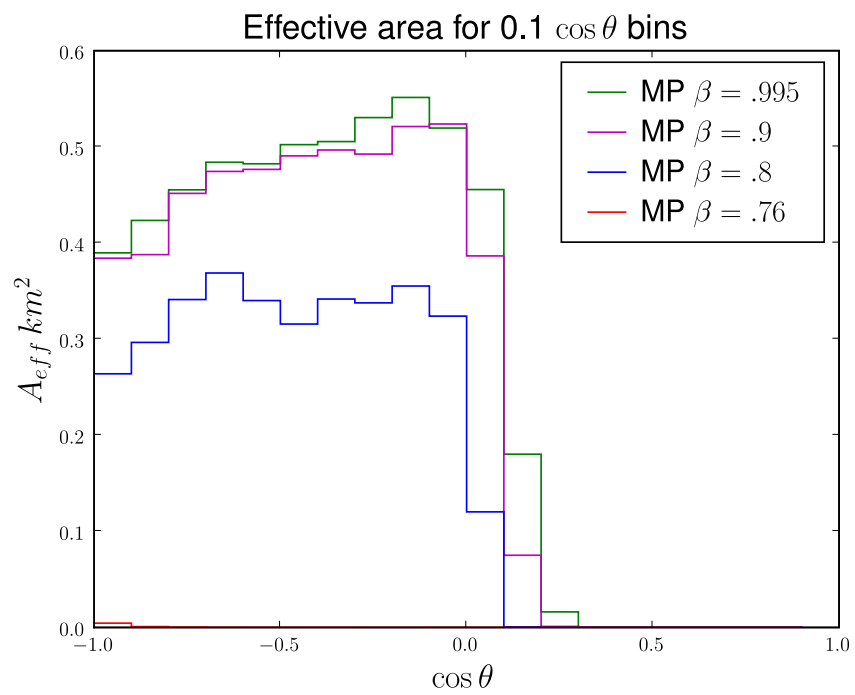
Figure 11.2: Effective area of the final cuts for each monopole speed.

expected number of signal events for a flux of monopoles with speed γ and mass M can be written as:

$$N_s^{\gamma,M} = T_{live} \times \int d\Omega \int dA_{eff}(\gamma_d, \cos\theta) \times \Phi_{detector}(\gamma_d, \cos\theta, \Phi^{\gamma,M}) \qquad (11.4)$$

The integral over the effective area is for the speed (γ_d) of the signal events when they arrive at the detector, since this may in principle be different from the speed given for the flux(γ). Note that $\Phi^{\gamma,M}$ could involve a general energy dependence instead of being mono-energetic. This would also be covered by the effective area integral.

11.3.1 Flux limit at the Detector

If the flux tested is isotropic at the detector, $\gamma_d = \gamma$ and $\Phi_{detector} = \Phi^{\gamma,M}$. Thus, Equation 11.4 can be simplified in the following way:

$$N_s^{\gamma,M} = T_{live} \times \Phi^{\gamma,M} \times \int d\Omega A_{eff}(\gamma, \cos\theta) \qquad (11.5)$$

For the four speeds simulated, $A_{eff}(\gamma, \cos\theta) = A_{eff}^{\gamma}(\cos\theta)$ (Equation 11.3) and the integral over Ω reduces to:

$$
\begin{aligned}
N_s^{\gamma,M} &= T_{live} \times \Phi^{\gamma,M} \times \int d\Omega A_{eff}(\gamma, \cos\theta) \\
&= T_{live} \times \Phi^{\gamma,M} \times 2\pi \times A_{gen}^{\gamma} \times \int d\cos\theta \frac{N_{det}^{\gamma}(\cos\theta)}{N_{gen}^{\gamma}(\cos\theta)} \\
&= T_{live} \times \Phi^{\gamma,M} \times 2\pi \times A_{gen}^{\gamma} \times 2 \times \frac{N_{det}^{\gamma}}{N_{gen}^{\gamma}} \\
&= T_{live} \times \Phi^{\gamma,M} \times \Omega_{gen} \times A_{gen}^{\gamma} \times \epsilon
\end{aligned} \qquad (11.6)
$$

171

Since the simulated flux is isotropic at the detector, the final integral produces the total number of events simulated and seen, with a factor of 2 representing the integral over $d\cos\theta$. Thus, Equation 6.4 is recovered.

For all other speeds, a conservative approximation for the effective area as a function of γ is to treat it as a step function:

$$A_{eff}(\gamma, \cos\theta) \begin{cases} A_{eff}^{\gamma=10}(\cos\theta) & \text{if } \gamma > 10 \\ A_{eff}^{\beta=0.9}(\cos\theta) & \text{if } 0.9 < \beta < 0.995 \\ A_{eff}^{\beta=0.8}(\cos\theta) & \text{if } 0.8 < \beta < 0.9 \\ A_{eff}^{\beta=0.76}(\cos\theta) & \text{if } 0.76 < \beta < 0.8 \\ 0 & \text{if } \beta < 0.76 \end{cases} \tag{11.7}$$

Figure 11.3 shows the result of this limit as it applies to the different mass and energy values tested. Note that the $\beta = 0.76$ limit is not included since it is not competitive. However, a striking feature of this plot is to demonstrate the relatively small parameter space the lower speeds occupy. Thus, the result of improving the $\gamma = 10$ limit at the expense of the $\beta = 0.76, 0.8$ limits is actually desirable.

11.3.2 Flux Limit at the Earth's Surface

A more physically valid limit applies to an isotropic flux at the Earth's surface. This limit must take into account the energy loss a monopole will experience as it travels the Earth, hence the flux at the detector will not in principle be isotropic.
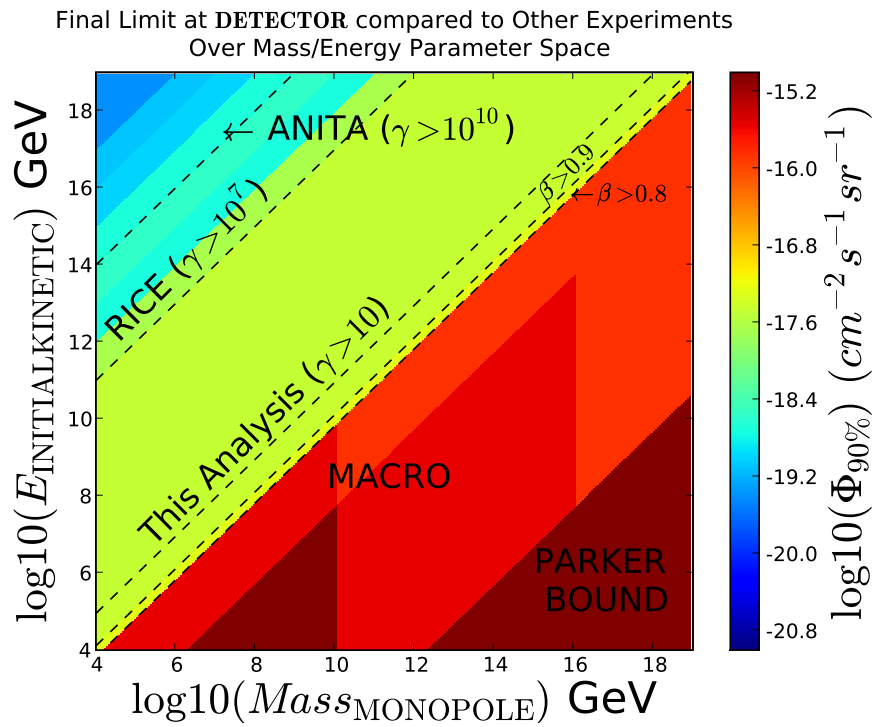
Figure 11.3: Final limits on Flux, together with other experiments, for different combinations of monopole mass and kinetic energy. Flux limits apply to an isotropic flux just outside the IceCube Detector.

Instead, this flux can be written as:

$$\Phi_{detector}(\gamma_d, \cos\theta, \Phi^{\gamma_{surf},M}) = \Phi^{\gamma_{surf},M} \times P^{\gamma_{surf}\rightarrow\gamma_d}(\cos\theta, M) \qquad (11.8)$$

Here, $P^{\gamma_{surf}\rightarrow\gamma_d}(\cos\theta, M)$ represents the probability that the monopole will have a speed γ_d at the detector when it starts with speed γ_{surf}. This value depends on the mass and direction of the monopole. Assuming the average stochastic energy loss that is calculated in Section 2.7, this can be written as a delta function:

$$P^{\gamma_{surf}\rightarrow\gamma_d}(\cos\theta, M) = \delta(\gamma_{surf} - \gamma_d - \frac{\Delta E(\gamma_{surf}, \cos\theta, M)}{M}) \qquad (11.9)$$

Substituting this back into Equation 11.4 results in:

$$N_s^{\gamma_{surf},M} = T_{live} \times \int d\Omega \int dA_{eff}(\cos\theta, \gamma_d) \times \Phi_{detector}(\gamma_d, \cos\theta, \Phi^{\gamma_{surf},M})$$

$$= T_{live} \times \Phi^{\gamma_{surf},M} \times \qquad (11.10)$$

$$\int d\Omega \int_{\gamma_d=0}^{\infty} dA_{eff}(\cos\theta, \gamma_d) \times \delta(\gamma_{surf} - \gamma_d - \frac{\Delta E(\gamma_{surf}, \cos\theta, M)}{M})$$

The key difference here is that the delta function could pick out different values of γ_d for different angles. If the integral is carried out as a summation over the 0.1 $\cos\theta$ bins and the effective area is again treated as a step function:

$$N_s^{\gamma_{surf},M} = T_{live} \times \Phi^{\gamma_{surf},M} \times 2\pi \times \sum_{i=0}^{20}(\Delta\cos\theta)_i \times A_{eff}(\cos\theta_i, \gamma_{surf} - \frac{\Delta E(\gamma_{surf}, \cos\theta, M)}{M})$$

$$= T_{live} \times \Phi^{\gamma_{surf},M} \times 2\pi \times A_{gen}^{\gamma} \times \sum_{i=0}^{20}(\Delta\cos\theta)_i \times \frac{N_{det}^{\gamma}(\cos\theta_i)}{N_{gen}^{\gamma}(\cos\theta_i)}$$

$$(11.11)$$

where $\frac{N_{det}^{\gamma}(\cos\theta_i)}{N_{sim}^{\gamma}(\cos\theta_i)}$ is calculated for each bin with γ representing the largest speed below $\gamma_{surf} - \frac{\Delta E(\gamma_{surf}, \cos\theta, M)}{M}$.

The final limit calculation remains:

$$\Phi_{90\%} = \frac{\mu_{90\%}^{\gamma_d}(0.0)}{N_s^{\gamma_{surf},M}} \Phi^{\gamma_{surf},M} \qquad (11.12)$$

174

Unfortunately, $\mu_{90\%}^{\gamma_d}$ is also different for each speed, even though the observed background is 0.0 for all four cases. This is because of the different uncertainties in each signal simulation. To remain conservative, for each value of (γ_{surf}, M) considered, the speed that produces the largest $\mu_{90\%}^{\gamma_d}$ used in the calculation of $N_s^{\gamma_{surf},M}$ is taken as the only value.

The result is shown in Figure 11.4, along with other experimental results. In order to help guide the eye, the angular acceptance lines for the $\beta = 0.9$ monopole are included. Note that once the detector starts to lose the full 4π acceptance, the limit gets worse. Above masses of $\sim 10^{11}\,\mathrm{GeV}$, the Earth is not large enough to provide stopping power, and an isotropic flux at the surface is the same as at the detector.
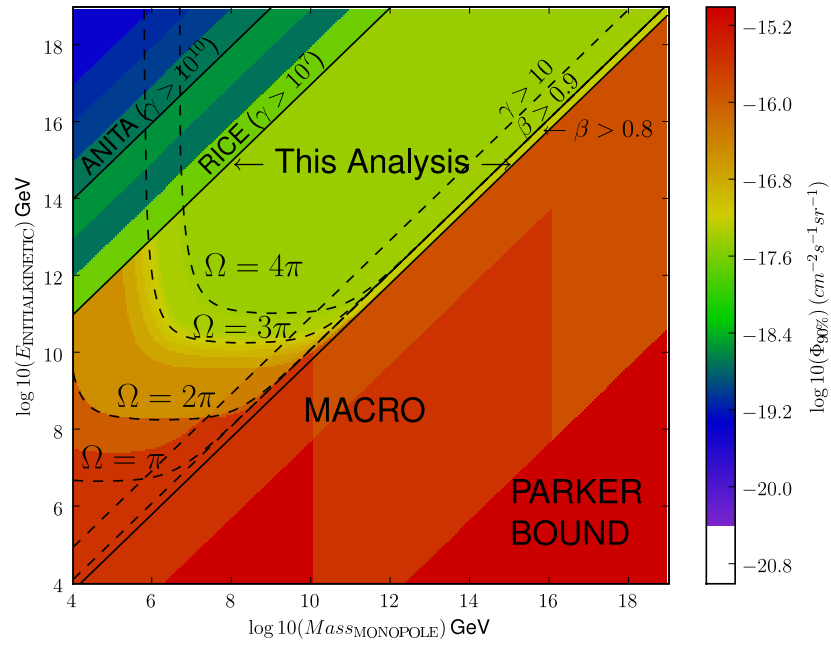
Figure 11.4: Final limits on Flux, together with other experiments, for different combinations of monopole mass and kinetic energy. Flux limits apply to an isotropic flux at the surface of the Earth.

Chapter 12

Summary

The result of this analysis is to provide an order of magnitude improvement on the model independent flux limits for relativistic magnetic monopoles for the speed region of $\beta > 0.8$ to $\gamma < 10^7$. This result is for one year of data with the 22 string IceCube detector.

There are many possible improvements to the analysis method, including:

* **Improving Speed Reconstruction.** The original analysis made agressive use of the speed reconstruction of the monopoles in order to improve the limits for slower speeds. Unfortunately, limitations in the simulation led to a poor result. However, as the model for the South Pole ice improves and more accurate reconstructions are preformed, this variable should become more robust.

* **Adding the effect of Delta Electrons.** Knock-off electrons from monopoles traveling at sub-relativistic speeds can still reach high enough energies to produce detectable cascades. Including these effects into the simulation could allow for searches down to the $\sim \beta = 0.52$ level.

* **Adding the stochastic cascades for ultra-relativistic monopoles.** By including the stochastic energy loss into the signal simulation through the detector, the light output of fast monopoles will increase dramatically, improving the sensitivity.

177

* **Increasing Livetime and Detector Volume.** Of course, the biggest improvement will come from being able to collect data from the full $\sim$ km^3 detector for several years.

This analysis is the first to be done with the IceCube detector. Relatively simple analysis parameters and conservative estimates for the light in the detector were necessary to ensure the robustness going forward. With each new analysis, improvements will be made to further increase the baseline sensitivity. Already, an analysis on the 40 string detector shows promise of increasing the sensitivity by a factor of $\sim$ 4 by utilizing a parameter to measure the total light yield in the detector[92]. With a starting point that is already the most competetive limits available for relativistic monopoles, the future is certainly bright for IceCube to play a vital role in the quest for these exotic particles. It might even find one before the Cubs win the world series[93].

Appendix A

Parameter Space

This appendix summarizes the validity range for the analysis of relativistic magnetic monopoles in the IceCube detector. Considerations from energy loss through the Earth are described in Section 2.7. Here, the effect of only simulating four discrete speeds and one mass are also considered. The result shows the final acceptance plots for all 21 $\cos\theta$ bins that were studied.

A.1 Constraints from Simulation

There are two major constraints to the parameter space that arise from the simplifications employed by the simulation.

The first constraint is that the boost factor of the monopole should be less than 1000 since only collisional energy losses are considered for the monopole traveling through the detector.

The second constraint is that the speed of the monopole should remain roughly constant as it travels through the detector. One reason for this constraint is that only one mass is simulated. Since the photon light yield in the calculation of the Cherenkov emission is velocity dependent, this number can change if different masses are used that respond differently to the $\approx 10^6\,\mathrm{GeV}$ collisional energy loss through the detector.

The second reason for this constraint stems from the fact that the tables used to propagate photons need to know the angle at which the Cherenkov light is emitted from the track. Due to the large resources required to generate these tables, only four speeds are produced and it is assumed the monopole stays within this speed for the duration of its trip through the detector.

A.1.1   Constant Mass

A way to measure how important the simplification of one mass is to the analysis is to calculate the effect that varying the speed will have on the total light yield. Using Equation 2.10, masses are checked starting at five speeds ($\beta = 0.76, 0.8, 0.9, \gamma = 10, 100$) to determine the lowest mass allowed that still produces the same amount of light within 1%. The energy loss is very conservatively approximated as 1.4×10^6 GeV, representing a track losing 12 GeV/cm and traveling 1.2 km through the ice. The results are summarized in Table A.1.

By the time $\gamma = 100$ is reached, all masses above the electroweak bound should not change enough to produce a drastic effect on the light yield. It should be noted that light yield is updated as the monopole travels through the detector, though the simulation of masses at 10^{11} GeV are large enough to not produce much of a difference.

Table A.1: Mass required to ensure a change in Photon Emission of less than 1%, assuming an energy loss of 1.4×10^6 GeV

Speed (β)	Speed for 1% Change	γ change	Lower Mass Bound (GeV)
0.76	0.7599785	5.94×10^{-5}	$2.4e \times 10^{10}$
0.8	0.79954	1.7×10^{-3}	8.5×10^8
0.9	0.89816	2.0×10^{-2}	7.3×10^7
0.995	0.99142	2.36	6.1×10^5
0.99995	0.99627	88.419	1.6×10^4

A.1.2   Cherenkov Angle

Figure A.1 shows how much the actual Cherenkov angle changes versus mass for the same five speeds as above. Table A.2 lists the lower mass bounds that are necessary to ensure that the relative change in the Cherenkov angle is less than 1%. All the lower bounds are below those of the photon yield condition studied in the previous section, and hence, are not considered further.

A.1.3   Summary

None of these constraints are considered in the final sensitivity/limit calculation, for several reasons. First, they are merely an indication of parameter space that was not simulated as part of the signal simulation, which does not mean that these events won't be seen. This is especially true of the $\gamma < 1000$ constraint since monopoles above this threshold would be even brighter and thus pass the cuts more
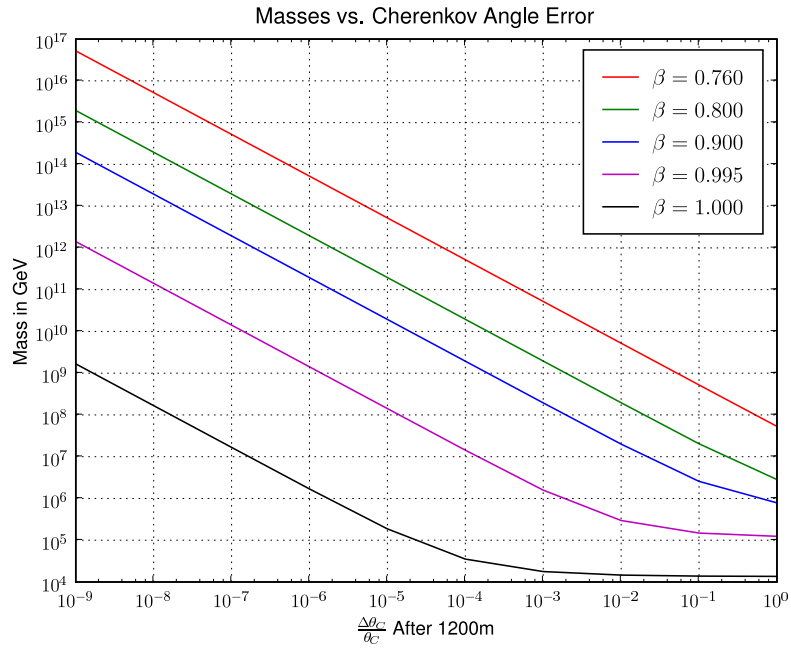
Figure A.1: Relative change of Cherenkov angle for various masses and speeds through 1200 m

Table A.2: Mass required to ensure a change in Cherenkov angle of less than 1%.

Speed (β)	Lower Mass Bound (GeV)
0.76	5.2×10^9
0.8	2.0×10^8
0.9	2.0×10^7
0.995	3.0×10^5
0.99995	1.5×10^4

efficiently than those simulated. The one case where this could lead to an optimistic limit is if the energy loss from stochastics are so large that the monopole essentially stops within the detector, thus missing late hits that a non-stochastic monopole would produce. However for masses above $10^4\,\mathrm{GeV}$, this does not occur. Once the monopole falls below $\gamma = 1000$, the collisional loss is dominant and, for ice, is $\sim 12\,\mathrm{GeV/cm}$. A $10^4\,\mathrm{GeV}$ with total energy of $10^7\,\mathrm{GeV}$ will still make it through the detector relativistically. Therefore, any monopole considered in the entire parameter space in which stochastic losses might play a role will not stop in the detector itself.

For the speed constraint, monopoles traveling relativistically through the detector but light enough for the light yield or Cherenkov angle to change significantly will still likely deposit enough light to survive cuts. With the exception of the $\beta = 0.76$ speed, which is not included in the final results, the mass limits are largely restricted to populations that cannot travel through the Earth, which are a very small portion of the final result (see 11.2). This can be verified numerically by considering F.2. For all values where a competitive limit is set (e.g., below $10^{-16}\,cm^{-2}sr^{-1}s^{-1}$), the mass is well above the lower bound for its particular boost factor.

The goal in this study was merely to confirm that the region is not so large as to be a potential issue.

A.2   Plots for all Angular Bins

Plots of acceptance for initial mass and energy values of a magnetic monopole striking the Earth's surface at various angles. $\cos \theta = -1.0$ corresponds to straight up-going.

The dotted black line represents the divide where the monopoles are traveling faster than $\gamma = 100$, a very conservative estimate of where light from stochastics might start to make a difference, hence the final limits will be conservative above this threshold. The solid black lines represent the mass cutoff for the speed constraints. As mentioned above, these only become apparent for the down-going cases.
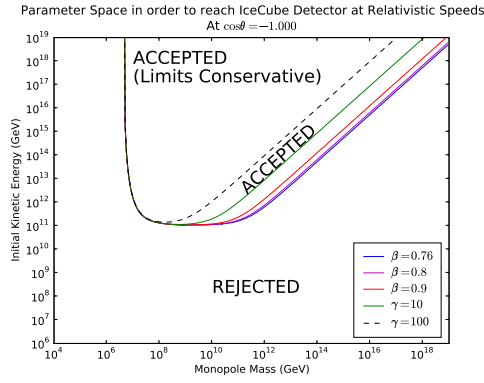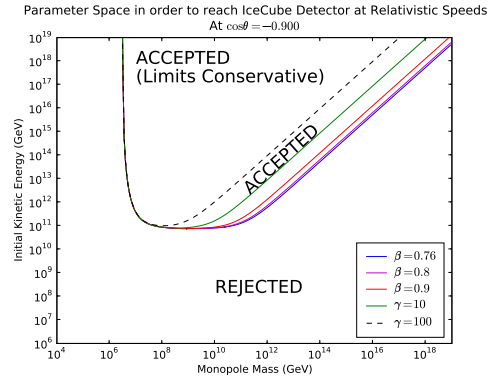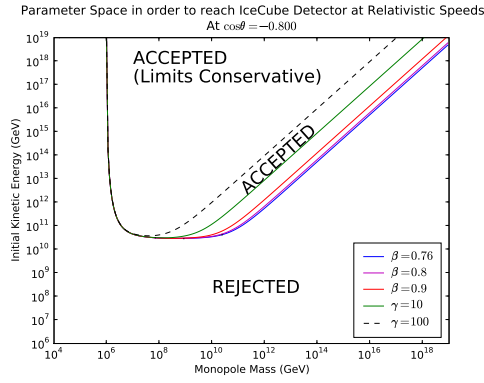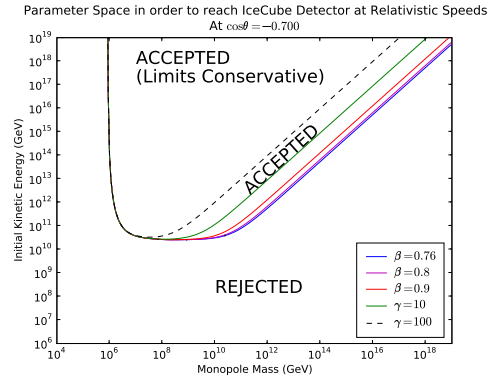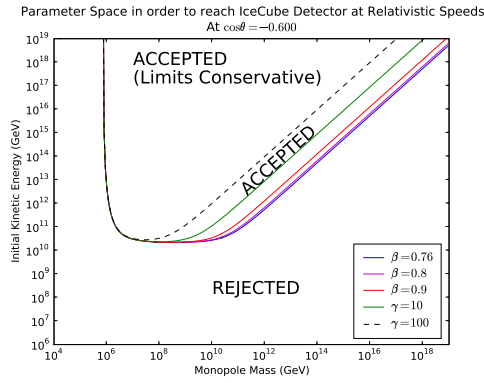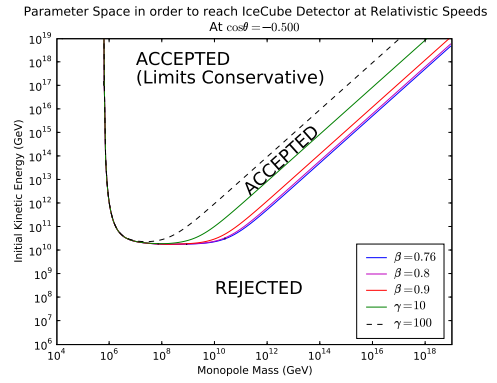
Figure A.2: Parameter Space plots for $\cos\theta$ from -1.0 to -0.5
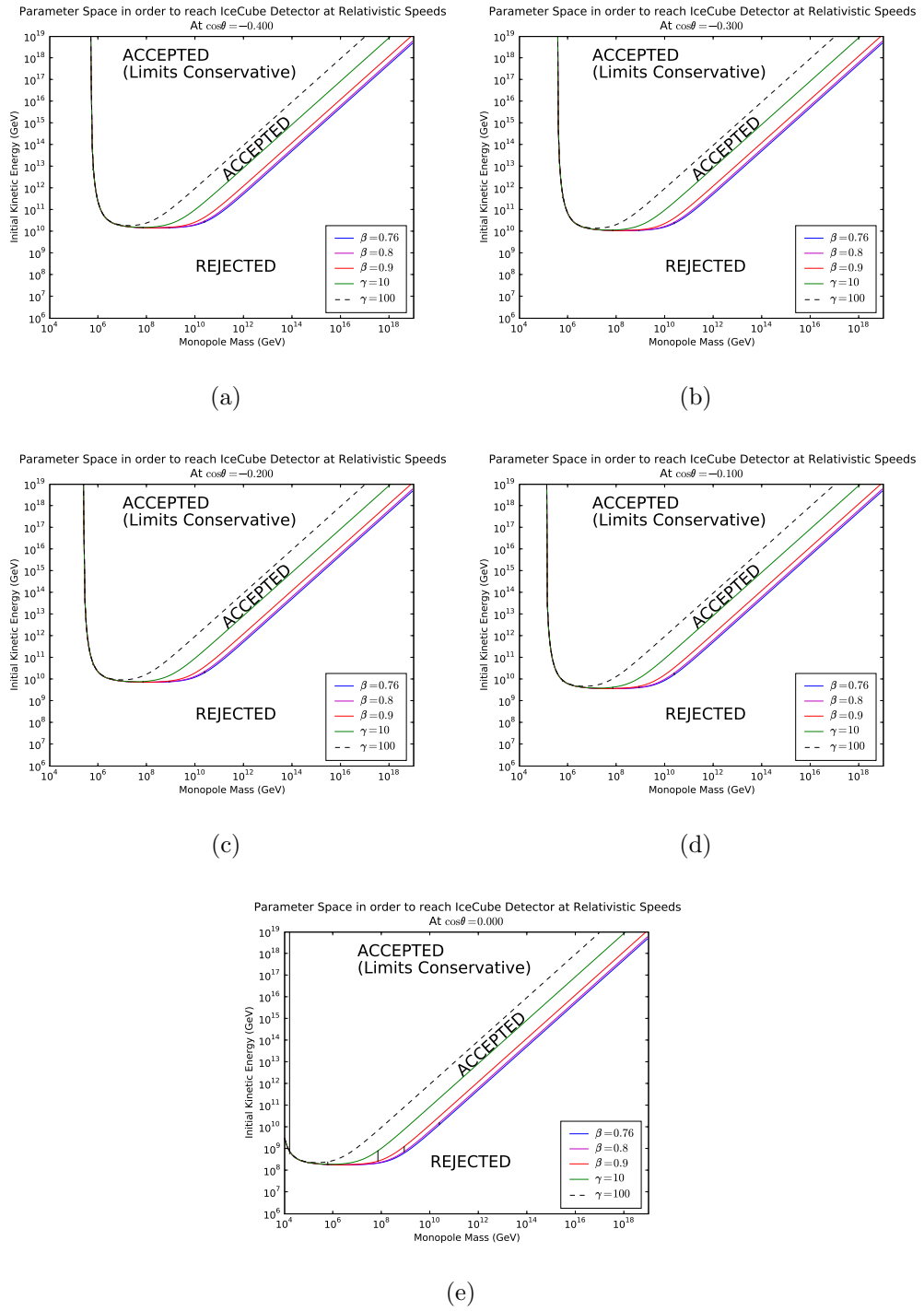
Figure A.3: Parameter Space plots for $\cos\theta$ from -0.4 to 0.0
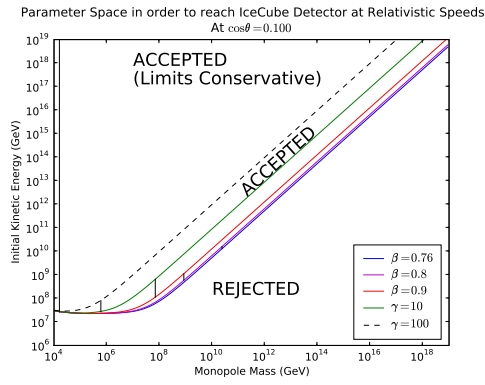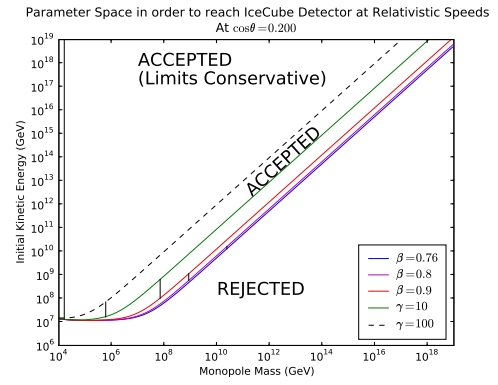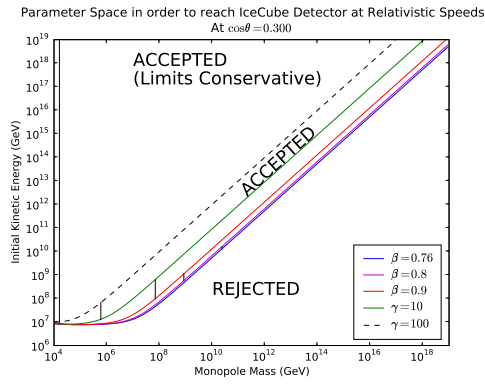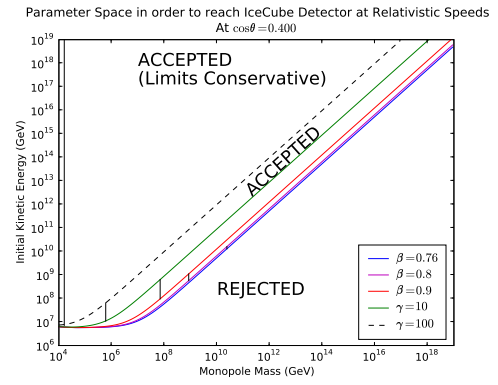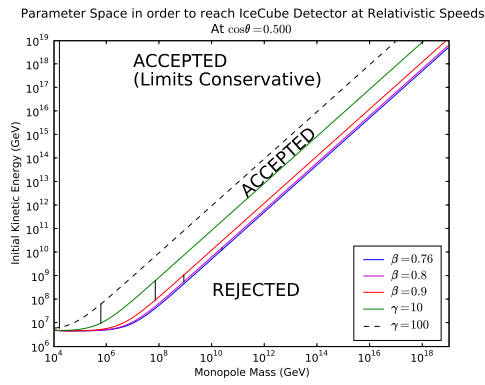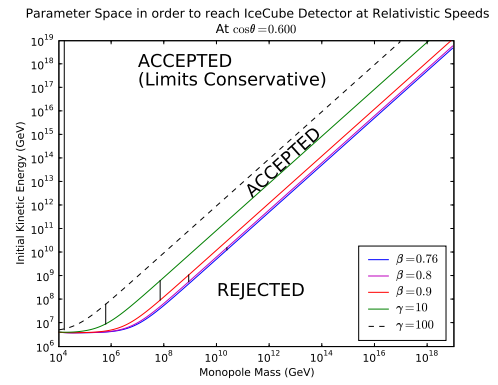
Figure A.4: Parameter Space plots for $\cos\theta$ from 0.1 to 0.6
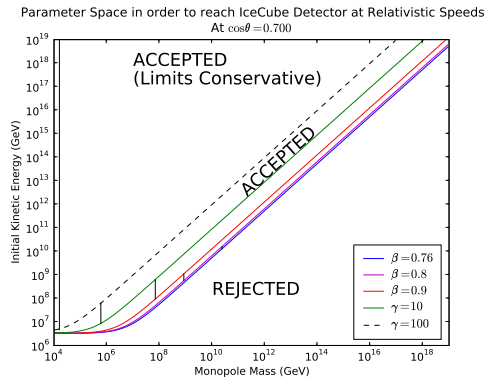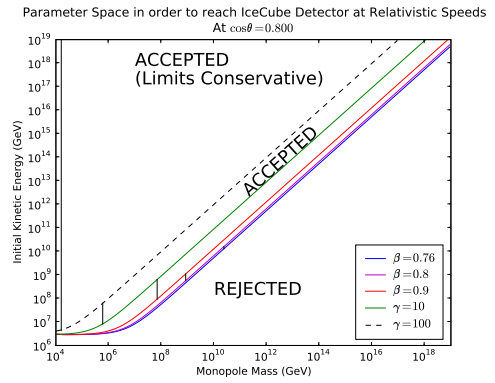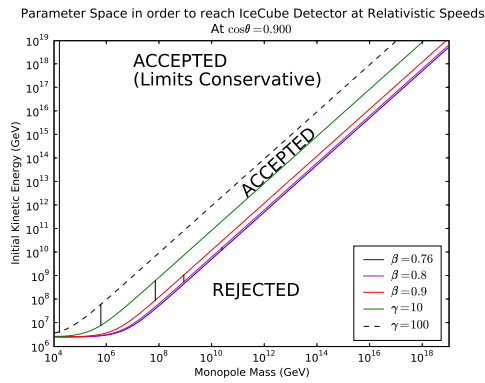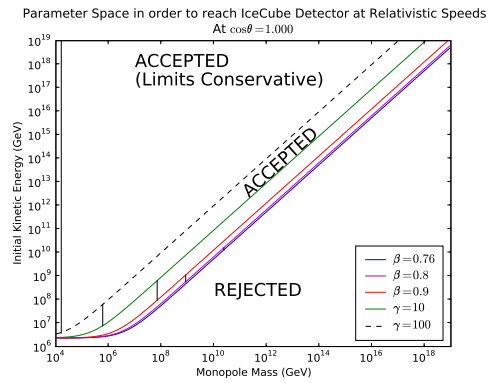
Figure A.5: Parameter Space plots for $\cos\theta$ from 0.7 to 1.0

Appendix B

Estimation of Expected Coincident Rate at the Final Level

Coincident muons present a very dangerous background to this analysis. They are not simulated, and can easily produce up-going tracks that are subject to cuts much looser than those for the down-going cases. However, it is important to remember that only coincident events in which *each one saturates a DOM* are important, since saturated hits are the only thing considered for the reconstruction.

This appendix describes the method used to estimate the rate of these events from data.

B.1   Single Saturated Hit Rate

The first step is to see how often an event will saturate at least N DOMs. Unfortunately, the data considered already passes the EHE filter, i.e. events that launch at least 80 DOMs. To deal with this, the event rate is histogrammed based on the number of DOM launches and a fit is used to extrapolate the rate down to lower values. The final result is a fit function which tells the rate for saturating at least N DOMs as a function of total DOM launches.

Two fit functions considered are considered: a Gaussian and an exponential. For all but the two lowest cases (one or two saturated hits), the Gaussian produced a better χ^2. This is expected, since the likelihood to saturate several hits should
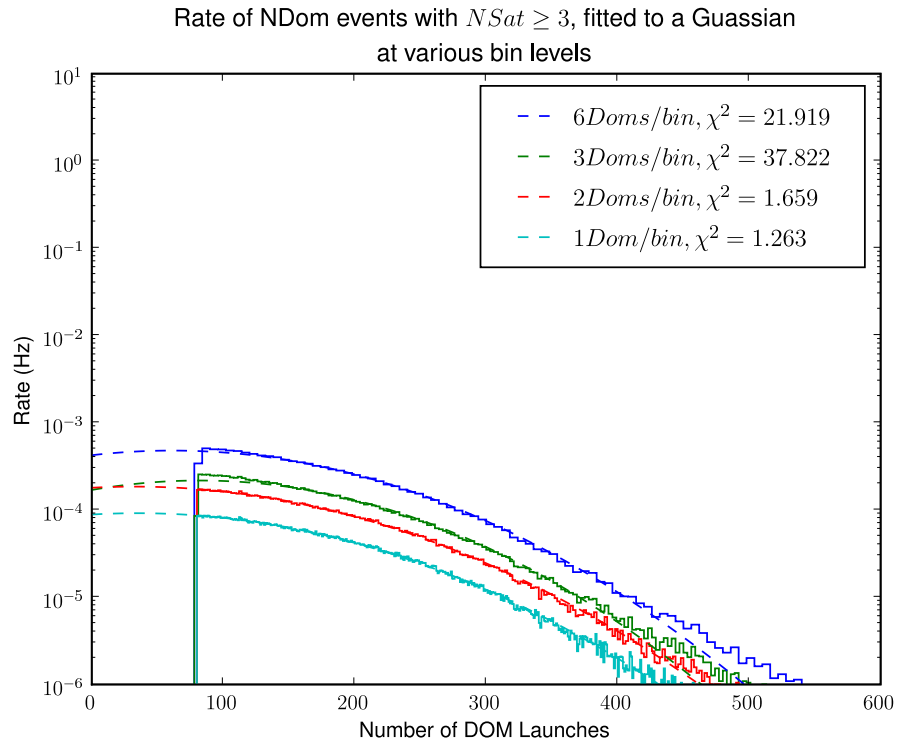
Figure B.1: Example of a fit performed on the expected rate of events that saturate at least 3 DOM's as a function of total number of DOM Launches. The cut-off at 80 is caused by only looking at the EHE filter. Four binning values are checked.

Table B.1: Values of the Exponential Fit Function for the rate of saturating at least one or two DOM's as a function of NDOM. Fits are given in the form of:

$$Rate(NDom) = \frac{C_0}{NDOM/bin} \times \exp{-(NDOM \times C_1)}$$

$NSAT \geq$	C_0	C_1	$\int_0^\infty (dNDOM) Rate$
1	0.01784	0.02427	0.735
2	0.00181	0.01597	0.113338

decrease as the number of total launches goes down to zero, while for the one or two saturated hits, the mean of the Gaussian is well below zero. Several different binning values were considered, but in all cases binning as 1 NDOM/bin produced the best χ^2. Figure B.1 shows an example of the distribution for the $NSAT \geq 3$ case. Tables B.1 and B.2 display all the fit values for events saturating at least N DOMs up to $NSAT \geq 9$, as well as the total integrated rate.

B.2   Estimating Coincident Rate

Detection of muons follows a Poisson process: $P(k, \lambda) = \frac{\lambda^k e^{-\lambda}}{k!}$, where P is the probability of detecting k events within some time window and λ is the expectation. Since the time window will begin with one event, the probability measures how many *other* events will occur within the time window. Thus, for single events, the probability becomes $f(0, \lambda) = e^{-\lambda}$ and coincident events will becme $f(1, \lambda) = \lambda e^{-\lambda}$. If λ is sufficiently small, triple coincident and above events can be ignored and the two probabilities can be approximated as:

Table B.2: Values of a Gaussian Fit Function for the rate of saturating at least N DOM's as a function of NDOM. Fits are given in the form of: $Rate(NDom) = \frac{C_0}{NDOM/bin} \times \exp \frac{(NDOM-C_1)^2}{2C_2^2}$

$NSAT \geq$	C_0	C_1	C_2	$\int_0^\infty (dNDOM)Rate$
1	5.632×10^4	-1381.781	251.218	9.19×10^{-8}
2	1.766×10^{-2}	-483.009	208.331	3.40×10^{-3}
3	9.179×10^{-5}	34.926	131.87	1.39×10^{-2}
4	2.411×10^{-5}	149.249	110.059	4.57×10^{-3}
5	1.153×10^{-5}	198.265	102.833	2.09×10^{-3}
6	6.737×10^{-6}	228.216	100.146	1.20×10^{-3}
7	4.306×10^{-6}	251.057	98.567	7.52×10^{-4}
8	2.899×10^{-6}	270.251	97.105	4.99×10^{-4}

$$f(0, \lambda) = e^{-\lambda} \approx (1 - \lambda)$$

$$f(1, \lambda) = \lambda e^{-\lambda} \approx (\lambda) \tag{B.1}$$

For a time window of Δt and event rate of R, $\lambda = \Delta t R$ thus the rate for coincident events will be $R_{single} \times P(1, \lambda) \approx R_{single} R_{double} \Delta t$.

Note that a distinction must be made between the rate for the event that starts the time window (R_{single}) and the one that adds the coincident event, since they may have different values.

B.3 Estimating Final Rate: Low Level

Since both the original and a posteriori analyses are the same through level 2, the rate can be estimated in the same way.

For the first level filter, the criterion is to have at least 80 DOMs that launch and at least two saturated hits. This can be accomplished by coincident events which total 80 DOM launches and each have at least one saturated hit (the lowest case considered). $R_{single} R_{double}$ of two events to reach a total of 80 DOM launches is:

$$\sum_{X=0}^{80} (C_0^1 e^{-X*C_1^1})(C_0^2 e^{-(80-X)*C_1^2}) \Delta t \tag{B.2}$$

For this case, $C^1 = C^2$ since both are the values for producing one saturated hit. Therefore, the rate is estimated as:

$$Rate \approx R_{single}(NDOM) \times R_{double}(NDOM) \times \Delta t$$

$$\approx \sum_{N=80}^{\infty}(C_0)^2 * \sum_{X=0}^{N} e^{-N*C_1}\Delta t$$

$$\approx \sum_{N=80}^{\infty}(C_0)^2 * N * e^{-N*C_1}\Delta t \qquad \text{(B.3)}$$

$$\approx \int_{N=80}^{\infty} dN(C_0)^2 * N * e^{-N*C_1}\Delta t$$

$$\approx \frac{(C_0)^2}{C_1} * (80e^{-80C_1} + (1/C_1)e^{-80C_1}\Delta t$$

For the time interval, a conservative choice of 80 μs is used to reflect the AMANDA software trigger implemented at the pole (see Section 4.4). Using the numbers from Table B.1, the rate squared term is 0.2246 Hz^2. This produces an expected coincident rate of 1.8×10^{-5} Hz, or ~ 360 events in the full data set. As a cross-check, the burn sample data is looked at to count the number of up-going coincident events, which can easily be picked out, and assuming all reconstructed directions are equally likely, this suggests a total in the burn sample of 47 events, which compares favorably to the ~ 36 this estimate predicts.

The hit cleaning at level two does not directly affect these types of coincident events, and thus should not change the estimate at all.

For level 3, the main cut that affects the coincident rate is from the LFSPEED cut that is the same for both analyses. It reduces the potential time window for the coincident events drastically since the linefit connecting the two events has a slower speed the further apart in time the two occur. A very conservative estimate of the effect is to consider the extreme case of two events lighting up DOMs on the opposite corners of the detector. In this case, the distance is ~ 1200 m. To have a speed above 0.2 m/ns, this requires the events to occur within $\sim 6\,\mu$s of each

other. Thus, the estimate reduces to 1.35×10^{-6} Hz, or about 3 in the burn sample. Counting from the actual burn sample suggests the true rate is about 5.

B.4 Estimating Final Rate: Original Analysis

For all but the slowest speed bin, the major affect of the final cut is to increase the threshold of saturated hits. The most conservative estimate is to require at least five (baseline value for $\beta = 0.9$ monopoles). To further simplify the calculation, the assumption is made that any combination of events that saturate at least five hits will also have at least 80 DOM launches. Therefore, one only needs to consider the overall rate, given as the last column in Tables B.1 and B.2. The rate estimate is found as:

$$Rate \approx (\Delta t)*$$

$$2 * (R(NSAT \geq 1) * R(NSAT \geq 4) + R(NSAT \geq 2) * R(NSAT \geq 3))$$

$$\approx 6\mu s * 2 * ((0.735) * (4.57 \times 10^{-3}) + (0.1134) * (0.0139))$$

$$\approx 5.9 \times 10^{-8} \, \text{Hz}$$

(B.4)

This produces about 1 event in the full year data with very conservative assumptions. There were no observed events, consistent with this conclusion.

For the slowest speed bin, the minimum saturated number of events remains 2, but the time window is significantly shortened in order to produce a speed between 0.2 to 0.234 m/ns. Therefore time between the two saturated hits must be, as a function of distance, between d/0.234 and d/0.2, yielding a time interval of d*(1/.2-1/.234). For the largest d possible (1200m), this becomes ~ 875 ns, i.e., the hits would have to happen between 5.128us and 6us apart. Using the

195

same rate squared as the level 1 estimate, this produces an expected rate of $R \sim 0.2246\,\mathrm{Hz}^2 \times 8.75 \times 10^{-7}\,\mathrm{s} \sim 2 \times 10^{-7}\,\mathrm{Hz}$. This suggests an expected 4 events in the total sample, consistent with the 3 observed.

B.5   Estimating the Final Rate: A posteriori analysis

The estimate here is essentially the same as that for the fast speed bins, except that the minimum number of saturated hits becomes eight. Thus, the approximate rate becomes:

$$Rate \approx (\Delta t)*$$

$$(2*(R(NSAT \geq 1)*R(NSAT \geq 7))$$

$$+2*(R(NSAT \geq 2)*R(NSAT \geq 6))$$

$$+2*(R(NSAT \geq 3)*R(NSAT \geq 5))$$

$$+R(NSAT \geq 4)^2) \tag{B.5}$$

$$\approx 6\mu s*$$

$$(2*(0.735)*(7.52 \times 10^{-4}) + 2*(0.1134)*(0.0012)$$

$$+2*(0.00139)*(0.00209) + (4.57 \times 10^{-3})^2)$$

$$\approx 8 \times 10^{-9}\,Hz$$

This produces less than 0.2 events for the full year. Again, this is utilizing a fairly conservative estimate since not all the events being counted will:

* Combine to launch 80 DOMs.

* Reconstruct with a linefit speed above 0.2, since a typical coincident event will have hits closer than 1200 m.

Moreover, for the original analysis case, the final estimate was above the observed value. The under-estimates from earlier levels are likely due to a poor modeling of the single saturated hit case or counting how many events will launch 80 DOMs, but this is completely removed for the final analysis. Thus, the assumption of no coincident events is robust.

Appendix C

Original Analysis Final Cut Data Events

Table C.1: Properties of the 12 data events that pass the final cut selection for the Original Analysis

Run ID	Event ID	NSAT(Cleaned)	$\cos\theta$	LFSPEED/c(β)	TRANGE (ns)
108869	2560659	97(89)	0.9103	0.942	3631
109325	12796685	3(3)	-0.827	0.778	2839
109456	3837803	2(2)	-0.821	0.693	4796
109498	13717945	15(14)	0.643	0.820	1366
109504	6223806	18(18)	0.796	0.832	1674
109507	3130762	11(11)	0.340	0.846	2103
109748	7628410	13(13)	0.618	0.822	1101
109755	988134	15(15)	0.700	0.813	1142
109858	3273025	15(15)	0.581	0.825	731
109908	9578727	63(51)	0.855	0.835	2360
109987	8702286	9(9)	0.228	0.840	608
110522	5328671	5(5)	0.901	0.751	2607

Zenith 0.426766
Azimuth 1.35979

Run 108869   Event 2560659
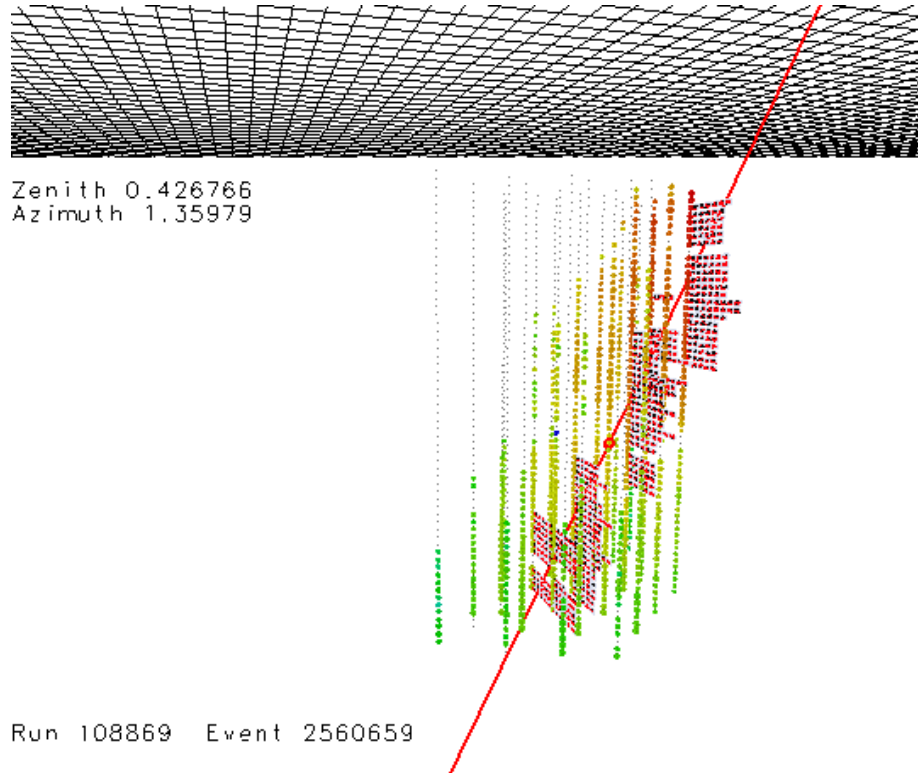
Figure C.1: Event Display of the event within the $0.85 < \beta \le 0.95$ speed bin. This event is the brightest event of the entire year. DOM's with the FADC saturated are marked by additional waveform information. The red line represents the reconstructed track.

Zenith 0.871871
Azimuth 4.59992

Run 109498 Event 13717945

(a)

Zenith 0.813695
Azimuth 1.5073

Run 109504 Event 6223806

(b)

Zenith 1.22409
Azimuth 5.37336

Run 109507 Event 3130762

(c)

Zenith 0.904725
Azimuth 2.62941

Run 109748 Event 7628410

(d)
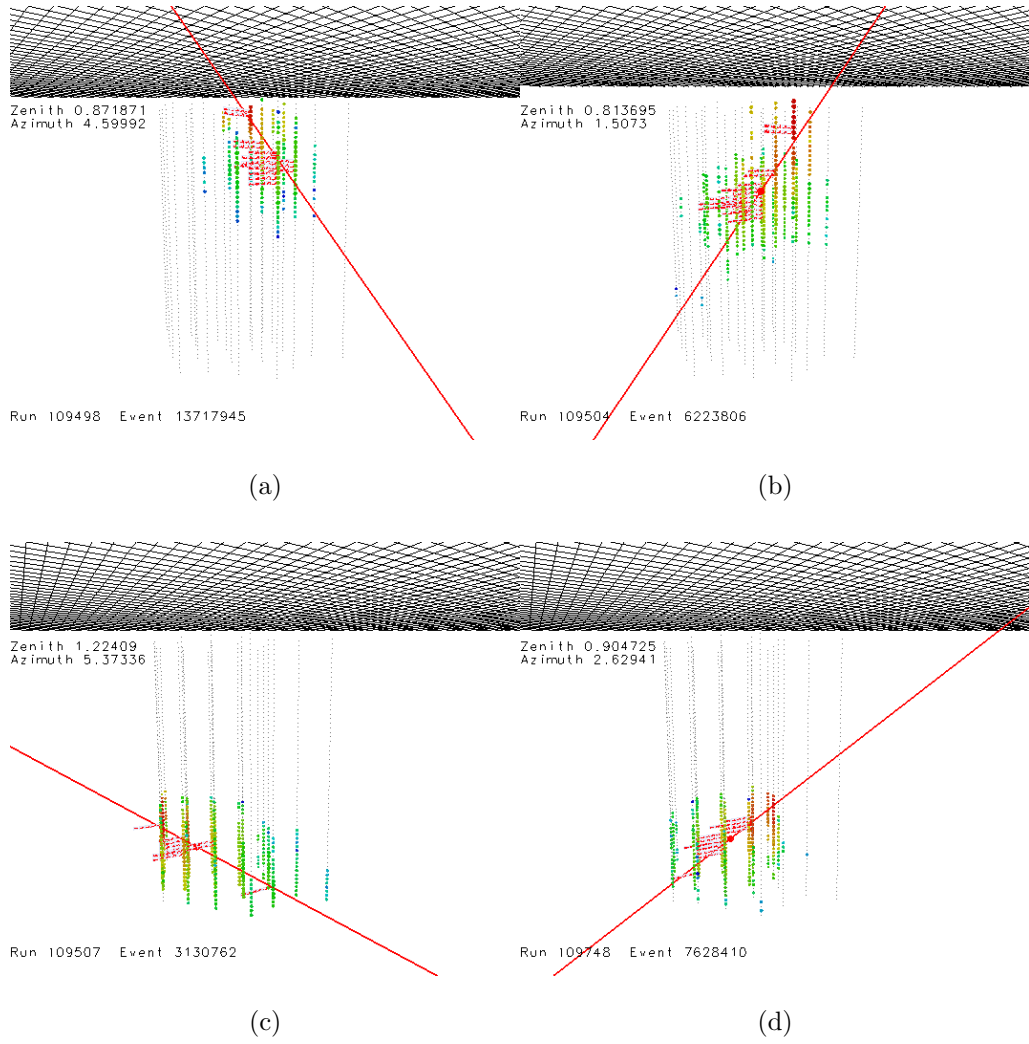
Figure C.2: Event Displays of the events within the $0.78 < \beta \leq 0.85$ speed bin.

(a)

(b)

(c)

(d)
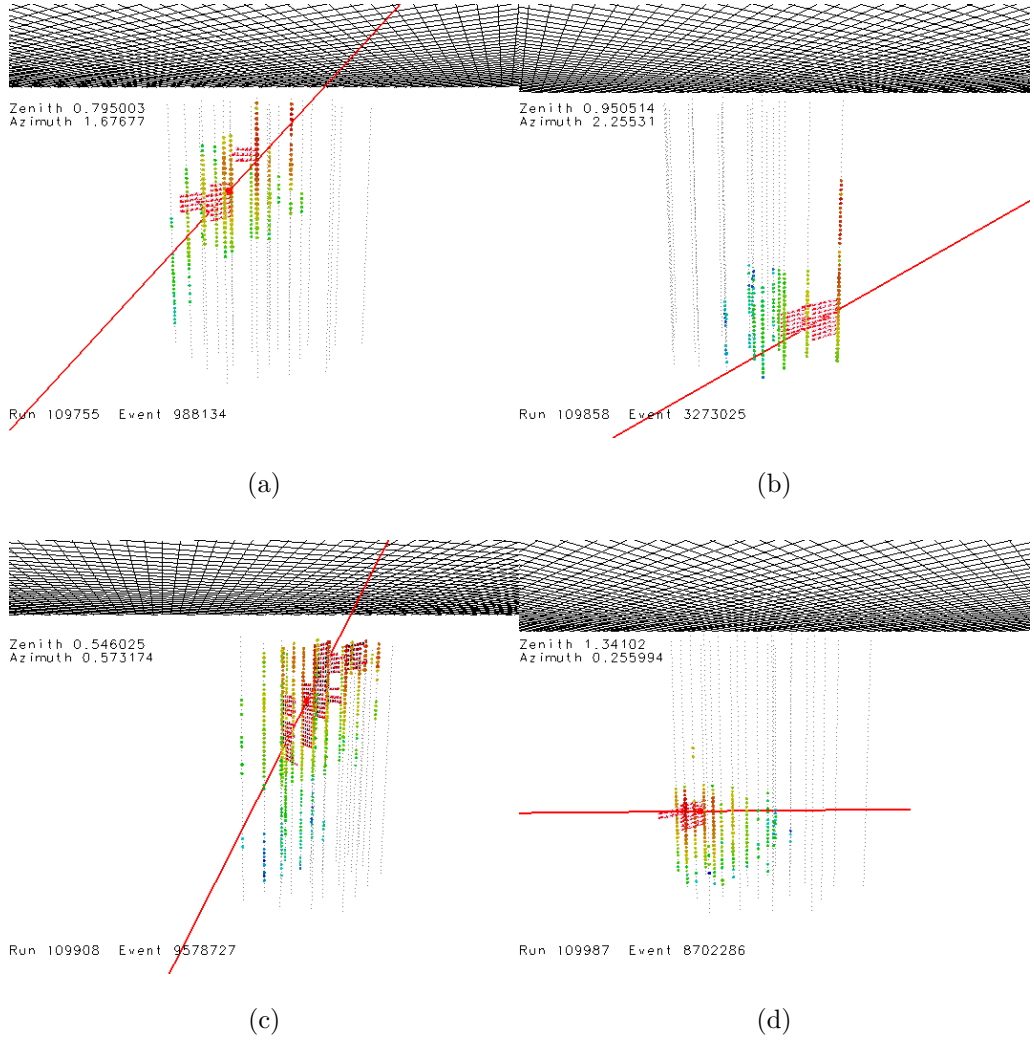
Figure C.3: Event Displays of the events within the $0.78 < \beta \leq 0.85$ speed bin.
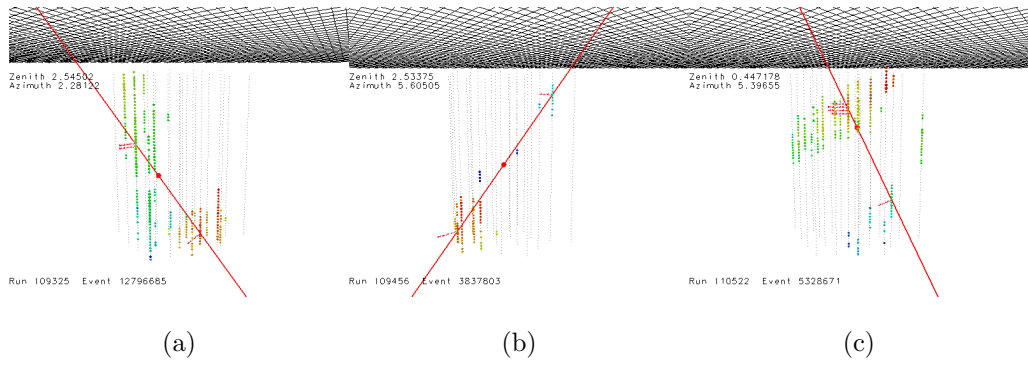
Figure C.4: Event Displays of the three events within the $\beta \leq 0.78$ speed bin. All three are obvious coincident events.

Appendix D

On the Question of Blindness

It has become accepted practice in the particle physics community to attempt 'blind' analyses. The goal of such analyses is to minimize or eliminate an experimenter's bias in developing the analysis. As outlined in a review article, Klein and Roodman summarize three types of experimental bias[94]:

* **Statistical Bias** This case arises when the sensitivity of the experiment may be relatively flat over a range of cut values. If knowledge of the result is known ahead of time, the cut can be chosen to maximize the sensitivity based on statistical fluctuations. The idea is that over many experiments, if all are chosen in this way, the significance of the result will begin to differ from the statistical uncertainty.

* **Small Signal Bias** Searches for a small signal at the edge of detectability are highly dependent on the exact value of the cut. If each event is examined individually, cuts can generally be constructed that either eliminate or allow more events into the signal region.

* **Stopping Bias** Perhaps the hardest to control (even impossible) is the tendency to continue working on an analysis until results are consistent with preconceived ideas of what it should be, then stopping.

The dangers of these biases result in one of two types of errors. Either the background is eliminated from the signal region above what should be expected and the upper limit represents a result that is too good (Type II error), or background is allowed into the signal region and a false discovery is claimed (Type I error). In the case of searching for new particles, Type I error is by far the more severe and, in case of doubt, effort should be made to avoid this over the Type II kind.

A common way of eliminating this bias is to develop the complete analysis based solely on simulation and not looking at the final data sample. Of course, simulation is not perfect and so a small subset of the data is taken to verify accuracy. This is the way the first analysis was performed. In revising the analysis in an a posteriori way, a strong effort is made to retain as much of the positive effects of a blind analysis as possible by basing all new cuts solely on simulation and not considering the full data sample. However, it is certainly true that the decision to not claim discovery, remove speed binning, and perform an a posteriori analysis at all is subject to scrutiny for experimenter bias. The following sections discuss each of the three cases in turn.

D.1   Statistical Bias

The most direct application of this bias is present in the choice of the quality cuts determined at Level 3. The goal is to eliminate poorly reconstructed background and as the passing rate plots demonstrate (Figures 7.7, 7.9, 7.12) the final cut is generally over a plateau in the background passing rate. The goal to remain

unbiased motivated the choice of cuts to lie roughly in the center of these plateaus. This is especially true in the revised Level 3, when the new cut of 750 ns is placed well beyond the 600 ns value for the one event that skews the total passing rate.

When considering the final cut, it is important to include an often overlooked fact: simulation datasets are not infinite. While they do provide more effective livetime than the real dataset, the final cuts might still depend on a small number of events. This is the case for the $0.78 < \beta \leq 0.85$ and $\beta \leq 0.78$ region cuts. The final cut plane contained only a handful of events. The decision to strengthen the cut beyond what minimized the MRF represents an attempt to reduce this effect and move 'beyond the choppy shallow waters', i.e. into a region where the danger of the cut producing a better upper limit than should be expected is reduced. The final result for the $0.78 < \beta \leq 0.85$ bin illustrates that the strengthening of the cut was not enough. For the a posteriori analysis, the statistics in the simulated background sample, which motivates the final cut, is sufficiently large to reduce this effect below the systematic uncertainty.

D.2   Small Signal Bias

This analysis is an obvious case of where this bias becomes important. Indeed, the process of going through the original 12 data events and finding new variables to demonstrate they are not signal is a perfect example of how a separate cut may have been developed to eliminate any suspicious event. This in part motivated the decision to not use these new variables for the a posteriori analysis.

205

The result, however, should not be affected greatly. Certainly, this is not a case where a false signal is detected. As for deriving a better upper limit than expected, the role of choosing the cut based on simulation should minimize this bias.

Moreover, several checks of the robustness of the analysis to changes in the cuts were performed, as detailed in Appendix E. In all permutations, the sensitivity that results by optimizing the final cut remained stable and largely within the systematic uncertainties. It is worth noting that no data event passed any of the varied optimized final cut values.

A second comparison is to see how the final rates change with variations while keeping the same final cut value, i.e., not re-running the optimization to find a new final cut. Here again, all the final sensitivities remain stable with the exception of cases when the TRANGE cut at Level 3 is at or below 600 ns and the one `SPICE` event described in Section 9.1.3 survives the final cut.

A final argument can be made from considering the data itself. The extreme case of this bias is to choose the cut as loose as possible while still eliminating all the data. This results in a baseline of 3 and slope of 110, much more loose than the final cut with baseline 7 and slope 150. This would have improved the final result for fast monopoles $\sim 10\%$ and above 90% for the $\beta = 0.76$ case.

D.3   Stopping Bias

The original result of the analysis did not meet expectation, hence more work went into understanding and improving it. After the a posteriori analysis, the

answer agreed with expectation and work stopped. A blind analysis attempts to avoid stopping bias by making the stop condition occur before the final result is considered. The problem, of course, is that no analysis is ever perfect. Had this rule of blind analysis been followed exactly, the results of this analysis would have produced a Type I error of falsely claiming discovery.

As Bob Cousins once said[95],

What do you do if you open the box and despite of all your due diligence, you see that you've been stupid and there is an obvious background that you did not anticipate?...we came up with the criterion that it is OK to throw away an event after you open the box, if you would look foolish by not throwing it away.

Appendix E

Robustness Studies for the A Posteriori Analysis

The following appendix describes the various checks to ensure the robustness of the final analysis result. They can be divided into three types. (1) Variation of the physics parameters to see what effect this has on the final cut, (2) Changes to the analysis design, e.g. the cut selection, and (3) Changes to the simulated datasets used.

Note that in all the results, the calculation of the average upper limit and sensitivity neglect systematic uncertainties. Hence, the numbers should be compared to those of Table 9.3.

E.1   Variation of Physics Parameters

One of the fundamental strengths of the analysis is that it depends only on three physical values: the time of the hit, the position of the hit, and whether or not the FADC reaches the saturated value (threshold of the hit). The position of the DOMs is fairly well measured, so the following will only consider variations to the time and threshold of the hit.

E.1.1 Threshold

Using the saturation limits the ability to test variations in this value to only those with a lower threshold. Datasets were generated with lower thresholds used for the hit definition of 999 and 900 (compared to 1022). Table E.1 summarizes the results.

E.1.2 Timing

To study how important the timing is on the final answer, datasets were generated where each hit time is smeared by a Gaussian with σ ranging from 5 to 25 ns in increments of 5. Note that the 20 ns dataseet is the same one discussed in Section 8.2. Table E.1 summarizes the resultss.

Table E.1: Results of performing the analysis with variations on both the FADC threshold and the hit times. FADC threshold is lowered to 999 and 900, while hit times are smeared by a Gaussian with σ given in ns. All variations are applied to both signal and background datasets.

	Final Cut				Final Sensitivity in $cm^{-2}sr^{-1}s^{-1}$			
Variation	Base	Slope	Bkgrd	μ_{AVG}	$\gamma = 10$	$\beta = 0.9$	$\beta = 0.8$	$\beta = 0.76$
Threshold								
1022	7	150	0.124	2.54924	3.581×10^{-18}	3.812×10^{-18}	5.779×10^{-18}	3.309×10^{-15}
999	7	150	0.126	2.55212	3.561×10^{-18}	3.792×10^{-18}	5.696×10^{-18}	2.910×10^{-15}
900	7	155	0.168	2.58842	3.523×10^{-18}	3.748×10^{-18}	5.374×10^{-18}	2.102×10^{-15}
Time Smear								
5 ns	7	150	0.124	2.5478	3.578×10^{-18}	3.808×10^{-18}	5.775×10^{-18}	3.292×10^{-15}
10 ns	6	135	0.190	2.60584	3.569×10^{-18}	3.805×10^{-18}	5.532×10^{-18}	1.968×10^{-15}
15 ns	6	135	0.190	2.60680	3.572×10^{-18}	3.803×10^{-18}	5.532×10^{-18}	1.974×10^{-15}
20 ns	6	135	0.192	2.60858	3.575×10^{-18}	3.809×10^{-18}	5.527×10^{-18}	1.970×10^{-15}
25 ns	7	150	0.124	2.54929	3.564×10^{-18}	3.804×10^{-18}	5.773×10^{-18}	3.294×10^{-15}

E.2   Variation of Cuts

Level 1 and 2 are essentially loose forms of the final level. The robustness of this cut to change can be demonstrated by considering the plot of the model rejection factor (see Figures 9.7). Furthermore, the LFSPEED and angle difference cuts of Level 3 all have very small affects on the background and signal rates. Hence, the focus of this study will be on the TRANGE cut. Note, this is also important since it represents one of the changes made between the original and a posteriori analyses. Table E.2 summarizes the results.

Table E.2: Results of performing the analysis with variations on the TRANGE cut at level 3.

| TRANGE Cut (ns) | Final Cut | | | | Final Sensitivity in $cm^{-2}sr^{-1}s^{-1}$ | | | |
	Base	Slope	Bkgrd	μ_{AVG}	$\gamma = 10$	$\beta = 0.9$	$\beta = 0.8$	$\beta = 0.76$
500 (original)	8	130	0.158	2.58354	3.342×10^{-18}	3.646×10^{-18}	6.121×10^{-18}	3.719×10^{-15}
550	8	130	0.150	2.57464	3.376×10^{-18}	3.667×10^{-18}	6.129×10^{-18}	3.706×10^{-15}
600	8	130	0.143	2.57403	3.429×10^{-18}	3.714×10^{-18}	6.168×10^{-18}	4.024×10^{-15}
650	7	130	0.181	2.60098	3.477×10^{-18}	3.738×10^{-18}	5.674×10^{-18}	2.876×10^{-15}
700	6	135	0.200	2.61820	3.534×10^{-18}	3.774×10^{-18}	5.451×10^{-18}	1.908×10^{-15}
750 (A Posteriori)	7	150	0.124	2.54924	3.581×10^{-18}	3.812×10^{-18}	5.779×10^{-18}	3.309×10^{-15}
800	7	135	0.153	2.57598	3.643×10^{-18}	3.868×10^{-18}	5.897×10^{-18}	3.452×10^{-15}
850	6	135	0.162	2.59264	3.706×10^{-18}	3.903×10^{-18}	5.680×10^{-18}	2.054×10^{-15}
900	6	135	0.154	2.58030	3.783×10^{-18}	3.972×10^{-18}	5.736×10^{-18}	2.090×10^{-15}
950	6	135	0.150	2.57286	3.871×10^{-18}	4.061×10^{-18}	5.828×10^{-18}	2.107×10^{-15}
1000	6	150	0.105	2.53232	3.968×10^{-18}	4.163×10^{-18}	5.909×10^{-18}	2.092×10^{-15}

E.3   Variation of Simulated Datasets

As described in detail in both Chapter 5 and Chapter 9, there were several options for the background datasets used in the final optimized cut. All permutations of ice models, as well as whether to include the prompt component of the atmospheric neutrino background, are studied to see the effect on the final result. The results are summarized in Table E.3.

Table E.3: Results of performing the analysis with different simulated datasets.

| Ice Model | | | Final Cut | | | | Final Sensitivity in $cm^{-2}sr^{-1}s^{-1}$ | | | |
CORSIKA	NUGEN	ν Prompt	Base	Slope	Bkgrd	μ_{AVG}	$\gamma = 10$	$\beta = 0.9$	$\beta = 0.8$	$\beta = 0.76$
SPICE	SPICE 1	Yes	7	150	0.124	2.54924	3.581×10^{-18}	3.812×10^{-18}	5.779×10^{-18}	3.309×10^{-15}
SPICE	SPICE 1	No	7	135	0.113	2.53926	3.525×10^{-18}	3.763×10^{-18}	5.737×10^{-18}	3.296×10^{-15}
SPICE	AHA	Yes	8	130	0.145	2.57310	3.602×10^{-18}	3.867×10^{-18}	6.352×10^{-18}	5.232×10^{-15}
SPICE	AHA	No	6	135	0.157	2.58186	3.542×10^{-18}	3.771×10^{-18}	5.482×10^{-18}	1.960×10^{-15}
SPICE 1	SPICE 1	Yes	7	140	0.127	2.55285	3.557×10^{-18}	3.793×10^{-18}	5.773×10^{-18}	3.314×10^{-15}
SPICE 1	SPICE 1	No	7	135	0.112	2.53917	3.504×10^{-18}	3.723×10^{-18}	5.402×10^{-18}	1.928×10^{-15}
SPICE 1	AHA	Yes	8	140	0.115	2.54436	3.591×10^{-18}	3.851×10^{-18}	6.294×10^{-18}	5.174×10^{-15}
SPICE 1	AHA	No	6	140	0.132	2.56456	3.539×10^{-18}	3.760×10^{-18}	5.456×10^{-18}	1.947×10^{-15}
AHA	SPICE 1	Yes	7	135	0.102	2.53268	3.516×10^{-18}	3.753×10^{-18}	5.722×10^{-18}	3.288×10^{-15}
AHA	SPICE 1	No	6	120	0.134	2.56375	3.460×10^{-18}	3.705×10^{-18}	5.419×10^{-18}	1.946×10^{-15}
AHA	AHA	Yes	8	115	0.144	2.56749	3.537×10^{-18}	3.822×10^{-18}	6.313×10^{-18}	5.221×10^{-15}
AHA	AHA	No	6	125	0.137	2.56150	3.480×10^{-18}	3.718×10^{-18}	5.423×10^{-18}	1.945×10^{-15}

E.4 Summary

The basic conclusion is that the analysis is in a very robust state. Variation of the parameters used to define the physics results leads to changes in the final sensitivity of less than 2% for the $\beta = .9$ and above signal ($\sim 6\%$ for $\beta = 0.8$).

Variation in the choice of background simulation and time range cut leads to changes in the final sensitivity of 20%.

Furthermore, all the final cuts found using each variation still produce a null result when applied to the full experimental data sample. For all three potential base values (6,7,and 8), a slope of 105 is all that is needed to remove the final data event. The slopes produced are all well above this, as they should be since the background expectations are all well below a single event.

Appendix F

Numerical Results for the final Limits

The following tables are intended to provide all the numbers necessary to calculate the individual limits displayed in 11.4. Since the $\beta = 0.76$ limit is non-competitive, only the results for $\beta = 0.8, 0.9$ and $\gamma = 10$ are shown.

F.1 Effective Area

Table F.1 displays the numerical values for effective area used in 11.3. The columns show the efficiency of simulated events that survive all the cuts for each speed and the final effective area for each $\cos\theta$ bin considered. As a reminder, the efficiency for each bin considers only the events within that bin and $N_{gen}(\cos\theta) = N_{gen}/20$ since the signal is simulated isotropically. To get the final column, the efficiency is multiplied by $A_{gen} = 1.33\,\mathrm{km}^2$.

F.2 Final Limits

To generate Figure 11.4, the final limit was calculated for pairs of mass and kinetic energy ranging from $10^4 - 10^{19}\,\mathrm{GeV}$ in increments of $\Delta\log_{10} = 0.05$. Table F.2 displays the results for $\Delta\log_{10} = 0.5$.

Columns 3-5 of the table represent the $\cos\theta$ values that contributed to the final limit for each speed region. For instance, for a mass of $10^7\,\mathrm{GeV}$ and kinetic

Table F.1: Effective Area values (in km^2) for each $\cos\theta$ bin.

$\cos\theta$ range	$\epsilon = \frac{N_{det}(\cos\theta)}{N_{gen}/20}$			$A^{\gamma}_{eff}(\cos\theta)$		
	$\beta = 0.8$	$\beta = 0.9$	$\gamma = 10$	$\beta = 0.8$	$\beta = 0.9$	$\gamma = 10$
[-1.0,-0.9)	0.199	0.289	0.294	0.264	0.384	0.390
[-0.9,-0.8)	0.223	0.292	0.319	0.297	0.388	0.423
[-0.8,-0.7)	0.257	0.340	0.343	0.341	0.452	0.455
[-0.7,-0.6)	0.278	0.357	0.365	0.369	0.474	0.484
[-0.6,-0.5)	0.256	0.359	0.363	0.340	0.477	0.482
[-0.5,-0.4)	0.238	0.370	0.378	0.316	0.491	0.502
[-0.4,-0.3)	0.257	0.374	0.381	0.342	0.497	0.505
[-0.3,-0.2)	0.254	0.371	0.400	0.338	0.492	0.530
[-0.2,-0.1)	0.268	0.393	0.415	0.355	0.521	0.551
[-0.1,0.0)	0.244	0.395	0.391	0.324	0.524	0.520
[0.0,0.1)	0.091	0.291	0.343	0.120	0.387	0.456
[0.1,0.2)	0.000	0.057	0.136	0.001	0.075	0.180
[0.2,0.3)	0.000	0.001	0.012	0.000	0.001	0.016
[0.3,0.4)	0.000	0.000	0.000	0.000	0.000	0.000
[0.4,0.5)	0.000	0.000	0.000	0.000	0.000	0.000
[0.5,0.6)	0.000	0.000	0.000	0.000	0.000	0.000
[0.6,0.7)	0.000	0.000	0.000	0.000	0.000	0.000
[0.7,0.8)	0.000	0.000	0.000	0.000	0.000	0.000
[0.8,0.9)	0.000	0.000	0.000	0.000	0.000	0.000
[0.9,1.0)	0.000	0.000	0.000	0.000	0.000	0.000

energy of $10^{7.5}$ GeV, $\cos\theta$ =0.2,0.3,0.4,0.5,0.6,0.7,0.8, and 0.9 resulted in a final γ below 10 but above 1.67 ($\beta = 0.9$). Hence, for these, the effective area for $\beta = 0.9$ is used. For $\cos\theta = 0.1$, the effective area for $\beta = 0.8$ is used. All other angles resulted in a β below 0.8 and are not used.

The sixth column represents the sum over the effective area used in Equation 11.11. It can be calculated by summing the effective areas from Table F.1 times 0.1 to represent $\Delta\cos\theta$. The effective area is for a range of $\cos\theta$ while the energy loss is calculated for a single $\cos\theta$ value. The single value (e.g., 0.2) uses the effective area for the bin that has this as the lowest value (e.g. [0.2,0.3)). This represents a conservative approach since the smaller $\cos\theta$ value corresponds to a longer distance through the Earth and hence more energy loss. For this reason, $\cos\theta = 1.0$, or straight down-going, is not checked.

The final columns are the sensitivity and limit. They are calculated using Equation 11.12 with either $\mu_{90\%\mathrm{Avg}}$ or $\mu_{90\%}$ (Table 11.1). For ones with different speeds contributing to the final limit, the highest μ is used.

Table F.2: Final Sensitivity and Limit values for all Mass and Initial Kinetic Energy values considered

$\log_{10}$ Mass GeV	$\log_{10}$ E$_{\text{Kin}}$ GeV	$\cos\theta$ bins used for each speed region			$\sum(\Delta\cos\theta)A_{\text{eff}}^{\gamma_d}$ km^2	Final Sensitivity $cm^{-2}sr^{-1}s^{-1}$	Final Limit $cm^{-2}sr^{-1}s^{-1}$
		$\gamma \geq 10$	$2.3 \leq \gamma < 10$	$1.7 \leq \gamma < 2.3$			
4.0	4.0	-	-	-	0.000	-	-
4.0	4.5	-	-	-	0.000	-	-
4.0	5.0	-	-	-	0.000	-	-
4.0	5.5	-	-	-	0.000	-	-
4.0	6.0	-	-	-	0.000	-	-
4.0	6.5	0.8,0.9	-	-	0.000	-	-
4.0	7.0	0.3,0.9	-	-	0.000	-	-
4.0	7.5	0.1,0.9	-	-	0.020	1.043×10^{-16}	9.462×10^{-17}
4.0	8.0	0.1,0.9	-	-	0.020	1.043×10^{-16}	9.462×10^{-17}
4.0	8.5	0.1,0.9	-	-	0.020	1.043×10^{-16}	9.462×10^{-17}
4.0	9.0	0.1,0.9	-	-	0.020	1.043×10^{-16}	9.462×10^{-17}
4.0	9.5	0.0,0.9	-	-	0.065	3.142×10^{-17}	2.851×10^{-17}
4.0	10.0	0.0,0.9	-	-	0.065	3.142×10^{-17}	2.851×10^{-17}
4.0	10.5	0.0,0.9	-	-	0.065	3.142×10^{-17}	2.851×10^{-17}
4.0	11.0	0.0,0.9	-	-	0.065	3.142×10^{-17}	2.851×10^{-17}
4.0	11.5	0.0,0.9	-	-	0.065	3.142×10^{-17}	2.851×10^{-17}
4.0	12.0	0.0,0.9	-	-	0.065	3.142×10^{-17}	2.851×10^{-17}
4.0	12.5	0.0,0.9	-	-	0.065	3.142×10^{-17}	2.851×10^{-17}
4.0	13.0	0.0,0.9	-	-	0.065	3.142×10^{-17}	2.851×10^{-17}
4.0	13.5	0.0,0.9	-	-	0.065	3.142×10^{-17}	2.851×10^{-17}
4.0	14.0	0.0,0.9	-	-	0.065	3.142×10^{-17}	2.851×10^{-17}
4.0	14.5	0.0,0.9	-	-	0.065	3.142×10^{-17}	2.851×10^{-17}
4.0	15.0	0.0,0.9	-	-	0.065	3.142×10^{-17}	2.851×10^{-17}
4.0	15.5	0.0,0.9	-	-	0.065	3.142×10^{-17}	2.851×10^{-17}

Table F.2: (continued)

$\log_{10}$ Mass GeV	$\log_{10}$ E$_{\mathrm{Kin}}$ GeV	$\cos\theta$ bins used for each speed region			$\sum(\Delta\cos\theta)A_{\mathrm{eff}}^{\gamma_d}$ km^2	Final Sensitivity $cm^{-2}sr^{-1}s^{-1}$	Final Limit $cm^{-2}sr^{-1}s^{-1}$
		$\gamma \geq 10$	$2.3 \leq \gamma < 10$	$1.7 \leq \gamma < 2.3$			
4.0	16.0	0.0,0.9	-	-	0.065	3.142×10^{-17}	2.851×10^{-17}
4.0	16.5	0.0,0.9	-	-	0.065	3.142×10^{-17}	2.851×10^{-17}
4.0	17.0	0.0,0.9	-	-	0.065	3.142×10^{-17}	2.851×10^{-17}
4.0	17.5	0.0,0.9	-	-	0.065	3.142×10^{-17}	2.851×10^{-17}
4.0	18.0	0.0,0.9	-	-	0.065	3.142×10^{-17}	2.851×10^{-17}
4.0	18.5	0.0,0.9	-	-	0.065	3.142×10^{-17}	2.851×10^{-17}
4.5	4.0	-	-	-	0.000	-	-
4.5	4.5	-	-	-	0.000	-	-
4.5	5.0	-	-	-	0.000	-	-
4.5	5.5	-	-	-	0.000	-	-
4.5	6.0	-	-	-	0.000	-	-
4.5	6.5	0.8,0.9	-	-	0.000	-	-
4.5	7.0	0.3,0.9	-	-	0.000	-	-
4.5	7.5	0.1,0.9	-	-	0.020	1.043×10^{-16}	9.462×10^{-17}
4.5	8.0	0.1,0.9	-	-	0.020	1.043×10^{-16}	9.462×10^{-17}
4.5	8.5	0.1,0.9	-	-	0.020	1.043×10^{-16}	9.462×10^{-17}
4.5	9.0	0.0,0.9	-	-	0.065	3.142×10^{-17}	2.851×10^{-17}
4.5	9.5	0.0,0.9	-	-	0.065	3.142×10^{-17}	2.851×10^{-17}
4.5	10.0	0.0,0.9	-	-	0.065	3.142×10^{-17}	2.851×10^{-17}
4.5	10.5	0.0,0.9	-	-	0.065	3.142×10^{-17}	2.851×10^{-17}
4.5	11.0	0.0,0.9	-	-	0.065	3.142×10^{-17}	2.851×10^{-17}
4.5	11.5	0.0,0.9	-	-	0.065	3.142×10^{-17}	2.851×10^{-17}
4.5	12.0	0.0,0.9	-	-	0.065	3.142×10^{-17}	2.851×10^{-17}
4.5	12.5	0.0,0.9	-	-	0.065	3.142×10^{-17}	2.851×10^{-17}

Table F.2: (continued)

$\log_{10}$ Mass GeV	$\log_{10}$ E$_{\mathrm{Kin}}$ GeV	$\cos\theta$ bins used for each speed region			$\sum(\Delta\cos\theta)A_{\mathrm{eff}}^{\gamma_d}$ km^2	Final Sensitivity $cm^{-2}sr^{-1}s^{-1}$	Final Limit $cm^{-2}sr^{-1}s^{-1}$
		$\gamma \geq 10$	$2.3 \leq \gamma < 10$	$1.7 \leq \gamma < 2.3$			
4.5	13.0	0.0,0.9	-	-	0.065	3.142×10^{-17}	2.851×10^{-17}
4.5	13.5	0.0,0.9	-	-	0.065	3.142×10^{-17}	2.851×10^{-17}
4.5	14.0	0.0,0.9	-	-	0.065	3.142×10^{-17}	2.851×10^{-17}
4.5	14.5	0.0,0.9	-	-	0.065	3.142×10^{-17}	2.851×10^{-17}
4.5	15.0	0.0,0.9	-	-	0.065	3.142×10^{-17}	2.851×10^{-17}
4.5	15.5	0.0,0.9	-	-	0.065	3.142×10^{-17}	2.851×10^{-17}
4.5	16.0	0.0,0.9	-	-	0.065	3.142×10^{-17}	2.851×10^{-17}
4.5	16.5	0.0,0.9	-	-	0.065	3.142×10^{-17}	2.851×10^{-17}
4.5	17.0	0.0,0.9	-	-	0.065	3.142×10^{-17}	2.851×10^{-17}
4.5	17.5	0.0,0.9	-	-	0.065	3.142×10^{-17}	2.851×10^{-17}
4.5	18.0	0.0,0.9	-	-	0.065	3.142×10^{-17}	2.851×10^{-17}
4.5	18.5	0.0,0.9	-	-	0.065	3.142×10^{-17}	2.851×10^{-17}
5.0	4.0	-	-	-	0.000	-	-
5.0	4.5	-	-	-	0.000	-	-
5.0	5.0	-	-	-	0.000	-	-
5.0	5.5	-	-	-	0.000	-	-
5.0	6.0	-	-	-	0.000	-	-
5.0	6.5	-	0.8,0.9	-	0.000	-	-
5.0	7.0	0.3,0.9	-	-	0.000	-	-
5.0	7.5	0.1,0.9	-	-	0.020	1.043×10^{-16}	9.462×10^{-17}
5.0	8.0	0.1,0.9	-	-	0.020	1.043×10^{-16}	9.462×10^{-17}
5.0	8.5	0.0,0.9	-	-	0.065	3.142×10^{-17}	2.851×10^{-17}
5.0	9.0	0.0,0.9	-	-	0.065	3.142×10^{-17}	2.851×10^{-17}
5.0	9.5	0.0,0.9	-	-	0.065	3.142×10^{-17}	2.851×10^{-17}

$\log_{10}$ Mass GeV	$\log_{10}$ E$_{\text{Kin}}$ GeV	$\cos\theta$ bins used for each speed region			$\sum(\Delta\cos\theta)A_{\text{eff}}^{\gamma_d}$ km^2	Final Sensitivity $cm^{-2}sr^{-1}s^{-1}$	Final Limit $cm^{-2}sr^{-1}s^{-1}$
		$\gamma \geq 10$	$2.3 \leq \gamma < 10$	$1.7 \leq \gamma < 2.3$			
5.0	10.0	0.0,0.9	-	-	0.065	3.142×10^{-17}	2.851×10^{-17}
5.0	10.5	0.0,0.9	-	-	0.065	3.142×10^{-17}	2.851×10^{-17}
5.0	11.0	0.0,0.9	-	-	0.065	3.142×10^{-17}	2.851×10^{-17}
5.0	11.5	0.0,0.9	-	-	0.065	3.142×10^{-17}	2.851×10^{-17}
5.0	12.0	0.0,0.9	-	-	0.065	3.142×10^{-17}	2.851×10^{-17}
5.0	12.5	0.0,0.9	-	-	0.065	3.142×10^{-17}	2.851×10^{-17}
5.0	13.0	0.0,0.9	-	-	0.065	3.142×10^{-17}	2.851×10^{-17}
5.0	13.5	0.0,0.9	-	-	0.065	3.142×10^{-17}	2.851×10^{-17}
5.0	14.0	0.0,0.9	-	-	0.065	3.142×10^{-17}	2.851×10^{-17}
5.0	14.5	0.0,0.9	-	-	0.065	3.142×10^{-17}	2.851×10^{-17}
5.0	15.0	0.0,0.9	-	-	0.065	3.142×10^{-17}	2.851×10^{-17}
5.0	15.5	0.0,0.9	-	-	0.065	3.142×10^{-17}	2.851×10^{-17}
5.0	16.0	0.0,0.9	-	-	0.065	3.142×10^{-17}	2.851×10^{-17}
5.0	16.5	0.0,0.9	-	-	0.065	3.142×10^{-17}	2.851×10^{-17}
5.0	17.0	0.0,0.9	-	-	0.065	3.142×10^{-17}	2.851×10^{-17}
5.0	17.5	0.0,0.9	-	-	0.065	3.142×10^{-17}	2.851×10^{-17}
5.0	18.0	0.0,0.9	-	-	0.065	3.142×10^{-17}	2.851×10^{-17}
5.0	18.5	0.0,0.9	-	-	0.065	3.142×10^{-17}	2.851×10^{-17}
5.5	4.0	-	-	-	0.000	-	-
5.5	4.5	-	-	-	0.000	-	-
5.5	5.0	-	-	-	0.000	-	-
5.5	5.5	-	-	-	0.000	-	-
5.5	6.0	-	-	-	0.000	-	-
5.5	6.5	-	0.9	0.8	0.000	-	-

Table F.2: (continued)

$\log_{10}$ Mass GeV	$\log_{10}$ E$_{\text{Kin}}$ GeV	$\cos\theta$ bins used for each speed region			$\sum(\Delta\cos\theta)A_{\text{eff}}^{\gamma_d}$ km²	Final Sensitivity $cm^{-2}sr^{-1}s^{-1}$	Final Limit $cm^{-2}sr^{-1}s^{-1}$
		$\gamma \geq 10$	$2.3 \leq \gamma < 10$	$1.7 \leq \gamma < 2.3$			
5.5	7.0	0.4,0.9	0.3	-	0.000	-	-
5.5	7.5	0.1,0.9	-	-	0.020	1.043×10^{-16}	9.462×10^{-17}
5.5	8.0	0.1,0.9	-	-	0.020	1.043×10^{-16}	9.462×10^{-17}
5.5	8.5	0.0,0.9	-	-	0.065	3.142×10^{-17}	2.851×10^{-17}
5.5	9.0	0.0,0.9	-	-	0.065	3.142×10^{-17}	2.851×10^{-17}
5.5	9.5	0.0,0.9	-	-	0.065	3.142×10^{-17}	2.851×10^{-17}
5.5	10.0	0.0,0.9	-	-	0.065	3.142×10^{-17}	2.851×10^{-17}
5.5	10.5	-0.1,0.9	-	-	0.117	1.749×10^{-17}	1.587×10^{-17}
5.5	11.0	-0.1,0.9	-	-	0.117	1.749×10^{-17}	1.587×10^{-17}
5.5	11.5	-0.1,0.9	-	-	0.117	1.749×10^{-17}	1.587×10^{-17}
5.5	12.0	-0.1,0.9	-	-	0.117	1.749×10^{-17}	1.587×10^{-17}
5.5	12.5	-0.1,0.9	-	-	0.117	1.749×10^{-17}	1.587×10^{-17}
5.5	13.0	-0.2,0.9	-	-	0.172	1.189×10^{-17}	1.079×10^{-17}
5.5	13.5	-0.2,0.9	-	-	0.172	1.189×10^{-17}	1.079×10^{-17}
5.5	14.0	-0.2,0.9	-	-	0.172	1.189×10^{-17}	1.079×10^{-17}
5.5	14.5	-0.2,0.9	-	-	0.172	1.189×10^{-17}	1.079×10^{-17}
5.5	15.0	-0.2,0.9	-	-	0.172	1.189×10^{-17}	1.079×10^{-17}
5.5	15.5	-0.2,0.9	-	-	0.172	1.189×10^{-17}	1.079×10^{-17}
5.5	16.0	-0.2,0.9	-	-	0.172	1.189×10^{-17}	1.079×10^{-17}
5.5	16.5	-0.2,0.9	-	-	0.172	1.189×10^{-17}	1.079×10^{-17}
5.5	17.0	-0.2,0.9	-	-	0.172	1.189×10^{-17}	1.079×10^{-17}
5.5	17.5	-0.2,0.9	-	-	0.172	1.189×10^{-17}	1.079×10^{-17}
5.5	18.0	-0.2,0.9	-	-	0.172	1.189×10^{-17}	1.079×10^{-17}
5.5	18.5	-0.2,0.9	-	-	0.172	1.189×10^{-17}	1.079×10^{-17}

Table F.2: (continued)

$\log_{10}$ Mass GeV	$\log_{10}$ E$_{\mathrm{Kin}}$ GeV	$\cos\theta$ bins used for each speed region			$\sum(\Delta\cos\theta)A_{\mathrm{eff}}^{\gamma_d}$ km^2	Final Sensitivity $cm^{-2}sr^{-1}s^{-1}$	Final Limit $cm^{-2}sr^{-1}s^{-1}$
		$\gamma \geq 10$	$2.3 \leq \gamma < 10$	$1.7 \leq \gamma < 2.3$			
6.0	4.0	-	-	-	0.000	-	-
6.0	4.5	-	-	-	0.000	-	-
6.0	5.0	-	-	-	0.000	-	-
6.0	5.5	-	-	-	0.000	-	-
6.0	6.0	-	-	-	0.000	-	-
6.0	6.5	-	-	-	0.000	-	-
6.0	7.0	-	0.3,0.9	-	0.000	-	-
6.0	7.5	0.1,0.9	-	-	0.020	1.043×10^{-16}	9.462×10^{-17}
6.0	8.0	0.1,0.9	-	-	0.020	1.043×10^{-16}	9.462×10^{-17}
6.0	8.5	0.0,0.9	-	-	0.065	3.142×10^{-17}	2.851×10^{-17}
6.0	9.0	0.0,0.9	-	-	0.065	3.142×10^{-17}	2.851×10^{-17}
6.0	9.5	0.0,0.9	-	-	0.065	3.142×10^{-17}	2.851×10^{-17}
6.0	10.0	-0.1,0.9	-	-	0.117	1.749×10^{-17}	1.587×10^{-17}
6.0	10.5	-0.2,0.9	-	-	0.172	1.189×10^{-17}	1.079×10^{-17}
6.0	11.0	-0.3,0.9	-	-	0.225	9.092×10^{-18}	8.249×10^{-18}
6.0	11.5	-0.4,0.9	-	-	0.276	7.426×10^{-18}	6.738×10^{-18}
6.0	12.0	-0.5,0.9	-	-	0.326	6.282×10^{-18}	5.700×10^{-18}
6.0	12.5	-0.5,0.9	-	-	0.326	6.282×10^{-18}	5.700×10^{-18}
6.0	13.0	-0.6,0.9	-	-	0.374	5.473×10^{-18}	4.966×10^{-18}
6.0	13.5	-0.6,0.9	-	-	0.374	5.473×10^{-18}	4.966×10^{-18}
6.0	14.0	-0.7,0.9	-	-	0.423	4.846×10^{-18}	4.397×10^{-18}
6.0	14.5	-0.7,0.9	-	-	0.423	4.846×10^{-18}	4.397×10^{-18}
6.0	15.0	-0.7,0.9	-	-	0.423	4.846×10^{-18}	4.397×10^{-18}
6.0	15.5	-0.7,0.9	-	-	0.423	4.846×10^{-18}	4.397×10^{-18}

Table F.2: (continued)

$\log_{10}$ Mass GeV	$\log_{10}$ E$_{\text{Kin}}$ GeV	$\cos\theta$ bins used for each speed region			$\sum(\Delta\cos\theta)A_{\text{eff}}^{\gamma_d}$ km^2	Final Sensitivity $cm^{-2}sr^{-1}s^{-1}$	Final Limit $cm^{-2}sr^{-1}s^{-1}$
		$\gamma \geq 10$	$2.3 \leq \gamma < 10$	$1.7 \leq \gamma < 2.3$			
6.0	16.0	-0.7,0.9	-	-	0.423	4.846×10^{-18}	4.397×10^{-18}
6.0	16.5	-0.7,0.9	-	-	0.423	4.846×10^{-18}	4.397×10^{-18}
6.0	17.0	-0.7,0.9	-	-	0.423	4.846×10^{-18}	4.397×10^{-18}
6.0	17.5	-0.7,0.9	-	-	0.423	4.846×10^{-18}	4.397×10^{-18}
6.0	18.0	-0.7,0.9	-	-	0.423	4.846×10^{-18}	4.397×10^{-18}
6.0	18.5	-0.8,0.9	-	-	0.468	4.375×10^{-18}	3.970×10^{-18}
6.5	4.0	-	-	-	0.000	-	-
6.5	4.5	-	-	-	0.000	-	-
6.5	5.0	-	-	-	0.000	-	-
6.5	5.5	-	-	-	0.000	-	-
6.5	6.0	-	-	-	0.000	-	-
6.5	6.5	-	-	-	0.000	-	-
6.5	7.0	-	0.4,0.9	0.3	0.000	-	-
6.5	7.5	0.8,0.9	0.1,0.7	-	0.008	2.689×10^{-16}	2.440×10^{-16}
6.5	8.0	0.1,0.9	-	-	0.020	1.043×10^{-16}	9.462×10^{-17}
6.5	8.5	0.0,0.9	-	-	0.065	3.142×10^{-17}	2.851×10^{-17}
6.5	9.0	0.0,0.9	-	-	0.065	3.142×10^{-17}	2.851×10^{-17}
6.5	9.5	0.0,0.9	-	-	0.065	3.142×10^{-17}	2.851×10^{-17}
6.5	10.0	-0.1,0.9	-	-	0.117	1.749×10^{-17}	1.587×10^{-17}
6.5	10.5	-0.4,0.9	-	-	0.276	7.426×10^{-18}	6.738×10^{-18}
6.5	11.0	-0.7,0.9	-	-	0.423	4.846×10^{-18}	4.397×10^{-18}
6.5	11.5	-0.8,0.9	-	-	0.468	4.375×10^{-18}	3.970×10^{-18}
6.5	12.0	-0.8,0.9	-	-	0.468	4.375×10^{-18}	3.970×10^{-18}
6.5	12.5	-0.8,0.9	-	-	0.468	4.375×10^{-18}	3.970×10^{-18}

Table F.2: (continued)

$\log_{10}$ Mass GeV	$\log_{10}$ E_{Kin} GeV	\multicolumn{3}{c}{$\cos\theta$ bins used for each speed region}			$\sum(\Delta\cos\theta)A_{eff}^{\gamma_d}$ km^2	Final Sensitivity $cm^{-2}sr^{-1}s^{-1}$	Final Limit $cm^{-2}sr^{-1}s^{-1}$
		$\gamma \geq 10$	$2.3 \leq \gamma < 10$	$1.7 \leq \gamma < 2.3$				
6.5	13.0	-0.8,0.9	-	-		0.468	4.375×10^{-18}	3.970×10^{-18}
6.5	13.5	-0.8,0.9	-	-		0.468	4.375×10^{-18}	3.970×10^{-18}
6.5	14.0	-0.8,0.9	-	-		0.468	4.375×10^{-18}	3.970×10^{-18}
6.5	14.5	-0.8,0.9	-	-		0.468	4.375×10^{-18}	3.970×10^{-18}
6.5	15.0	-0.8,0.9	-	-		0.468	4.375×10^{-18}	3.970×10^{-18}
6.5	15.5	-0.8,0.9	-	-		0.468	4.375×10^{-18}	3.970×10^{-18}
6.5	16.0	-0.8,0.9	-	-		0.468	4.375×10^{-18}	3.970×10^{-18}
6.5	16.5	-0.8,0.9	-	-		0.468	4.375×10^{-18}	3.970×10^{-18}
6.5	17.0	-0.8,0.9	-	-		0.468	4.375×10^{-18}	3.970×10^{-18}
6.5	17.5	-0.8,0.9	-	-		0.468	4.375×10^{-18}	3.970×10^{-18}
6.5	18.0	-0.8,0.9	-	-		0.468	4.375×10^{-18}	3.970×10^{-18}
6.5	18.5	-0.9,0.9	-	-		0.511	4.012×10^{-18}	3.640×10^{-18}
7.0	4.0	-	-	-		0.000	-	-
7.0	4.5	-	-	-		0.000	-	-
7.0	5.0	-	-	-		0.000	-	-
7.0	5.5	-	-	-		0.000	-	-
7.0	6.0	-	-	-		0.000	-	-
7.0	6.5	-	-	-		0.000	-	-
7.0	7.0	-	-	0.7,0.9		0.000	-	-
7.0	7.5	-	0.2,0.9	0.1		0.000	1.305×10^{-14}	1.190×10^{-14}
7.0	8.0	0.3,0.9	0.1,0.2	-		0.008	2.689×10^{-16}	2.440×10^{-16}
7.0	8.5	0.0,0.9	-	-		0.065	3.142×10^{-17}	2.851×10^{-17}
7.0	9.0	0.0,0.9	-	-		0.065	3.142×10^{-17}	2.851×10^{-17}
7.0	9.5	0.0,0.9	-	-		0.065	3.142×10^{-17}	2.851×10^{-17}

Table F.2: (continued)

$\log_{10}$ Mass GeV	$\log_{10}$ E$_{\text{Kin}}$ GeV	$\cos\theta$ bins used for each speed region			$\sum(\Delta\cos\theta)A_{\text{eff}}^{\gamma_d}$ km²	Final Sensitivity $cm^{-2}sr^{-1}s^{-1}$	Final Limit $cm^{-2}sr^{-1}s^{-1}$
		$\gamma \geq 10$	$2.3 \leq \gamma < 10$	$1.7 \leq \gamma < 2.3$			
7.0	10.0	-0.2,0.9	-	-	0.172	1.189×10^{-17}	1.079×10^{-17}
7.0	10.5	-0.6,0.9	-	-	0.374	5.473×10^{-18}	4.966×10^{-18}
7.0	11.0	-0.8,0.9	-	-	0.468	4.375×10^{-18}	3.970×10^{-18}
7.0	11.5	-0.8,0.9	-	-	0.468	4.375×10^{-18}	3.970×10^{-18}
7.0	12.0	-0.9,0.9	-	-	0.511	4.012×10^{-18}	3.640×10^{-18}
7.0	12.5	-1.0,0.9	-	-	0.550	3.728×10^{-18}	3.382×10^{-18}
7.0	13.0	-1.0,0.9	-	-	0.550	3.728×10^{-18}	3.382×10^{-18}
7.0	13.5	-1.0,0.9	-	-	0.550	3.728×10^{-18}	3.382×10^{-18}
7.0	14.0	-1.0,0.9	-	-	0.550	3.728×10^{-18}	3.382×10^{-18}
7.0	14.5	-1.0,0.9	-	-	0.550	3.728×10^{-18}	3.382×10^{-18}
7.0	15.0	-1.0,0.9	-	-	0.550	3.728×10^{-18}	3.382×10^{-18}
7.0	15.5	-1.0,0.9	-	-	0.550	3.728×10^{-18}	3.382×10^{-18}
7.0	16.0	-1.0,0.9	-	-	0.550	3.728×10^{-18}	3.382×10^{-18}
7.0	16.5	-1.0,0.9	-	-	0.550	3.728×10^{-18}	3.382×10^{-18}
7.0	17.0	-1.0,0.9	-	-	0.550	3.728×10^{-18}	3.382×10^{-18}
7.0	17.5	-1.0,0.9	-	-	0.550	3.728×10^{-18}	3.382×10^{-18}
7.0	18.0	-1.0,0.9	-	-	0.550	3.728×10^{-18}	3.382×10^{-18}
7.0	18.5	-1.0,0.9	-	-	0.550	3.728×10^{-18}	3.382×10^{-18}
7.5	4.0	-	-	-	0.000	-	-
7.5	4.5	-	-	-	0.000	-	-
7.5	5.0	-	-	-	0.000	-	-
7.5	5.5	-	-	-	0.000	-	-
7.5	6.0	-	-	-	0.000	-	-
7.5	6.5	-	-	-	0.000	-	-

Table F.2: (continued)

log$_{10}$ Mass GeV	log$_{10}$ E$_{\text{Kin}}$ GeV	cos θ bins used for each speed region			$\sum (\Delta \cos \theta) A_{\text{eff}}^{\gamma_d}$ km^2	Final Sensitivity $cm^{-2}sr^{-1}s^{-1}$	Final Limit $cm^{-2}sr^{-1}s^{-1}$
		$\gamma \geq 10$	$2.3 \leq \gamma < 10$	$1.7 \leq \gamma < 2.3$			
7.5	7.0	-	-	-	0.000	-	-
7.5	7.5	-	-	0.3,0.9	0.000	-	-
7.5	8.0	-	0.1,0.9	-	0.008	2.673×10^{-16}	2.436×10^{-16}
7.5	8.5	0.1,0.9	0.0	-	0.058	3.514×10^{-17}	3.189×10^{-17}
7.5	9.0	0.0,0.9	-	-	0.065	3.142×10^{-17}	2.851×10^{-17}
7.5	9.5	0.0,0.9	-	-	0.065	3.142×10^{-17}	2.851×10^{-17}
7.5	10.0	-0.2,0.9	-	-	0.172	1.189×10^{-17}	1.079×10^{-17}
7.5	10.5	-0.7,0.9	-	-	0.423	4.846×10^{-18}	4.397×10^{-18}
7.5	11.0	-0.8,0.9	-	-	0.468	4.375×10^{-18}	3.970×10^{-18}
7.5	11.5	-1.0,0.9	-	-	0.550	3.728×10^{-18}	3.382×10^{-18}
7.5	12.0	-1.0,0.9	-	-	0.550	3.728×10^{-18}	3.382×10^{-18}
7.5	12.5	-1.0,0.9	-	-	0.550	3.728×10^{-18}	3.382×10^{-18}
7.5	13.0	-1.0,0.9	-	-	0.550	3.728×10^{-18}	3.382×10^{-18}
7.5	13.5	-1.0,0.9	-	-	0.550	3.728×10^{-18}	3.382×10^{-18}
7.5	14.0	-1.0,0.9	-	-	0.550	3.728×10^{-18}	3.382×10^{-18}
7.5	14.5	-1.0,0.9	-	-	0.550	3.728×10^{-18}	3.382×10^{-18}
7.5	15.0	-1.0,0.9	-	-	0.550	3.728×10^{-18}	3.382×10^{-18}
7.5	15.5	-1.0,0.9	-	-	0.550	3.728×10^{-18}	3.382×10^{-18}
7.5	16.0	-1.0,0.9	-	-	0.550	3.728×10^{-18}	3.382×10^{-18}
7.5	16.5	-1.0,0.9	-	-	0.550	3.728×10^{-18}	3.382×10^{-18}
7.5	17.0	-1.0,0.9	-	-	0.550	3.728×10^{-18}	3.382×10^{-18}
7.5	17.5	-1.0,0.9	-	-	0.550	3.728×10^{-18}	3.382×10^{-18}
7.5	18.0	-1.0,0.9	-	-	0.550	3.728×10^{-18}	3.382×10^{-18}
7.5	18.5	-1.0,0.9	-	-	0.550	3.728×10^{-18}	3.382×10^{-18}

Table F.2: (continued)

$\log_{10}$ Mass GeV	$\log_{10}$ E_{Kin} GeV	$\cos\theta$ bins used for each speed region			$\sum(\Delta\cos\theta)A_{eff}^{\gamma_d}$ km^2	Final Sensitivity $cm^{-2}sr^{-1}s^{-1}$	Final Limit $cm^{-2}sr^{-1}s^{-1}$
		$\gamma \geq 10$	$2.3 \leq \gamma < 10$	$1.7 \leq \gamma < 2.3$			
8.0	4.0	-	-	-	0.000	-	-
8.0	4.5	-	-	-	0.000	-	-
8.0	5.0	-	-	-	0.000	-	-
8.0	5.5	-	-	-	0.000	-	-
8.0	6.0	-	-	-	0.000	-	-
8.0	6.5	-	-	-	0.000	-	-
8.0	7.0	-	-	-	0.000	-	-
8.0	7.5	-	-	-	0.000	-	-
8.0	8.0	-	-	0.1,0.9	0.000	3.914×10^{-14}	3.570×10^{-14}
8.0	8.5	-	0.0,0.9	-	0.046	4.401×10^{-17}	4.011×10^{-17}
8.0	9.0	0.1,0.9	0.0	-	0.058	3.514×10^{-17}	3.189×10^{-17}
8.0	9.5	0.0,0.9	-	-	0.065	3.142×10^{-17}	2.851×10^{-17}
8.0	10.0	-0.2,0.9	-	-	0.172	1.189×10^{-17}	1.079×10^{-17}
8.0	10.5	-0.8,0.9	-	-	0.468	4.375×10^{-18}	3.970×10^{-18}
8.0	11.0	-0.9,0.9	-	-	0.511	4.012×10^{-18}	3.640×10^{-18}
8.0	11.5	-1.0,0.9	-	-	0.550	3.728×10^{-18}	3.382×10^{-18}
8.0	12.0	-1.0,0.9	-	-	0.550	3.728×10^{-18}	3.382×10^{-18}
8.0	12.5	-1.0,0.9	-	-	0.550	3.728×10^{-18}	3.382×10^{-18}
8.0	13.0	-1.0,0.9	-	-	0.550	3.728×10^{-18}	3.382×10^{-18}
8.0	13.5	-1.0,0.9	-	-	0.550	3.728×10^{-18}	3.382×10^{-18}
8.0	14.0	-1.0,0.9	-	-	0.550	3.728×10^{-18}	3.382×10^{-18}
8.0	14.5	-1.0,0.9	-	-	0.550	3.728×10^{-18}	3.382×10^{-18}
8.0	15.0	-1.0,0.9	-	-	0.550	3.728×10^{-18}	3.382×10^{-18}
8.0	15.5	-1.0,0.9	-	-	0.550	3.728×10^{-18}	3.382×10^{-18}

Table F.2: (continued)

$\log_{10}$ Mass GeV	$\log_{10}$ E_{Kin} GeV	$\cos\theta$ bins used for each speed region			$\sum(\Delta\cos\theta)A_{eff}^{\gamma_d}$ km^2	Final Sensitivity $cm^{-2}sr^{-1}s^{-1}$	Final Limit $cm^{-2}sr^{-1}s^{-1}$
		$\gamma \geq 10$	$2.3 \leq \gamma < 10$	$1.7 \leq \gamma < 2.3$			
8.0	16.0	-1.0,0.9	-	-	0.550	3.728×10^{-18}	3.382×10^{-18}
8.0	16.5	-1.0,0.9	-	-	0.550	3.728×10^{-18}	3.382×10^{-18}
8.0	17.0	-1.0,0.9	-	-	0.550	3.728×10^{-18}	3.382×10^{-18}
8.0	17.5	-1.0,0.9	-	-	0.550	3.728×10^{-18}	3.382×10^{-18}
8.0	18.0	-1.0,0.9	-	-	0.550	3.728×10^{-18}	3.382×10^{-18}
8.0	18.5	-1.0,0.9	-	-	0.550	3.728×10^{-18}	3.382×10^{-18}
8.5	4.0	-	-	-	0.000	-	-
8.5	4.5	-	-	-	0.000	-	-
8.5	5.0	-	-	-	0.000	-	-
8.5	5.5	-	-	-	0.000	-	-
8.5	6.0	-	-	-	0.000	-	-
8.5	6.5	-	-	-	0.000	-	-
8.5	7.0	-	-	-	0.000	-	-
8.5	7.5	-	-	-	0.000	-	-
8.5	8.0	-	-	-	0.000	-	-
8.5	8.5	-	-	0.1,0.9	0.000	3.914×10^{-14}	3.570×10^{-14}
8.5	9.0	-	0.0,0.9	-	0.046	4.401×10^{-17}	4.011×10^{-17}
8.5	9.5	0.0,0.9	-	-	0.065	3.142×10^{-17}	2.851×10^{-17}
8.5	10.0	-0.1,0.9	-0.2	-	0.169	1.210×10^{-17}	1.098×10^{-17}
8.5	10.5	-0.7,0.9	-0.8	-	0.468	4.378×10^{-18}	3.973×10^{-18}
8.5	11.0	-0.9,0.9	-	-	0.511	4.012×10^{-18}	3.640×10^{-18}
8.5	11.5	-1.0,0.9	-	-	0.550	3.728×10^{-18}	3.382×10^{-18}
8.5	12.0	-1.0,0.9	-	-	0.550	3.728×10^{-18}	3.382×10^{-18}
8.5	12.5	-1.0,0.9	-	-	0.550	3.728×10^{-18}	3.382×10^{-18}

Table F.2: (continued)

log$_{10}$ Mass GeV	log$_{10}$ E$_{\text{Kin}}$ GeV	cos θ bins used for each speed region			$\sum (\Delta \cos\theta) A^{\gamma_d}_{\text{eff}}$ km^2	Final Sensitivity $cm^{-2}sr^{-1}s^{-1}$	Final Limit $cm^{-2}sr^{-1}s^{-1}$
		$\gamma \geq 10$	$2.3 \leq \gamma < 10$	$1.7 \leq \gamma < 2.3$			
8.5	13.0	-1.0,0.9	-	-	0.550	3.728×10^{-18}	3.382×10^{-18}
8.5	13.5	-1.0,0.9	-	-	0.550	3.728×10^{-18}	3.382×10^{-18}
8.5	14.0	-1.0,0.9	-	-	0.550	3.728×10^{-18}	3.382×10^{-18}
8.5	14.5	-1.0,0.9	-	-	0.550	3.728×10^{-18}	3.382×10^{-18}
8.5	15.0	-1.0,0.9	-	-	0.550	3.728×10^{-18}	3.382×10^{-18}
8.5	15.5	-1.0,0.9	-	-	0.550	3.728×10^{-18}	3.382×10^{-18}
8.5	16.0	-1.0,0.9	-	-	0.550	3.728×10^{-18}	3.382×10^{-18}
8.5	16.5	-1.0,0.9	-	-	0.550	3.728×10^{-18}	3.382×10^{-18}
8.5	17.0	-1.0,0.9	-	-	0.550	3.728×10^{-18}	3.382×10^{-18}
8.5	17.5	-1.0,0.9	-	-	0.550	3.728×10^{-18}	3.382×10^{-18}
8.5	18.0	-1.0,0.9	-	-	0.550	3.728×10^{-18}	3.382×10^{-18}
8.5	18.5	-1.0,0.9	-	-	0.550	3.728×10^{-18}	3.382×10^{-18}
9.0	4.0	-	-	-	0.000	-	-
9.0	4.5	-	-	-	0.000	-	-
9.0	5.0	-	-	-	0.000	-	-
9.0	5.5	-	-	-	0.000	-	-
9.0	6.0	-	-	-	0.000	-	-
9.0	6.5	-	-	-	0.000	-	-
9.0	7.0	-	-	-	0.000	-	-
9.0	7.5	-	-	-	0.000	-	-
9.0	8.0	-	-	-	0.000	-	-
9.0	8.5	-	-	-	0.000	-	-
9.0	9.0	-	-	0.0,0.9	0.012	1.720×10^{-16}	1.569×10^{-16}
9.0	9.5	-	0.0,0.9	-	0.046	4.401×10^{-17}	4.011×10^{-17}

Table F.2: (continued)

log$_{10}$ Mass GeV	log$_{10}$ E$_{\text{Kin}}$ GeV	cosθ bins used for each speed region			$\sum(\Delta\cos\theta)A_{\text{eff}}^{\gamma_d}$ km^2	Final Sensitivity $cm^{-2}sr^{-1}s^{-1}$	Final Limit $cm^{-2}sr^{-1}s^{-1}$
		$\gamma \geq 10$	$2.3 \leq \gamma < 10$	$1.7 \leq \gamma < 2.3$			
9.0	10.0	0.0,0.9	-0.2,-0.1	-	0.170	1.207×10^{-17}	1.095×10^{-17}
9.0	10.5	-0.6,0.9	-0.8,-0.7	-	0.467	4.387×10^{-18}	3.981×10^{-18}
9.0	11.0	-0.9,0.9	-	-	0.511	4.012×10^{-18}	3.640×10^{-18}
9.0	11.5	-1.0,0.9	-	-	0.550	3.728×10^{-18}	3.382×10^{-18}
9.0	12.0	-1.0,0.9	-	-	0.550	3.728×10^{-18}	3.382×10^{-18}
9.0	12.5	-1.0,0.9	-	-	0.550	3.728×10^{-18}	3.382×10^{-18}
9.0	13.0	-1.0,0.9	-	-	0.550	3.728×10^{-18}	3.382×10^{-18}
9.0	13.5	-1.0,0.9	-	-	0.550	3.728×10^{-18}	3.382×10^{-18}
9.0	14.0	-1.0,0.9	-	-	0.550	3.728×10^{-18}	3.382×10^{-18}
9.0	14.5	-1.0,0.9	-	-	0.550	3.728×10^{-18}	3.382×10^{-18}
9.0	15.0	-1.0,0.9	-	-	0.550	3.728×10^{-18}	3.382×10^{-18}
9.0	15.5	-1.0,0.9	-	-	0.550	3.728×10^{-18}	3.382×10^{-18}
9.0	16.0	-1.0,0.9	-	-	0.550	3.728×10^{-18}	3.382×10^{-18}
9.0	16.5	-1.0,0.9	-	-	0.550	3.728×10^{-18}	3.382×10^{-18}
9.0	17.0	-1.0,0.9	-	-	0.550	3.728×10^{-18}	3.382×10^{-18}
9.0	17.5	-1.0,0.9	-	-	0.550	3.728×10^{-18}	3.382×10^{-18}
9.0	18.0	-1.0,0.9	-	-	0.550	3.728×10^{-18}	3.382×10^{-18}
9.0	18.5	-1.0,0.9	-	-	0.550	3.728×10^{-18}	3.382×10^{-18}
9.5	4.0	-	-	-	0.000	-	-
9.5	4.5	-	-	-	0.000	-	-
9.5	5.0	-	-	-	0.000	-	-
9.5	5.5	-	-	-	0.000	-	-
9.5	6.0	-	-	-	0.000	-	-
9.5	6.5	-	-	-	0.000	-	-

Table F.2: (continued)

$\log_{10}$ Mass GeV	$\log_{10}$ E_{Kin} GeV	$\cos\theta$ bins used for each speed region			$\sum(\Delta\cos\theta)A_{eff}^{\gamma_d}$ km^2	Final Sensitivity $cm^{-2}sr^{-1}s^{-1}$	Final Limit $cm^{-2}sr^{-1}s^{-1}$
		$\gamma \geq 10$	$2.3 \leq \gamma < 10$	$1.7 \leq \gamma < 2.3$			
9.5	7.0	-	-	-	0.000	-	-
9.5	7.5	-	-	-	0.000	-	-
9.5	8.0	-	-	-	0.000	-	-
9.5	8.5	-	-	-	0.000	-	-
9.5	9.0	-	-	-	0.000	-	-
9.5	9.5	-	-	0.0,0.9	0.012	1.720×10^{-16}	1.569×10^{-16}
9.5	10.0	-	-0.1,0.9	-0.2	0.134	1.549×10^{-17}	1.413×10^{-17}
9.5	10.5	0.0,0.9	-0.7,-0.1	-0.8	0.447	4.650×10^{-18}	4.241×10^{-18}
9.5	11.0	-0.8,0.9	-0.9	-	0.507	4.040×10^{-18}	3.666×10^{-18}
9.5	11.5	-1.0,0.9	-	-	0.550	3.728×10^{-18}	3.382×10^{-18}
9.5	12.0	-1.0,0.9	-	-	0.550	3.728×10^{-18}	3.382×10^{-18}
9.5	12.5	-1.0,0.9	-	-	0.550	3.728×10^{-18}	3.382×10^{-18}
9.5	13.0	-1.0,0.9	-	-	0.550	3.728×10^{-18}	3.382×10^{-18}
9.5	13.5	-1.0,0.9	-	-	0.550	3.728×10^{-18}	3.382×10^{-18}
9.5	14.0	-1.0,0.9	-	-	0.550	3.728×10^{-18}	3.382×10^{-18}
9.5	14.5	-1.0,0.9	-	-	0.550	3.728×10^{-18}	3.382×10^{-18}
9.5	15.0	-1.0,0.9	-	-	0.550	3.728×10^{-18}	3.382×10^{-18}
9.5	15.5	-1.0,0.9	-	-	0.550	3.728×10^{-18}	3.382×10^{-18}
9.5	16.0	-1.0,0.9	-	-	0.550	3.728×10^{-18}	3.382×10^{-18}
9.5	16.5	-1.0,0.9	-	-	0.550	3.728×10^{-18}	3.382×10^{-18}
9.5	17.0	-1.0,0.9	-	-	0.550	3.728×10^{-18}	3.382×10^{-18}
9.5	17.5	-1.0,0.9	-	-	0.550	3.728×10^{-18}	3.382×10^{-18}
9.5	18.0	-1.0,0.9	-	-	0.550	3.728×10^{-18}	3.382×10^{-18}
9.5	18.5	-1.0,0.9	-	-	0.550	3.728×10^{-18}	3.382×10^{-18}

Table F.2: (continued)

$\log_{10}$ Mass GeV	$\log_{10}$ E$_{\text{Kin}}$ GeV	$\cos\theta$ bins used for each speed region			$\sum(\Delta\cos\theta)A_{\text{eff}}^{\gamma_d}$ km^2	Final Sensitivity $cm^{-2}sr^{-1}s^{-1}$	Final Limit $cm^{-2}sr^{-1}s^{-1}$
		$\gamma \geq 10$	$2.3 \leq \gamma < 10$	$1.7 \leq \gamma < 2.3$			
10.0	4.0	-	-	-	0.000	-	-
10.0	4.5	-	-	-	0.000	-	-
10.0	5.0	-	-	-	0.000	-	-
10.0	5.5	-	-	-	0.000	-	-
10.0	6.0	-	-	-	0.000	-	-
10.0	6.5	-	-	-	0.000	-	-
10.0	7.0	-	-	-	0.000	-	-
10.0	7.5	-	-	-	0.000	-	-
10.0	8.0	-	-	-	0.000	-	-
10.0	8.5	-	-	-	0.000	-	-
10.0	9.0	-	-	-	0.000	-	-
10.0	9.5	-	-	-	0.000	-	-
10.0	10.0	-	-	0.0,0.9	0.012	1.720×10^{-16}	1.569×10^{-16}
10.0	10.5	-	-0.5,0.9	-0.6	0.333	6.245×10^{-18}	5.696×10^{-18}
10.0	11.0	-0.2,0.9	-0.9,-0.3	-	0.499	4.103×10^{-18}	3.723×10^{-18}
10.0	11.5	-1.0,0.9	-	-	0.550	3.728×10^{-18}	3.382×10^{-18}
10.0	12.0	-1.0,0.9	-	-	0.550	3.728×10^{-18}	3.382×10^{-18}
10.0	12.5	-1.0,0.9	-	-	0.550	3.728×10^{-18}	3.382×10^{-18}
10.0	13.0	-1.0,0.9	-	-	0.550	3.728×10^{-18}	3.382×10^{-18}
10.0	13.5	-1.0,0.9	-	-	0.550	3.728×10^{-18}	3.382×10^{-18}
10.0	14.0	-1.0,0.9	-	-	0.550	3.728×10^{-18}	3.382×10^{-18}
10.0	14.5	-1.0,0.9	-	-	0.550	3.728×10^{-18}	3.382×10^{-18}
10.0	15.0	-1.0,0.9	-	-	0.550	3.728×10^{-18}	3.382×10^{-18}
10.0	15.5	-1.0,0.9	-	-	0.550	3.728×10^{-18}	3.382×10^{-18}

Table F.2: (continued)

$\log_{10}$ Mass GeV	$\log_{10}$ E$_{\text{Kin}}$ GeV	$\cos\theta$ bins used for each speed region			$\sum(\Delta\cos\theta)A_{\text{eff}}^{\gamma_d}$ km²	Final Sensitivity $cm^{-2}sr^{-1}s^{-1}$	Final Limit $cm^{-2}sr^{-1}s^{-1}$
		$\gamma \geq 10$	$2.3 \leq \gamma < 10$	$1.7 \leq \gamma < 2.3$			
10.0	16.0	-1.0,0.9	-	-	0.550	3.728×10^{-18}	3.382×10^{-18}
10.0	16.5	-1.0,0.9	-	-	0.550	3.728×10^{-18}	3.382×10^{-18}
10.0	17.0	-1.0,0.9	-	-	0.550	3.728×10^{-18}	3.382×10^{-18}
10.0	17.5	-1.0,0.9	-	-	0.550	3.728×10^{-18}	3.382×10^{-18}
10.0	18.0	-1.0,0.9	-	-	0.550	3.728×10^{-18}	3.382×10^{-18}
10.0	18.5	-1.0,0.9	-	-	0.550	3.728×10^{-18}	3.382×10^{-18}
10.5	4.0	-	-	-	0.000	-	-
10.5	4.5	-	-	-	0.000	-	-
10.5	5.0	-	-	-	0.000	-	-
10.5	5.5	-	-	-	0.000	-	-
10.5	6.0	-	-	-	0.000	-	-
10.5	6.5	-	-	-	0.000	-	-
10.5	7.0	-	-	-	0.000	-	-
10.5	7.5	-	-	-	0.000	-	-
10.5	8.0	-	-	-	0.000	-	-
10.5	8.5	-	-	-	0.000	-	-
10.5	9.0	-	-	-	0.000	-	-
10.5	9.5	-	-	-	0.000	-	-
10.5	10.0	-	-	-	0.000	-	-
10.5	10.5	-	-	-0.2,0.9	0.080	2.598×10^{-17}	2.369×10^{-17}
10.5	11.0	-	-0.8,0.9	-0.9	0.469	4.434×10^{-18}	4.044×10^{-18}
10.5	11.5	-0.8,0.9	-1.0,-0.9	-	0.545	3.756×10^{-18}	3.408×10^{-18}
10.5	12.0	-1.0,0.9	-	-	0.550	3.728×10^{-18}	3.382×10^{-18}
10.5	12.5	-1.0,0.9	-	-	0.550	3.728×10^{-18}	3.382×10^{-18}

Table F.2: (continued)

$\log_{10}$ Mass GeV	$\log_{10}$ E$_{\text{Kin}}$ GeV	$\cos\theta$ bins used for each speed region			$\sum(\Delta\cos\theta)A_{\text{eff}}^{\gamma_d}$ km^2	Final Sensitivity $cm^{-2}sr^{-1}s^{-1}$	Final Limit $cm^{-2}sr^{-1}s^{-1}$
		$\gamma \geq 10$	$2.3 \leq \gamma < 10$	$1.7 \leq \gamma < 2.3$			
10.5	13.0	-1.0,0.9	-	-	0.550	3.728×10^{-18}	3.382×10^{-18}
10.5	13.5	-1.0,0.9	-	-	0.550	3.728×10^{-18}	3.382×10^{-18}
10.5	14.0	-1.0,0.9	-	-	0.550	3.728×10^{-18}	3.382×10^{-18}
10.5	14.5	-1.0,0.9	-	-	0.550	3.728×10^{-18}	3.382×10^{-18}
10.5	15.0	-1.0,0.9	-	-	0.550	3.728×10^{-18}	3.382×10^{-18}
10.5	15.5	-1.0,0.9	-	-	0.550	3.728×10^{-18}	3.382×10^{-18}
10.5	16.0	-1.0,0.9	-	-	0.550	3.728×10^{-18}	3.382×10^{-18}
10.5	16.5	-1.0,0.9	-	-	0.550	3.728×10^{-18}	3.382×10^{-18}
10.5	17.0	-1.0,0.9	-	-	0.550	3.728×10^{-18}	3.382×10^{-18}
10.5	17.5	-1.0,0.9	-	-	0.550	3.728×10^{-18}	3.382×10^{-18}
10.5	18.0	-1.0,0.9	-	-	0.550	3.728×10^{-18}	3.382×10^{-18}
10.5	18.5	-1.0,0.9	-	-	0.550	3.728×10^{-18}	3.382×10^{-18}
11.0	4.0	-	-	-	0.000	-	-
11.0	4.5	-	-	-	0.000	-	-
11.0	5.0	-	-	-	0.000	-	-
11.0	5.5	-	-	-	0.000	-	-
11.0	6.0	-	-	-	0.000	-	-
11.0	6.5	-	-	-	0.000	-	-
11.0	7.0	-	-	-	0.000	-	-
11.0	7.5	-	-	-	0.000	-	-
11.0	8.0	-	-	-	0.000	-	-
11.0	8.5	-	-	-	0.000	-	-
11.0	9.0	-	-	-	0.000	-	-
11.0	9.5	-	-	-	0.000	-	-

$\log_{10}$ Mass GeV	$\log_{10}$ E$_{\text{Kin}}$ GeV	$\cos\theta$ bins used for each speed region			$\sum(\Delta\cos\theta)A_{\text{eff}}^{\gamma_d}$ km^2	Final Sensitivity $cm^{-2}sr^{-1}s^{-1}$	Final Limit $cm^{-2}sr^{-1}s^{-1}$
		$\gamma \geq 10$	$2.3 \leq \gamma < 10$	$1.7 \leq \gamma < 2.3$			
11.0	10.0	-	-	-	0.000	-	-
11.0	10.5	-	-	-	0.000	-	-
11.0	11.0	-	-	-0.8,0.9	0.284	7.305×10^{-18}	6.662×10^{-18}
11.0	11.5	-	-1.0,0.9	-	0.516	3.945×10^{-18}	3.596×10^{-18}
11.0	12.0	-0.9,0.9	-1.0	-	0.549	3.731×10^{-18}	3.386×10^{-18}
11.0	12.5	-1.0,0.9	-	-	0.550	3.728×10^{-18}	3.382×10^{-18}
11.0	13.0	-1.0,0.9	-	-	0.550	3.728×10^{-18}	3.382×10^{-18}
11.0	13.5	-1.0,0.9	-	-	0.550	3.728×10^{-18}	3.382×10^{-18}
11.0	14.0	-1.0,0.9	-	-	0.550	3.728×10^{-18}	3.382×10^{-18}
11.0	14.5	-1.0,0.9	-	-	0.550	3.728×10^{-18}	3.382×10^{-18}
11.0	15.0	-1.0,0.9	-	-	0.550	3.728×10^{-18}	3.382×10^{-18}
11.0	15.5	-1.0,0.9	-	-	0.550	3.728×10^{-18}	3.382×10^{-18}
11.0	16.0	-1.0,0.9	-	-	0.550	3.728×10^{-18}	3.382×10^{-18}
11.0	16.5	-1.0,0.9	-	-	0.550	3.728×10^{-18}	3.382×10^{-18}
11.0	17.0	-1.0,0.9	-	-	0.550	3.728×10^{-18}	3.382×10^{-18}
11.0	17.5	-1.0,0.9	-	-	0.550	3.728×10^{-18}	3.382×10^{-18}
11.0	18.0	-1.0,0.9	-	-	0.550	3.728×10^{-18}	3.382×10^{-18}
11.0	18.5	-1.0,0.9	-	-	0.550	3.728×10^{-18}	3.382×10^{-18}
11.5	4.0	-	-	-	0.000	-	-
11.5	4.5	-	-	-	0.000	-	-
11.5	5.0	-	-	-	0.000	-	-
11.5	5.5	-	-	-	0.000	-	-
11.5	6.0	-	-	-	0.000	-	-
11.5	6.5	-	-	-	0.000	-	-

Table F.2: (continued)

log$_{10}$ Mass GeV	log$_{10}$ E$_{\text{Kin}}$ GeV	cos θ bins used for each speed region			$\sum(\Delta \cos\theta)A_{\text{eff}}^{\gamma_d}$ km²	Final Sensitivity $cm^{-2}sr^{-1}s^{-1}$	Final Limit $cm^{-2}sr^{-1}s^{-1}$
		$\gamma \geq 10$	$2.3 \leq \gamma < 10$	$1.7 \leq \gamma < 2.3$			
11.5	7.0	-	-	-	0.000	-	-
11.5	7.5	-	-	-	0.000	-	-
11.5	8.0	-	-	-	0.000	-	-
11.5	8.5	-	-	-	0.000	-	-
11.5	9.0	-	-	-	0.000	-	-
11.5	9.5	-	-	-	0.000	-	-
11.5	10.0	-	-	-	0.000	-	-
11.5	10.5	-	-	-	0.000	-	-
11.5	11.0	-	-	-	0.000	-	-
11.5	11.5	-	-	-0.9,0.9	0.314	6.615×10^{-18}	6.033×10^{-18}
11.5	12.0	-	-1.0,0.9	-	0.516	3.945×10^{-18}	3.596×10^{-18}
11.5	12.5	-1.0,0.9	-	-	0.550	3.728×10^{-18}	3.382×10^{-18}
11.5	13.0	-1.0,0.9	-	-	0.550	3.728×10^{-18}	3.382×10^{-18}
11.5	13.5	-1.0,0.9	-	-	0.550	3.728×10^{-18}	3.382×10^{-18}
11.5	14.0	-1.0,0.9	-	-	0.550	3.728×10^{-18}	3.382×10^{-18}
11.5	14.5	-1.0,0.9	-	-	0.550	3.728×10^{-18}	3.382×10^{-18}
11.5	15.0	-1.0,0.9	-	-	0.550	3.728×10^{-18}	3.382×10^{-18}
11.5	15.5	-1.0,0.9	-	-	0.550	3.728×10^{-18}	3.382×10^{-18}
11.5	16.0	-1.0,0.9	-	-	0.550	3.728×10^{-18}	3.382×10^{-18}
11.5	16.5	-1.0,0.9	-	-	0.550	3.728×10^{-18}	3.382×10^{-18}
11.5	17.0	-1.0,0.9	-	-	0.550	3.728×10^{-18}	3.382×10^{-18}
11.5	17.5	-1.0,0.9	-	-	0.550	3.728×10^{-18}	3.382×10^{-18}
11.5	18.0	-1.0,0.9	-	-	0.550	3.728×10^{-18}	3.382×10^{-18}
11.5	18.5	-1.0,0.9	-	-	0.550	3.728×10^{-18}	3.382×10^{-18}

Table F.2: (continued)

$\log_{10}$ Mass GeV	$\log_{10}$ E$_{\text{Kin}}$ GeV	$\cos\theta$ bins used for each speed region			$\sum(\Delta\cos\theta)A_{\text{eff}}^{\gamma_d}$ km^2	Final Sensitivity $cm^{-2}sr^{-1}s^{-1}$	Final Limit $cm^{-2}sr^{-1}s^{-1}$
		$\gamma \geq 10$	$2.3 \leq \gamma < 10$	$1.7 \leq \gamma < 2.3$			
12.0	4.0	-	-	-	0.000	-	-
12.0	4.5	-	-	-	0.000	-	-
12.0	5.0	-	-	-	0.000	-	-
12.0	5.5	-	-	-	0.000	-	-
12.0	6.0	-	-	-	0.000	-	-
12.0	6.5	-	-	-	0.000	-	-
12.0	7.0	-	-	-	0.000	-	-
12.0	7.5	-	-	-	0.000	-	-
12.0	8.0	-	-	-	0.000	-	-
12.0	8.5	-	-	-	0.000	-	-
12.0	9.0	-	-	-	0.000	-	-
12.0	9.5	-	-	-	0.000	-	-
12.0	10.0	-	-	-	0.000	-	-
12.0	10.5	-	-	-	0.000	-	-
12.0	11.0	-	-	-	0.000	-	-
12.0	11.5	-	-	-	0.000	-	-
12.0	12.0	-	-	-1.0,0.9	0.341	6.102×10^{-18}	5.566×10^{-18}
12.0	12.5	-	-1.0,0.9	-	0.516	3.945×10^{-18}	3.596×10^{-18}
12.0	13.0	-1.0,0.9	-	-	0.550	3.728×10^{-18}	3.382×10^{-18}
12.0	13.5	-1.0,0.9	-	-	0.550	3.728×10^{-18}	3.382×10^{-18}
12.0	14.0	-1.0,0.9	-	-	0.550	3.728×10^{-18}	3.382×10^{-18}
12.0	14.5	-1.0,0.9	-	-	0.550	3.728×10^{-18}	3.382×10^{-18}
12.0	15.0	-1.0,0.9	-	-	0.550	3.728×10^{-18}	3.382×10^{-18}
12.0	15.5	-1.0,0.9	-	-	0.550	3.728×10^{-18}	3.382×10^{-18}

Table F.2: (continued)

log₁₀ Mass GeV	log₁₀ E$_{\text{Kin}}$ GeV	$\cos\theta$ bins used for each speed region			$\sum(\Delta\cos\theta)A_{\text{eff}}^{\gamma_d}$ km²	Final Sensitivity $cm^{-2}sr^{-1}s^{-1}$	Final Limit $cm^{-2}sr^{-1}s^{-1}$
		$\gamma \geq 10$	$2.3 \leq \gamma < 10$	$1.7 \leq \gamma < 2.3$			
12.0	16.0	-1.0,0.9	-	-	0.550	3.728×10^{-18}	3.382×10^{-18}
12.0	16.5	-1.0,0.9	-	-	0.550	3.728×10^{-18}	3.382×10^{-18}
12.0	17.0	-1.0,0.9	-	-	0.550	3.728×10^{-18}	3.382×10^{-18}
12.0	17.5	-1.0,0.9	-	-	0.550	3.728×10^{-18}	3.382×10^{-18}
12.0	18.0	-1.0,0.9	-	-	0.550	3.728×10^{-18}	3.382×10^{-18}
12.0	18.5	-1.0,0.9	-	-	0.550	3.728×10^{-18}	3.382×10^{-18}
12.5	4.0	-	-	-	0.000	-	-
12.5	4.5	-	-	-	0.000	-	-
12.5	5.0	-	-	-	0.000	-	-
12.5	5.5	-	-	-	0.000	-	-
12.5	6.0	-	-	-	0.000	-	-
12.5	6.5	-	-	-	0.000	-	-
12.5	7.0	-	-	-	0.000	-	-
12.5	7.5	-	-	-	0.000	-	-
12.5	8.0	-	-	-	0.000	-	-
12.5	8.5	-	-	-	0.000	-	-
12.5	9.0	-	-	-	0.000	-	-
12.5	9.5	-	-	-	0.000	-	-
12.5	10.0	-	-	-	0.000	-	-
12.5	10.5	-	-	-	0.000	-	-
12.5	11.0	-	-	-	0.000	-	-
12.5	11.5	-	-	-	0.000	-	-
12.5	12.0	-	-	-	0.000	-	-
12.5	12.5	-	-	-1.0,0.9	0.341	6.102×10^{-18}	5.566×10^{-18}

Table F.2: (continued)

log$_{10}$ Mass	log$_{10}$ E$_{\text{Kin}}$	cos θ bins used for each speed region			$\sum(\Delta\cos\theta)A_{\text{eff}}^{\gamma_d}$	Final Sensitivity	Final Limit
GeV	GeV	$\gamma \geq 10$	$2.3 \leq \gamma < 10$	$1.7 \leq \gamma < 2.3$	km^2	$cm^{-2}sr^{-1}s^{-1}$	$cm^{-2}sr^{-1}s^{-1}$
12.5	13.0	-	-1.0,0.9	-	0.516	3.945×10^{-18}	3.596×10^{-18}
12.5	13.5	-1.0,0.9	-	-	0.550	3.728×10^{-18}	3.382×10^{-18}
12.5	14.0	-1.0,0.9	-	-	0.550	3.728×10^{-18}	3.382×10^{-18}
12.5	14.5	-1.0,0.9	-	-	0.550	3.728×10^{-18}	3.382×10^{-18}
12.5	15.0	-1.0,0.9	-	-	0.550	3.728×10^{-18}	3.382×10^{-18}
12.5	15.5	-1.0,0.9	-	-	0.550	3.728×10^{-18}	3.382×10^{-18}
12.5	16.0	-1.0,0.9	-	-	0.550	3.728×10^{-18}	3.382×10^{-18}
12.5	16.5	-1.0,0.9	-	-	0.550	3.728×10^{-18}	3.382×10^{-18}
12.5	17.0	-1.0,0.9	-	-	0.550	3.728×10^{-18}	3.382×10^{-18}
12.5	17.5	-1.0,0.9	-	-	0.550	3.728×10^{-18}	3.382×10^{-18}
12.5	18.0	-1.0,0.9	-	-	0.550	3.728×10^{-18}	3.382×10^{-18}
12.5	18.5	-1.0,0.9	-	-	0.550	3.728×10^{-18}	3.382×10^{-18}
13.0	4.0	-	-	-	0.000	-	-
13.0	4.5	-	-	-	0.000	-	-
13.0	5.0	-	-	-	0.000	-	-
13.0	5.5	-	-	-	0.000	-	-
13.0	6.0	-	-	-	0.000	-	-
13.0	6.5	-	-	-	0.000	-	-
13.0	7.0	-	-	-	0.000	-	-
13.0	7.5	-	-	-	0.000	-	-
13.0	8.0	-	-	-	0.000	-	-
13.0	8.5	-	-	-	0.000	-	-
13.0	9.0	-	-	-	0.000	-	-
13.0	9.5	-	-	-	0.000	-	-

$\log_{10}$ Mass GeV	$\log_{10}$ E_{Kin} GeV	$\cos\theta$ bins used for each speed region $\gamma \geq 10$	$2.3 \leq \gamma < 10$	$1.7 \leq \gamma < 2.3$	$\sum(\Delta\cos\theta)A_{eff}^{\gamma_d}$ km^2	Final Sensitivity $cm^{-2}sr^{-1}s^{-1}$	Final Limit $cm^{-2}sr^{-1}s^{-1}$
13.0	10.0	-	-	-	0.000	-	-
13.0	10.5	-	-	-	0.000	-	-
13.0	11.0	-	-	-	0.000	-	-
13.0	11.5	-	-	-	0.000	-	-
13.0	12.0	-	-	-	0.000	-	-
13.0	12.5	-	-	-	0.000	-	-
13.0	13.0	-	-	-1.0,0.9	0.341	6.102×10^{-18}	5.566×10^{-18}
13.0	13.5	-	-1.0,0.9	-	0.516	3.945×10^{-18}	3.596×10^{-18}
13.0	14.0	-1.0,0.9	-	-	0.550	3.728×10^{-18}	3.382×10^{-18}
13.0	14.5	-1.0,0.9	-	-	0.550	3.728×10^{-18}	3.382×10^{-18}
13.0	15.0	-1.0,0.9	-	-	0.550	3.728×10^{-18}	3.382×10^{-18}
13.0	15.5	-1.0,0.9	-	-	0.550	3.728×10^{-18}	3.382×10^{-18}
13.0	16.0	-1.0,0.9	-	-	0.550	3.728×10^{-18}	3.382×10^{-18}
13.0	16.5	-1.0,0.9	-	-	0.550	3.728×10^{-18}	3.382×10^{-18}
13.0	17.0	-1.0,0.9	-	-	0.550	3.728×10^{-18}	3.382×10^{-18}
13.0	17.5	-1.0,0.9	-	-	0.550	3.728×10^{-18}	3.382×10^{-18}
13.0	18.0	-1.0,0.9	-	-	0.550	3.728×10^{-18}	3.382×10^{-18}
13.0	18.5	-1.0,0.9	-	-	0.550	3.728×10^{-18}	3.382×10^{-18}
13.5	4.0	-	-	-	0.000	-	-
13.5	4.5	-	-	-	0.000	-	-
13.5	5.0	-	-	-	0.000	-	-
13.5	5.5	-	-	-	0.000	-	-
13.5	6.0	-	-	-	0.000	-	-
13.5	6.5	-	-	-	0.000	-	-

Table F.2: (continued)

$\log_{10}$ Mass GeV	$\log_{10}$ E$_{\text{Kin}}$ GeV	$\cos\theta$ bins used for each speed region			$\sum(\Delta\cos\theta)A_{\text{eff}}^{\gamma_d}$ km^2	Final Sensitivity $cm^{-2}sr^{-1}s^{-1}$	Final Limit $cm^{-2}sr^{-1}s^{-1}$
		$\gamma \geq 10$	$2.3 \leq \gamma < 10$	$1.7 \leq \gamma < 2.3$			
13.5	7.0	-	-	-	0.000	-	-
13.5	7.5	-	-	-	0.000	-	-
13.5	8.0	-	-	-	0.000	-	-
13.5	8.5	-	-	-	0.000	-	-
13.5	9.0	-	-	-	0.000	-	-
13.5	9.5	-	-	-	0.000	-	-
13.5	10.0	-	-	-	0.000	-	-
13.5	10.5	-	-	-	0.000	-	-
13.5	11.0	-	-	-	0.000	-	-
13.5	11.5	-	-	-	0.000	-	-
13.5	12.0	-	-	-	0.000	-	-
13.5	12.5	-	-	-	0.000	-	-
13.5	13.0	-	-	-	0.000	-	-
13.5	13.5	-	-	-1.0,0.9	0.341	6.102×10^{-18}	5.566×10^{-18}
13.5	14.0	-	-1.0,0.9	-	0.516	3.945×10^{-18}	3.596×10^{-18}
13.5	14.5	-1.0,0.9	-	-	0.550	3.728×10^{-18}	3.382×10^{-18}
13.5	15.0	-1.0,0.9	-	-	0.550	3.728×10^{-18}	3.382×10^{-18}
13.5	15.5	-1.0,0.9	-	-	0.550	3.728×10^{-18}	3.382×10^{-18}
13.5	16.0	-1.0,0.9	-	-	0.550	3.728×10^{-18}	3.382×10^{-18}
13.5	16.5	-1.0,0.9	-	-	0.550	3.728×10^{-18}	3.382×10^{-18}
13.5	17.0	-1.0,0.9	-	-	0.550	3.728×10^{-18}	3.382×10^{-18}
13.5	17.5	-1.0,0.9	-	-	0.550	3.728×10^{-18}	3.382×10^{-18}
13.5	18.0	-1.0,0.9	-	-	0.550	3.728×10^{-18}	3.382×10^{-18}
13.5	18.5	-1.0,0.9	-	-	0.550	3.728×10^{-18}	3.382×10^{-18}

Table F.2: (continued)

$\log_{10}$ Mass GeV	$\log_{10}$ E$_{\text{Kin}}$ GeV	$\cos\theta$ bins used for each speed region			$\sum(\Delta\cos\theta)A_{\text{eff}}^{\gamma_d}$ km^2	Final Sensitivity $cm^{-2}sr^{-1}s^{-1}$	Final Limit $cm^{-2}sr^{-1}s^{-1}$
		$\gamma \geq 10$	$2.3 \leq \gamma < 10$	$1.7 \leq \gamma < 2.3$			
14.0	4.0	-	-	-	0.000	-	-
14.0	4.5	-	-	-	0.000	-	-
14.0	5.0	-	-	-	0.000	-	-
14.0	5.5	-	-	-	0.000	-	-
14.0	6.0	-	-	-	0.000	-	-
14.0	6.5	-	-	-	0.000	-	-
14.0	7.0	-	-	-	0.000	-	-
14.0	7.5	-	-	-	0.000	-	-
14.0	8.0	-	-	-	0.000	-	-
14.0	8.5	-	-	-	0.000	-	-
14.0	9.0	-	-	-	0.000	-	-
14.0	9.5	-	-	-	0.000	-	-
14.0	10.0	-	-	-	0.000	-	-
14.0	10.5	-	-	-	0.000	-	-
14.0	11.0	-	-	-	0.000	-	-
14.0	11.5	-	-	-	0.000	-	-
14.0	12.0	-	-	-	0.000	-	-
14.0	12.5	-	-	-	0.000	-	-
14.0	13.0	-	-	-	0.000	-	-
14.0	13.5	-	-	-	0.000	-	-
14.0	14.0	-	-	-1.0,0.9	0.341	6.102×10^{-18}	5.566×10^{-18}
14.0	14.5	-	-1.0,0.9	-	0.516	3.945×10^{-18}	3.596×10^{-18}
14.0	15.0	-1.0,0.9	-	-	0.550	3.728×10^{-18}	3.382×10^{-18}
14.0	15.5	-1.0,0.9	-	-	0.550	3.728×10^{-18}	3.382×10^{-18}

Table F.2: (continued)

$\log_{10}$ Mass GeV	$\log_{10}$ E_{Kin} GeV	$\cos\theta$ bins used for each speed region			$\sum(\Delta\cos\theta)A_{eff}^{\gamma_d}$ km²	Final Sensitivity $cm^{-2}sr^{-1}s^{-1}$	Final Limit $cm^{-2}sr^{-1}s^{-1}$
		$\gamma \geq 10$	$2.3 \leq \gamma < 10$	$1.7 \leq \gamma < 2.3$			
14.0	16.0	-1.0,0.9	-	-	0.550	3.728×10^{-18}	3.382×10^{-18}
14.0	16.5	-1.0,0.9	-	-	0.550	3.728×10^{-18}	3.382×10^{-18}
14.0	17.0	-1.0,0.9	-	-	0.550	3.728×10^{-18}	3.382×10^{-18}
14.0	17.5	-1.0,0.9	-	-	0.550	3.728×10^{-18}	3.382×10^{-18}
14.0	18.0	-1.0,0.9	-	-	0.550	3.728×10^{-18}	3.382×10^{-18}
14.0	18.5	-1.0,0.9	-	-	0.550	3.728×10^{-18}	3.382×10^{-18}
14.5	4.0	-	-	-	0.000	-	-
14.5	4.5	-	-	-	0.000	-	-
14.5	5.0	-	-	-	0.000	-	-
14.5	5.5	-	-	-	0.000	-	-
14.5	6.0	-	-	-	0.000	-	-
14.5	6.5	-	-	-	0.000	-	-
14.5	7.0	-	-	-	0.000	-	-
14.5	7.5	-	-	-	0.000	-	-
14.5	8.0	-	-	-	0.000	-	-
14.5	8.5	-	-	-	0.000	-	-
14.5	9.0	-	-	-	0.000	-	-
14.5	9.5	-	-	-	0.000	-	-
14.5	10.0	-	-	-	0.000	-	-
14.5	10.5	-	-	-	0.000	-	-
14.5	11.0	-	-	-	0.000	-	-
14.5	11.5	-	-	-	0.000	-	-
14.5	12.0	-	-	-	0.000	-	-
14.5	12.5	-	-	-	0.000	-	-

$\log_{10}$ Mass GeV	$\log_{10}$ E$_{\text{Kin}}$ GeV	$\cos\theta$ bins used for each speed region $\gamma \geq 10$	$2.3 \leq \gamma < 10$	$1.7 \leq \gamma < 2.3$	$\sum(\Delta\cos\theta)A_{\text{eff}}^{\gamma_d}$ km^2	Final Sensitivity $cm^{-2}sr^{-1}s^{-1}$	Final Limit $cm^{-2}sr^{-1}s^{-1}$
14.5	13.0	-	-	-	0.000	-	-
14.5	13.5	-	-	-	0.000	-	-
14.5	14.0	-	-	-	0.000	-	-
14.5	14.5	-	-	-1.0,0.9	0.341	6.102×10^{-18}	5.566×10^{-18}
14.5	15.0	-	-1.0,0.9	-	0.516	3.945×10^{-18}	3.596×10^{-18}
14.5	15.5	-1.0,0.9	-	-	0.550	3.728×10^{-18}	3.382×10^{-18}
14.5	16.0	-1.0,0.9	-	-	0.550	3.728×10^{-18}	3.382×10^{-18}
14.5	16.5	-1.0,0.9	-	-	0.550	3.728×10^{-18}	3.382×10^{-18}
14.5	17.0	-1.0,0.9	-	-	0.550	3.728×10^{-18}	3.382×10^{-18}
14.5	17.5	-1.0,0.9	-	-	0.550	3.728×10^{-18}	3.382×10^{-18}
14.5	18.0	-1.0,0.9	-	-	0.550	3.728×10^{-18}	3.382×10^{-18}
14.5	18.5	-1.0,0.9	-	-	0.550	3.728×10^{-18}	3.382×10^{-18}
15.0	4.0	-	-	-	0.000	-	-
15.0	4.5	-	-	-	0.000	-	-
15.0	5.0	-	-	-	0.000	-	-
15.0	5.5	-	-	-	0.000	-	-
15.0	6.0	-	-	-	0.000	-	-
15.0	6.5	-	-	-	0.000	-	-
15.0	7.0	-	-	-	0.000	-	-
15.0	7.5	-	-	-	0.000	-	-
15.0	8.0	-	-	-	0.000	-	-
15.0	8.5	-	-	-	0.000	-	-
15.0	9.0	-	-	-	0.000	-	-
15.0	9.5	-	-	-	0.000	-	-

Table F.2: (continued)

| $\log_{10}$ Mass GeV | $\log_{10}$ E$_{\mathrm{Kin}}$ GeV | $\cos\theta$ bins used for each speed region | | | $\sum(\Delta\cos\theta)A_{\mathrm{eff}}^{\gamma_d}$ km² | Final Sensitivity $cm^{-2}sr^{-1}s^{-1}$ | Final Limit $cm^{-2}sr^{-1}s^{-1}$ |
		$\gamma \geq 10$	$2.3 \leq \gamma < 10$	$1.7 \leq \gamma < 2.3$			
15.0	10.0	-	-	-	0.000	-	-
15.0	10.5	-	-	-	0.000	-	-
15.0	11.0	-	-	-	0.000	-	-
15.0	11.5	-	-	-	0.000	-	-
15.0	12.0	-	-	-	0.000	-	-
15.0	12.5	-	-	-	0.000	-	-
15.0	13.0	-	-	-	0.000	-	-
15.0	13.5	-	-	-	0.000	-	-
15.0	14.0	-	-	-	0.000	-	-
15.0	14.5	-	-	-	0.000	-	-
15.0	15.0	-	-	-1.0,0.9	0.341	6.102×10^{-18}	5.566×10^{-18}
15.0	15.5	-	-1.0,0.9	-	0.516	3.945×10^{-18}	3.596×10^{-18}
15.0	16.0	-1.0,0.9	-	-	0.550	3.728×10^{-18}	3.382×10^{-18}
15.0	16.5	-1.0,0.9	-	-	0.550	3.728×10^{-18}	3.382×10^{-18}
15.0	17.0	-1.0,0.9	-	-	0.550	3.728×10^{-18}	3.382×10^{-18}
15.0	17.5	-1.0,0.9	-	-	0.550	3.728×10^{-18}	3.382×10^{-18}
15.0	18.0	-1.0,0.9	-	-	0.550	3.728×10^{-18}	3.382×10^{-18}
15.0	18.5	-1.0,0.9	-	-	0.550	3.728×10^{-18}	3.382×10^{-18}
15.5	4.0	-	-	-	0.000	-	-
15.5	4.5	-	-	-	0.000	-	-
15.5	5.0	-	-	-	0.000	-	-
15.5	5.5	-	-	-	0.000	-	-
15.5	6.0	-	-	-	0.000	-	-
15.5	6.5	-	-	-	0.000	-	-

Table F.2: (continued)

log$_{10}$ Mass GeV	log$_{10}$ E$_{\text{Kin}}$ GeV	$\cos\theta$ bins used for each speed region			$\sum(\Delta\cos\theta)A_{\text{eff}}^{\gamma_d}$ km^2	Final Sensitivity $cm^{-2}sr^{-1}s^{-1}$	Final Limit $cm^{-2}sr^{-1}s^{-1}$
		$\gamma \geq 10$	$2.3 \leq \gamma < 10$	$1.7 \leq \gamma < 2.3$			
15.5	7.0	-	-	-	0.000	-	-
15.5	7.5	-	-	-	0.000	-	-
15.5	8.0	-	-	-	0.000	-	-
15.5	8.5	-	-	-	0.000	-	-
15.5	9.0	-	-	-	0.000	-	-
15.5	9.5	-	-	-	0.000	-	-
15.5	10.0	-	-	-	0.000	-	-
15.5	10.5	-	-	-	0.000	-	-
15.5	11.0	-	-	-	0.000	-	-
15.5	11.5	-	-	-	0.000	-	-
15.5	12.0	-	-	-	0.000	-	-
15.5	12.5	-	-	-	0.000	-	-
15.5	13.0	-	-	-	0.000	-	-
15.5	13.5	-	-	-	0.000	-	-
15.5	14.0	-	-	-	0.000	-	-
15.5	14.5	-	-	-	0.000	-	-
15.5	15.0	-	-	-	0.000	-	-
15.5	15.5	-	-	-1.0,0.9	0.341	6.102×10^{-18}	5.566×10^{-18}
15.5	16.0	-	-1.0,0.9	-	0.516	3.945×10^{-18}	3.596×10^{-18}
15.5	16.5	-1.0,0.9	-	-	0.550	3.728×10^{-18}	3.382×10^{-18}
15.5	17.0	-1.0,0.9	-	-	0.550	3.728×10^{-18}	3.382×10^{-18}
15.5	17.5	-1.0,0.9	-	-	0.550	3.728×10^{-18}	3.382×10^{-18}
15.5	18.0	-1.0,0.9	-	-	0.550	3.728×10^{-18}	3.382×10^{-18}
15.5	18.5	-1.0,0.9	-	-	0.550	3.728×10^{-18}	3.382×10^{-18}

Table F.2: (continued)

log$_{10}$ Mass GeV	log$_{10}$ E$_{\text{Kin}}$ GeV	cos θ bins used for each speed region			$\sum(\Delta\cos\theta)A_{\text{eff}}^{\gamma_d}$ km^2	Final Sensitivity $cm^{-2}sr^{-1}s^{-1}$	Final Limit $cm^{-2}sr^{-1}s^{-1}$
		$\gamma \geq 10$	$2.3 \leq \gamma < 10$	$1.7 \leq \gamma < 2.3$			
16.0	4.0	-	-	-	0.000	-	-
16.0	4.5	-	-	-	0.000	-	-
16.0	5.0	-	-	-	0.000	-	-
16.0	5.5	-	-	-	0.000	-	-
16.0	6.0	-	-	-	0.000	-	-
16.0	6.5	-	-	-	0.000	-	-
16.0	7.0	-	-	-	0.000	-	-
16.0	7.5	-	-	-	0.000	-	-
16.0	8.0	-	-	-	0.000	-	-
16.0	8.5	-	-	-	0.000	-	-
16.0	9.0	-	-	-	0.000	-	-
16.0	9.5	-	-	-	0.000	-	-
16.0	10.0	-	-	-	0.000	-	-
16.0	10.5	-	-	-	0.000	-	-
16.0	11.0	-	-	-	0.000	-	-
16.0	11.5	-	-	-	0.000	-	-
16.0	12.0	-	-	-	0.000	-	-
16.0	12.5	-	-	-	0.000	-	-
16.0	13.0	-	-	-	0.000	-	-
16.0	13.5	-	-	-	0.000	-	-
16.0	14.0	-	-	-	0.000	-	-
16.0	14.5	-	-	-	0.000	-	-
16.0	15.0	-	-	-	0.000	-	-
16.0	15.5	-	-	-	0.000	-	-

Table F.2: (continued)

log$_{10}$ Mass GeV	log$_{10}$ E$_{\text{Kin}}$ GeV	$\cos\theta$ bins used for each speed region			$\sum(\Delta\cos\theta)A_{\text{eff}}^{\gamma_d}$ km^2	Final Sensitivity $cm^{-2}sr^{-1}s^{-1}$	Final Limit $cm^{-2}sr^{-1}s^{-1}$
		$\gamma \geq 10$	$2.3 \leq \gamma < 10$	$1.7 \leq \gamma < 2.3$			
16.0	16.0	-	-	-1.0,0.9	0.341	6.102×10^{-18}	5.566×10^{-18}
16.0	16.5	-	-1.0,0.9	-	0.516	3.945×10^{-18}	3.596×10^{-18}
16.0	17.0	-1.0,0.9	-	-	0.550	3.728×10^{-18}	3.382×10^{-18}
16.0	17.5	-1.0,0.9	-	-	0.550	3.728×10^{-18}	3.382×10^{-18}
16.0	18.0	-1.0,0.9	-	-	0.550	3.728×10^{-18}	3.382×10^{-18}
16.0	18.5	-1.0,0.9	-	-	0.550	3.728×10^{-18}	3.382×10^{-18}
16.5	4.0	-	-	-	0.000	-	-
16.5	4.5	-	-	-	0.000	-	-
16.5	5.0	-	-	-	0.000	-	-
16.5	5.5	-	-	-	0.000	-	-
16.5	6.0	-	-	-	0.000	-	-
16.5	6.5	-	-	-	0.000	-	-
16.5	7.0	-	-	-	0.000	-	-
16.5	7.5	-	-	-	0.000	-	-
16.5	8.0	-	-	-	0.000	-	-
16.5	8.5	-	-	-	0.000	-	-
16.5	9.0	-	-	-	0.000	-	-
16.5	9.5	-	-	-	0.000	-	-
16.5	10.0	-	-	-	0.000	-	-
16.5	10.5	-	-	-	0.000	-	-
16.5	11.0	-	-	-	0.000	-	-
16.5	11.5	-	-	-	0.000	-	-
16.5	12.0	-	-	-	0.000	-	-
16.5	12.5	-	-	-	0.000	-	-

Table F.2: (continued)

$\log_{10}$ Mass GeV	$\log_{10}$ E_{Kin} GeV	\multicolumn{3}{c}{$\cos\theta$ bins used for each speed region}	$\sum(\Delta\cos\theta)A_{eff}^{\gamma_d}$ km²	Final Sensitivity $cm^{-2}sr^{-1}s^{-1}$	Final Limit $cm^{-2}sr^{-1}s^{-1}$
		$\gamma \geq 10$	$2.3 \leq \gamma < 10$	$1.7 \leq \gamma < 2.3$			
16.5	13.0	-	-	-	0.000	-	-
16.5	13.5	-	-	-	0.000	-	-
16.5	14.0	-	-	-	0.000	-	-
16.5	14.5	-	-	-	0.000	-	-
16.5	15.0	-	-	-	0.000	-	-
16.5	15.5	-	-	-	0.000	-	-
16.5	16.0	-	-	-	0.000	-	-
16.5	16.5	-	-	-1.0,0.9	0.341	6.102×10^{-18}	5.566×10^{-18}
16.5	17.0	-	-1.0,0.9	-	0.516	3.945×10^{-18}	3.596×10^{-18}
16.5	17.5	-1.0,0.9	-	-	0.550	3.728×10^{-18}	3.382×10^{-18}
16.5	18.0	-1.0,0.9	-	-	0.550	3.728×10^{-18}	3.382×10^{-18}
16.5	18.5	-1.0,0.9	-	-	0.550	3.728×10^{-18}	3.382×10^{-18}
17.0	4.0	-	-	-	0.000	-	-
17.0	4.5	-	-	-	0.000	-	-
17.0	5.0	-	-	-	0.000	-	-
17.0	5.5	-	-	-	0.000	-	-
17.0	6.0	-	-	-	0.000	-	-
17.0	6.5	-	-	-	0.000	-	-
17.0	7.0	-	-	-	0.000	-	-
17.0	7.5	-	-	-	0.000	-	-
17.0	8.0	-	-	-	0.000	-	-
17.0	8.5	-	-	-	0.000	-	-
17.0	9.0	-	-	-	0.000	-	-
17.0	9.5	-	-	-	0.000	-	-

Table F.2: (continued)

$\log_{10}$ Mass GeV	$\log_{10}$ E_{Kin} GeV	$\cos\theta$ bins used for each speed region			$\sum(\Delta\cos\theta)A_{\text{eff}}^{\gamma_d}$ km^2	Final Sensitivity $cm^{-2}sr^{-1}s^{-1}$	Final Limit $cm^{-2}sr^{-1}s^{-1}$
		$\gamma \geq 10$	$2.3 \leq \gamma < 10$	$1.7 \leq \gamma < 2.3$			
17.0	10.0	-	-	-	0.000	-	-
17.0	10.5	-	-	-	0.000	-	-
17.0	11.0	-	-	-	0.000	-	-
17.0	11.5	-	-	-	0.000	-	-
17.0	12.0	-	-	-	0.000	-	-
17.0	12.5	-	-	-	0.000	-	-
17.0	13.0	-	-	-	0.000	-	-
17.0	13.5	-	-	-	0.000	-	-
17.0	14.0	-	-	-	0.000	-	-
17.0	14.5	-	-	-	0.000	-	-
17.0	15.0	-	-	-	0.000	-	-
17.0	15.5	-	-	-	0.000	-	-
17.0	16.0	-	-	-	0.000	-	-
17.0	16.5	-	-	-	0.000	-	-
17.0	17.0	-	-	-1.0,0.9	0.341	6.102×10^{-18}	5.566×10^{-18}
17.0	17.5	-	-1.0,0.9	-	0.516	3.945×10^{-18}	3.596×10^{-18}
17.0	18.0	-1.0,0.9	-	-	0.550	3.728×10^{-18}	3.382×10^{-18}
17.0	18.5	-1.0,0.9	-	-	0.550	3.728×10^{-18}	3.382×10^{-18}
17.5	4.0	-	-	-	0.000	-	-
17.5	4.5	-	-	-	0.000	-	-
17.5	5.0	-	-	-	0.000	-	-
17.5	5.5	-	-	-	0.000	-	-
17.5	6.0	-	-	-	0.000	-	-
17.5	6.5	-	-	-	0.000	-	-

Table F.2: (continued)

$\log_{10}$ Mass GeV	$\log_{10}$ E$_{\text{Kin}}$ GeV	$\cos\theta$ bins used for each speed region			$\sum(\Delta\cos\theta)A_{\text{eff}}^{\gamma_d}$ km²	Final Sensitivity $cm^{-2}sr^{-1}s^{-1}$	Final Limit $cm^{-2}sr^{-1}s^{-1}$
		$\gamma \geq 10$	$2.3 \leq \gamma < 10$	$1.7 \leq \gamma < 2.3$			
17.5	7.0	-	-	-	0.000	-	-
17.5	7.5	-	-	-	0.000	-	-
17.5	8.0	-	-	-	0.000	-	-
17.5	8.5	-	-	-	0.000	-	-
17.5	9.0	-	-	-	0.000	-	-
17.5	9.5	-	-	-	0.000	-	-
17.5	10.0	-	-	-	0.000	-	-
17.5	10.5	-	-	-	0.000	-	-
17.5	11.0	-	-	-	0.000	-	-
17.5	11.5	-	-	-	0.000	-	-
17.5	12.0	-	-	-	0.000	-	-
17.5	12.5	-	-	-	0.000	-	-
17.5	13.0	-	-	-	0.000	-	-
17.5	13.5	-	-	-	0.000	-	-
17.5	14.0	-	-	-	0.000	-	-
17.5	14.5	-	-	-	0.000	-	-
17.5	15.0	-	-	-	0.000	-	-
17.5	15.5	-	-	-	0.000	-	-
17.5	16.0	-	-	-	0.000	-	-
17.5	16.5	-	-	-	0.000	-	-
17.5	17.0	-	-	-	0.000	-	-
17.5	17.5	-	-	-1.0,0.9	0.341	6.102×10^{-18}	5.566×10^{-18}
17.5	18.0	-	-1.0,0.9	-	0.516	3.945×10^{-18}	3.596×10^{-18}
17.5	18.5	-1.0,0.9	-	-	0.550	3.728×10^{-18}	3.382×10^{-18}

$\log_{10}$ Mass GeV	$\log_{10}$ E_{Kin} GeV	$\cos\theta$ bins used for each speed region			$\sum(\Delta\cos\theta)A_{\text{eff}}^{\gamma_d}$ km^2	Final Sensitivity $cm^{-2}sr^{-1}s^{-1}$	Final Limit $cm^{-2}sr^{-1}s^{-1}$
		$\gamma \geq 10$	$2.3 \leq \gamma < 10$	$1.7 \leq \gamma < 2.3$			
18.0	4.0	-	-	-	0.000	-	-
18.0	4.5	-	-	-	0.000	-	-
18.0	5.0	-	-	-	0.000	-	-
18.0	5.5	-	-	-	0.000	-	-
18.0	6.0	-	-	-	0.000	-	-
18.0	6.5	-	-	-	0.000	-	-
18.0	7.0	-	-	-	0.000	-	-
18.0	7.5	-	-	-	0.000	-	-
18.0	8.0	-	-	-	0.000	-	-
18.0	8.5	-	-	-	0.000	-	-
18.0	9.0	-	-	-	0.000	-	-
18.0	9.5	-	-	-	0.000	-	-
18.0	10.0	-	-	-	0.000	-	-
18.0	10.5	-	-	-	0.000	-	-
18.0	11.0	-	-	-	0.000	-	-
18.0	11.5	-	-	-	0.000	-	-
18.0	12.0	-	-	-	0.000	-	-
18.0	12.5	-	-	-	0.000	-	-
18.0	13.0	-	-	-	0.000	-	-
18.0	13.5	-	-	-	0.000	-	-
18.0	14.0	-	-	-	0.000	-	-
18.0	14.5	-	-	-	0.000	-	-
18.0	15.0	-	-	-	0.000	-	-
18.0	15.5	-	-	-	0.000	-	-

Table F.2: (continued)

$\log_{10}$ Mass GeV	$\log_{10}$ E$_{\text{Kin}}$ GeV	$\cos\theta$ bins used for each speed region			$\sum(\Delta\cos\theta)A_{\text{eff}}^{\gamma_d}$ km^2	Final Sensitivity $cm^{-2}sr^{-1}s^{-1}$	Final Limit $cm^{-2}sr^{-1}s^{-1}$
		$\gamma \geq 10$	$2.3 \leq \gamma < 10$	$1.7 \leq \gamma < 2.3$			
18.0	16.0	-	-	-	0.000	-	-
18.0	16.5	-	-	-	0.000	-	-
18.0	17.0	-	-	-	0.000	-	-
18.0	17.5	-	-	-	0.000	-	-
18.0	18.0	-	-	-1.0,0.9	0.341	6.102×10^{-18}	5.566×10^{-18}
18.0	18.5	-	-1.0,0.9	-	0.516	3.945×10^{-18}	3.596×10^{-18}
18.5	4.0	-	-	-	0.000	-	-
18.5	4.5	-	-	-	0.000	-	-
18.5	5.0	-	-	-	0.000	-	-
18.5	5.5	-	-	-	0.000	-	-
18.5	6.0	-	-	-	0.000	-	-
18.5	6.5	-	-	-	0.000	-	-
18.5	7.0	-	-	-	0.000	-	-
18.5	7.5	-	-	-	0.000	-	-
18.5	8.0	-	-	-	0.000	-	-
18.5	8.5	-	-	-	0.000	-	-
18.5	9.0	-	-	-	0.000	-	-
18.5	9.5	-	-	-	0.000	-	-
18.5	10.0	-	-	-	0.000	-	-
18.5	10.5	-	-	-	0.000	-	-
18.5	11.0	-	-	-	0.000	-	-
18.5	11.5	-	-	-	0.000	-	-
18.5	12.0	-	-	-	0.000	-	-
18.5	12.5	-	-	-	0.000	-	-

Table F.2: (continued)

$\log_{10}$ Mass GeV	$\log_{10}$ E$_{\text{Kin}}$ GeV	$\cos\theta$ bins used for each speed region			$\sum(\Delta\cos\theta)A_{\text{eff}}^{\gamma_d}$ km^2	Final Sensitivity $cm^{-2}sr^{-1}s^{-1}$	Final Limit $cm^{-2}sr^{-1}s^{-1}$
		$\gamma \geq 10$	$2.3 \leq \gamma < 10$	$1.7 \leq \gamma < 2.3$			
18.5	13.0	-	-	-	0.000	-	-
18.5	13.5	-	-	-	0.000	-	-
18.5	14.0	-	-	-	0.000	-	-
18.5	14.5	-	-	-	0.000	-	-
18.5	15.0	-	-	-	0.000	-	-
18.5	15.5	-	-	-	0.000	-	-
18.5	16.0	-	-	-	0.000	-	-
18.5	16.5	-	-	-	0.000	-	-
18.5	17.0	-	-	-	0.000	-	-
18.5	17.5	-	-	-	0.000	-	-
18.5	18.0	-	-	-	0.000	-	-
18.5	18.5	-	-	-1.0,0.9	0.341	6.102×10^{-18}	5.566×10^{-18}

Bibliography

[1] Needham, J. *Magnetism and Electricity* Science and Civilization in China, Cambridge Univeristy Press, Cambridge Vol. 4 (1962) 229-334

[2] Maricourt,P. *On the Magnet* Letter to Siger de Foucaucort (1296) translated in *The Letter of Petrus Peregrinus on the Magnet*, ed. by Brother Arnold, McGraw, New York (1904), Pt. 1

[3] Gilbert, W. *On the Loadstone and Magnetic Bodies* translated by P. Fleury Mottelay in *Great Books of the Western World*, ed. by R. M. Hutchins, Encyclopedia Britannica, Inc. (1952) Vol. 28

[4] Coulomb, C.A. *Law of Magnetic Force* (1788) translated in *A Source Book in Physics*, ed. by W.F. Magie, Harvard University Press, Cambridge (1935) 417-420

[5] Ampere, A.M. *Electrodynamic Model of Magnetism* (1820) translated in *A Source Book in Physics*, ed. by W.F. Magie, Harvard University Press, Cambridge (1935) 447-460

[6] Maxwell, J.C. *A dynamical theory of the electromagnetic field* Philosophical Transactions of the Royal Society of London 155 (1865) 459-512 [doi:10.1098/rstl.1865.0008]

[7] Maxwell, J.C. *On physical lines of force* Philosophical Magazine (1861)

[8] Curie, P. *On the Possible Existence of Magnetic Conductivity and Free Magnetism*(in French). Seacnes Soc. Phys. Paris (1894), 76-77

[9] Ehrenhaft, F. *Magnetophotophoresis and Electrophotophoresis*(in German). Phys. Z. 31 (1930) 478-485

[10] Goldhaber, A.S. and Trower, W.P. *Resource Letter MM-1: Magnetic Monopoles* Am. J. Phys. 58 (1990) 429-439

[11] Dirac, P.A.M. *Quantized Singularities in the Electromagnetic Field* Proc. Roy. Soc. A 133 (1931) 60

[12] Jackson, J.D., *Classical Electrodynamcs* second ed., John Wiley and Sons, New York, London, Sydney, and Toronto (1975)

[13] Wu and Yang, *Concept of nonintegrable phase factors and global formulation of gauge fields* Phys. Rev. D 12 (1975) 3854

[14] Sakurai, J.J., *Modern Quantum Mechanics* Pearson Education (1994) IBSN 81-7808-006-0

[15] t'Hooft, G. *Magnetic Monopoles in Unified Gauge Theories* Nucl. Phys. B 79 (1974) 276

[16] Polyakov, A. *Spektr tschastiz w kwantowoi teorii polya* Pisma Zhournal ETP 20 (1974) 430

[17] Kibble, T.W.B. *Topology of Cosmic Domains and Strings* J. of Phys. **A9** (1976) 1387-98

[18] Vilenkin, A. and Shellard, E.P.S. *Cosmic Strings and Other Topological Defects* Cambridge University, Cambridge, England 1994

[19] Preskill, J. *Cosmological Production of Superheavy Magnetic Monopoles* Phys. Rev. Lett. **43** (1979) 1365-8

[20] Guth, A. *The Inflationary Universe* Addison-Wesley, Reading MA IBSN: 0-201-14942-7

[21] Kephart, T.W. and Shafi, Q. *Family Unification, exotic States and magnetic monopoles* Phys. Lett. B. 520 (2001) 313-316

[22] Wick,S. D. et al., *Signatures for a Cosmic Flux of Magnetic Monopoles* Astropart. Phys. 18 (2003) 663

[23] Cherenkov,P.A. *Visible radiation produced by electrons moving in a medium with velocities exceeding that of light* Phys. Rev. Lett. 52 (1937) 378

[24] D. Tompkins. *Total Energy Loss and Cherenkov Emission from Monopoles* Phys. Rev. B 138 (1965) 248

[25] C. A. Mead. *Quantum theory of the refractive index.* Phys. Rev., **110(2)** (1958) 359-369.

[26] Abbasi et al. (IceCube Collaboration) *Calibration and characterization of the IceCube photomultiplier tube* Nuclear Instr. and Meth. in Phys. Res. A **618** (2010) 139-152

[27] S. Ahlen, *Stopping Power Formula for Magnetic Monopoles* Phys. Rev. D 17 (1978) 229

[28] Sternheimer, R.M. and Peierls, R.F.*General Expression for the Density Effect for the Ionization Loss of Charged Particles* Phys. Rev. B 3 (1971) 3681

[29] M. Detrixhe et al. (The ANITA Collaboration). *Ultra-Relativistic Magnetic Monopole Search with the ANITA-II Balloon-borne Radio Interferometer.* arXiv:1008.1282v2 [astro-ph.HE].

[30] Dutta et al. *Propagation of Muons and Taus at High Energies.* [arXiv:hep-ph/0012350v1].

[31] B. Cabrera. *First Results from a Superconductive Detector for Moving Magnetic Monopoles* Phys. Rev. Lett. 48 (1982) 1378

[32] Parker, E.N. *The Generation of Magnetic Fields in Astrophysical Bodies II: The Galactic Field* Astrophys. J. 134 (1971) 225

[33] Turner, M. et al. *Magnetic Monopoles and the Survival of the Galactic Magnetic Fields* Phys. Rev. D 26 (1982) 1296

[34] Adams, F.C. et al. *Extension of the Parker Bound on the Flux of Magnetic Monopoles* Phys. Rev. Lett. 70 (1993) 2511-2514

[35] Callan, C.G. *Disappearing Dyons* Phys. Rev. D 25 (1982) 2141

[36] Rubakov, V.A. *Monopole catalysis of proton decay* Rept. Prog. Phys. 51 (1988) 189-241

[37] Kolb,E.W., Colgate,S.A. and Harvey, J.A. *Monopole catalysis of nucleon decay in neutron stars* Phys. Rev. Lett. 49 (1982) 1373

[38] Dimopoulos, S., Preskill, J., and Wilczek, F. *Catalyzed nucleon decay in neutron stars* Phys. Lett. B 119 (1982) 320

[39] Giacomelli, G. and Margiotta, A. *The MACRO Experiment at Gran Sasso* Talk given for Chales Peck at Fest, Caltech (2005) [arXiv:0707.1691v1 [hep-ex]]

[40] Ambrosio, M. et al (The MACRO Collaboration) *Final results of magnetic monopole searches with the MACRO experiment* Eur. Phys. J. C25 (2002), 511-522 [arXiv:hep-ex/0207020v2]

[41] Ahlen, S. et al (The MACRO Collaboration) *First supermodule of the MACRO detector at Gran Sasso* Nucl. Inst. Meth. A 324 (1993), 337-362

[42] Drell, S. et al *Energy Loss of Slowly Moving Magnetic Monopoles in Matter* Phys. Rev. Lett. 50 (1983) 644-648

[43] Price, P.B. and Salamon, M.H. *Search for Supermassive Magnetic Monopoles using Mica Crystals* Phys. Rev. Lett. 56 (1986), 1226-1229

[44] Abbasi et al. (The IceCube Collaboration) *Search for relativistic magnetic monopoles with the AMANDA-II neutrino telescope* Eur. Phys. J. C (2010) 69: 361-378

[45] Neissen, P. *Search for Relativistic Magnetic Monopoles with the AMANDA Detector* Doctoral Dissertation 2001

[46] K. Antipin et al. *Search for Relativistic Magnetic Monopoles with the Baikal Neutrino Telescope* Astropart. Phys. 29 (2008) 366-372

[47] Hogan,D.P. et al. *Relativistic Magnetic Monopole Flux Constraints from RICE* Phys Rev D. 78, (2008) [arXiv:0806.2129v2 [astro-ph]]

[48] Davis, R., Harmer, D., and Hoffman, K. *Search for Neutrinos from the Sun* Phys. Rev. Lett. **20** (1968) 1205-1209

[49] Koshiba et al. (Kamiokande Collaboration) *Observation of a neutrino burst from the supernova SN1987A* Phys. Rev. Lett. **58** (1987) 1490-1493

[50] Waxman, E. and Bahcall, J. *High Energy Neutrinos from Astrophysical Sources: An Upper Bound* Phys. Rev. D. **59** (1999) arXiv:hep-ph/9807282v2
Waxman, E. and Bahcall, J. *High Energy Astrophysical Neutrinos: the Upper Bound is Robust* Phys. Rev. D. **64** (2001) arXiv:hep-ph/9902383v2

[51] Nakamura, K. et al. (Particle Data Group) *24. Cosmic Rays* J. Phys. G **37**, (2010) 075021 http://pdg.lbl.gov/2010/reviews/rpp2010-rev-cosmic-rays.pdf

[52] Taken from: http://www.physics.utah.edu/ whanlon/spectrum.html Includes references to:
Seo et al. (LEAP) Astrophys J, **378** (1991) 736-772
Grigorov et al. (Proton Satellite) Proceedings of the 12th ICRC **5** (1971) 1760
Afanasiev et al. (Yakutsk) Porc. Int. Symp. On Extremely High Energy Cosmic Rays; Astrophysics and Future Observations, ed. M. Nagano, ICRR, U. of Tokyo (1996)

Lawrence et al. (Haverah) J. Phys. G. Nucl. Part. Phys. **17** (1991) 733

Nagano et al. (AGASA) J. Phys. G. Nucl. Part. Phys. **18** (1992) 423

Bird et al. (Fly's Eye) Astrophys. J. **424** (1994) 491

Abbasi et al. (HiRes) Phys. Rev. Lett. **100** (2008)

Abbasi et al. (HiRes) Astropart. Phys. **32** (2009) 53

Abraham et al. (Auger) Phys. Rev. Lett. **101** (2008)

[53] Greisen, K. *End to the cosmic ray spectrum?* Phys. Rev. Lett. **16** (1966) 748

[54] Sokolsky, P. and Thomson, G.B. *Highest Energy Cosmic Rays and the results from the HiRes Experiment* J. Phys. G **34**:R401 (2007) arXiv:0706.1248v1 [astro-ph]

Abreu et al. (Pierre Auger Collaboration) *Measurement of the energy spectrum of cosmic rays above 10^{18} eV using the Pierre Auger Observatory* Phys. Lett. B **685** (2010) 239-246 arXiv:1002.1975v1 [astro-ph.HE]

[55] Bluemer, J., Engel, R., and Hoerandel, J.R. *Cosmic Rays from the Knee to the Highest Energies* Prog. Part. Nucl. Phys. **63** (2009) 293-338 arXiv:0904.0725v1 [astro-ph.HE]

Hoerendal, J.R. *On the knee in the energy spectrum of cosmic rays* Astropart. Phys. **19** (2003) 193-220

[56] Fermi, E. *On the Origin of Cosmic Radiation* Phys. Rev. **75** (1949) 1169-1174

[57] Abbasi et al. (IceCube Collaboration) *Measurement of the Anisotropy of Cosmic Ray Arrival Directions with IceCube* Astrophys. J. **718** (2010) 194 arXiv:1005.2960v1 [astro-ph.HE]

[58] Abbasi et al. (IceCube Collaboration) *Measurement of the atmospheric neutrino energy spectrum from 100 GeV to 400 TeV with IceCube* Phys. Rev. D **83** (2011) arXiv:1010.3980v2 [astro-ph.HE]

[59] Abbasi et al. (IceCube Collaboration) *First Neutrino Point-Source Results from the 22-String IceCube Detector* Astrophys. J. **701** (2009) 47-51 arXiv:0905.2253v2 [astro-ph.HE]

[60] Gaisser, T.K. and Honda, M. *Flux of atmospheric neutrinos* Ann. Rev. Nucl. Part. Sci. **52** (2002) 153-199 arXiv:hep-ph/0203272

[61] Lipari, P. *Lepton spectra in the earth's atmosphere* Astropart. Phys. **1** (1993) 195-227

[62] Abbasi et al. (IceCube Collaboration) *Time-Integrated Searches for Point-like Sources of Neutrinos with the 40-string IceCube Detector* Astrophys. J. **732** (2011) arXiv:1012.2137v1 [astro-ph.HE]

[63] Abbasi et al. (IceCube Collaboration) *A Search for a Diffuse Flux of Astrophysical Muon Neutrinos with the IceCube 40-String Detector* Submitted to Phys. Rev. D (2011) arXiv:1104.5187v1 [astro-ph.HE]

[64] Abbasi et al. (IceCube Collaboration) *Limits on Neutrino emission from Gamma-Ray Bursts with the 40 String IceCube Detector* Phys. Rev. Lett. **106** (2011) arXiv:1101.1448v2 [astro-ph.HE]

[65] Waxman, E., and Bahcall, J. *High Energy Neutrinos from Cosmological Gamma-Ray Burst Fireballs* Phys. Rev. Lett. **78** (1997) 2292-2295 arXiv:astro-ph/9701231v1
Guetta et al. *Neutrinos from Individual Gamma-Ray Bursts in the BATSE Catalog* Astropart. Phys. **20** (2004) 429-455 arXiv:astro-ph/0302524v2

[66] Redl, P. *A Search for Muon Neutrinos Coincident with Gamma-Ray Bursts with the IceCube 59-String Detector* Ph.D. Dissertation, University of Maryland (2011)

[67] Abbasi et al. (IceCube Collaboration) *Constraints on the Extremely-high Energy Cosmic Neutrino Flux with the IceCube 2008-2009 Data* Phys. Rev. D **83** (2011) arXiv:1103.4250v2 [astro-ph.CO]

[68] Ackermann, M. et al. (AMANDA Collaboration) *Optical Properties of Deep Glacial ice at the South Pole* Geophys. Res. **111** D13203 (2006)

[69] A. Achterberg et al. (IceCube Collaboration) *First Year Performance of the IceCube Neutrino Telescope* Astropart.Phys. 26 (2006) 155

[70] Abbasi et al. (IceCube Collaboration) *The IceCube Data Acquisition System: Signal Capture, Digitization, and Timestamping* Nuclear Instr. and Meth. in Phys. Res. A **601** (2009) 294-316

[71] Heck, D. et al. **CORSIKA**: *A Monte Carlo Code to Simulate Extensive Air Showers* Technical Report 6019, Forschungszentrum Karlsruhe, 1998

[72] Glasstetter,R. et al. *Analysis of Electron and Muon Size Spectra of EAS*, Proc. 26th ICRC, Salt Lake City, USA (1999). HE.2.2.03

[73] Chirkin, D. and Rhode, W. *Propagating leptons through matter with Muon Monte Carlo (MMC)* arXiv:hep-ph/0407075v2

[74] Honda et al. *Calculation of atmospheric neutrino flux using the interaction model calibrated with atmospheric muon data* Phys. Rev. D **75** 043006 (2007). arXiv:astro-ph/0611418v3

[75] Enberg, R., Reno, M.H., and Sarcevic, I. *Prompt neutrino fluxes from atmospheric charm* Phys. Rev. D. **78**, 043005 (2008).

[76] Lundberg, J. et al. *Light Tracking for Glaciers and Oceans - Scattering and Absorbtion in heterogeneous media with Photonics* Nucl. Instr. and Meth. Phys. Res. Sect. A **581** 619 (2007) astro-ph/0702108

[77] taken from http://wiki.icecube.wisc.edu/index.php/New_ice_model

[78] Chirkin, D. *Study of ice transparency with IceCube flashers* IceCube Internal Report 200911002
Abbasi et al. (IceCube Collaboration) *Study of ice transparency with IceCube flashers* To be submitted to Nuclear Inst. and Methods in Physics Research A

[79] Weibusch, C. *The detection of Faint Light in Deep Underwater Neutrino Telescopes.* Ph.D. thesis, Rheinisch Westflische Technische Hochschule Aachen, Aachen, Germany (December 1995). PITHA 95/37.

[80] Kowalski, M. *On the Cherenkov Light Emission of Hadronic and Electro-Magnetic Cascades.* AMANDA Internal Report 20020803 http://icecube.berkeley.edu/amanda-private/reports/20020803-track.pdf

[81] Gonick and Smith *The Cartoon Guide to Statiscics* HarperCollins, New York, NY. (1993) 191

[82] Feldman, G. and Cousins, R. *Unified Approach to the Classical Statistical Analysis of Small Signals* Phys. Rev. D 57 (1998) 3873

[83] Neyman, J. *Outline of a Theory of Statistical Estimation Based on the Classical Theory of Probability* Phil. Trans. Royal Soc. London **A**236 (1937) 333

[84] Hill, G. and Rawlins, K. *Unbiased Cut Selection for Optimal Upper Limits in Neutrino Detectors: the Model Rejection Potential Technique* Astropart. Phys. **19** (2003) 393 arXiv:astro-ph/0209350v1

[85] Mase, K. Private Communication.

[86] Feintzeig, J. *Systematic Studies of Direct Hits using DeltaT Analysis* IceCube Internal Report 201101004

[87] Klein, S. Private Communication.

[88] Barr, G. et al. *A 3-dimensional calculation of atmospheric neutrinos* Phys. Rev. D **70** (2004) arXiv:astro-ph/0403630

[89] Seo, S. Private Communication.

[90] Tegenfeldt and Conrad. *On Bayesian Treatment of Systematic Uncertainties in Confidence Interval Calculation* Nucl. Instrum. Meth. A **539** (2005) 407-413. arXiv:physics/0408039v2
Conrad, J., Botner, O., Hallgren, A., and Perez de los Heros, C. *Including Systematic Uncertainties in Confidence Interval Construction for Poisson Statistics* Phys. Rev. D. **67** (2003) 012002 arXiv:hep-ex/0202013v2

[91] Hill, G. *Comment on "Including Systematic Uncertainties in Confidence Interval Construction for Poisson Statistics"* Phys. Rev. D. **67** (2003) 118101 arXiv:physics/0302057v1 [physics.data-an]

[92] Posselt, J and Christy, B. for the IceCube Collaboration *Search Strategies for Relativistic Monopoles with the IceCube Neutrino Telescope* Proc. of the 32nd International Cosmic Ray Conference, Beijing (2011)

[93] Christy, K. et al. *Evaluating the realistic likelihood of the Chicago Cubs ever winning another World Series* Committee for the Cubs to win so Brian will shave his beard (2011)

[94] Klein, J. and Roodman, A. *Blind Analysis in Nuclear and Particle Physics* Annu. Rev. Nucl. Part. Sci. **55** (2005) 141-163

[95] Cousins, B. Panel discussion for PHYSTAT05 Conference. Courtesy of G. Hill